Bioengineered Collagen Composite Materials as Implantable Artificial Corneas

Mehrdad Rafat

A thesis submitted to the Faculty of Graduate and Postdoctoral Studies
in partial fulfillment of the requirements for the degree of
Doctor of Philosophy
in the Department of Chemical Engineering
University of Ottawa
Ottawa, Canada

May 2007

Canada

uOttawa

L'Université canadienne
Canada's university

FACULTÉ DES ÉTUDES SUPÉRIEURES
ET POSTOCTORALES

u Ottawa

L'Université canadienne
Canada's university

FACULTY OF GRADUATE AND
POSDOCTORAL STUDIES

Mehrdad Rafat

AUTEUR DE LA THÈSE / AUTHOR OF THESIS

Ph.D. (Chemical Engineering)

GRADE / DEGREE

Department of Chemical Engineering

FACULTÉ, ÉCOLE, DÉPARTEMENT / FACULTY, SCHOOL, DEPARTMENT

Bioengineered Collagen Composite Materials as Implantable Artificial Corneas

TITRE DE LA THÈSE / TITLE OF THESIS

Takeshi Matsuura

DIRECTEUR (DIRECTRICE) DE LA THÈSE / THESIS SUPERVISOR

May Griffith

CO-DIRECTEUR (CO-DIRECTRICE) DE LA THÈSE / THESIS CO-SUPERVISOR

EXAMINATEURS (EXAMINATRICES) DE LA THÈSE / THESIS EXAMINERS

David Kaplan

Christopher Lan

Xudong Cao

Kevin Kennedy

Gary W. Slater

Le Doyen de la Faculté des études supérieures et postdoctorales / Dean of the Faculty of Graduate and Postdoctoral Studies

ABSTRACT

The clinical need for an alternative to donor corneal tissue has encouraged much interest in recent years. The development of a reconstructed human cornea is necessary in view of the world-wide shortage of donors, the increasing risk of transmissible diseases, the widespread use of corrective surgery, which renders corneas unsuitable for grafting, and the severe limitations of currently available synthetic polymer-based artificial corneas. The development of a reconstructed human cornea is vital and will represent a real breakthrough, allowing diseased or damaged corneas to be replaced by tissue-engineered corneal implants that resemble in all respects their natural counterparts.

An artificial cornea whether it is a synthetic keratoprosthesis or bio-engineered must fulfill the key functions of the native cornea including transparency, strength, elasticity, biocompatibility, and non-immunogenic. A wide range of implants and biomedical devices have been developed in an attempt to correct corneal blindness. Limitation of existing biomaterials is evident when reviewing keratoprosthesis surgery complications, e.g., infection, intraocular inflammation, retro corneal membrane formation, insufficient interface seal thus epithelial cells down growth, and glaucoma, as well as issues involved with bio-engineered materials such as inadequate mechanical strength and elasticity for implantation, and rapid biodegradation.

My main objective was to address these issues by reconstructing an implantable bio-engineered human cornea with proper bulk and surface properties. More specifically, one of the aims was to develop a well-defined slowly-degradable corneal material with sufficient mechanical elasticity and strength, high optical transparency, and good biocompatibility that allows regeneration of corneal epithelial, stromal, and nerve cells.

Another aim was to engineer material's surfaces to inhibit endothelial cell attachment onto the posterior surface while enhancing epithelial cell attachment onto the anterior one using surface modification techniques such as radio frequency (RF) plasma.

The originality of this study lies in the use of systematic multivariate experimental designs (MED) combined with a novel bio-inspired material development approach to construct hybrid polymer networks (HPN) for artificial cornea application. Material development was carried out by crosslinking of bio-functional natural polymers, e.g., collagen and chitosan with a hybrid amalgamation of synthetic bio-inert molecules, e.g., poly (ethylene glycol) dibutyraldehyde (PEG-DBA), 1-ethyl-3-(3-dimethylaminopropyl) carbodiimide (EDC), and N-hydroxysuccinimide (NHS).

HPNs were designed and fabricated with the aid of a 2^3 full factorial experimental design (FED) merged with a response surface design (RSD). The combined FED/RSD approach allowed us to efficiently evaluate the key experimental factors (e.g., molar ratios of the components), their interactions and their impacts on key responses (mechanical, optical, and biological properties), and to screen and develop optimum material formulations. This strategy resulted in a synergistic effect on physical and biological properties of the materials. It became possible to simultaneously enhance mechanical strength, and elasticity while retaining biological characteristics and optical clarity of the matrices. The select HPN materials were implanted into pig corneas for 12 months and demonstrated successful *in vivo* regeneration of the host corneal epithelium, stroma, and nerves with seamless host-graft integration.

In addition to studies focused on bulk design of corneal materials, design principles for the engineering of surfaces that direct epithelial and endothelial cell

adhesion to the corneal implants were investigated and developed. The designs contributed to the development of epithelial cell-adhering and endothelial cell-resistance surfaces.

Attempts were made to augment attachment of epithelial cells to the surfaces of corneal materials that were crosslinked with glutaraldehyde (GA) and glutaraldehyde-polyethylene oxide dialdehyde (PEO-DA). Argon plasma treatment of corneal surfaces at a RF power of 100 Watts for 30 minutes enhanced the cell attachment, surface hydrophilicity, and roughness.

Prevention of endothelial cell migration onto the posterior surface of HPN corneal implants was achieved using a NH_3 plasma-assisted surface modification technique. Briefly, hydrogels were subjected to ammonia plasma functionalization followed by grafting of alginate macromolecules to the target surface. Treated hydrogel surfaces showed observable decreases in endothelial cell attachment. The decrease in cell adhesion was dependant upon the concentration of alginate and plasma radio frequency (RF) power. High concentrations of alginate of 5% (w/v) and high RF power of 100 W produced surfaces with minimal cell attachment.

I demonstrated that alliance of MED with material and surface sciences played a significant role in development of novel materials that might lay a foundation for a new generation of implantable biomaterials that could be tailor-made into cornea or other tissue/organ transplants such as skin, crystalline lens, liver, and heart.

RÉSUMÉ

Le besoin clinique pour une alternative aux donateurs de tissu cornéen a suscité beaucoup d'intérêt ces dernières années. Le développement d'une cornée humaine reconstruite est nécessaire vu la pénurie mondiale de donateurs, le risque croissant de maladies transmissibles, l'usage répandu de chirurgie corrective qui rend les cornées inaptes au greffage, et les limitations sévères de la disponibilité de cornées artificielles produites à partir de polymères. Le développement d'une cornée humaine reconstruite est vital et représentera une vraie percée, en permettant aux cornées malades ou endommagées d'être remplacé par les implants cornéens tissu-construits qui ressemblent dans tous les hommages leurs équivalents naturels.

Une cornée artificielle qui est soit une kératoprosthèse synthétique ou un bio-construit, doit accomplir les fonctions clés de la cornée native telles que la transparence, la force, l'élasticité. Elle doit aussi être non-immunogène. Une grande gamme d'implants et appareils biomédicaux ont été développés dans une tentative de corriger l'aveuglement cornéen. La limitation des biomatériaux déjà existants se voit évidente avec les complications de la chirurgie du kératoprosthèse, ex : infection, inflammation de l'intraoculaire, rétro formation de la membrane cornéenne, cachet de l'interface insuffisant donc augmentation découragée épithéliale, et glaucome, ainsi que les problèmes associes avec les matières bio-construites tel que la force mécanique inadéquate, l'élasticité pour implantation, et la biodégradation rapide .

Notre objectif principal était de traiter ces problèmes en synthétisant un implantable bio-construit de la cornée humaine avec charge et propriétés de la surface adéquates. Plus spécifiquement, un des buts était de développer une matière cornéenne

lentement-dégradable, précise, avec élasticité mécanique et force suffisantes, une haute transparence optique et une bonne biocompatibilité qui permet la régénération de la cornée épithélial, stromal, et cellules nerveuses. Un autre but était de construire des surfaces de matière qui inhibent l'attachement des cellules endothéliales sur la surface postérieure tout en rehaussant l'attachement des cellules épithéliales sur le côté antérieur, en utilisant des techniques de modification des surfaces par plasma de fréquence radio (RF).

L'originalité de cette étude se trouve dans l'usage de systèmes de dessins expérimentaux à multi variables (MED) combinés avec une approche de développement de matières nouvelles bio-inspirées, afin de construire un polymère hybride établit de contacts (HPN) pour l'application aux cornées artificielles. Le développement de matériel a été effectué par réticulation de polymères naturels bio-utilitaires, ex., collagène et chitosan avec une amalgamation d'hybride de molécules bio-inertes synthétiques, ex., dibutyraldehyde du poly (PEG-DBA) (glycol de l'éthylène), 1-éthyle-3 - (3-dimethylaminopropyl) carbodiimide (EDC), et N-hydroxysuccinimide (NHS).

HPNs ont été conçus et fabriqué avec l'aide d'un plan factoriel plein du type 2^3 (FED) fusionnée avec un dessin de la surface de la réponse (RSD). L'approche de FED/RSD combinée nous a permis d'évaluer efficacement les facteurs expérimentaux clés (ex., ratios molaires des composants), leurs interactions et leurs impacts sur les réponses clés (mécanique, propriétés optiques, et biologiques), et masquer et développer des formulations de matériaux optimums. Cette stratégie a résulté en un effet synergiste sur visite médicale et propriétés biologiques des matières. Il est devenu possible de rehausser simultanément la force mécanique et l'élasticité tout en retenant les

caractéristiques biologiques et la clarté optique des matrices. Les matières HPN choisies ont été implantées dans des cornées de cochons pendant 12 mois et ont démontré être prospère dans la régénération in vivo d'épithélium cornéen, stroma et nerfs de l'hôte avec intégration de l'hôte-greffe sans couture.

En plus d'études concentrées sur la conception de matières cornéennes, la conception de principes pour l'ingénierie de surfaces qui ont pour but de diriger les cellules épithéliales et endothéliales aux implants cornéens, a été enquêtée et développée. Les modèles crées , ont contribué au développement de surfaces résistantes à l'adhésion des cellules 'endothéliales d'un côté, tandis que de l'autres, favorisent l'adhésion des cellules épithéliales. Des tentatives pour augmenter l'attachement de cellules épithéliales aux surfaces de matières cornéennes ont aussi été conçus. Ces dernières surfaces étaient réticulés avec du glutaraldehyde (GA) et de l'oxyde de dialdéhyde du glutaraldehyde-polyéthylène (PEO-DA). Le traitement avec du plasma d'argon des surfaces cornéennes à un pouvoir RF de 100 Watts pendant 30 minutes, a rehaussé l'attachement des cellules, l'hydrophobicité de la surface et la rugosité.

La prévention de la migration de cellules endothéliales sur la surface postérieure des implants cornéens HPN ont été accomplis par modification de surface avec la technique du plasma et un gaz de NH_3. Brièvement, les hydrogels ont été soumis à une fonctionnalisation par plasma avec du gaz ammoniac suivi d'un greffage de macromolécules d'alginate à la surface de la cible. Les surfaces de l'hydrogel traitées ont montré des baisses observables de l'attachement de cellules endothéliales. La baisse de l'adhésion cellulaire était directement reliée à la concentration d'alginate et le pouvoir de

la fréquence radio (RF) du plasma. Les hautes concentrations d'alginate 5% (w/v) et haut pouvoir RF de 100 W ont produit des surfaces ou l' attachement cellulaire était minime.

Nous avons démontré que la combinaison du système MED avec les sciences de la matière et des surfaces, a joué un rôle considérable dans le développement de nouveaux matérielles qui pourraient mettre une fondation pour une nouvelle souche de biomatériaux implantable qui pourraient éventuellement donner naissance à une génération de cornée ou d'autres greffes de tissu/organe tel que peau, lentille cristalline, foie et cœur synthétisés sur mesure.

Acknowledgement

Dedicated to

my dear wife, Shideh, for her love, strength,

encouragement, and unceasing support, in all my undertakings.

TABLE OF CONTENTS

CHAPTER 5: PAPER IV
Surface modification of collagen-based artificial cornea for

List of Tables

List of Figures

*   Pigs were scarified on month 8 post-operation due to high haze and
extensive blood vessels in HPN-1 implanted corneas.
** Arrows show nerve branches.

¥ GA: Artificial corneas fabricated by glutaraldehyde crosslinking of collagen matrices.
¥¥ GA-PEODA: Artificial corneas fabricated by glutaraldehyde crosslinking of collagen matrices followed by crosslinking with poly (ethylene oxide dialdehyde).

¥ Five replicate samples were used in determining the mean value and standard deviation for each data set.
¥¥ The statistical difference between data sets was analyzed using one-way ANOVA.
* $p = 0.0025$ and $p=0.0022$ for the differences between GA & Plasma-treated-GA on day 1 and day 3, respectively.
** $p = 0.0264$ and $p=0.0032$ for the differences between GA-PEODA & Plasma-treated-GA-PEODA on day 1 and day 3, respectively.

¥ Five replicate samples were used in determining the mean value and standard deviation for each data set. The statistical difference between untreated and plasma treated data sets was analyzed using one-way ANOVA.
¥¥ X axis represents the number of days after plasma treatment.
* $p=2.2 \times 10^{-14}$ for GA and $p=1.2 \times 10^{-5}$ for GA-PEODA.

¥ The statistical difference between data sets was analyzed using one-way ANOVA.
¥¥ Three replicate samples were used in determining the mean value and standard deviation for each data set. * $p=0.049 < 0.05$, ** $p=0.002 < 0.05$

Nomenclature

List of Symbols

β	effect coefficient
$f(x, y)$	surface function relative to the center plane
F	F statistics
L_x	surface dimension in the x direction in AFM, nm
L_y	surface dimension in the y direction in AFM, nm
R	surface roughness or the ratio of the actual to the projected area.
R_a	mean roughness, nm
P	probability value
r^2	coefficient of determination
θ_e	equilibrium contact angle

Abbreviations

AC	artificial cornea
AFM	atomic force microscopy
ANOVA	analysis of variance
CAM	contact angle measurement
CFU	colony-forming unit
CTN	chitosan to collagen molar ratio
DRG	dorsal root ganglia
GA	glutaraldehyde
GA-PEODA	glutaraldehyde-polyethylene oxide dialdehyde
HC	human cornea

EB	energy to break
ECG	epithelial cell growth
ECC	endothelial cell count
EDC	1-ethyl-3-(3-dimethylaminopropyl) carbodiimide
EM	elastic modulus
ENDO	endothelium
EPI	epithelium
NHS	N-hydroxysuccinimide
FED	factorial experimental design
FTIR	Fourier transform infrared spectroscopy
HDC	hexamethylen diisocyanate
HCEC	human corneal epithelial cells
H&E	hematoxylin and eosin
HPN	hybrid polymer networks
IOP	intraocular pressure
IVCM	*in vivo* confocal microscopic
KPro	keratoprostheses
KSFM	keratinocyte serum-free medium
LEF	late endothelial failure
LKP	Lamellar Keratoplasty
LT	light transmission
MED	Multivariate experimental design
MES	2-(N-Morpholino) ethanesulfunic acid

NFB	nerve fiber bundle
OFAT	one factor at a time
PBS	phosphate buffer saline
PAR	Pseudomonas Aeruginosa
PEG-DBA	poly (ethylene glycol) dibutyraldehyde
PEGDA	poly (ethylene glycol) diacrylate
PHEMA	poly (2-hydroxyethyl methacrylate)
PKP	penetrating keratoplasty
PLGA	poly(DL-lactic-co-glycolic acid)
PMMA	poly (methyl methacrylate)
PN	polymer network
PPF	poly (propylene fumarate)
PVA	poly (vinyl alcohol)
PEODA	poly (ethylene oxide) dialdehyde
RCFM	retrocorneal fibrous membrane
RF	radio frequency
RSD	response surface design
SA	staphylococcus aureus
SHEM	supplemented hormonal epithelial medium
SPM	Streptococcus Pneumoniae
SP	stromal pressure
UE	ultimate elongation
US	ultimate stress

Statement of Contributions of Collaborators

This research was made possible through support and collaborations from key individuals. I would like to acknwlegde their contributions as following:

1. Professor May Griffith for her advice and guidance through the whole work presented in this dissertation. She and her team at the Ottawa Eye Institute managed to perform all *in vitro* and *in vivo* biological characterizations. Also, she contributed significiantly into the corrections and revisions of the thesis. I acknowledge that without her leadership, technical and financial supports, none of this would have been possible.

2. Professor Takeshi Matsuura for his knowledege, experience, and trust. He contributed significantly in the development of plasma surface modification techniques as well as surface characterization techniques such as Atomic Force Microscopy (AFM) and Contact Angle Measurement (CAM) used in this work. Also, his invalueable comments during revision process of this thesis is gratefully appreciated.

3. Dr. Fengfu Li for his chemistry and biomaterials knowledege and experiences. He contributed toward the application of the right chemistry principles to biomaterials developed in this work.

4. Dr. Malik Hakim for his knowledege on artificial cornea as well as introducing me to the field of cornea. He developed the glutaraldehyde-crosslinked artificial corneas in paper III that were used as substrate for argon plasma treatment.

5. Dr. David Carlsson for his constructive comments on the development of corneal materials. He also helped me develop a standard mechnical testing method for corneal materials and natural tissues. His careful review of paper IV is very much appreciated.

6. Lea Muzakare contributed significantly into the *in vitro* and *in vivo* biocompatibility testing of corneal materials including epithelial and endothelial cells culture, and post-operative evaluations of implanted corneal materials in pigs including slit lamp in vivo histology studies.

7. Donna Grant contributed significantly into the *in vitro* biocompatibility testing of corneal materials including epithelial, endothelial, and DRG nerve cells culture.

8. Dr. Neil Lagali for performing *in vivo* confocal microscopy (IVCM) and interpretation of IVCM results.

9. Dr. Per Fagerholm for implantation of corneal scaffolds into pigs eyes.

10. Dr. Yuwen Liu for DSC results and useful discussions.

11. Dr. Lisha Gan for her help in implanting HPN-1 and HPN-2 corneal materials into pigs and post-operative evaluations including slit lamp studies.

12. Dr. Kilash C. Khulbe for taking AFM images used in paper IV.

13. Cecilia Becerril for excellent lab support and project coordination.

14. Dr. Mitchell A. Watsky for glucose and albumin diffusivity tests.

15. Dr. Tito Scaiano and Belinda Heyne for conducting UV irradiation tests.

Major Contributions to Knowledge

Patents
- Interpenetrating Networks, and Related Methods and Compositions, PCT/CA2006/001520, IPN: WO 2007/028258 A2. Co-inventor.
- Vision Enhancing Ophthalmic Devices and Related Methods and Compositions. PCT/US2005/028723. Co-inventor.
- Ophthalmic Devices and Related Methods and Compositions, CT/CA2005/001240.Co-inventor.
- Collagen-Based Artificial Cornea for Transplantation, Application has been filed with the technology transfer and business enterprise (TTBE) office of the University of Ottawa. Co-inventor.

Publications

Manuscripts Published or In Press:
- **Mehrdad Rafat**, May Griffith, Malik Hakim, Lea Muzakare, Frank Li, K.C. Khulbe, and Takeshi Matsuura, "Surface Modification and Characterization of Artificial Cornea for Enhanced Epithelialization", *Journal of Applied Polymer Science*, in press, Manuscript ID: APP-2006-01-0204 accepted on July 27, 2006.
- **Mehrdad Rafat**, Takeshi Matsuura, Frank Li, and May Griffith "Surface Modification and Characterization of Artificial Cornea for Reduced Endothelialization", Journal *of Biomedical Materials Research*, Manuscript ID: JBMR-A-07-0320-R1, Accepted on November 9, 2007.
- Takeshi Matsuura, and **Mehrdad Rafat**, "Polymeric Membranes", *Encyclopaedia of Chemical Processing*, Ed. K.B. LEE, Marcel Dekker, New York, NY, USA, 2005.
- K. C. Khulbe, C. Y. Feng, T. Matsuura, D. C. Mosqueada-Jimenaez, **Mehrdad Rafat**, D. Kingston, R.M. Narbaitz, M. Khayet,"Characterization of Surface Modified Hollow Fiber Polyethersulfone Membranes Prepared at Different Air Gaps", *Journal of Applied Polymer Science*, Vol. 104, 710–721, 2007.
- Christopher McLaughlin, P. Fagerholm, Lea Muzakare, Neil Legali, J.V. Forrester, L. Kuffova, **Mehrdad Rafat**, Yuwen Liu, N. Shinozaki, S.G. Vascotto, David Carlsson, Rejean Munger, and May Griffith, "Tissue Engineered Collagen Corneal Substitutes for Transplantation", Accepted, *Cornea*, 2007.

Manuscripts Submitted, or Ready for Submission:
- **Mehrdad Rafat**, Li F, Fagerholm P, Lagali N, Watsky MA, Heyne B, Hasanloo M, Scaiano JC, Munger R, Hodge W, Matsuura T, Griffith M. "PEG-Stabilized Carbodiimide Crosslinked Collagen-Chitosan Hydrogels for Corneal Tissue Engineering, to be submitted to *Biomaterials*, 2007.
- **Mehrdad Rafat**, Takeshi Matsuura, and May Griffith, "Multivariate Experimental Design for Rational Development of Bioengineered Hybrid Polymer Networks for Corneal Tissue Engineering", to be submitted to *Biomaterials*, 2007.

Manuscripts in Preparation:
- **Mehrdad Rafat**, Diana Malouf, May Griffith, and Takeshi Matsuura, "Surface Grafting of Polyethyleneglycol Dibuthylaldehyde to Artificial Cornea Surfaces for Reduced Endothelialization", to be submitted to the *Journal of Biomedical Materials Research*, 2008.
- Wenguang Liu, Kenneth D. Camm, Fengfu Li, Lisha Gan, **Mehrdad Rafat**, Lea Muzakare, Jennifer L. Snelgrove, Mitchell A. Watsky, Yuwen Liu, Deryn E. Fogg, and May Griffith, "ROMP-Based Neoglycopolymers as Biomimetic Cross-linkers for Tissue Engineering", to be submitted to *Nature Materials*, 2008.
- Wenguang Liu, Frank Li, **Mehrdad Rafat**, Donna Grant, Cecilia Beceril, Mitchel Watsky and May Griffith, "Corneal Substitutes from Recombinant Human Collagen", to be submitted to *Biomaterials*, 2008.

Conference Presentations
- International Conference on Advances in Biomaterials for Drug Delivery and Regenerative Medicine, Capri, Italy, June 11-16, 2006, "Surface Modification and Characterization of Artificial Cornea for Reduced Endothelialization".
- 19th Annual Eye Institute Research Day, Ottawa, Canada, May 2005, Novel Biosynthetic Polymers for Corneal Applications.
- BioNorth 2004 Conference, Ottawa, Canada, Nov. 2004, "Surface Modification and Characterization of Collagen-based Artificial Cornea for Enhanced Epithelialization".
- Universidad Complutense, University of Madrid, seminars of the Department of Applied Physics I, March 31, 2004, "Surface Modification and Characterization of Collagen-based Artificial Cornea for Enhanced Epithelialization".
- 11th Iranian Biomedical Engineering Conference, Tehran, Iran, Feb. 2004, Argon Plasma Treatment of Collagen-based Artificial Cornea for Enhanced Epithelialization".
- Ottawa Health Research Institute Research day, Ottawa, Canada, Nov.2003, "Surface Modification and Characterization of Artificial Cornea for Enhanced Epithelialization".

2. Unpublished Contributions
- Developed a biopolymer solution mixing system reducing mixing time from 14 days to 6 hrs (See Appendix A).
- Developed a standard mechnical testing method for corneal materials and natural tissues (See Appendix B).

Chapter 1

Introduction

1.1 Rational for Developing Artificial Corneas

Corneal diseases are a main cause of blindness, second to cataract in overall importance. There are nearly 45 million blind people worldwide and an additional 135 million with severely impaired vision [1] about 20% of which are corneal related (corneal scarring (trachoma), corneal opacity, and childhood blindness) (See Fig.1.1). In addition, blindness is believed to be on the rise and every five seconds one person in the world goes blind that is equivalent of about 1.2 million new cases of corneal blindness every year [2]. In addition, there is an immediate need for corneal replacement, over 10 million patients worldwide [3].
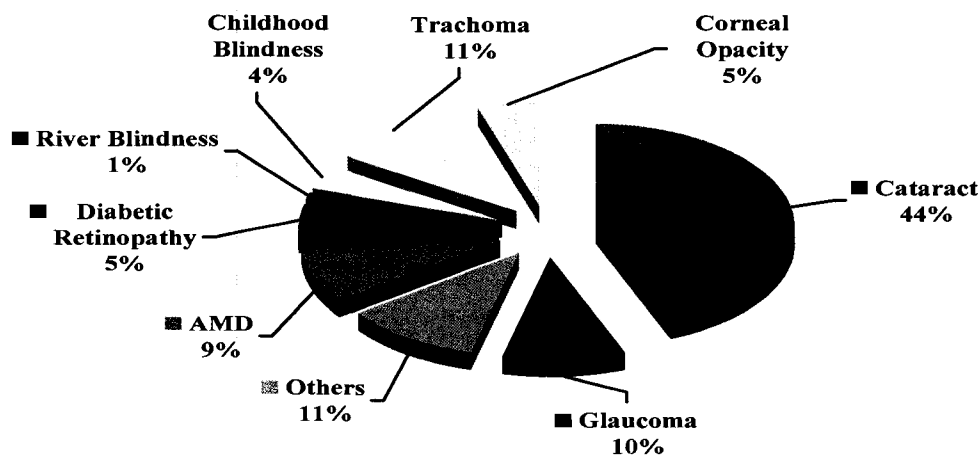
Figure 1.1 Global causes of blindness in year 2001. Trachoma (corneal scarring), corneal opacity, and childhood blindness are corneal related diseases comprising about 20% of total blindness [1,2,6].

1

Diseased or damaged corneas are typically replaced by donor human corneas from deceased patients using corneal transplantation including Penetrating Keratoplasty (PKP) and Lamellar Keratoplasty (LKP). Corneal transplants are the most commonly performed and successful type of organ transplant because there are so few blood vessels in the cornea that corneal antigens may never enter the host's system to stimulate an immune reaction [4]. Although, corneal transplantation is highly successful in restoring vision a significant shortfall in donor numbers exists; it is estimated that only about 100,000 corneal transplants are performed each year worldwide, only a fraction of the number that need a new cornea urgently [5]. Demographic factors such as human population's size and growth combined with adverse environmental factors such as air and water pollution and an increase in UV irradiation have increased the need for corneal replacement while same factors have decreased the supply of healthy donor corneas. In 2001, there were 2,600 corneal transplants performed across Canada with 3,300 Canadians still on the waiting list. There is a critical shortage across Canada and the need for corneal transplants has been doubled over the past 12 years. The increasing need in the Western nations is mostly due to the aging population while it is mostly associated with the population's growth and environmental factors in developing contries [6].

It is also reported that the success rate of donor corneal transplants drops dramatically when the host cornea is extensively scarred, deeply vascularized, with the characteristics of the tear film altered, or in the presence of *glaucoma*. There is also a poor outcome when patients are affected by specific conditions such as *severe chemical burns, Stevens-Johnson syndrome, trachoma, severe dry eye syndrome* involving limbal stem cell deficiencies [7]. In addition to the shortage of donor cornea and the low success

rate in specific cases, there are other drawbacks including risk of disease and infection transferal from donor patient to recipient, problems involved with the storage and transportation of donor corneas from one continent to another, and difficulty in manipulating human donor corneas characteristics to meet specific needs of the recipient.

An alternative implant is therefore needed urgently to replace the damaged and clouded cornea and satisfy the rapidly growing need for corneal replacement globally. Such an alternative is an artificial corneal (AC) implant or a keratoprosthesis that may offer hope for the many patients in underdeveloped countries, for whom donor corneal tissue and an organized eye banking system seem unlikely to become widely available in the foreseeable future [8]. If an AC is to replace a diseased or damaged cornea it must be biocompatible and have many functional properties including transparency, refraction, and sufficient mechanical strength and elasticity to protect the eye. To this aim, over the past 40 years, an increasing interest into the design of an artificial cornea in the form of a synthetic keratoprosthesis, and more recently that of the bioengineered cornea has been developed.

1.2 Problem Statement

To date, despite the outstanding advances in all categories of corneal materials, the currently available ones are far from being ideal and there have been no reports of widely accepted corneal matrices that optimally meet all of the criteria necessary for the success of a transplantable artificial cornea [8, 9]. This is mostly attributed to the poor biological characteristics of synthetic matrices and deprived mechanical properties (lack of strength and elasticity) of naturally derived bioengineered scaffolds. This is a tragic,

unacceptable situation in the world today in both humanitarian and economic terms that needs to be addressed immediately.

Keratoprosthesis (KPro) that have been developed to date have been primarily composed of synthetic polymers such as poly methyl(methacrylate) (PMMA), poly (2-hydroxyethyl methacrylate) (pHEMA), and poly (vinyl alcohol) (PVA). Majority of these KPro devices have suffered from bioincompatibility that results in an inability of host cells such as epithelial cells and keratocytes to colonize the material leading to the postoperative complications such as inflammation, ulceration, epithelial downgrowth, formation of retrocorneal membrane behind optic, leakage of aqueous humor, corneal melt, and eventual implant extrusion [8]. Although there have been many attempts at development of biocompatible synthetic implants [10] many complications still persist and the only KPro that has continued to human clinical trials [11] suffers from non-appealing appearance and lack of support for epithelialization, and nerve innervations [12, 13].

Bio-engineering is a more novel technique, and still at the investigatory stage, for the development of corneal materials whereby healthy mammalian cells are used with a supporting matrix to produce a composite implant *in vitro* or *in vivo*. Various investigators have developed methods for the fabrication of bio-engineered corneas from corneal cell lines and naturally derived materials such as collagen [13-20]. However, the materials developed so far are not tough and elastic enough for PKP transplantation and further design and fabrication is necessary to produce an implant with similar tensile strength and durability as a normal cornea while conserving/enhancing the optical characteristics and biocompatibility.

1.3   Objectives and Scope of the Research

The main objective of this study was to develop bioengineered transplantable corneal materials that combine the bioactive features of natural materials (e.g., collagen) and physical characteristics of synthetic ones (e.g., poly (ethylene) glycol) to achieve synergy between the desirable mechanical properties of some components with the biological compatibility and physiological relevance of others. More specifically, the goals of this research were:

1. To utilize *Multivariate Experimental Design* such as factorial design aiming at the development and engineering of complex networks, e.g., hybrid polymer networks (HPN) as implantable materials that mimic human tissues such as cornea in key physical and physiological functions.

2. To develop a hybrid strategy to simultaneously enhance mechanical strength and elasticity of bioengineered corneal materials while retaining biocompatibility and optical clarity of the matrices.

3. To apply surface modification techniques such as radio frequency (RF) plasma treatment to engineer surfaces that modulate cell adhesion without changing the bulk properties in order to direct cell functionality at the interface of the corneal materials and the biological environment.

4. To enhance epithelial cells migration and adhesion to the artificial cornea's anterior surfaces for *in vitro* and *in vivo* studies. The growth of native corneal epithelial cells over the anterior surface of an AC is desired because it functions to block the passage of foreign materials and provides a smooth surface that can easily absorb oxygen and nutrients from tear film.

5.   To deter endothelial cells migration and adhesion to the artificial cornea's posterior surfaces for *in vivo* studies. Endothelial migration from surrounding host tissue is know to effect the formation of retrocorneal membrane onto the posterior of the implants that may compromise the optical characteristics of the implanted artificial cornea as well as eliciting immunogenetic response.

1.4   Thesis Outline

The design concepts for bio-engineered corneal materials and their *in vitro* and *in vivo* characterizations have been summarized in this study. This thesis addresses the specific aims outlined in section 1.3, and is organized in the following format: Chapter 1 provides background of the field, problem statement, significance of this study, and review of the prior art. Chapter 2 addresses objective 1 and details *Multivariate Experimental Designs* such as *factorial* and *surface designs* to systematically design, fabricate, and optimize HPN scaffolds. The hybrid concept and chemistry underneath the development of HPN scaffolds and their extensive characterization for corneal application aimed at objective 2 is described in Chapter 3

Chapter 4 addresses the topic in objectives 3 and 4 showing that surface chemistry that was modulated by argon plasma could enhance epithelial cells adhesion to collagen-based glutaraldehye-crosslined corneal materials. Chapter 5 presents development of a plasma-assisted surface modification technique to deter endothelial cells migration and adhesion to the artificial corneas' posterior surfaces (objectives 3 and 5). Chapter 6 provides an overall discussion, conclusion, and recommendations followed by supplemental materials summarized in appendices in Chapter 7 of the thesis.

1.5 General Review of the Literature

1.5.1 Anatomy and Functionality of the Cornea.

The cornea acts as a clear, transparent window at the front of the eye, and as such has various properties and functions, which are a prerequisite to any artificial replacement (See Fig.1.2) [21]. The cornea offers 75% of the refractive power of the human eye, allowing transmission of light through it to be focused onto the retina. As well as photo-protection, by significant absorbance of UV radiation [22], the cornea acts as a thick, elastic physical barrier protecting the internal ocular structures from outside insults, which may be physical, chemical or microbial. Furthermore, the cornea withstands changes in intraocular pressure (IOP) and curvature changes of the eye. Transparency is obviously essential to vision. It is the cornea's complex multilayered structure that allows it to fulfill its functions as described above. If the cornea is affected by diseases or external insults, it loses its transparency resulting in partial or full blindness.
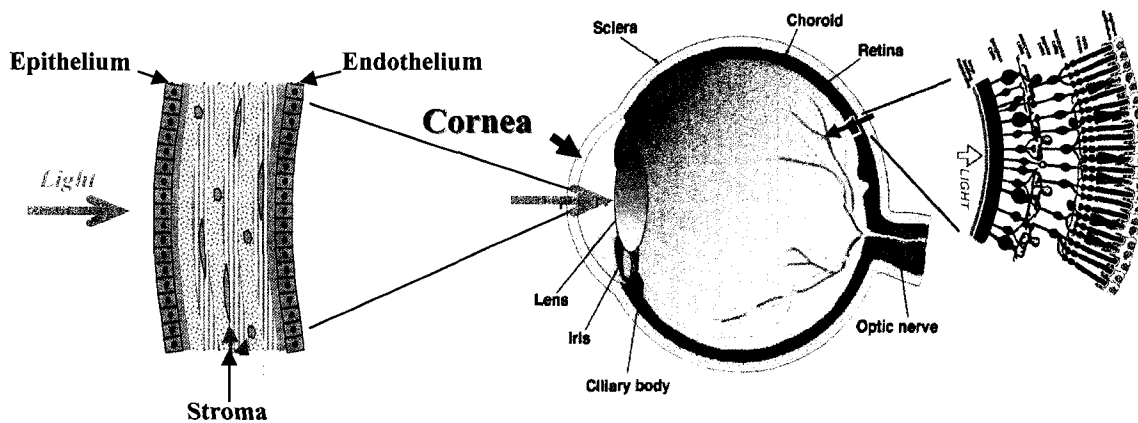
Figure 1.2   Anatomy of the eye and the cornea [21].

The cornea is a smooth, clear tissue with a thickness that is approximately 0.52 mm centrally and 0.65 mm peripherally and its average horizontal diameter is 11.7 mm [23]. Unlike most tissues in the body, the cornea contains no blood vessels to nourish or protect itself against infection. Instead, the cornea receives its nourishment from the tears and aqueous humor that fills the chamber behind it. The cornea must remain transparent to refract light properly, and the presence of even the tiniest blood vessels can interfere with this process [24]. To see well, all layers of the cornea must be free of any cloudy or opaque areas. Though the cornea is clear and seemingly lacks substance, it is densely innervated with sensory nerve fibres that make it one of the most sensitive tissues of the body [25]. As shown in Fig. 1.3, the cornea is a highly organized group of cells and proteins arranged into five differentiated layers [26]:

Epithelium: The outermost surface consists of 5-7 layers of cells which are connected by intercellular junctions and embedded into the underlying basement membrane by hemidesmosomes to form a stratified epithelium. This accounts for 10% of the corneal depth and provides its protective semi permeable barrier function, provides a smooth surface that can absorb oxygen and nutrients from tear film, and creates a barrier to the flow of water into the cornea from tear film [23]. The epithelium is filled with thousands of tiny nerve endings that make the cornea extremely sensitive to pain when rubbed or scratched.

Bowman's layer: The thin layer underneath the epithelium that serves as the foundation on which the epithelial cells anchor and organize themselves. It is a transparent sheet of tissue composed of irregularly-arranged collagen fibers. Once

8

injured, Bowman's layer can form a scar as it heals. If these scars are large and centrally located, some vision loss can occur.
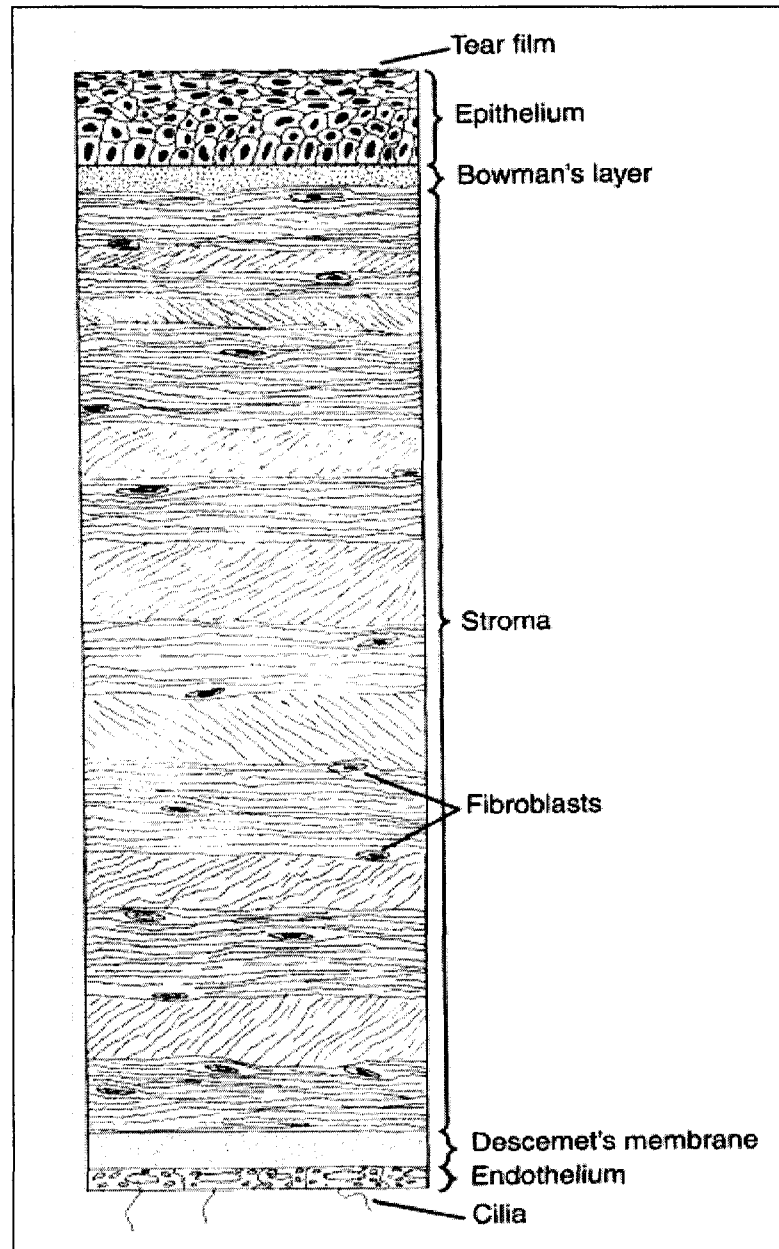
Figure 1.3 Schematic of cornea cross section: five layers of human cornea [23].

Stroma: A layer accounting for 90% of the cornea's thickness, consisting primarily of hydrated extracellular matrix (ECM) (78 % water, 16% collagen, 6% proteoglycans and other minor proteins) with a population of fibroblast-like cells known as keratocytes. Stromal collagen consists of small diameter ($\approx$45nm) type I (70%) and type V (20%) collagen fibrils that give the cornea its strength, elasticity, and form. The collagen fibers' unique shape, highly ordered lattice structure and spacing are essential in producing the cornea's light-conducting transparency [9]. The ordered structure is maintained by optimal stromal deturgescence (the balance of hydration in the eye.) under physiological conditions, which in turn is dependent on a balance of stromal imbibition's, due to the presence of water-seeking proteoglycans and water extrusion from the stroma via the actively pumping monolayer of endothelial cells that form the innermost layer of the cornea (Fig. 1.4 (a)).

Descemet's Membrane: A thin but strong sheet of tissue that serves as a protective barrier against infection and injuries. Descemet's membrane is composed of collagen fibers (different from those of the stroma) and is made by the endothelial cells that lie below it. Descemet's membrane is regenerated readily after injury.

Endothelium: The extremely thin, innermost layer of the cornea. Endothelial cells are essential in keeping the cornea clear. Normally, fluid leaks slowly from inside the eye into the middle corneal layer (stroma). The endothelium's primary task is to pump this excess fluid out of the stroma. Without this pumping action, the stroma would swell with water, become hazy and ultimately opaque (Fig. 1.4.b). In a healthy eye, a perfect balance is maintained between the fluid moving into the cornea and fluid being pumped

out of the cornea. Once endothelium cells are destroyed by disease or trauma, they are lost forever, resulting in corneal edema and blindness.

(a)   (b)
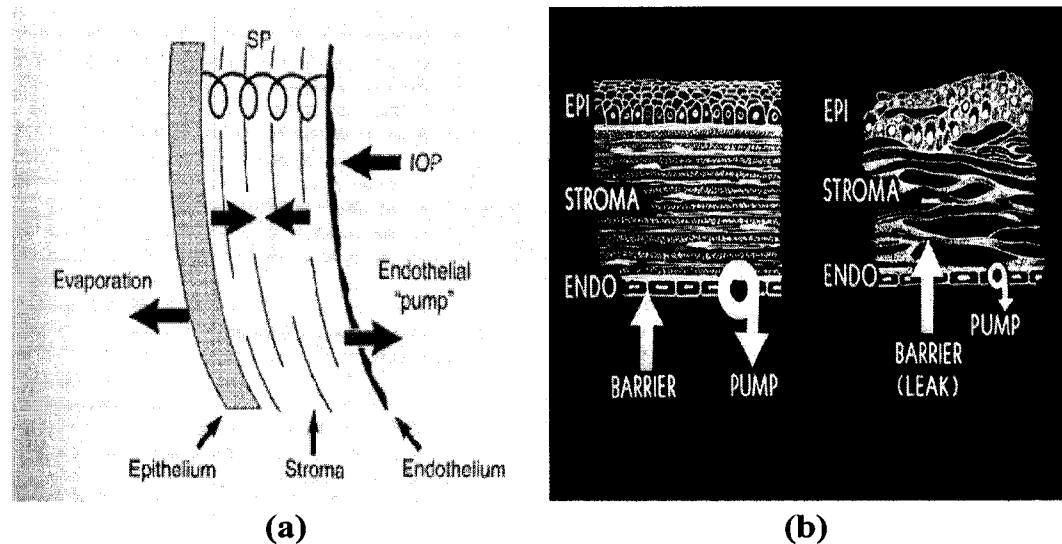
Figure 1.4   Stromal swelling pressure is balanced by (a) the endothelium and epithelium barriers and (b) endothelial metabolic pump system [23].
*SP: Stromal pressure, IOP: intraocular pressure,
EPI: Epithelium, ENDO: Endothelium.

1.5.2 Tissue Engineering of the Cornea: Scaffold Materials

Tissue-engineering is a relatively new approach whereby healthy mammalian cells are used with a supporting matrix to produce a composite implant. *In vitro* Tissue Engineering techniques involve the manipulation of these cells and scaffolds prior to their use for implantation into the *in vivo* environment [27]. Before the tissue can be assembled for implantation, some major requirements must be met. One such requirement and engineering design problem is the choice of proper bioactive scaffold material with

correct chemical/physical properties to promote cell differentiation/integration and tissue formation in a uniform manner that is repeatable and reliable [28].

These scaffold materials are basically selected from biopolymers defined as biological macromolecules in which many identical or similar small molecules are covalently linked to one another to form long chains [29]. These materials are produced by/from micro-organisms, plant or animal materials, or chemically synthesized, and can be classified into five major groups: proteins, polysaccharides, nucleic acids, lipids, and hybrids as shown in Fig. 1.5. Because of the focus of this research we only describe three of biopolymers in the following sections including collagen, chitosan, and alginate.
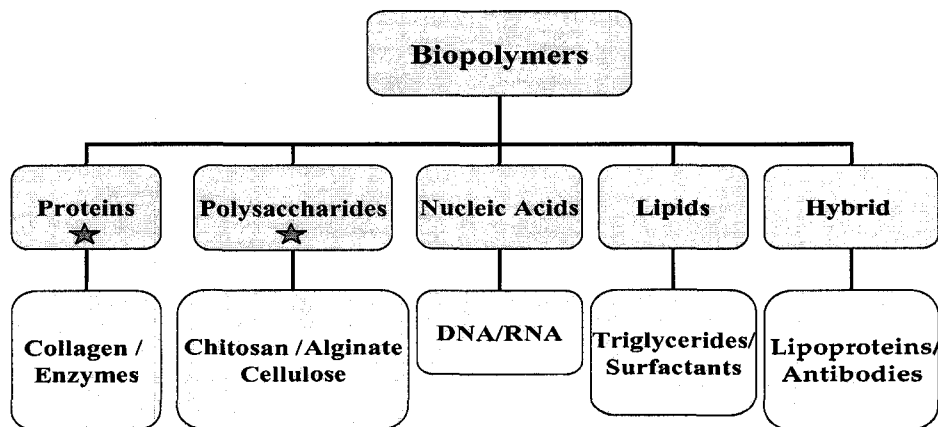
Figure 1.5   Classification of biopolymers [29].

1.5.2.1   Collagen

Collagen is the most commonly used naturally occurring scaffold material. The word "collagen" comes from the Greek, and means "glue producing". The collagens are a family of highly characteristic fibrous proteins to provide tensile strength and elasticity to matrices supporting body cells and tissues. Collagens are found

in all multi-cellular animals and accounts for approximately 30% of all body proteins

[30]. Collagen is a protein of great structural importance to the eye just as it is for other

parts of the body. Approximately 80% to 90% of the bulk of the eye contains collagen.

This protein is an extracellular, insoluble molecular complex that has a variety of

morphological roles. Collagens act as: (1) supporting scaffolds to maintain tissue

structure, (2) anchoring devices to hold cells onto non-cellular areas (See Fig. 1.6). In the

eye, collagen also makes up the *semi-liquid gel* of the *vitreous humor*, therefore, has a

third role as well [31].
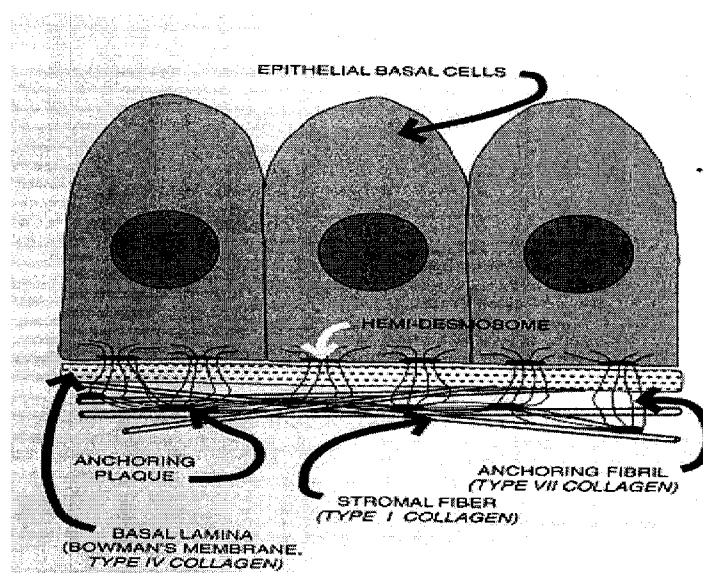
Figure 1.6   Collagen roles in the cornea as supporting scaffolds to maintain tissue
structure, and anchoring device to hold epithelial cells onto place [31].

There are at least 12 types of collagen (out of 19 in total) that have been found in

the eye [32]. All collagens are protein complexes whose basic units consist of some triple

helices (tropocollagen) in which three polypeptide chains are wound around each other

like a piece of rope. Collagen molecules are self-assembled into micro-fibrils and then

fibrils. Collagen fibrils will then form a collagen fiber by their aggregation as shown in

Fig. 1.7.
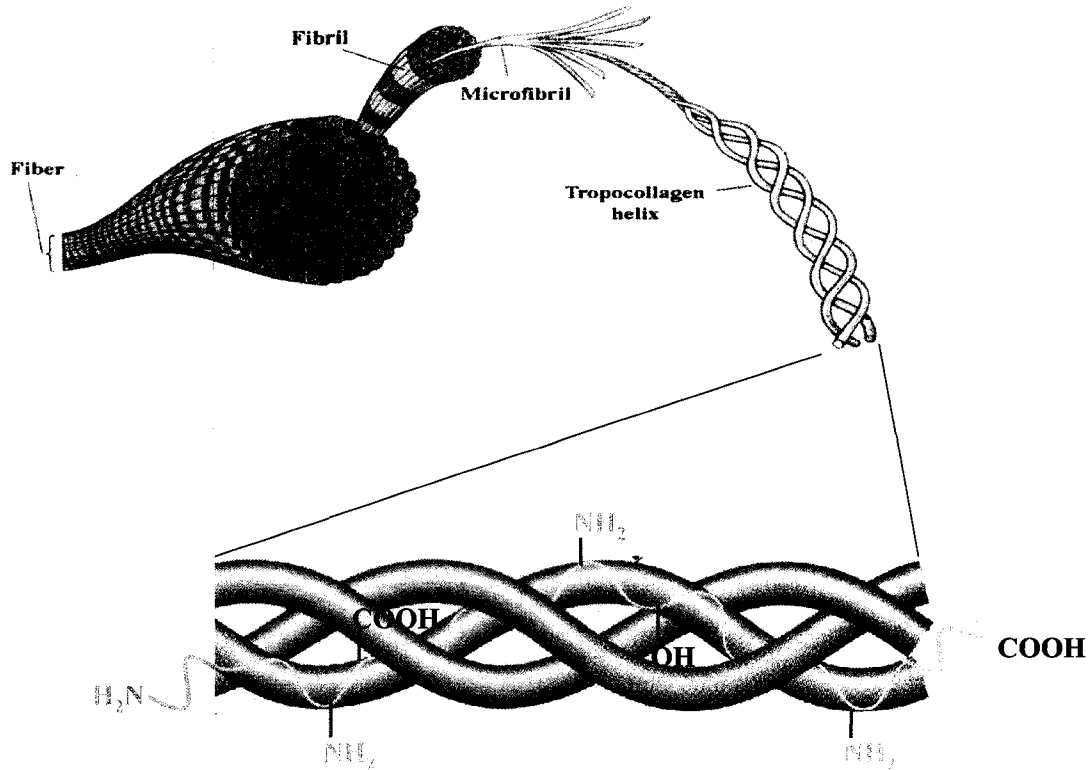
Figure 1.7   Schematic of collagen triple helix (tropocollagen), microfibrils, fibrils, and fibers [33].

The assembled structure of collagen molecules are best understood in terms of how cells make them. As with all proteins, collagen peptide synthesis occurs by reading their specific sequence (code) from messenger RNA. After synthesis of collagen polypeptide chains in the cell, three chains associate together along common hydrophobic areas. The formation of disulfide bonds at the C-terminals causes the three chains to wrap around each other and form a triple helix (procollagen) as shown in Fig. 1.8.

14

(a) Formation of tropocollagen

Procollagen

H₂N COOH

Procollagen peptidase

N-terminus end cleaved   C-terminus end cleaved
Tropocollagen 3000Å

(b) Association of tropocollagen into collagen fiber

Glycine Residues ( )

15Å

Formation of cross-links

400Å
C-terminus   N-terminus

Aldol
cross-link

Aldol-histidine
cross-link
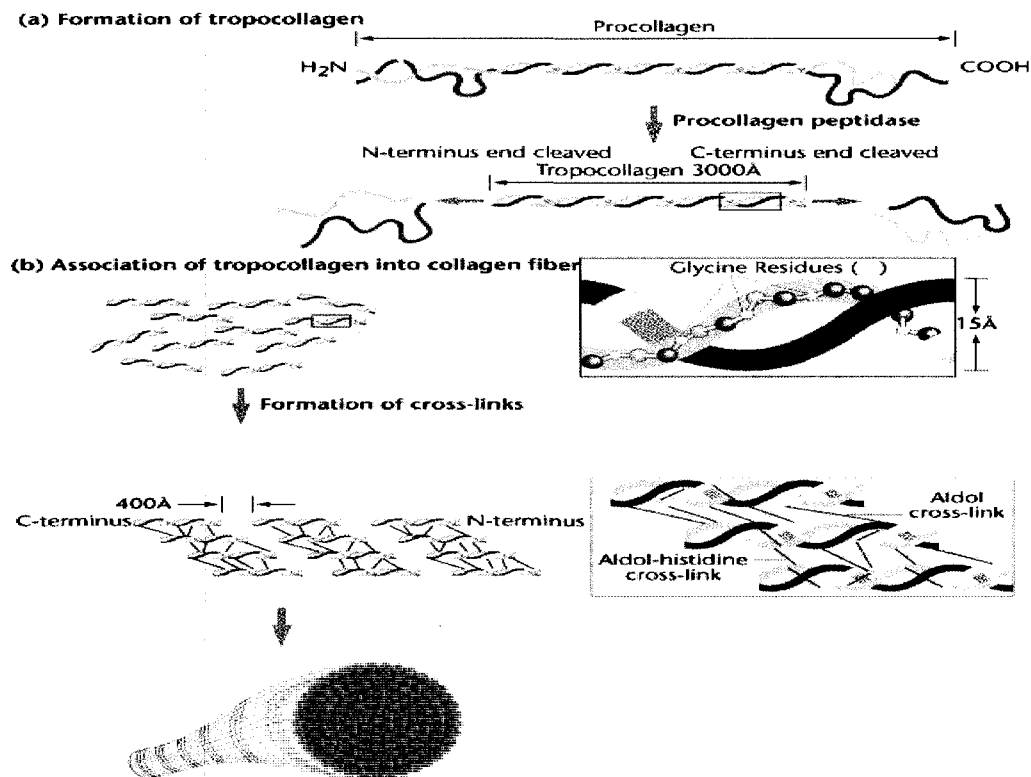
Figure 1.8   Collagen fiber formation from tropocollagen [34].

The procollagen molecule is now ready for transport outside the cell. Take note that the ends of the molecule do not form a helix. The ends of the molecule become hydrolyzed by peptidase to form tropocollagen molecule, which is the building block of collagen fibers. Once outside the cell tropocollagen molecules go through a process of assembly in close proximity of cell's surface. The process consists of the lateral association of tropocollagen units that are staggered lengthwise in three dimensional space. This association is made up of hydrophobic interactions and the formation of crosslinks of lysine and hydroxylysine as shown by slanted lines of the microfibrils in Fig. 1.8 [34]. Crosslinking adds considerable strength to the growing fiber.

15

As depicted in Fig. 1.9, collagen can also be extracted from native tissues such as tendons and ligaments from human or animal sources by pepsin treatment. Immunogenic components are removed and collagen molecules dissolved in acidic solutions, and then reconstituted into fibrils that can be fashioned into a variety shapes and sizes that mimic body structures such as skin, and cornea.
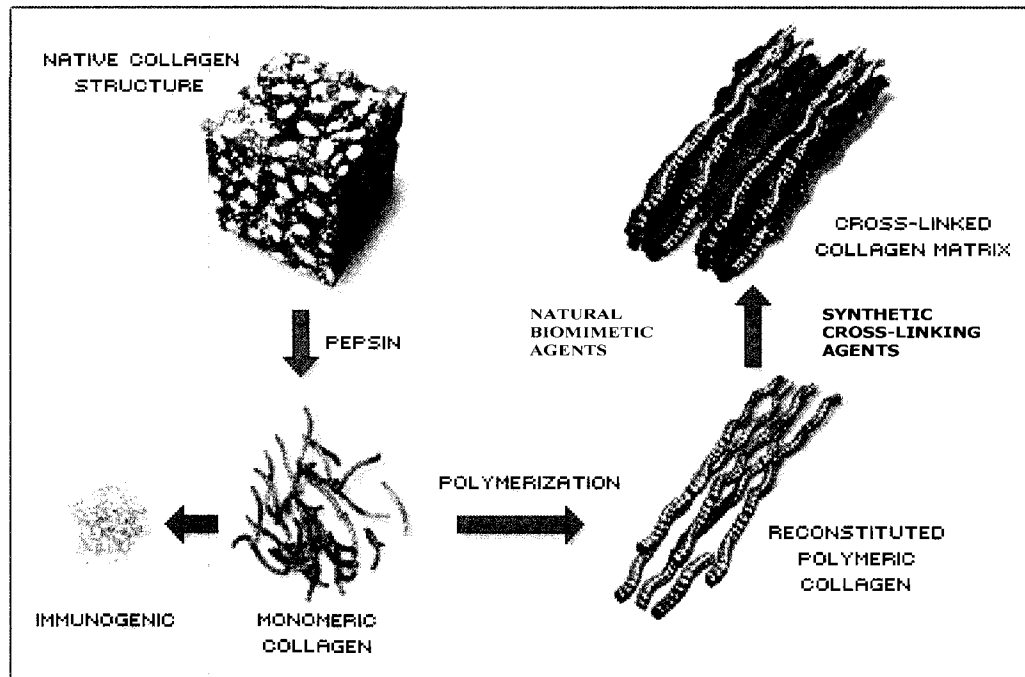
Figure 1.9   Collagen extraction and reconstruction [33].

1.5.2.2   Chitosan

Chitosan is an amino polysaccharide (poly-1, 4-d-glucoamine) derived from chitin by deacetylation. Chitin is one of the most abundant polysaccharides found in nature. It is almost as common as cellulose, and possesses many of the structural and chemical characteristics of cellulose. Chemical structures of chitin, chitosan, and cellulose are shown in Fig. 1.10 for comparison. Chitin and chitosan are identical in composition except for the acetylated amine groups ($NHCOCH_3$).The only difference between

cellulose and chitosan is that cellulose has hydroxyl (OH) groups instead of amino (NH_2) groups.
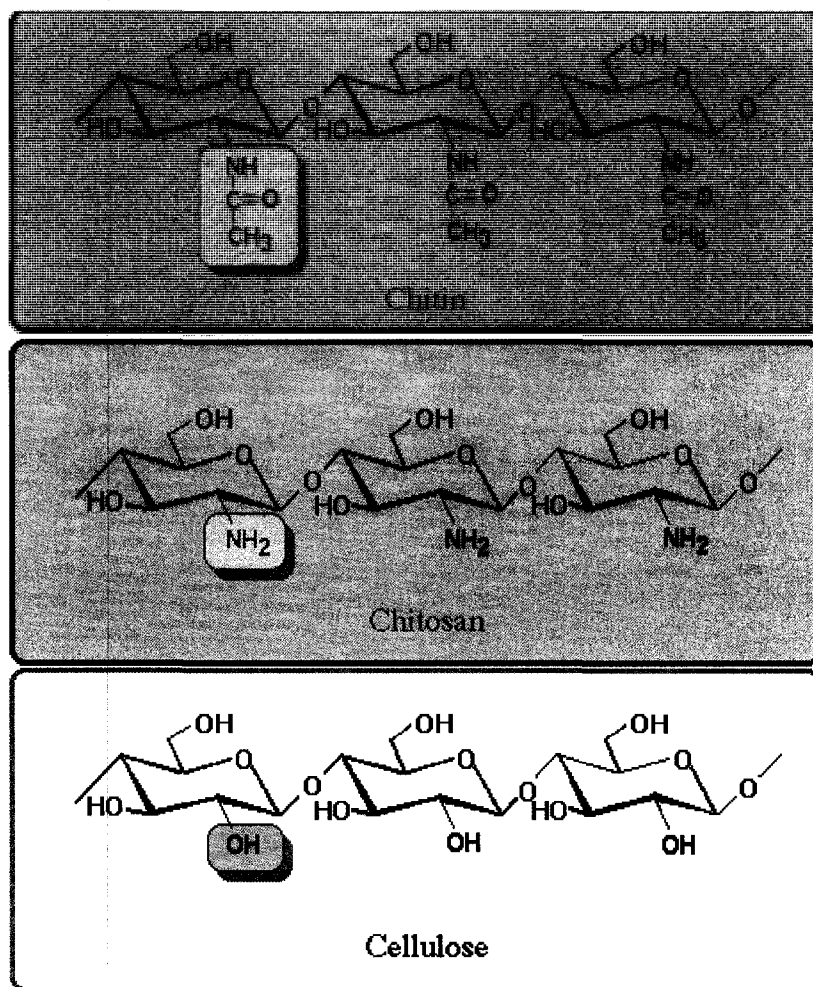
Figure 1.10 Chemical structures of some important polysaccharides: chitin, chitosan, and cellulose [35].

Chitin is an important structural component of the exoskeleton of a great number of organisms such as insects, shrimp and shellfish. It also serves as a cell wall component of fungi and of numerous plankton and other small organisms in the ocean. Because of the different biological requirements of these various species, chitin is an extremely versatile natural polymer. Chitin and its most important derivative, chitosan, have a number of useful physical and chemical properties, including high strength,

biodegradability, and non-toxicity. Chitosan has been widely used in biomedical applications, e.g., for development of scaffolds for artificial liver [36], as skin transplant [37], wound dressings [38], and drug delivery systems [39]. Chitosan makes a good biomimetic component for extracellular matrices (ECM) owing that to its structural similarity to proteoglycans that are one of the main constituents of ECM. This is mostly attributed to its reactive amino and hydroxyl groups that can be chemically modified and also the fact that it can be easily manipulated for different pore structures [40, 41]. However, it is reported that chitosan promotes surface-induced thrombosis [42, 43].The high thrombogenetic property has limited its applications in blood-contacting biomaterials while it is still a good potential biomaterial for corneal application because of non-vascular nature of the cornea (no blood vessels).

1.5.2.3   *Alginate*

Alginate is a naturally abundant anionic polysaccharide that is widely used in biomedical applications such as dental impression materials and wound dressing. It is a hydrophilic polysaccharide extracted from seaweed. Alginate has a linear structure that is composed of a disaccharide repeating unit, made of two uronic acids, α-L-guluronic acid (G) and β-D-mannuronic acid (M) and as shown in Fig. 1.11 [44].
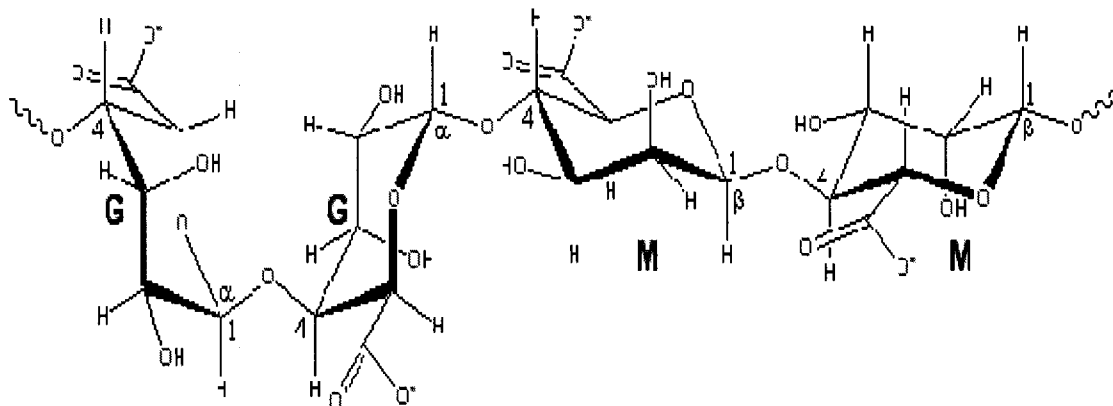
Figure 1.11 Molecular structure of alginate composed of block alternating sequences of two sugars: poly (L-guluronate)(G), and poly (D-mannuronate)(M) [44].

The relative abundance of G and M blocks affects the properties and structure of alginate macromolecular chains and their interaction with water and dissolved cations. Higher G containing alginate solutions tend to form more rigid gels at a very specific concentration of cations whereas higher M containing solutions tend to form softer gels and over a wider range of conditions [45, 46].

1.5.3 Desired Characteristics for a Transplantable Artificial Cornea.

All materials that are considered for corneal implants must meet not only the material requirements specified for this application, e.g., transparency, and elasticity, but also being compatible with the biological environment of the eye, and not induce inflammatory or immune responses. In detail, artificial corneas must meet the following requirements, without exception, for their successful applications:

• Biocompatible and non-cytotoxic so they can properly integrate into the host tissue.

• Provide a watertight junction with the host tissue preventing infection and epithelial down growth.

- Support epithelial cell growth over the anterior surface forming a wettable, self-renewing layer that promotes a healthy tear film.

- Support nerve innervations for high touch sensitivity.

- Prevent migration of host endothelial cells onto its posterior surface, which is known to be responsible for the formation of retro-corneal membranes.

- Promote penetration and proliferation of host fibroblast cells for tissue regeneration.

- Exhibit optical transparency higher than 85% and light scatter of lower than 5%.

- Exhibit suitable morphology and curvature to obtain the appropriate refractive index.

- Exhibit flexibility and sufficient tensile strength to allow surgical manipulation and fixation and can protect the eye.

- Exhibit sufficient swelling in aqueous solutions similar to that of native cornea.

- Permeable to oxygen and nutrients such as glucose and albumin.

- Non-expensive and easy to fabricate.

1.5.4 Prior Studies on the Development of Artificial Cornea

The history of artificial cornea has been reviewed in great detail by several reviewers [47-54]. Research into the development of an artificial cornea has existed for more than two hundred years [48], with the original glass and quartz optics being put forward in 1789 by Guillaume Pellier de Quengsy [49]. Since then, there have been several attempts at developing artificial corneas [13-20, 56-60]. As mentioned earlier, artificial corneas can be broadly divided into two categories: synthetic-based (Keratoprosthesis or KPro) and natural-based (bioengineered) that will be briefly described below.

1.5.4.1   Synthetic-based Artificial Cornea (Keratoprosthesis):

The early attempts to develop artificial corneal transplants utilized rigid synthetic polymers such as poly (methyl methacrylate) or PMMA because of their excellent optical properties. However, serious complications were encountered, due to the incompatibility of these materials with the corneal epithelium. Afterwards, the researchers focused on using soft, elastomeric polymers such as Silastic hydrogels. Although the biocompatibility was improved, these materials had relatively poor optical properties [57]. While PMMA still remains a popular material, PHEMA has been used more frequently in various types of KPro.

As shown in Fig. 1.12, there are currently three different types of KPro that are in clinical use: the OCULAID® KPro, Dohlman (Boston) KPro, and AlphaCor™ Kpro. Fig. 1.12 (a & b) represent OCULAID® KPro that is composed of an anti-conical shape shaft that can be fixed into the host cornea or sclera. It creates a "valve" on the cornea to ensure a watertight situation. The pressure in the eye pushes the corneal rim around the 3 mm top of the KPro and the steel suture fixation on the sclera is designed to prevent extrusion [59]. Dohlman artificial cornea is a collar-button design KPro that is made of PMMA. It consists of a central optical stem that penetrates the full thickness of the cornea, which is sandwiched between the two plates connected and sutured into place like a PKP graft (See Fig. 1.12(c)) [57, 60].
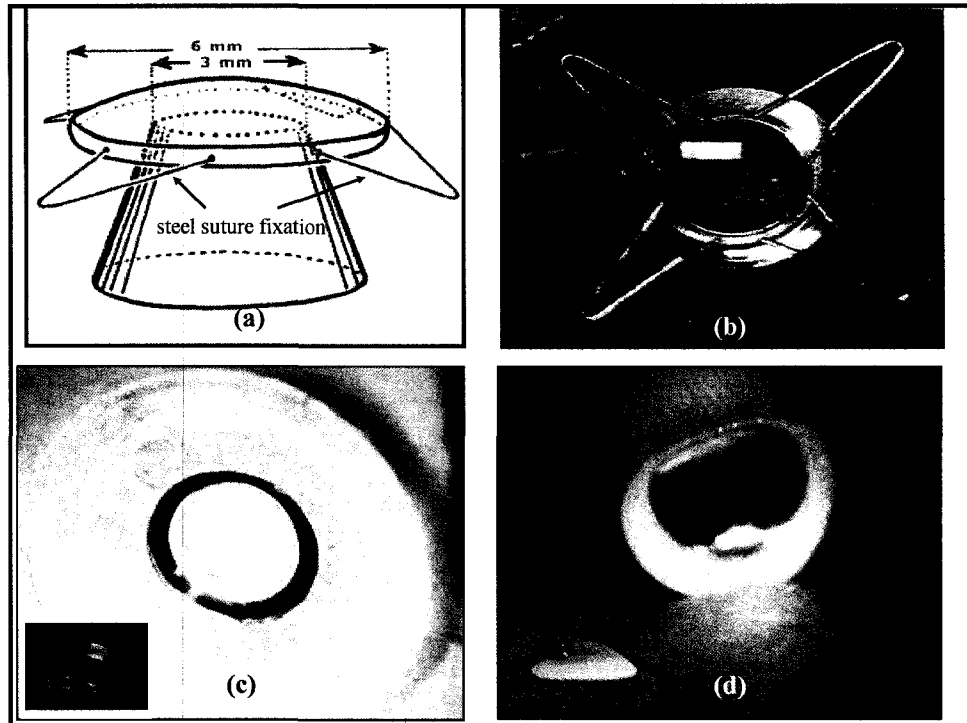
Figure 1.12 A glance at some of the keratoprosthesis used in human clinical trials:
(a) and (b) OCULAID® KPro [58, 59], (c) Dohlman or Boston KPro [60],
and (d) AlphaCor™ Kpro [52].

AlphaCor™ Kpro is the newest keratoprosthetic device that is based on a *"core-skirt"* design. The implant is a 7-mm diameter, one-piece, non-rigid synthetic cornea (See Fig. 1.12(d)). It is composed of a transparent central optic core of PHEMA gel, designed to allow the passage of light to the posterior of the eye, and an outer porous skirt, that is an opaque, high-water PHEMA that is designed to allow cell infiltration from the host to anchor the prosthesis into place [52].

To date, no KPro meets the gold standards for a successful corneal implant summarized in section 1-5.3. In fact, none even come close; the history of KPro is riddled with failures and surgical complications. However, AlphaCor™ KPro has shown some success to some extent over the past few years [11]. It was FDA-approved in August 2002 for patients at high risk for donor penetrating keratoplasty (PKP). Early results

suggest that the AlphaCor™ Kpro, previously known as the Chirila KPro, has a low incidence of the complications traditionally associated with keratoprostheses and can effectively restore a degree of vision in patients considered untreatable by conventional corneal transplantation [12].

1.5.4.2 Bioengineered Natural-based Artificial Corneas:

There have been various attempts at fabrication of natural-based artificial corneas. These range from the use of purely biological materials synthesized by corneal cells in culture to the use of non-corneal tissues as substitutes and combinations of biological and synthetic materials [9]. As mentioned before, most tissue engineering approaches to the restoration and repair of damaged tissue require scaffold materials upon which cells can attach, proliferate, and differentiate.

Reconstituted collagen matrices have been previously used for *in vitro* applications involving the cornea. Reconstruction of a bovine cornea that comprises of a three dimensional collagen matrix using bovine dermal collagen was developed for *in vitro* studies [15]. Zieske et al. [16] developed another *in vitro* cornea using primary rabbit stromal cells. A three-dimensional matrix comprising of bovine dermal collagen was developed by Germain et al. [17] to support an *in vitro* human cornea.

Griffith et al. [18] reconstructed a human cornea using immortalized human corneal cell lines. Each cell line underwent electrophysiological, biochemical and morphological tests to determine their phenotype in comparison with post-mortem human corneal cells, before being used in the 3D reconstruction. Collagen-chondroitin sulfate was the base scaffold in which keratocytes were incorporated, before epithelial and endothelial cells were layered above or below. Two weeks following construction, the

resulting corneal equivalent was found to behave similarly to a normal cornea with respect to morphology, transparency, ion and fluid transport, and gene expression following injury. Although, this human corneal equivalent shared functional properties with the natural cornea, it was not designed to meet the mechanical characteristics needed for transplantation. However, this study represented an important future directive towards the development of corneal implants synthesized from human cells and natural-based scaffolds. In general, the majority of studies on purely biological corneal materials indicated problems associated with the lack of mechanical strength and elasticity.

Although reconstructed corneal equivalents already have their potential uses in the biomedical world: as replacements for animals in toxicology testing and pharmacological studies, there has been a paradigm shift taking place in tissue engineering of the cornea from purely biological materials to biosynthetic ones to overcome the present disadvantages of corneal materials [61-63].

1.5.4.3   Future of Corneal Materials, Scope of This Work, and Working Hypothesis

Despite the successes that have been achieved for keratoprosthesis and bioengineered corneal materials, modifications, both at the bulk and the surface of current materials are still to be made. All scaffold materials are to be subjected to certain processing steps before use in therapeutic devices. These processing procedures can affect both the native material properties and the subsequent clinical utility of scaffolds intended for certain tissue engineering applications [64]. Whatever the way forward, the artificial cornea must be biocompatible and of suitable shape and size to fulfill the corneal functions of transparency, refraction and protection.

There are obviously benefits and negative factors to both areas of research in the development of the ideal artificial cornea. Perhaps the ideal future artificial implant is a composite of natural and synthetic biomaterials with corneal cell lines, to provide a transparent biocompatible implant that can be both flexible and have tensile strength to ensure it can withstand any future surgical procedures, as well as normal day to day mechanical stresses of the eye.

In this work, we have attempted to address some of the above-mentioned issues by developing collagen-based biosynthetic scaffolds using bulk and surface modification techniques as well as systematic engineering and analytical approaches such as *Factorial Experimental Design and ANOVA*.

We have hypothesized that the resultant tissue-engineered corneas would essentially be robust and elastic enough for implantation. Although they would still be collagen-based, they would incorporate biomimetic molecules that emulate natural extracellular matrix molecules (ECM) found within the human cornea while conferring significantly increased tensile strength and elasticity. The hope is that this work offers an in-depth and exciting approach to the study of biomaterials design in the context of tissue-specific needs for the cornea. Particularly, the use of multivariate experimental design approaches are hypothesized to provide a novel approach in the filed of biomaterials to help identify suitable materials combinations to address specific functional features for the materials and the biological components in the cornea. The ultimate hope is that such novel approaches lay a foundation for new generation of implantable biomaterials that can also be used as other tissue/organ transplants such as liver, kidney, and heart.

1.6 References

1. WHO, Global initiative for the elimination of avoidable blindness. World Health Organization, Geneva 1997 (unpublished document WHO/PBL/97.61/Rev 1).

2. Whitcher JP, Srinivasan M, Upadhyay MP. Corneal blindness: a global perspective. Bull. WHO 2001; **79:** 214-221.

3. EBAA, Eye Banking Statistical Report. Eye Bank Association of America,Washington 1999.

4. Gutkind L, Many sleepless nights: the world of organ transplantation. Publications of the United Network for Organ Sharing 1988.

5. The Australian Society for Medical Research, Following in the footsteps of Fred Hollow, Key Statistics 2006. Available online: http://www.asmr.org.au

6. The National Coalition for Vision Health: There's still a critical shortage of corneas for transplan 2005. Available online: http://www.visionhealth.ca/news/insert/shortage.htm

7. Chiou AGY, Florakis GJ, Kazim M. Management of conjunctival cicatrizing diseases and severe ocular surface dysfunction. Surv Ophthalmol 1998; 43: 19-46.

8. Chirila TV, Hicks CR, Dalton P, Asekaran SV, Lou X, Hong Y, Clayton AB, Ziegelaar BW, Fitton JH, Platton S, Crawford GJ, Constable IJ. Artificial Cornea. Prog Polym Sci 1998; 23: 447-473.

9. Griffith M, Hakim M, Shimmura S, Watsky M A, Li F, Carlsson D, Dillon CJ, Nakamura M, Suuronen E, Shinozaki N, Nakata K, Sheardown H. Artificial human corneas: scaffolds for transplantation and host regeneration. Cornea 2002; 21(7): S54-S61.

10. Lund OE. Keratoprosthesis: 25 years experience. Refract Corneal Surg 1993; 9: 186-187.

11. Hicks C, Crawford G, Chirila T, Wiffen S, Vijayasekaran S, Lou X, Fitton J, Maley M, Clayton A, Dalton P, Platten S, Ziegelaar B, Hong Y, Russo A, Constable I. Development and clinical assessment of an artificial cornea. Prog Ret Eye Res 2000; 19:149-170.

12. Crawford GJ, Hicks CR, Lou X, Vijayasekaran S, Tan D, Mulholland B, Chirila TV, Constable IJ. The Chirila keratoprosthesis: phase I human clinical trial. Ophthalmology 2002; 109: 883-889.

13. Liu Y, Gan L, Carlsson DJ, Fagerholm P, Lagali N, Watsky MA, Munger R, Hodge WJ, Priest D, Griffith M. A simple cross-linked collagen tissue substitute for corneal implantation. IOVS 2006; 47: 1869-1875.

14. Germain L, Carrier P, Auger FA, Salesse C, Guerin, , Can we produce a human corneal equivalent by tissue engineering? Prog Ret Eye Res 2000; 19: 497-527.

15. Minami Y, Sugihara H, Oono S. Reconstruction of cornea in three-dimensional collagen gel matrix. Culture Invest. Ophthalmol Vis Sci 1993; 34: 2316-2324.

16. Zieske JD, Mason VS, Wasson ME, Meunier SF, Nolte CJ, Fukai N, Olsen BR, Parenteau NL. Basement membrane assembly and differentiation of cultured corneal cells: importance of culture environment and endothelial cell interaction. Exp Cell Res 1994; 214: 621-633.

17. Germain L, Auger FA, Grandbois E, Guignard R, Giasson M, Boisjoly H, Guérin SL. Reconstructed human cornea produced in vitro by tissue engineering. Pathobiol 1999; 67: 140-147.

18. Griffith M, Osborne R, Munger R, Xiong X, Doillon CJ, Laycock NLC, Hakim M, Song Y, Watsky MA. Functional human corneal equivalents constructed from cell lines. Science 1999; 286: 2169-2172.

19. Scwabe IR, Reyes M, Isserhoff RR. Successful transplantation of bioengineered tissue replacements in patients with ocular surface disease. Cornea 2000; 19: 421-426.

20. Li F, Carlsson DJ, Lohmann C, Suuronen E, Vascotto S, Kobuch K, Sheardown H, Munger R, Nakamura M, Griffith M. Cellular and nerve regeneration within a biosynthetic extracellular matrix for corneal transplantation. Proc Nat Acad Sci USA 2003; 100: 15346-15351.

21. Simple Anatomy of the Retina, 2003, Available online: http://www.webvision.med.utah.edu/imageswv/Sagschem.jpeg

22. Kolozsvari L, Nogradi A, Hopp B, Bor Z. UV absorbance of the human cornea in the 240 to 400 nm range, Invest Ophthalmol Vis Sci 2002; 43: 2165-2168.

23. Hom MM, Bennett ES. Manual of contact lens prescribing and fitting. Newton, MA: Butterworth-Heinemann, 1997.

24. Tripathi BJ, Tripathi, RC, Chalam KV. Eye anatomy. In: Dulbecco R, editors. Encyclopedia of human biology. 2nd Edition, San Diego: Academic Press, 1997. p. 883-901.

25. Nishida T. Basic science: cornea, sclera and ocular adnexa anatomy, biochemistry, physiology and biomechanics. In: Krachmer JH, Mannis MJ, Holland EJ, editors. Cornea: fundamentals of cornea and external disease. Toronto: Mosby, 1997. p. 1-67.

26. Thomas C. The Cornea. 1st Edition, Illinois: Bannerstone House, 1955. p. 3-140.

27. Godbey WT, Atala A. In vitro systems for tissue engineering. Ann NY Acad Sci 2002; 961: 10-26.

28. Griffith L, Naughton G. Tissue engineering-current challenges and expanding opportunities. Science 2002; 295: 1014.

29. Horton H, Moran L, Ochs R, Rawn J, Scrimgeour K. Principles of biochemistry. 3rd Edition, Upper Saddle River, NJ: Prentice Hall, 2002.

30. Nimni ME, Cheung D, Strates B, Kodama M, Sheikh K. Chemically modified collagen: A natural biomaterial for tissue replacement. J. Biomed. Mater. Res. 1987; 21: 741-771.

31. Whikehart DR. Biochemistry of the eye. Pennsylvania: Butterworth Heinemann, 2003. p.15.

32. Berman ER, Biochemistry of the eye. Plenum Press: New York, 1991.

33. Campbell, BA, Biology. Editions du Renouveau Pedagogique Inc. St-Laurent, 1995.

34. Klug WS, Cummings MR, Concepts of Genetics. 5th Edition. Prentice Hall: New York, 1997.

35. Chitin, chitosan, and oligomers, 2002. Available online: http://nano.nstl.gov.cn/sea/MirrorResources/1241/index.html#chemistry. Dalwoo BLS.

36. Wang XH, Li DP, Wang WJ, Feng QL, Cui FZ, Xu YX, Song XH, Van der Werf M. Crosslinked collagen/chitosan matrix for artificial livers. Biomaterials 2003; 24: 3213–3220.

37. Gingras M, Paradis I, Berthod F.C. Nerve regeneration in a collagen–chitosan tissue-engineered skin transplanted on nude mice. Biomaterials 2003; 24: 1653–1661.

38. Kratz G, Arnander C, Swedenborg J, Back M, Falk C, Gouda I, Larm O. Heparin–chitosan complexes stimulate wound healing in human skin. Scand J Plast Reconstr Surg Hand Surg 1997; 31:119–23.

39. Aiedeh K, Gianasai E, Orienti I, Zecchi V. Chitosan microcapsules as controlled release systems for insulin. J Microencapsul 1997;14:567–76.

40. Yagi K, Michibayashi N, Kurikawa N, Nakashima Y, Mizoguichi T, Harada A, Higashiyama S, Muranaka H, Kawase M. Effectiveness of fructose-modified chitosan as a scaffold for hepatocyte attachment. Biol Pharm Bull 1997; 20:1290-1294.

41. Madihally SV, Matthew HWT. Porous chitosan scaffolds for tissue engineering. Biomaterials 1999; 20:1133-1142.

42. Amiji MM. Permeability and blood compatibility properties of chitosan-poly(ethylene oxide) blend membrane for hemodialysis. Biomaterials 1995; 16: 593–599.

43. Beena MS, Chandy T, Sharma CP.Heparin immobilized chitosan-poly ethylene glycol interpenetrating network: antithrombogenicity. Artif Cells Blood Subs Immob Biotech 1995; 23: 175-92.

44. Chaplin M, Online: Alginate, October 25, 2005, Accessed on April 2, 2006, Available: http://www.lsbu.ac.uk/water/hyalg.html

45. Rowley JA, Mooney DJ. Alginate type and RGD density control myoblast phenotype. J Biomed Mater Res 2002; 60: 217-223.

46. Morra M, Cassinelli C. Simple model for the XPS analysis of polysaccharide-coated surfaces. Surface Interface Anal 1998; 26: 742-747.

47. Cardona H. Keratoprosthesis, Am J Ophthalmol 1962; 54: 284-294.

48. Cardona H. Mushroom transcorneal keratoprosthesis. Am J Ophthalmol 1969; 68: 604-612.

49. Barnham JJ, Roper-Hall MJ. Keratoprosthesis: a long term review. Br J Ophthalmol 1983; 67: 468-474.

50. Cardona H. The cardona keratoprosthesis: 40 years experience, Refract Corneal Surg 1991; 7: 468-471.

51. Leibowitz HM, Trinkhaus-Randall V, Tsuk AG, Franzbau C. Progress in the development of a synthetic cornea. Prog Ret Eye Res 1994; 13: 605-621.

52. Hicks CR, Fitton JH, Chirila TV, Crawford TV, Constable IJ. Keratoprostheses: advancing toward a true artificial cornea. Surv Ophthamol 1997; 42: 175-189.

53. Khan B, Dudenhoefer EJ, Dohlman CH. Keratoprosthesis: an update. Curr Opin Ophthalmol 2001; 12: 282-287.

54. Duan D, Klenkler BJ, Sheardown H. Progress in the development of a corneal replacement: keratoprostheses and tissue-engineered corneas. Expert Rev Med Devices 2006; 3: 59-72.

55. Moffatt SL, Cartwright VA, Stumpf TH. Centennial review of corneal transplantation. Clinical and Experimental Ophthalmology 2005; 33: 642–657.

56. Strampelli B. Osteo-donto- keratoprosthesis. Ann Optalmol Clin Ocul 1963; 89: 1039.

57. Dohlman CH, Doane MG. Some factors influencing the outcome after keratoprosthesis. Am J Ophthalmol 1994; 77: 694-700.

58. Yaghouti F, Nouri M, Abad JC, Power WJ. Keratoprosthesis: Preoperative prognostic categories. Cornea 2001; 20: 19-23.

59. Jan Worst, The "Champagne Cork" keratoprosthesis (KP), Jan 14 2007, Available online: http://www.janworst.com/projects/kp/frames/framekp1.htm

60. Dohlman CH, Harissi-Dagher M, Khan BF, Sippel KC, Aquavella J, Graney JM. Introduction to the use of the Boston Keratoprosthesis. Expert Review of Ophth 2006; 1: (1) 41-48.

61. Trinkaus-Randall V. Cornea: biological responses. In: Lanza RP, Langer R, Chick WL, editors. Principles of tissue engineering, San Diego: Academic Press, 2000. p. 471-491.

62. Cahane M. Artificial cornea and the future of eye banking. Cell and Tissue Banking 2000; 1: 319-320.

63. Nishida K. Tissue engineering of the cornea. Cornea 2003; 22(1): 28-34.

64. Badylak SF. Modification of natural polymers: collagen. In: Atala A, Lanza RP, editors. Methods of tissue engineering. New York: Academic Press, 2002. p.505-514.

Chapter 2

Multivariate Experimental Design for Rational Development of Bioengineered Hybrid Polymer Networks for Corneal Tissue Engineering *

Mehrdad Rafat,[1,2] May Griffith,[2,3*] Takeshi Matsuura[1]

[1] Department of Chemical Engineering, University of Ottawa, Ottawa, ON K1N 6N5

[2] University of Ottawa Eye Institute, Ottawa, ON K1H 8L6

[3] Department of Cellular and Molecular Medicine, University of Ottawa, Ottawa, ON

K1H 8M5, Canada

2.1   Abstract

The main objective of this study was to utilize *Multivariate Experimental Design* aiming at the development of novel implantable materials that mimic human tissues such as cornea in key physical and physiological functions. Hybrid polymer networks (HPN) comprised of natural polymers, e.g., collagen and chitosan with synthetic bio-inert molecules, e.g., poly (ethylene glycol) dibutyraldehyde (PEG-DBA) and 1-ethyl-3-(3-dimethylaminopropyl) carbodiimide (EDC), and N-hydroxysuccinimide (NHS) were designed and fabricated with the aid of a 2^3 full factorial experimental design (FED) combined with a response surface design (RSD). The combined FED/RSD approach allowed us to efficiently evaluate the key experimental factors, their interactions and their impacts on key responses, and to develop an optimum material formulation. Several formulations were fabricated with varying key factors such as chitosan to collagen molar ratio [CTN], EDC to collagen/chitosan molar ratio [EDC], and PEG-DBA to collagen/chitosan molar ratio [PEG]. The suitability of resultant tissue-engineered materials was evaluated for corneal implantation. All formulations were tested for physical (i.e., mechanical, and optical) and *in vitro* biological properties (i.e., corneal epithelial cell growth). The optimum formulation was successfully evaluated *in vivo* by implantation in pigs' corneas the results of which have been reported in a separate article. Physical and biological results suggested that optimum scaffold was tough, elastic, biocompatible, and superior to human eye bank corneas in optical clarity. The results were statistically validated using Analysis of Variance (ANOVA).

Key words: collagen, cornea, experimental design, epithelial cell, in vitro test, mechanical properties.

2.2   Introduction

During the last three decades, significant advances have been made in the development of polymeric materials for use as scaffolds for various tissue engineering and regenerative medicine strategies. To be successful for specific applications in medicine, polymeric scaffolds must hold a number of properties. First, the material must be biocompatible to avoid an inflammatory response that might lead to host rejection. The material must provide a favorable site for the recruitment of cells from the surrounding biological environment, support cellular migration and proliferation with the subsequent cellular processes leading to the expression of matrix and tissue formation [1]. To achieve these, the polymer scaffold must have porosity and pore size distribution that is adequate for cellular penetration as well as the transport of nutrients into and cellular waste products out of the scaffold. In addition, the scaffold should acquire mechanical properties as similar as possible to the surrounding host tissue in order to provide temporary or permanent structural and physiological stability to a defect site [2]. Moreover, as the scaffold serves as a temporary support until host tissue is formed within the defect site the scaffold must be biodegradable as described by *Vert et al.*[3]. It means that the scaffold must gradually break down into nontoxic products by hydrolysis or enzymatic degradation. Ideally, the polymer scaffold would degrade at a rate equal to the rate of tissue in-growth, allowing for maintenance of the scaffold structure and mechanical support during the early stages of tissue formation [4]. In addition to the above-mentioned properties, the corneal scaffolds must meet other crucial requirements such as optical transparency, and suitable refractive properties.

It is highly challenging to simultaneously achieve these key physical and biological properties because they most often appear to be of conflictive nature and influenced by various factors. For example, by enhancing mechanical properties of scaffolds, we may compromise for their biocompatibility or optical transparency. Development of hybrid polymer networks (HPNs), which combines the bioactive features of natural materials and physical characteristics of synthetic ones, could address these conflicts to achieve synergy between the desirable mechanical properties of some components with the biological compatibility and physiological relevance of others as we reported in another study [5] (See chapter 3 for more details). However, one factor at a time (OFAT) approach that is the typical experimental technique used for development of biomaterials [6] is not efficient for development of such HPN materials.

Up until the early in the twentieth century, scientific experimentation largely followed OFAT method, which varies only one factor or variable at a time while keeping others fixed. The first *factorial experimental design (FED)* was developed by *Fisher* [7] and it was *Taguchi* [8] who introduced these methods into the design process itself. It has become possible to estimate the sensitivity of a system to variation in a large number of input parameters whilst reducing experimental effort by employing FED strategy [9]. Statistically designed approaches such as FED that vary several factors simultaneously are more efficient when there is more than one factor to study. FED requires fewer resources (experiments, time, material, etc.) for the amount of information obtained. The estimates of the effects of each factor are more precise. FED uses more observations to estimate an effect, resulting in higher precision and reduced variability. The interaction between factors can be estimated systematically if FED is performed. Despite the

instrumental advantages of FED over OFAT, majority of scientists and engineers especially those in the field of biomaterials continue to perform OFAT experiments most likely due to its simplicity [10, 11].

In recent years, researchers have shown an increased interest in the use of FED in biomedical engineering. However, far too little attention has been paid to the importance of this technique for the development of novel biomaterials. The potential of factorial design in biomaterials has recently been studied. The first application dates back to 1996 when *Henriksen et al.* [12] employed a 2^3 factorial design to investigate the effect of selected parameters on the affinity of dissolved chitosan for the corneal surface. They found that contact time, pH, ionic strength and chitosan molecular weight had significant effects on the adsorption. *Lucas-Girot et al.*[13] explored the influence of process parameters such as weight fraction and particle size of pore-former, and isostatic pressure, on porosity and compressive strength of calcium carbonate biomaterials as bone substitutes using a two-level 2^k factorial design.

Fisher et al. [14] investigated the photocrosslinking of poly(propylene fumarate) (PPF) dissolved in its precursor, diethyl fumarate (DEF), using low levels of ultraviolet light exposure as novel biomaterials for use as a bone graft. A three factor, 2 x 2 x 4 factorial design was developed, studying the effects of PPF number average molecular weight, initiator content, and DEF content upon photocrosslinking characteristics and mechanical properties. *Hedberg et al.* [2] has examined the in vitro degradation of porous PPF composites incorporating micro particles of blends of poly(DL-lactic-co-glycolic acid) (PLGA) and poly(ethylene glycol) using a 2^3 fractional factorial design. In that study, three factors were considered: the amount of poly(ethylene glycol) within the

composite, the microparticle loading of the composites, and the NaCl initial mass percent of the composites. They found that these factors did not have a significant effect on degradation rate of the scaffolds. They demonstrated that microparticle carriers could be incorporated into PPF scaffolds for localized delivery of tissue morphogens without altering the expected rate of degradation compared to blank, unloaded PPF scaffolds. The most recent FED application was the work of *Chen et al.*[6] who developed glycosaminoglycan /chitosan membranes for chondrocyte culture, with the aid of a 2-level 2^{4-1} fractional factorial design.

Despite the recent increasing interest in FED in biomaterials sciences [15-18], there has been little discussion about the use of multivariate experimental design for more complex biomaterials systems such as biosynthetic hybrid scaffolds. So far this method has only been applied to less complicated systems for which the OFAT technique could be sufficient

In this article, we basically describe a combined FED/RSD approach that was used to develop novel hybrid biomaterials for corneal tissue engineering applications. Based on prior bench-top experiments, we determined to study the effects and the optimum levels of three key factors: chitosan to collagen molar ratio, EDC to collagen/chitosan molar ratio, and PEG-DBA to collagen/chitosan molar ratio on four key properties, i.e., elastic modulus [EM], energy to break [ETB], epithelial cell growth [ECG], and optical light transmission [LT]. A spectrum of bioengineered scaffolds (nine formulations) were initially developed, characterized and then evaluated by ANOVA. Based on the results, one optimum formulation was developed and further evaluated *in vivo* in pigs. Although materials were collagen-based, they incorporate both natural and

synthetic biomimetic molecules that emulate natural extracellular matrix (ECM) found within the human tissues such as the cornea. Optimum formulation demonstrated sufficient tensile strength and elasticity for corneal transplantation. In summary, this systematic approach provided a means of rational development, evaluation, and prediction of proper formulations of HPN materials as well as facilitating the design and evaluation of wide range of tissue-engineered scaffolds with potential applications in medicine.

2.3   Materials and Methods

2.3.1   Materials

Freeze dried porcine collagen powder (MW$\approx$300000 Da) was obtained from Nippon Meat Packers, Inc, Japan. Chitosan (85% deacetylated, MW$\approx$400,000 Da from crab shells) was purchased from Fluka/Sigma-Aldrich. 1-ethyl-3-(3-dimethylaminopropyl) carbodiimide (EDC)(MW$\approx$192 Da), and N-hydroxysuccinimide (NHS)(MW$\approx$115 Da) were purchased from Sigma-Aldrich. PEG-dibutyraldehyde (PEG-DBA) (MW$\approx$3400 Da) was purchased from Nektar Inc.

2.3.2   Preparation of HPN corneal implants

The details of the chemistry and methods used for preparation of HPN corneal materials are reported elsewhere [5]. As summarized in Table 2.1, a total of 10 compositions were formulated: eight of which were initially obtained from 2^3 factorial design (PN-1 to PN-8), one as the design center point (PN-9), and one formulation as the optimum formulation (PN-10) developed based on the FED/SRD and ANOVA predictions.

Table 2.1 A 2^3 full factorial design (3 factors, 2 levels)[a] for bioengineered materials and their composition.

Formulation	X_1	X_2	X_3	Chitosan to Collagen Molar ratio (X_1)	EDC to Collagen/Chitosan- Molar Ratio (X_2)[b]	PEG-DBA to Collagen/Chitosan- Molar Ratio (X_3)[b]
PN-1	-1	-1	-1	0.00	3.00	0.00
PN-2	1	-1	-1	0.05	3.00	0.00
PN-3	-1	1	-1	0.00	6.00	0.00
PN-4	1	1	-1	0.05	6.00	0.00
PN-5	-1	-1	1	0.00	3.00	0.60
PN-6	1	-1	1	0.05	3.00	0.60
PN-7	-1	1	1	0.00	6.00	0.60
PN-8	1	1	1	0.05	6.00	0.60
PN-9 [c]	0	0	0	0.025	4.50	0.30
PN-10 [d]	**Optimum**			**0.01**	**4.50**	**0.30**

Notes:

a Factors and their levels were chosen according to literature information and authors' previous screening experiments.

b No. of amine (lysine) groups per mole of collagen was determined to be 106 (MW of collagen ≈ 300KD).
No. of amine groups per mole of chitosan (85% deacetylated) was determined to be 2024 (MW of chitosan ≈ 400KD).

c PN-9 is the center point.

d PN-10 is the optimum formulation.

2.3.3 Factorial experimental design (FED) and statistical analysis

A 2^3 full factorial design was planned to investigate the impact of three key factors including chitosan to collagen molar ratio [CTN], EDC to collagen/chitosan molar ratio [EDC], and PEG-DBA to collagen/chitosan molar ratio [PEG] on mechanical, optical, and biological properties of the scaffolds. Typically, crosslinkers such as EDC and PEG-DBA can be used at equal molar ratios to collagen/chitosan. However, to discover the optimum crosslinking conditions and to utilize the full potential of crosslinkable amino groups it will be necessary to add up to a several-fold molar amount of crosslinker relative to collagen/chitosan. If the protein/polysaccharide's amino acid composition is known, a molar ratio of crosslinker to protein/polysaccharide amino groups of 1-10 to 1 will usually suffice [19]. Based on the information available in the literature [20] and a series of bench-top exploratory experiments performed prior to the FED, the key factors and their levels were determined as listed in Table 2.1.

The number of possible treatments (compositions) was determined to be nine including eight (2^3) treatments and one centre point. Four responses in three categories of mechanical, biological, and optical properties were measured including elastic modulus [EM], energy to break [ETB], optical light transmission [LT], and biocompatibility (epithelial cell growth on the scaffolds [ECG]) as shown in Table 2.2.

The FED was performed and experimental results were subjected to analysis of variance (ANOVA) using MINITAB® statistical software (Release 14) to evaluate whether differences between data were statistically significant or not, the interactions among responses, and also to identify the vital few factors or key variables that influence the responses the most. Because three factors were investigated, a total of seven

Table 2.2   ANOVA results obtained from FED linear regression models for four key responses including elastic modulus (EM), energy to break (ETB), light transmission (LT), and epithelial cell growth (ECG).

Responses

Term	Coefficient	R_1(EM)			R_2(ETB)			R_3(LT)			R_4(ECG)		
		β	T	P	β	T	P	β	T	P	β	T	P
Constant	β_0	553.5	40.4	0.000	12.9	41.7	0.000	86.2	286	0.000	2801.7	34.3	0.000
X_1 (CTN)	β_1	54.5	4.0	0.001	1.7	5.5	0.000	-2.6	-8.5	0.000	-238.5	-2.9	0.010
X_2 (EDC)	β_2	184.5	13.5	0.000	-2.4	-7.7	0.000	-13.2	-43.7	0.000	-448.6	-5.5	0.000
X_3 (PEG)	β_3	-232.9	-17.1	0.000	-3.7	-12.1	0.000	-12.8	-42.6	0.000	-79.90	-1.0	0.343
X_1X_2	β_{12}	-85.3	-6.2	0.000	0.2	0.6	0.581	-2.5	-8.4	0.000	-218.1	-2.7	0.017
X_1X_3	β_{13}	-7.6	-0.6	0.585	-1.2	-3.9	0.001	-2.2	-7.3	0.000	249.9	3.1	0.008
X_2X_3	β_{23}	-38.4	-2.8	0.013	-2.7	-8.7	0.000	-13.0	-43.2	0.000	341.2	4.2	0.001
$X_1X_2X_3$	β_{123}	127.0	9.3	0.000	-0.2	-0.8	0.417	-2.2	-7.3	0.000	192.3	2.3	0.032
Ct.Pt.	β_{cp}	1140.2	27.8	0.000	17.7	19.1	0.000	-12.9	-14.3	0.000	670.3	2.7	0.015
r^2 (%)		98.9 %			97.8%			99.7%			84.8%		

Notes:

- Model: $R_n = \beta_0 + \beta_1 X_1 + \beta_2 X_2 + \beta_3 X_3 + \beta_{12} X_1 X_2 + \beta_{13} X_1 X_3 + \beta_{23} X_2 X_3 + \beta_{123} X_1 X_2 X_3$
  - β: Effect coefficient, T: T-statistics = β/standard error, P: Probability value
  - r^2: Coefficient of determination, $r^2_{perfect\ fit} = 100\%$
- Ct.Pt.: Centre point data is not included in the linear models.
- *P-values* and the coefficient of determination, r^2 ($\alpha = 0.05$), were used for identification of significant effects.

40

combinations were possible: three main factor effects, three two factor interaction effects, and one three factor interaction effect. The values of probability [P-value] were calculated for each of the combinations. A significance level of 95% was chosen, thus a combination with a P-value less than 0.05 was considered to be significant. To mathematically describe the effects of factors on responses, each response data set was fitted with a standard form of a 3rd order linear regression model:

$$R_n = \beta_0 + \beta_1 X_1 + \beta_2 X_2 + \beta_3 X_3 + \beta_{12} X_1 X_2 + \beta_{13} X_1 X_3 + \beta_{23} X_2 X_3 + \beta_{123} X_1 X_2 X_3$$

where R_n represents the response, while X_1, X_2, and X_3 indicate the key factors. $X_1 X_2$, $X_1 X_3$ and $X_2 X_3$ denote the two-way interactions, and $X_1 X_2 X_3$ denotes the three-way interaction. β_0 is the coefficient for constant term while β_1 to β_{123} stand for the effect coefficients associated with the individual factors and their interactions.

2.3.4   Response surface design (RSD) development and statistical analysis

Because the linear models developed by FED showed pronounced curvature, they were not able to represent all experimental behaviors, e.g. the center points, and needed to be converted into quadratic models. To model the curvature over the entire range of factors I performed more experiments and added axial points to the above factorial design to make it into a response surface design. To mathematically describe the effects of factors on responses, each response data set was fitted with a standard form of a quadratic multiple regression model:

$$R_n = \beta_0 + \beta_1 X_1 + \beta_2 X_2 + \beta_3 X_3 + \beta_{11} X_1^2 + \beta_{22} X_2^2 + \beta_{33} X_3^2 + \beta_{12} X_1 X_2 + \beta_{13} X_1 X_3 + \beta_{23} X_2 X_3$$

Such design and analyses made it feasible to investigate the dependence of responses on individual factors, and their two-way and three-way interactions to find out the optimum conditions. The RSD ANOVA results are summarized in Table 2.3.

Table 2.3 ANOVA results obtained from RSD quadratic models developed for four key responses including elastic modulus (EM), energy to break (ETB), light transmission (LT), and epithelial cell growth (ECG).

Term	Coefficient	Responses											
		R_1(EM)			R_2(ETB)			R_3(LT)			R_4(ECG)		
		β	T	P	β	T	P	β	T	P	β	T	P
Constant	β_0	-1781	-5.7	0.000	-3.2	-0.7	0.513	88.0	13.3	0.000	4147	8.5	0.000
X_1 (CTN)	β_1	56000	6.2	0.000	801.2	5.6	0.000	-510.1	-2.7	0.012	13517	1.0	0.344
X_2 (EDC)	β_2	1020	10.4	0.000	7.1	4.6	0.000	2.2	1.05	0.300	79	0.5	0.606
X_3 (PEG)	β_3	1236	2.0	0.050	42.2	4.3	0.000	94.6	7.2	0.000	-2743	-2.9	0.007
X_1^2	β_{11}	-913323	-7.4	0.000	-14962.7	-7.7	0.000	15285.1	5.8	0.000	-138343	-0.72	0.475
X_2^2	β_{22}	-91	-10.5	0.000	-0.7	-4.9	0.000	0.2	0.90	0.375	-51	-3.8	0.001
X_3^2	β_{33}	-2207	-5.2	0.000	-33.2	-5.0	0.000	-3.1	-0.35	0.727	-2571	-3.9	0.000
X_1X_2	β_{12}	-2274	-1.8	0.085	4.7	0.2	0.818	-67.8	-2.51	0.017	-5816	-2.9	0.006
X_1X_3	β_{13}	-1017	-0.16	0.875	-160.0	-1.6	0.121	-292.2	-2.2	0.037	33322	3.4	0.002
X_2X_3	β_{23}	-85	-0.8	0.430	-6.0	-3.6	0.000	-29.0	-12.9	0.000	758	4.6	0.000
r^2 (%)		82.6 %			80.0%			96.1%			86.1%		

Notes:

- Model: $R_n = \beta_0 + \beta_1 X_1 + \beta_2 X_2 + \beta_3 X_3 + \beta_{11} X_1^2 + \beta_{22} X_2^2 + \beta_{33} X_3^2 + \beta_{12} X_1 X_2 + \beta_{13} X_1 X_3 + \beta_{23} X_2 X_3$
- β: Effect coefficient, T: T-statistics = β/standard error, P: Probability value
- r^2: Coefficient of determination, $r^2_{perfect\ fit}$ = 100%
- P-values and the coefficient of determination, r^2 (α = 0.05), were used for identification of significant effects.

2.3.5 Evaluation of mechanical properties

The elastic modulus (stiffness), and energy to break (toughness) of tissue-engineered matrices were determined using an Instron Series IX Automated Materials Testing System with a load cell of 10N capacity at a crosshead speed of 10 mm/min and an initial grip separation of 6 mm. PBS equilibrated samples were cut into dumb-bell shaped specimens of identical rectangular gage area (width 5 mm, gage length 5 mm, thickness 0.5 mm) with two 3 mm end tabs. To avoid breakage and slippage of the sample in the jaws, the 6 mm wide tabs on the end of each dumb bell sample were adhesive coated (using DERMABOND™, a fast curing, cyanoacrylate-based skin adhesive) and reinforced with tape on both sides. This method of sample mounting completely prevented jaw breaks. Samples were not stress preconditioned prior to testing to failure. Every recorded value is the average of three to five measurements.

2.3.6 Evaluation of optical properties

Light transmission measurement was made at 21°C, for white light (quartz-halogen lamp source) for corneal materials using an optical method developed by *Priest et al.* [21]. Samples were hydrated in 0.5%(w/v) PBS before and during the measurement.

2.3.7 Evaluation of biological properties

Immortalized human corneal epithelial cells (HCECs) were used to evaluate epithelial coverage. HCECs were seeded on top of 1.5 cm^2 hydrogel pieces and supplemented with a serum-free medium containing epidermal growth factor (keratinocyte serum-free medium [KSFM]; Life Technologies, Burlington, Ontario, Canada) until confluence. The medium was then switched to a serum-containing modified supplemented hormonal epithelial medium (SHEM) for 2 days, followed by

maintenance at an air–liquid interface. Microscopic images were taken on days 1, 3, 5, and 7 post-seeding and number of cells that had attached and spread were measured using Northern Eclipse software (EMPIX IMAGING Inc., North Tonawanda, NY, USA). Four randomly selected areas of the same dimensions were counted for each sample and the number of cells counted was normalized to the area of gel selected, i.e. counts were expressed as cells per square millimeter of surface area. As an internal control for HCEC viability, growth rates of cells from each HCEC batch were also measured on tissue culture dishes (plasma-treated polystyrene) under identical culture conditions. At two weeks, constructs were fixed in 4% paraformaldehyde in 0.1 M PBS and were processed for routine hematoxylin and eosin (H&E) staining to evaluate the epithelial stratification on the hydrogels and controls.

2.4 Results and Discussion

2.4.1 Results and analysis for factorial fit (FED) models

The two-level 2^3 factorial design method was used to investigate the influence of three process parameters (factors) on four materials properties (responses). This method allowed a minimum number of samples and an improved interpretation process. We have represented each response under study by a linear third order regression model. Table 2.2 summarizes the effect coefficients (β), T-statistics (T), probability values (P) for the factors, and the coefficient of determination (r^2) in the regression models calculated by ANOVA. After an estimation of a coefficient, T for that coefficient is the ratio of the coefficient to its standard error (SE). T preserves the sign and relative magnitude of the effect coefficient and represents the direction and extends of an effect. For models where SE variation is not significant or there is no SE variation, i.e. linear FED models, T and

β can be used interchangeably. However, for models with high SE variability, i.e. non-linear quadratic models, it is only T-statistics that can be used for determining the direction and extends of an effect as it is a normalized form of β for SE.

Also, for all responses, positive coefficients (or T-statistics) indicate that a higher level is favorable for the response, whereas negative ones indicate that a lower level is desired. The magnitudes of β or T indicate the relative contributions of the factors to a response while the magnitudes of the P-values represent how significant the effects are. For instance, a large positive or negative value for β and a small value for P, e.g., $P < 0.05$ represent that a factor is highly influential and significantly contributes into the response.

An initial look at r^2 and P values for all four responses in Table 2.2 implies that the models are capable of providing good predictions ($r^2 \geq 80\%$) and most of the factors and their interactions have significant impacts on responses (most of the *P-values* are smaller than 0.05). However, a closer look at the magnitude of interactions coefficients and center point coefficients, and their small P values that are highly significant compared to the ones for individual factors suggest the presence of curvature in the responses [22] that needs to be taken into account. These indicate that the FED models are incapable of providing good predictions for responses and further experiments and data points are required to develop quadratic RSD models that properly represent all responses and their curvature.

2.4.2 Results and analysis for response surface design (RSD) models

Because the factorial models consider only the low and high levels of each factor and not the center point they cannot make good predictions and cannot be directly used for response optimization. As mentioned earlier, curvature was indicated for all responses

and each final model required a center point term. Standard quadratic models were developed for all four responses using MINITAB® 14. The quadratic RSD models and their corresponding ANOVA results are summarized in Table 2.3. The r^2 values equal or larger than 80% for all responses are implying that the models are capable of providing good predictions especially for their significant terms.

2.4.2.1 Effect of materials composition on elastic modulus [EM]

Elastic modulus or stiffness represents materials' ability to resist deformation. The larger the EM, the greater the force required to cause a given deformation [23]. It is also mathematically defined as the ratio of tensile strength to elongation (elasticity). RSD ANOVA results for EM are detailed in Table 2.3. P-values less than 0.05 reveal that three factors and their squared terms had significant impacts on EM while their interaction terms were not significant. Also, the positive T-statistics for X_1, X_2, and X_3 indicate that higher levels of CTN, EDC, and PEG favored mechanical stiffness of the scaffolds especially at their low settings. However, negative values for their corresponding second-order terms (X_1^2, X_2^2, and X_3^2) imply that each factor's impact is counter-balanced by its squared term and its impact may be reversed and have a decreasing impact on the stiffness especially at the high settings.

Also, it is clearly seen from the data that EDC molar ratio (X_2) is the most influential variable as it has the highest T-statistics magnitude followed by CTN and PEG, respectively ($|T_2=10.4| > |T_1=6.2| > |T_3=2|$). This is likely associated with the capability of EDC in forming zero-length cross-links that are highly contributing to the stiffness of the scaffolds.

Also, Fig. 2.1 shows EM of various scaffold formulations, which were developed in this study, as a function of CTN, EDC, and PEG molar ratios. This figure is an interval plot that depicts the variation of EM group mean values by plotting confidence intervals. For all data points in Fig. 2.1 with the exception of center point, there is a clear trend of increasing EM with increasing EDC and decreasing PEG.
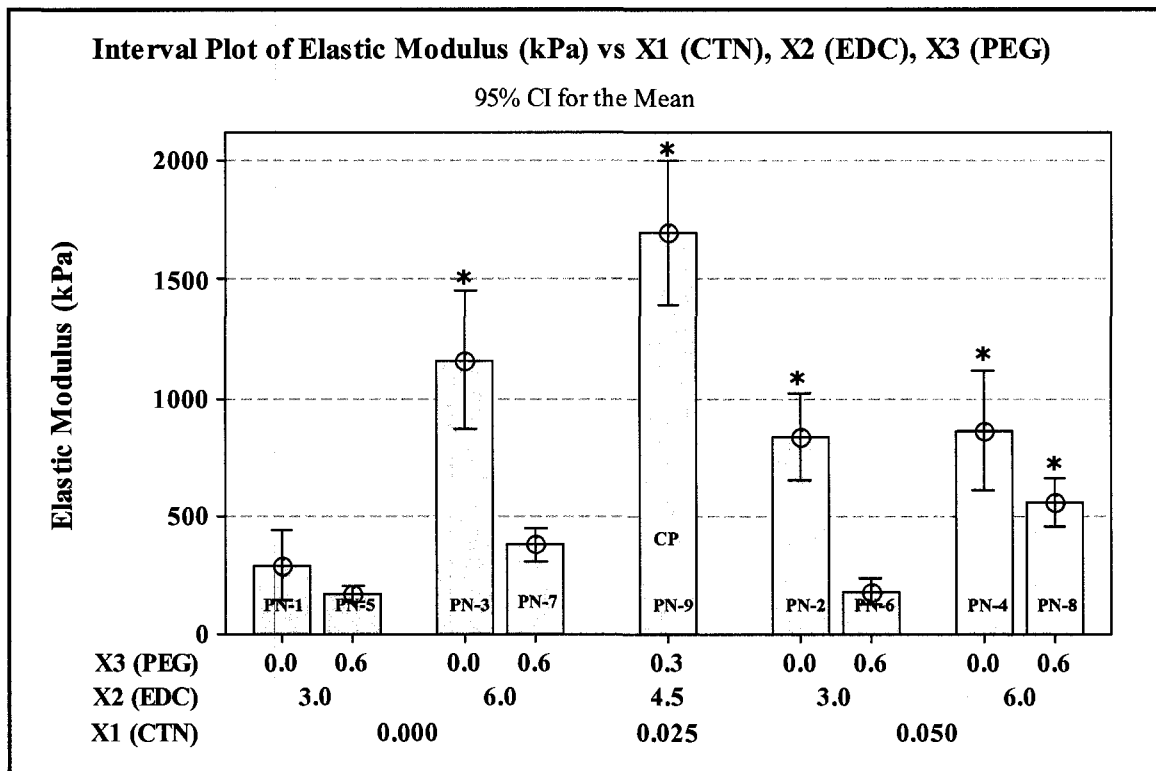
Figure 2.1   Interval plot for elastic modulus as a function of CTN, EDC, and PEG.

Note: * denotes significant difference between each scaffold and PN-1 control
scaffold using ANOVA ($p \leq 0.050$). CI: Confidence Interval,
CP: Centre Point

The decrease in stiffness with an increase in PEG ratio maybe attributed to the presence of long range PEG-DBA cross-links in the scaffolds that resulted in enhanced material elasticity or reduced stiffness. Another important observation from Fig. 2.1 is that the increase of cross-linkers ratios, i.e. EDC and PEG, is not always associated with the enhancement of the stiffness and in this study maximum EM was achieved at or in the

vicinity of a middle composition (center point). This is a clear evidence of non-linear correlation between factors and EM and also the kind of observation that can be made when a multivariate strategy (FED/RSD) is used as opposed to one factor at a time (OFAT) or try and error strategy.

It is also shown in Fig. 2.1 that chitosan has a significant positive impact on EM at low EDC ($X_2=3$) and in the absence of PEG-DBA ($X_3=0$) (compare EM value of PN-2 to that of PN-1). Similar trend was observed at high EDC ($X_2=6$) and in the presence of PEG-DBA ($X_3=0.6$) (compare EM value of PN-8 to that of PN-7). However, chitosan had a negative impact on EM at high EDC ($X_2=6$) in the absence of PEG-DBA ($X_3 = 0$) (compare EM value of PN-4 to that of PN-3) or at low EDC ($X_2=3$) and high PEG ($X3=0.6$) (compare EM value of PN-6 to that of PN-5).

These findings further support the idea that chitosan, and EDC mostly enhance the tensile strength while PEG-DBA enhances the elasticity of the matrix. Chitosan can amplify the number of amine reaction sites in the collagen matrix to increase the cross-linking density, and can form an ionic complex with collagen resulting in mechanically stronger matrices. Each mole of chitosan has about 22 times more reactive amine groups than collagen according to their molecular structure. The effect of chitosan was more pronounced at low EDC values while it was EDC that was more dominating at high concentrations. We hypothesized that at low EDC ratio and in the absence of PEG-DBA, the formation of chitosan/collagen ionic complex contributes more into the increase in EM while at high EDC and in the presence of PEG-DBA it is the formation of covalent bonds that makes larger contribution.

However, EM results show that at certain middle-range values of CTN, EDC, and PEG (i.e. PN-9 formulation) stiffness of the scaffolds significantly increased well above those of other formulations. This is likely due to the combined effects of ionic complex formation and increased covalent bonds (i.e. amide bonds formed by EDC and amine bonds formed by PEG-DBA) that impose synergistic effects on elastic modulus resulting in magnified EM values. EDC provides short-range zero-length cross-links that are necessary to enhance matrix's strength but reduces the elasticity while PEG-DBA forms long-range intermolecular/interfibrilar cross-links resulting in significantly enhanced robustness and elasticity due to its large polymer chain. In summary, in order to get the highest elastic modulus, the results suggest that we should set the factors at or close to the center of the design, e.g., chitosan ratio at 0.025, EDC ratio at 4.5, and PEG ratio at 0.3.

2.4.2.2 Effect of materials composition on energy to break [ETB]

ETB represents the energy (per unit volume) absorbed by the material until it breaks. It is mathematically defined as the area under the force-deformation curve of a material taken to failure that is a measure of the material's toughness or resilience [24]. The results obtained from RDS-ANOVA analysis of ETB as a function of CTN, EDC, and PEG are presented in Table 3. P-values less than 0.05 suggest that all factors had significant impacts on ETB except X_1X_2, and X_1X_3 interaction effects. The positive T-statistics for X_1, X_2, and X_3 indicate that initial increases in CTN, EDC, and PEG favored toughness of the scaffolds. However, negative T-statistics for X_1^2, X_2^2, and X_3^2 imply that their increasing impacts were reversed beyond certain levels of factors resulted in a decreasing effect on the toughness. The P-value less than 0.05 and negative T-statistic associated with X_2X_3 term indicates that the interaction between EDC and PEG-DBA had

a significant negative impact on scaffolds toughness. The relative magnitudes of T-statistics for all factors in Table 3 also indicate that there is no clear superiority of any factor over others in terms of the influences on ETB.

Figure 2.2 is another interval plot that shows the toughness of scaffolds as a function of CTN, EDC, and PEG molar ratios. Most of the data points show a trend of increasing ETB with increasing CTN, and decreasing EDC and PEG ratios.
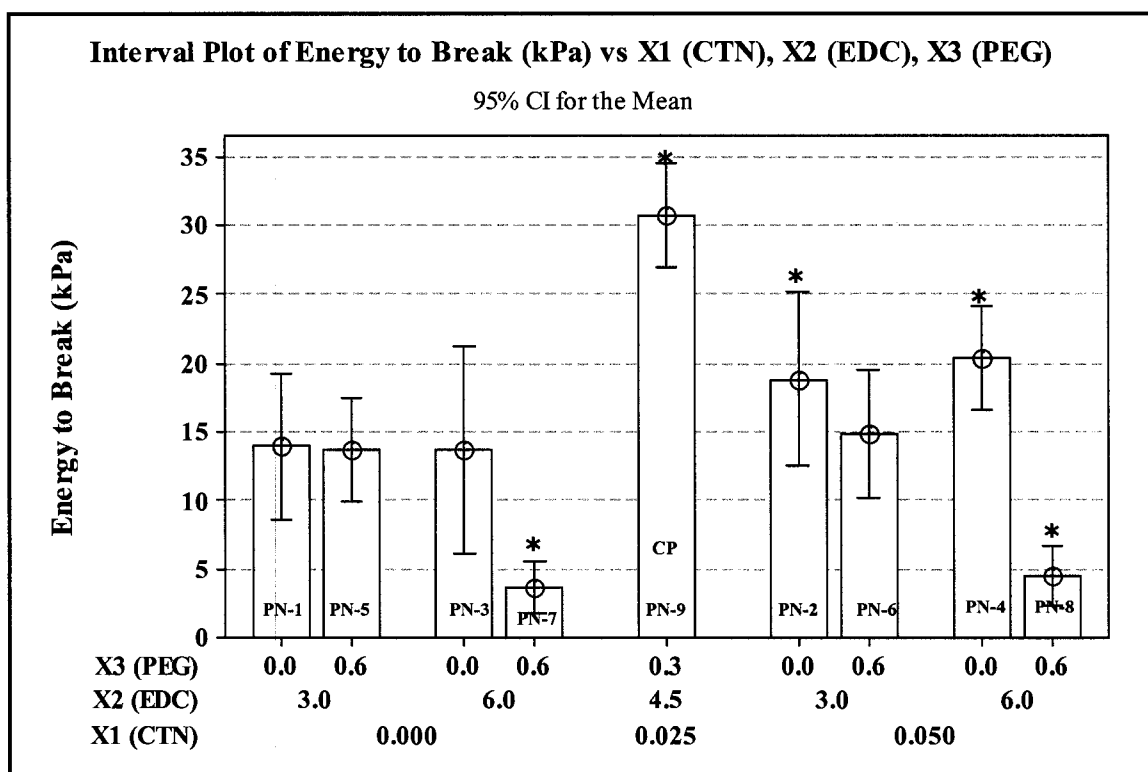
Figure 2.2   Interval plot for energy to break as a function of CTN, EDC, and PEG.

Note: * denotes significant difference between each scaffold and PN-1 control scaffold using ANOVA (p ≤ 0.050). CI: Confidence Interval, CP: Centre Point

It is generally believed that any increase in crosslinker ratio is associated with an increase in strength and toughness of the material due to the enhanced crosslinking density. Therefore, the decreasing trends of ETB associated with increases in EDC and

PEG over experimental range of this study are somewhat surprising. The unexpected results may be attributed to the following:

- Possible wide range of EDC and PEG-DBA molar ratios used in this study.

- Presence of EDC and PEG-DBA crosslinkers in excess of reaction sites on collagen or collagen/chitosan blends that were available for crosslinking.

- The interaction among the factors may have canceled out their main effects.

By comparing PN-3 to PN-1 in Fig. 2.2, no significant change in ETB is observable by doubling EDC ratio in the absence of chitosan ($X_1=0$). This possibly means that there are not enough reactive sites (NH_2 and COOH functional groups) available for crosslinking with excess EDC. Also, by comparing PN-5 to PN-1, no significant change in ETB is observable in the absence of chitosan ($X_1=0$) and at low EDC ($X_2=3$) while at high EDC ($X_2=6$) a significant decrease in ETB is obvious ($p \leq 0.05$) (PN-7 vs. PN-3). This is likely due to the fact that both EDC and PEG molar ratios exceeded the practical number of reactive sites available for crosslinking to a high extent and resulted in free EDC and PEG-DBA molecules or partially cross-linked ones in the scaffold that might have interrupted crosslinking processes.

Similar trends were observed in the presence of chitosan at high PEG ratios (See the results for PN-6 and PN-8). However, in the absence of PEG-DBA (PN-2, and PN-4) or at middle PEG ratio (PN-9) significant increases in ETB were observed. The highest increase in toughness was noted at the center point (PN-9). This may suggest that crosslinking reactions are completed and reached an equilibrium state at mid-composition.

Similar to the elastic modulus results, this observation confirms the hypothesis that the increase of cross-linkers ratios, i.e. EDC and PEG, is not always associated with the enhancement of materials toughness and maximum ETB can be achieved at or in the vicinity of a middle composition (center point). This also justifies the need for a non-linear quadratic model, such as the one developed in this work, that can properly predict ETB response. The experimental results and the model suggest that the factors should be set at or close to the center of the design in order to obtain scaffolds with the highest possible strength and elasticity.

2.4.2.3 Effect of materials composition on light transmission [LT]

It is clear from *P-values* for LT in Table 2.3 that chitosan and PEG-DBA and their interaction term (X_1X_3) had significant effects on light transmission (P< 0.05). EDC factor did not have a significant effect on LT on its own (P≥0.05). However, EDC's interaction terms with chitosan (X_1X_2) and PEG-DBA (X_2X_3) were significantly influential on LT (P< 0.05). The negative T-statistics for chitosan and its interactions with EDC (X_1X_2) and PEG-DBA (X_1X_3) indicate that higher levels of chitosan molar ratio decreased light transmission, therefore, it may be a key determining factor for optical transparency of HPN scaffolds.

The signs and magnitudes of T-statistics for PEG (X_3) in Table 2.3 indicate that higher levels of PEG-DBA increases optical transparency of the scaffolds while the one for its interaction term with EDC (X_2X_3) suggests the opposite and the fact that PEG-DBA can induce an overall decrease in transparency when conjugated and in interaction with EDC. In a separate study, we confirmed this property of PEG-DBA by fabricating similar corneal scaffolds of high transparency using PEG-DBA only.

Figure 2.3 shows percent light transmission of tissue-engineered materials as a function of CTN, EDC, and PEG molar ratios. All compositions produced optically transparent materials with LT higher than 90% for white light except for three compositions of PN-7, PN-8, and PN-9 that had significantly lower LT of 56, 37, and 73 %, respectively, than that of PN-1 control ($p \leq 0.05$). By comparing LT results of PN-7 and PN-8 formulations with their corresponding ETB results, it was noticed that these two formulations had the lowest toughness and light transparency. This may support the idea of incomplete crosslinking reactions and phase transition of partially cross-linked scaffolds that caused some degree of opacity.
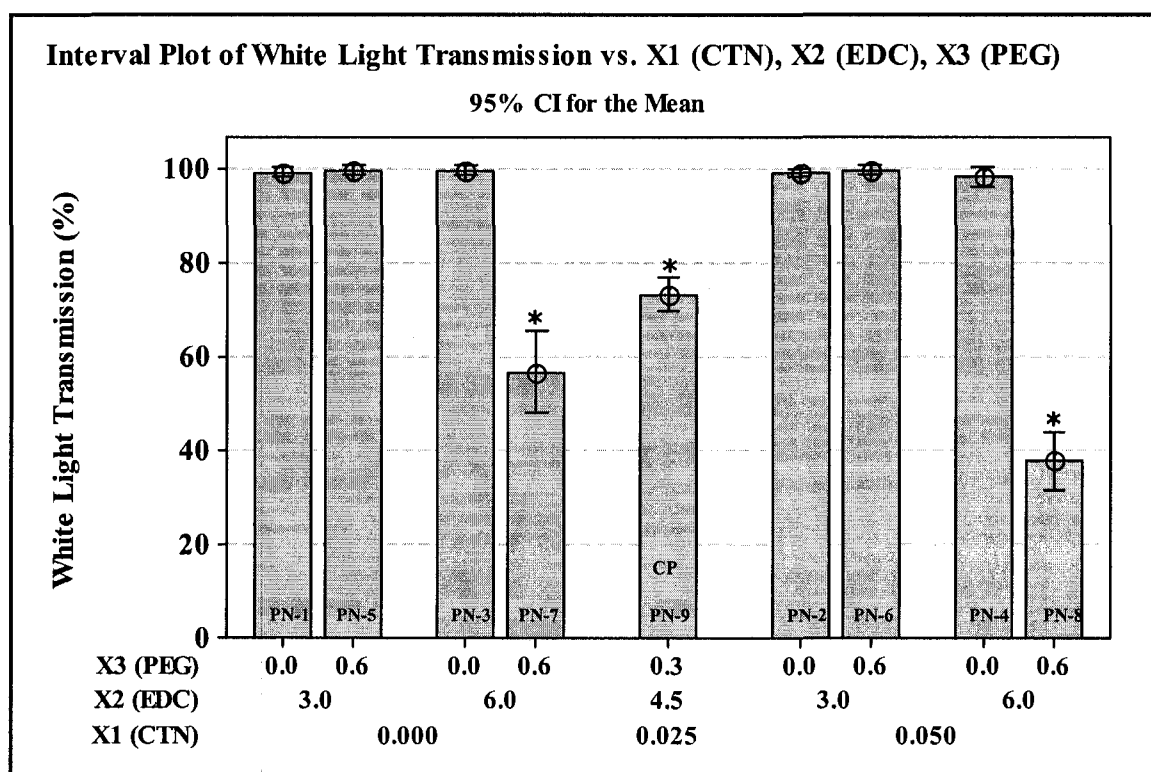
Figure 2.3   Interval plot for light transmission as a function of CTN, EDC, and PEG.

Note: * denotes significant difference between each scaffold and PN-1 control scaffold using ANOVA ($p \leq 0.050$). CI: Confidence Interval, CP: Centre Point

In general, the loss of transparency with simultaneous increases in molar ratios of chitosan, EDC, and PEG-DBA may be attributed to the changes in lower critical solution temperature (LCST) or cloud point of the overall system that is a point at which a loss in transparency is observed due to light scattering caused by a transition from a single to a two-phase state [25]. It seems that the simultaneous increase of EDC, PEG, and EDC decreased LCST of the overall system resulting in translucent (PN-9) and opaque materials (PN-7, and PN-8).

Although, the model for LT suggests that low levels of CTN, EDC and PEG are more desired to achieve a higher value of LT, the magnitude of LT at the center point as well as models predictions for other responses must be taken into consideration for prediction of the optimum conditions. Unlike the results for EM and ETB, the LT results do not support the fact that factors should be set at the center of the design in order to achieve the highest value for light transmission.

2.4.2.4 Effect of materials composition on epithelial cell growth [ECG]

Figure 2.4 shows the number of viable epithelial cells attached to the surfaces of materials on day five post-seeding as a function of chitosan, EDC, and PEG-DBA content of the scaffolds. The results show that all scaffolds generally support epithelial cells migration and growth. However, ECG values for PN-4, PN-7, and PN-8 formulations are significantly lower than that of PN-1 control. This may be associated with their higher EDC content compared to other formulations.
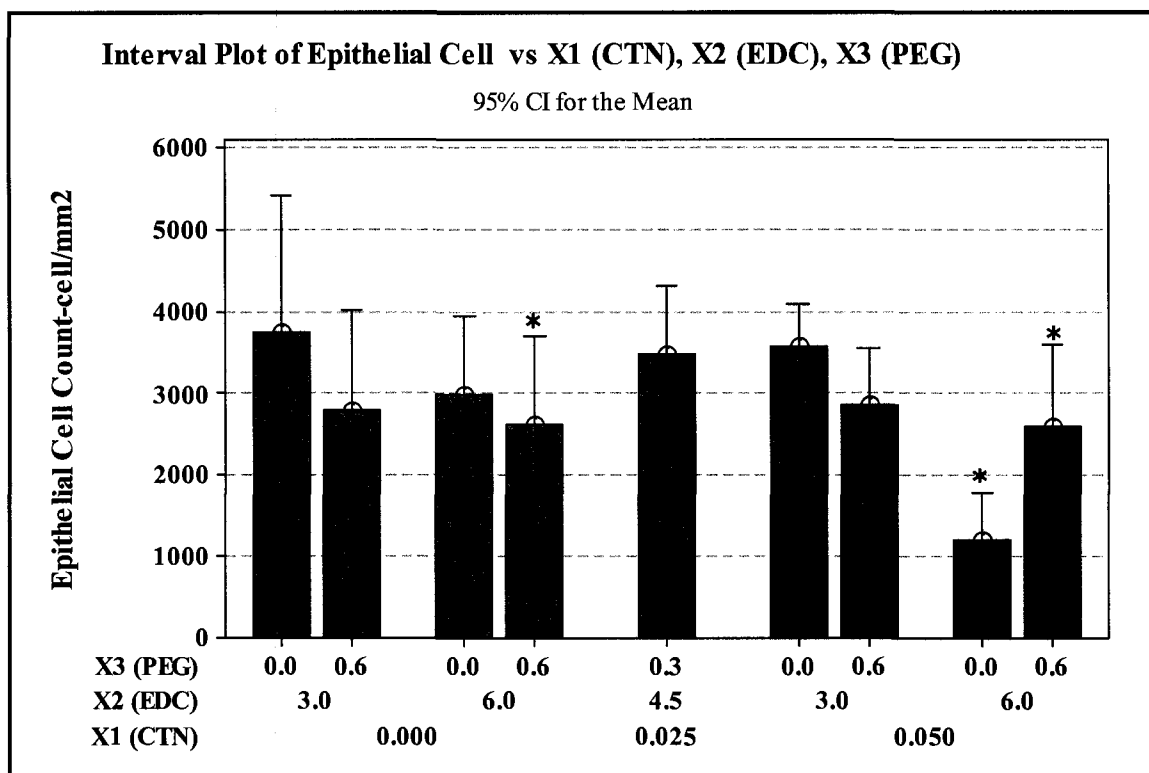
Figure 2.4   Interval plot for epithelial cell count as a function of CTN, EDC, and PEG.

Note: * denotes significant difference between each scaffold and PN-1 control
scaffold using ANOVA (p ≤ 0.050). CI: Confidence Interval,
CP: Centre Point

To determine the factors level of significance, the cell count results were
statistically analyzed by ANOVA as summarized in Table 2.3. Using the *P-values* for
ECG, we can claim that all of the effects including main and interaction effects are
significant with the exception of chitosan first (X_1) and second order (X_1^2) effects $(P >$
0.05), and EDC first order effect (X_2). Insignificant effect of CTN on cell count data is
possibly due to the biocompatible nature of chitosan. Though EDC does not have a first
order significant term, it has a second-order term that is highly significant and negatively
affecting cell biocompatibility of the scaffolds (P< 0.05, and T=-3.8). The negative sign
and magnitude of T-statistics for PEG first order (X_3) and second order (X_3^2) effects $(P <$
0.05), suggest that PEG has a negative impact on ECG response. The general decrease in

ECG with EDC and PEG is likely due to the cytotoxic effects of non-reacted EDC and PEG-DBA aldehyde groups in the scaffolds. This suggests that all constituents of a scaffold must be used in such proportions that all their functional groups are used up toward the formation of cross-links resulting in the minimum toxicity.

The interaction effects among factors for ECG are also shown in Table 2.3 and suggest that all factors are highly interacting and their interactions are significant ($P<0.05$). For example, by looking at negative sign and magnitude of T-statistics for X_1X_2 Binteraction, it is clear that CTN/EDC interaction decreases epithelial cell count. This is likely attributed to the fact that the increase of chitosan and EDC in the absence of PEG-DBA, only results in an increase in non-reacting or partially reacting cytotoxic components in the scaffold that do not produce stable covalent bonds. The positive signs for T-statistics that correspond to X_1X_3 and X_2X_3 interactions, suggest an increasing impact on cell counts. This phenomenon may be explained by the fact that most of the functional groups of collagen, chitosan, and those of cross-linkers reacted iteratively forming non-hydrolysable amide, and amine linkages, which further resulted in reduction in active groups of potential cytotoxic impacts on cells.

2.4.3 Response Optimization

The goal of this optimization process is to find the material composition at which elastic modulus, energy to break, light transmission, and cell count are maximized. During optimization process, we have noted the higher importance of optical transparency, and cell biocompatibility over mechanical properties for corneal applications. As mentioned before, although the center point (PN-9) is the optimum condition at which EM and ETB are almost maximized, it does not meet the optimum

criteria in terms of optical transparency and biocompatibility, both the most desirable properties. For example, light transmission for PN-9 was found to be 73 ± 1.5% that was lower than that of the eye bank human cornea (77 ± 1.3%) and PN-1 control formulation. A similar trend was observed for the growth of corneal epithelial cells. Therefore, it was necessary to use response optimization techniques to help identify the factor settings that optimize the set of responses in this study.

Now that we have validated RSD predictor models for each response, we can apply graphical techniques such as optimization contour plots to obtain the highest possible response yields. Optimization contour plots for all four responses are created based on the quadratic models as shown in Figs. 2.5 to 2.8. The optimization contour plots show how the factors affect the predicted responses and will allow to modify the factor settings interactively.

Figures 2.5 to 2.8 represent the contour plots for all four key responses as functions of X_1 and X_2, X_1 and X_3, and X_2 and X_3. A contour plot shows how a response variable relates to two factors while holding the third factor or the rest of the factors in the model at a fixed setting. The arrows on each graph represent the possible directions toward the optimum factor settings to improve transparency and epithelial cell growth while not compromising or minimally compromising for mechanical properties.

Figures 2.5 and 2.6 indicate the contour plots for light transmission, and epithelial cell count, respectively. It is clear from these plots that in order to gain the transparency and high cell growth there are several paths to be taken. Among those we focus on three important ones indicated by arrows 1 to 3.
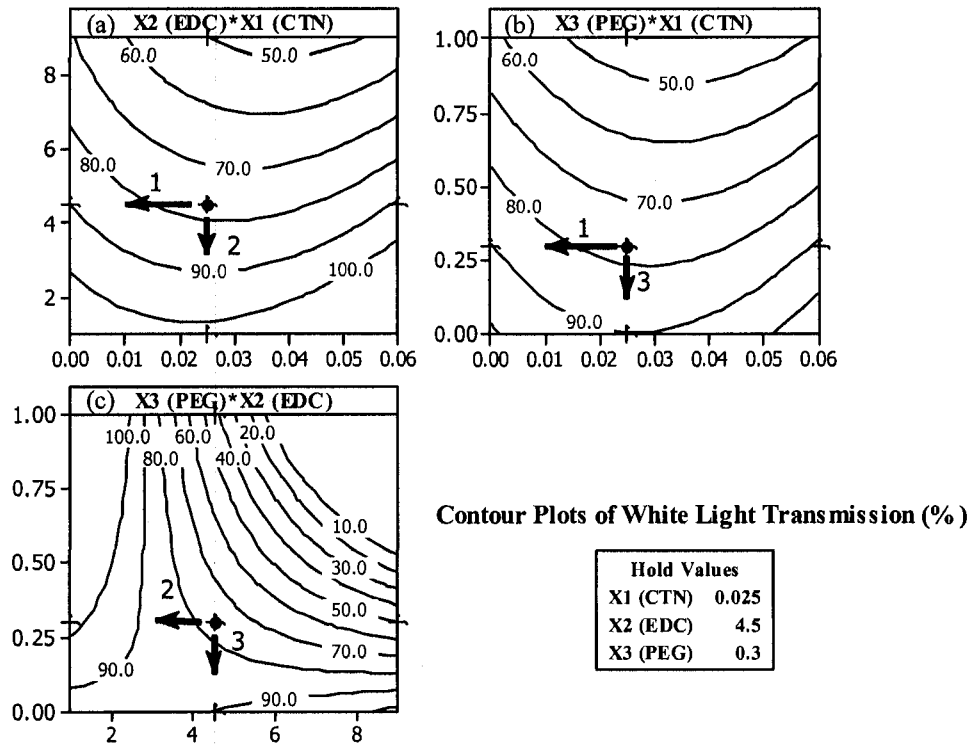
Figure 2.5 Contour plots for light transmission response for factor combinations of (a) EDC vs. CTN, (b) PEG vs. CTN, and (c) PEG vs. EDC.
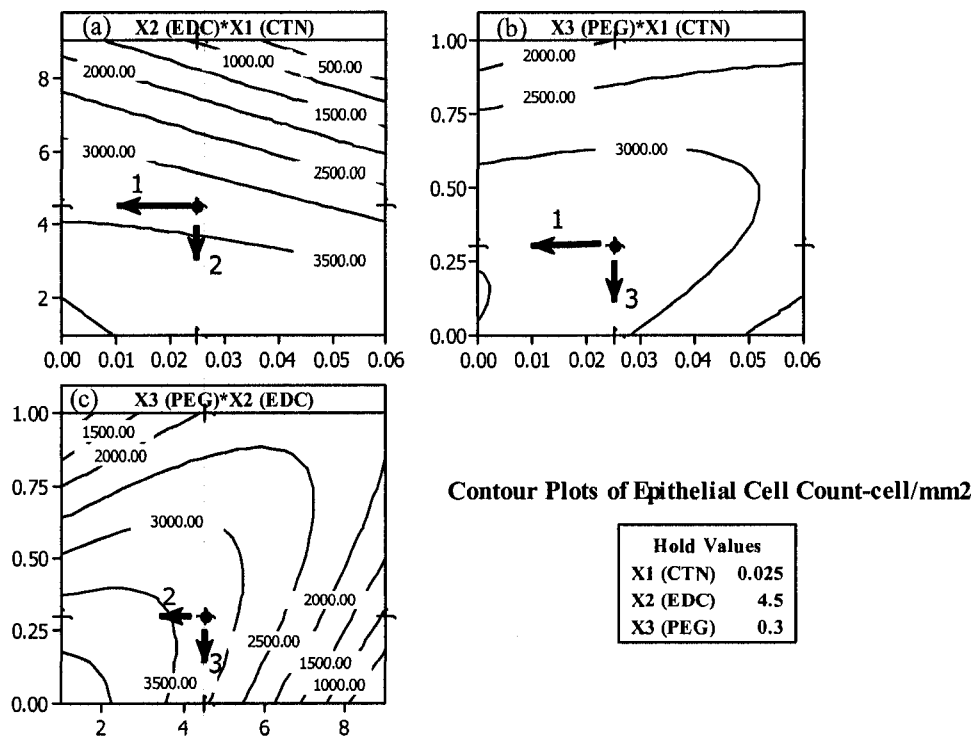
Figure 2.6 Contour plots for epithelial cell count response for factor combinations of EDC vs. CTN, (b) PEG vs. CTN, and (c) PEG vs. EDC.

2.4.3.1 Optimization path #1: decreasing chitosan molar ratio (CTN)

As shown in Fig. 2.5 and 2.6, decreasing CTN may increase LT and ECG toward their target values of 90 %, and 3500 cells/mm^2, respectively. However, as depicted in Figs. 2.7 and 2.8, this may slightly decrease EM and ETB. Therefore, if we move along direction #1 to lower CTN setting to, e.g. 0.01, while holding other factors at their midpoints, e.g. EDC = 4.5, and PEG = 0.3, we may be able to increase the transparency of the materials and epithelial cell growth while minimally compromising for scaffold's stiffness and toughness. Also, if we have another look at ANOVA data in Table 2.3, we notice that chitosan was the only factor with all its terms (i.e. X_1, X_1^2, X_1X_2, and X_1X_3) significantly influential on LT (P<0.05). Furthermore, the quadratic model for light transmission was the best fit for the data with the highest coefficient of determination (r^2=96.1) among models.

2.4.3.2 Optimization path #2: decreasing EDC molar ratio (EDC)

As depicted in Figs. 2.5 and 2.6, although decreasing EDC along direction #2 may move LT and ECG closer to their targets, it may reduce EM and move ETB away from its optimum value as shown in Figs. 2.7 and 2.8, respectively.

Also, according to LT and ECG data in Table 2.3, EDC is neither an influential factor (P_{X2}=0.3, P_{X2}^2=0.375) on LT and nor on cell count responses (P_{X2}=0.6). Therefore, the prediction drawn from plots in Figs. 2.5 and 2.6 that EDC reduction may significantly increase light transmission and cell count may not be accurate enough and the overall desirability of responses may not benefit from decreasing EDC.
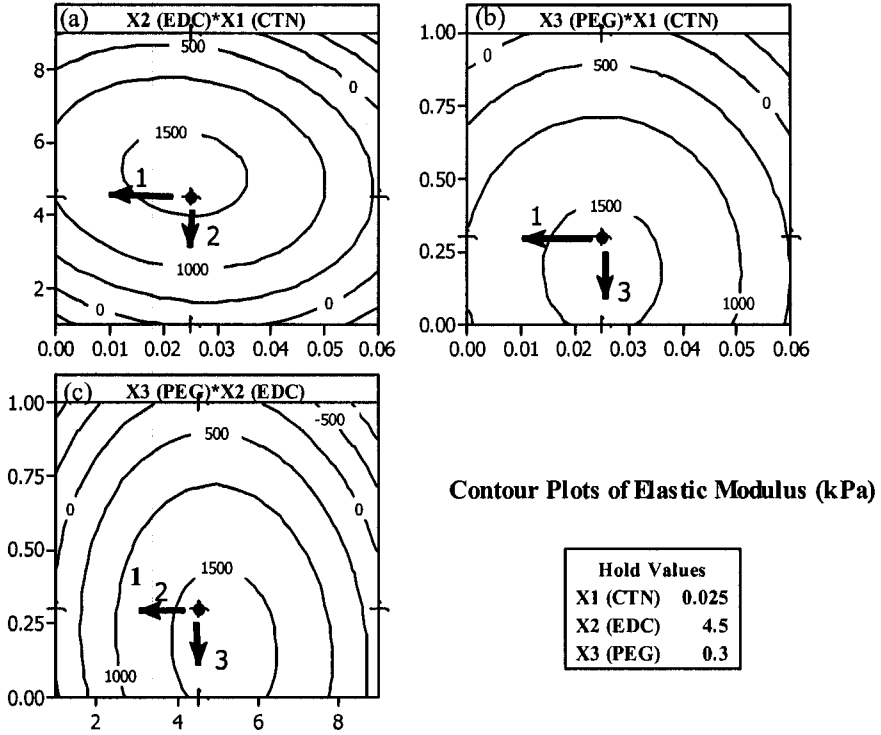
Figure 2.7   Contour plots for elastic modulus response for factor combinations of (b) EDC vs. CTN, (b) PEG vs. CTN, and (c) PEG vs. EDC.
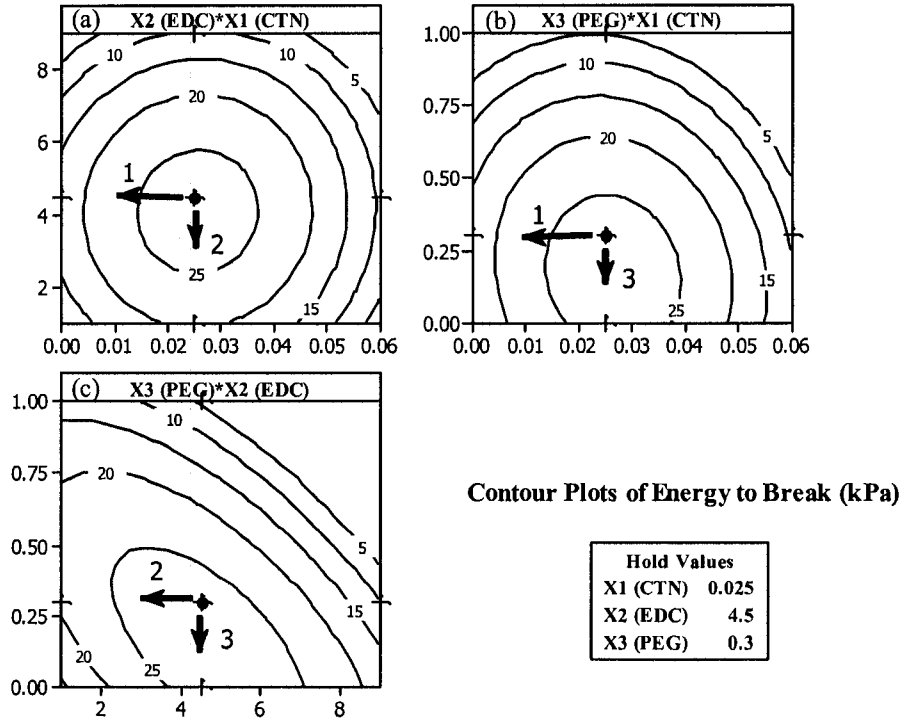
Figure 2.8   Contour plots for energy to break response for factor combinations of (c) EDC vs. CTN, (b) PEG vs. CTN, and (c) PEG vs. EDC.

2.4.3.3 Optimization path #3: decreasing PEG-DBA molar ratio (PEG)

According to Fig. 2.5, the third choice is to move along direction #3 and decrease PEG ratio that may increase LT significantly with no significant effect on EM and ETB (Figs 2.7, and 2.8) but it may reduce ECG as shown in Fig. 2.6. The small P value of 0.007 for ECG data in Table 2.3 confirms that PEG is a highly determining factor on an important response such as epithelial cells count. This suggests that the prediction drawn from plots in Fig. 2.6 that decrease in PEG ratio may have a negative impact on cell count is accurate enough and the overall desirability of responses may not benefit from decreasing PEG. Therefore, it is advantageous to keep PEG ratio constant and as close as possible to its middle range setting.

2.4.4 Development and characterization of the optimum formulation

Based on the above optimization process and the fact that the importance of LT and ECG is higher than EM and ETB, the overall desirability of responses benefits most from minimizing chitosan molar ratio than other strategies. The optimal setting suggested in previous sections (CTN=0.01, EDC = 4.5, PEG = 0.3) was used to formulate a new scaffold (PN-10). The optimum formulation was then tested and validated for optical, biological, and mechanical properties with satisfactory results.

Figure 2.9 demonstrates the results for light transmission and epithelial cell growth for the optimum formulation compared to those for other formulations and the human cornea (HC).
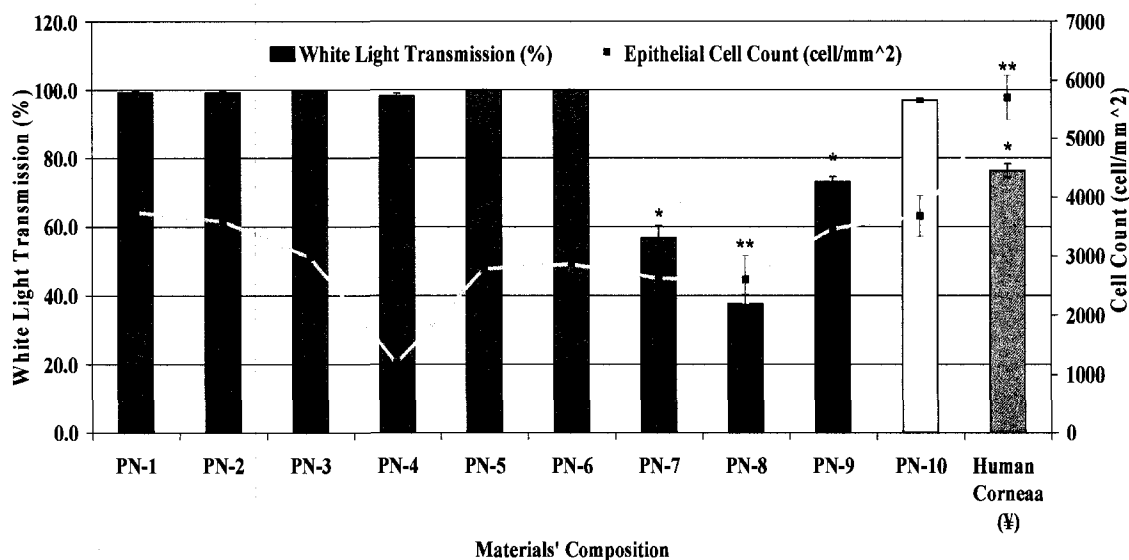
Figure 2.9   Results for % light transmission and epithelial cell growth (cell/mm^2) for the optimum formulation compared to those for other formulations and eye bank human cornea.

Notes: ¥ Human corneas were provided by the Eye Bank of Canada for research use only and were obtained from deceased patients.

¥ Cell count data for HC was adopted from Mustonen et al. (26).

* denotes significant difference between each scaffold and PN-1 control scaffold using ANOVA (p $\leq$ 0.050) for light transmission.

**denotes significant difference between each scaffold and PN-1 control scaffold using ANOVA (p $\leq$ 0.050) for cell count.

As predicted by the model, the optimum formulation (PN-10) was found to be optically transparent with a light transmission of 96.6 $\pm$ 0.6, which was superior to that of PN-9 formulation and HC. We could also observe a slight increase in ECG value for PN-10 compared to PN-9.

Figure 2.10 shows the elastic modulus and energy to break results for the optimum formulation compared to those for other formulations and HC. EM and ETB slightly decreased for PN-10 compared to PN-9 that is a small compromise to make in exchange for optical transparency and biocompatibility.
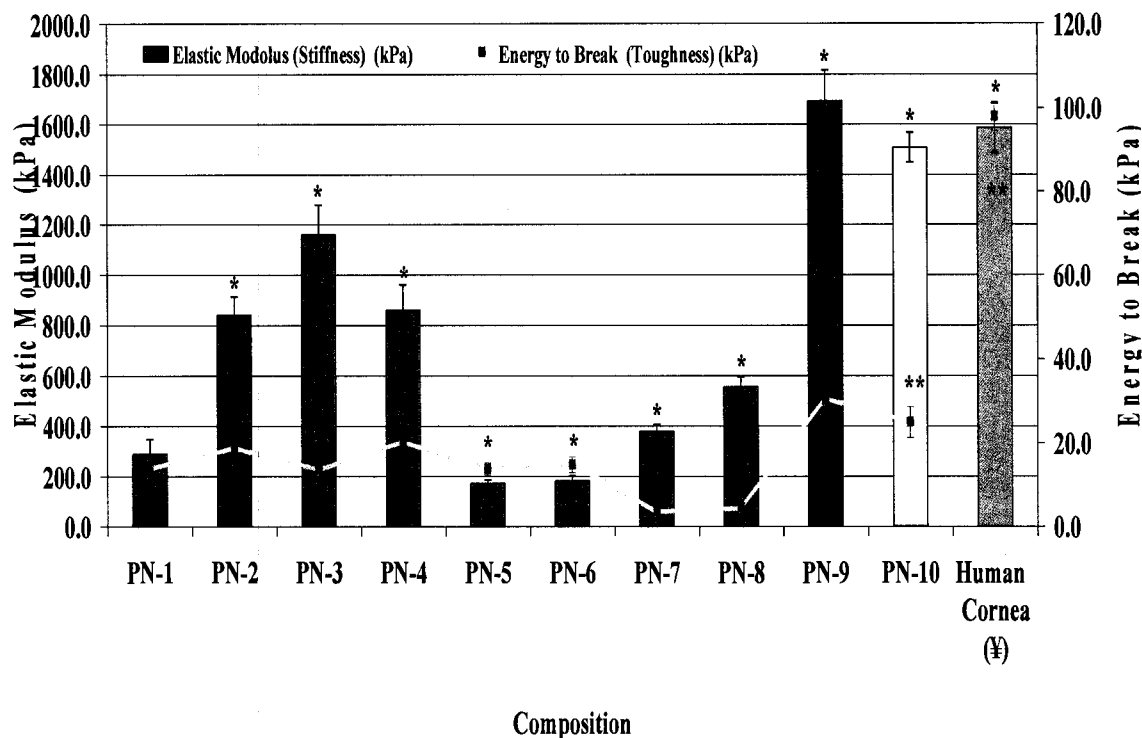
Figure 2.10 Results for mechanical properties (elastic modulus and energy to break) for the optimum formulation compared to those for other formulations and eye bank human cornea.

Notes: ¥ The data for human cornea was divided by 10 to fit into the chart.

¥¥ Human corneas were provided by the Eye Bank of Canada for research use only and were obtained from deceased patients.

* denotes significant difference between each scaffold and PN-1 control scaffold using ANOVA ($p \leq 0.050$) for elastic modulus.

** denotes significant difference between each scaffold and PN-1 control scaffold using ANOVA ($p \leq 0.050$) for energy to break.

Despite the mechanical superiority of HC over PN-10, results suggest that the optimum formulation is still superior to other formulations in mechanical properties. The optimum material was successfully transplanted into pigs' eyes as an artificial cornea and studied for 12 months following a more comprehensive set of tests for physical and biological properties with satisfactory results [5].

2.5   Conclusions

The aim of the study was to develop systematic strategies for development of new biomaterials for tissue engineering applications such as corneal transplantation. A full factorial experimental design (FED) was combined with a response surface design (RSD) strategy for screening, optimization, and fabrication of novel implantable materials that mimic human tissues such as cornea. The influence of three important factors representative of materials' composition (chitosan to collagen molar ratio [CTN], EDC to collagen/chitosan molar ratio [EDC], and PEG-DBA to collagen/chitosan molar ratio [PEG]) on four materials properties (elastic modulus [EM], energy to break [ETB], light transmission [LT], and epithelial cell number [ECG]) was investigated. As a result, hybrid polymer networks (HPN) comprised of collagen and chitosan were developed with the aid of synthetic cross-linkers such as PEG-DBA and EDC-NHS. The resulting FED and RSD models offered good insight into the possibilities of material formulations. It also offered solutions to the problems and gave clear directions toward optimum formulation. More specifically, the following conclusions could be drawn from this work over the range of investigation:

1- Higher levels of CTN, EDC, and PEG favored mechanical stiffness [EM] of the scaffolds at low factor levels, while at high levels of factors a decreasing impact on EM was observed. For example, the increase in cross-linkers ratios, i.e. EDC and PEG, was associated with decrease of the stiffness and maximum EM was achieved at or in the vicinity of a middle composition (center point).

2- Higher levels of CTN, EDC, and PEG had an increasing impact on the toughness before a middle range point and a decreasing impact beyond that point. Also,

there was no clear superiority of any factor over others in terms of the influences on ETB.

3- Higher levels of CTN had a significant decreasing impact on the transparency of the scaffolds. EDC ratio did not have a significant effect on LT on its own while its interaction terms with CTN and PEG were significantly influential. Higher levels of PEG increased optical transparency of the scaffolds while it had a negative impact on light transmission when conjugated with EDC.

4- Unlike the results for EM and ETB, the LT results did not support the fact that all factors should be set at the center of the design in order to achieve the highest value for light transmission.

5- All factors except chitosan ratio had significant effects on epithelial cell growth. Though EDC did not have a first order significant effect, it had a second-order effect that was highly significant and negatively impacted cell count on the scaffolds. Also, PEG ratio had a negative impact on ECG response.

6- Scaffold materials optimization was successfully performed using standard quadratic models, ANOVA analysis, and contour plots.

7- The formulation (PN-10) was identified as the optimum one that could satisfy key requirements for a transplantable artificial cornea.

2.6   References

1.   Bonfield W. Biomaterials and tissue engineering: a new medical horizon? The eighty-seventh Thomas Hawksley memorial lecture, Suffolk: Moreton Hull Press Limited, 1999.

2.   Hedberg EL, Shih CK, Lemoine JJ, Timmer MD, Liebschner MAK, Jansen JA. In vitro degradation of porous poly(propylene fumarate)/poly(DL-lactic-co-glycolic acid) composite scaffolds. Biomater 2005; 26: 3215–3225.

3.   Vert M, Li MS, Spenlehauer G, Guerin P. Bioresorbability and biocompatibility of aliphatic polyesters. J Mater Sci 1992; 3: 432-446.

4.   Hutmacher DW. Scaffolds in tissue engineering bone and cartilage. Biomater 2000; 21: 2529–2543.

5.   Rafat M, Li F, Fagerholm P, Lagali N, Watsky MA, Heyne B, Hasanloo M, Scaiano JC, Munger R, Hodge W, Matsuura T, Griffith M. PEG-Stabilized Carbodiimide Crosslinked Collagen-Chitosan Hydrogels for Corneal Tissue Engineering. To be submitted to Biomaterials 2007.

6.   Chen YL, Chen HC, Lee HP, Chan HY, HU YC. Rational development of GAG-augmented chitosan membranes by fractional factorial design methodology. Biomater 2006; 27: 2222–2232.

7.   Fisher RA. Statistical Methods for Research Workers. London: Oliver & Boyd, 1925.

8.   Taguchi G. System of experimental design. New York: UNIPUB Kraus International Publications, 1987.

9.   Fazilat H, Dara B, Meakina JR, Aspden RM. Statistical methods in finite element analysis. J Biomech 2002; 35: 1155–1161.

10.   Czitrom V. One-Factor-at-a-Time versus designed experiments. The American Statistician. 1999; 53 (2): 126-131.

11.   Shaw R, Festing MFW, Peers I, Furlong L. Use of factorial designs to optimize animal experiments and reduce animal use. ILAR (Inst. Lab. Anim Res.) 2002; 43(4): 223-232.

12.   Henriksen I, Green KL, Smart JD, Smistad G, Karlsen J. Bioadhesion of hydrated chitosans: an in vitro and in vivo study. Int J Pharm 1996; 145: 231-240.

13. Lucas-Girota A, Langloisb P, Sangleboeufc JC, Ouammoud A, Rouxelc T, Gaude J. A synthetic aragonite-based bioceramic: influence of process parameters on porosity and compressive strength. Biomater 2002; 23: 503–510.

14. Fisher JP, Dean D, Mikos AG. Photocrosslinking characteristics and mechanical properties of diethyl fumarate/poly(propylene fumarate) biomaterials. Biomater 2002; 23:4333–4344.

15. Radisic M, Euloth M, Yang L, Langer R, Freed LE, Vunjak-Novakovic G. High-density seeding of myocyte cells for cardiac tissue engineering. Biotechnol Bioeng 2003; 82: 403–414.

16. Chang KH, Zandstra PW. Quantitative Screening of Embryonic Stem Cell Differentiation: Endoderm Formation as a Model. Biotechnol Bioeng 2004; 88 (3): 287-298.

17. Moreau JE, Chen J, Bramono DS, Volloch V, Chernoff H, Vunjak-Novakovic G, Richmond JC, Kaplan DL, Altman GH. Growth factor induced fibroblast differentiation from human bone marrow stromal cells in vitro. J Orthopedic Research 2005; 23:164–174.

18. Weiss LE, Amon CH, Finger S, Miller ED, Romero D, Verdinelli I, Walker LM, Campbell PG. Bayesian computer-aided experimental design of heterogeneous scaffolds for tissue engineering. Computer-Aided Design 2005; 37 1127–1139.

19. Harris JM. Polyethylene Glycol and Derivatives for Advanced PEGylation, Nektar Advanced PEGylation CATALOG 2005-2006; Available online: www.nektar.com/peg.

20. Liu Y, Gan L, Carlsson DJ, Fagerholm P, Lagali Neil, Watsky MA, Munger R, Hodge WG, Priest D, Griffith M. A simple, cross-linked collagen tissue substitute for corneal implantation. IOVS 2006; 47: 1869-1875.

21. Priest D, Munger R. A new instrument for monitoring the optical properties of corneas. Invest Ophthalmol Vis Sci 1998; 39: 352.

22. Brossard Perez LE, Cortez LAB, Mesa J, Bezzon G, Olivares Gómez E. The strategy of empirical research and optimization process. Pesquisa Operacional 2001; 21(1): 89-105.

23. Frost HM. An introduction to biomechanics. Springfield: Charles C. Thomas Publisher, 1971.

24.   FungYC. Biomechanics: mechanical properties of living tissues. New York: Springer-Verlag Publishing Company, 1981.

25.   Work WJ, Horie K, Hess M, Stepto RFT. Definitions of terms related to polymer Blends, composites, and multiphase polymeric materials (IUPAC Recommendations 2004). Pure Appl Chem 2004; 76 (11): 1985–2007.

26.   Mustonen RK, McDonald MB, Srivannaboon S, Tan AL, Doubrava MW, Kim CK. Normal human corneal cell populations evaluated by in vivo scanning slit confocal microscopy. Cornea 1998; 17(5): 485.

Chapter 3

PEG-Stabilized Carbodiimide Crosslinked Collagen-Chitosan Hydrogels for Corneal Tissue Engineering

Mehrdad Rafat,[a,b] Fengfu Li,[b] Per Fagerholm[d], Neil Lagali,[b] Mitchell A. Watsky,[e]

Rejean Munger,[b] William Hodge,[b] Takeshi Matsuura,[a] and May Griffith[b,c*]

[a] Department of Chemical Engineering, University of Ottawa, Ottawa, ON K1N 6N5, Canada

[b] University of Ottawa Eye Institute, Ottawa, ON K1H 8L6, Canada

[c] Department of Cellular and Molecular Medicine, University of Ottawa, Ottawa, ON K1H 8M5,

[d] Department of Ophthalmology, Linko"ping University Hospital, Linko"ping, Sweden

[e] University of Tennessee Health Center, Memphis, Tennessee, USA

3.1 Abstract

Implantable biomaterials that mimic the extracellular matrix in key physical and physiological functions require components and microarchitectures that are carefully designed to maintain the correct balance between biofunctional and physical properties. The goal was to develop hybrid polymer networks (HPN) that combine the bioactive features of natural materials and physical characteristics of synthetic ones to achieve synergy between the desirable mechanical properties of some components with the biological compatibility and physiological relevance of others. In this study, we developed collagen/chitosan composite hydrogels as corneal implants stabilized by either a simple carbodiimide crosslinker or a hybrid cross-linking system comprised of a long-range bifunctional cross-linker (e.g. Poly(ethylene glycol) dibutyraldehyde (PEG-DBA)), and short-range amide type cross-linkers (e.g. 1-ethyl-3-(3-dimethylaminopropyl) carbodiimide (EDC), and N-hydroxysuccinimide (NHS)). Optimum hybrid hydrogel demonstrated significantly enhanced mechanical strength and elasticity by 100 % and 20%, respectively, compared to its non-hybrid counterpart. It demonstrated excellent optical properties, suturability, good resistance to UV photodegradation, and good permeability to glucose and albumin. It had excellent biocompatibility and when implanted into pig corneas for 12 months, allowed seamless host-graft integration with successful regeneration of host corneal epithelium, stroma, and nerves.

Key words: biomimetic material, collagen, cornea, confocal microscopy, in vivo test, nerve regeneration,

3.2 Introduction

Biomaterials used in tissue engineering have traditionally been biocompatible, non-reactive synthetic materials [1]. Although many of these materials have achieved widespread clinical use, seamless integration and immunological response issues still remain. This had led to the more recent paradigm shift to the development of natural based biomaterials that are biointeractive and will allow seamless host-graft integration [2]. Macromolecules that mimic the microarchitecture and function of naturally occurring extracellular matrix (ECM) molecules are therefore being examined for tissue engineering applications.

The most common ECM component in mammalian tissues is collagen, which accounts for approximately 30% of all body proteins [3]. Extracted, purified collagen has been popular in tissue engineering due to its high biocompatibility. Although very robust *in vivo*, extracted collagen is rapidly degraded and lacks the mechanical toughness and elasticity, due to the dissociation of natural cross-links during isolation and purification process [4].

Chitosan is a biocompatible, amino cationic polysaccharide derived by deacetylation of chitin, the main component of the exoskeleton of crustaceans [5]. Chitosan emulates ECM glycosaminoglyucans molecules such as chondroitin sulphate, and amplifies the number of amine reaction sites and forms an ionic complex with collagen that may result in enhanced stability.

Polymeric blends of collagen and chitosan have been previously used to emulate the collagen-glycosaminoglycans scaffolding of the ECM in various tissue engineering applications [6], such as scaffolds for artificial liver [7], as skin scaffolds with nerves [8]

71

and dermal models [9], as membranes for controlled drug release [10], and as an *in vitro* model to test anti-cancerous drugs [11]. The first study on collagen-chitosan blends for corneal application was reported by Chen et al. in 2005 [12]. They demonstrated that non-crosslinked collagen–chitosan–sodium hyaluronate blends were non-cytotoxic toward rabbit corneal cells and tissue. Despite the emerging interests in collagen/chitosan blends, to this date, there has been no report on the use of crosslinked collagen/chitosan composite scaffolds as implantable tissue-engineered corneas.

Many efforts have been made to stabilize collagen and/or chitosan by chemical cross-linking methods that are generally divided into two categories, bi-functional and amide-type [13]. However, hybrid use of these two cross-linking methods has not been explored yet. Several bi-functional reagents such as glutaraldehyde (GTA) [14, 15], polyethylene glycol diacrylate (PEGDA) [16, 17], and hexamethylene diisocyanate (HDC) [18] have been used to bridge amine groups of lysine or hydroxylysine residues of collagen polypeptide chains and those of chitosan. A major handicap of these cross-linking agents is the potential toxic effect of residual molecules and/or compounds released when the biomaterial is exposed to biological environments, i.e. during in vivo degradation.

Amide-type cross-linkers such as carbodiimide especially EDC and NHS offer the main advantage of lower toxicity and better compatibility over GTA and HDC [19]. However, collagen scaffolds stabilized by carbodiimide are not tough and elastic enough for PKP transplantation due to limited zero-length cross-links and there are reaction sites on collagen molecules that are not linkable by carbodiimide. It is reported that EDC-NHS can link carboxylic acid and amino groups located within 1.0 nm from each other [20].

Therefore, functional groups that are located on adjacent collagen microfibrils are too far apart to be bridged by carbodiimide. One more general issue with systems such as EDC-NHS is that the increase in tensile strength, especially when induced by the increasing of cross-linking agent, is associated with the decrease in elasticity and toughness and cells biocompatibility, which could be due to additional restraints to the mobility of the polymer network, decrease in scaffold porosity and diffusion of reactive residues and byproducts out of the scaffolds, respectively.

Despite these drawbacks, these crosslinking agents have been separately used to fabricate collagen and/or chitosan based matrices for mostly diagnostic applications, where the tissue is made and used in vitro for testing drug metabolism and uptake, and toxicity. Reconstruction of a bovine cornea that comprises of a three dimensional collagen scaffold was developed for *in vitro* studies using bovine dermal collagen [21]. *Zieske et al.* [22] developed another *in vitro* cornea using primary rabbit stromal cells. A three-dimensional scaffold comprising of bovine dermal collagen was developed by *Germain et al.* [23] to support an *in vitro* human cornea.

We have previously reported collagen-based materials that range from *in vitro* corneal equivalents reconstructed from immortalized human cell lines [24] to corneal scaffolds based on the copolymer poly(*N*-isopropylacrylamide-co-acrylic acid-co-acryloxylsuccinimide) [25, 26], and simple cross-linkers such as EDC-NHS [27]. These scaffolds allowed regeneration of corneal cells and nerves when implanted as lamellar grafts. However, these materials still lacked the optimal toughness and elasticity to ensure they could withstand Penetrating Keratoplasty (PKP) surgical procedures, as well as normal day to day mechanical stresses. To this date, there have been no reports on hybrid

tissue-engineered corneal scaffolds that optimally meet the criteria for a transplantable artificial cornea [28]. An improved artificial cornea that can be implanted by standard PKP procedures would offer hope to desperate constituency of patients, more than 10 million worldwide, many of whom are in developing countries [29, 30].

Here we report the development of HPN corneal hydrogels that are implantable by PKP surgical procedure. This is the first report on collagen/chitosan composites as corneal implants that are stabilized by either a simple EDC-NHS cross-linking system or a hybrid crosslinking system comprised of PEG-DBA and EDC-NHS. HPN hydrogels are prototyped into corneal substitutes that have excellent physical properties (e.g. optical, swelling, and permeability), excellent biocompatibility, adequate robustness for PKP transplantation, and seamless host-graft integration and regeneration of corneal cells and nerves when implanted into pigs' corneas. However, the only HPN hydrogel that optimally met the requirement of an implantable corneal graft was the one stabilized by a hybrid PEG-DBA/EDC-NHS crosslinking system.

3.3 Materials and Methods

3.3.1 Chemical and structural design of HPN scaffolds

As shown in Fig. 3.1(a), chitosan was first incorporated into the collagen gel by physical mixing. In the second stage, the homogeneous collagen/chitosan composite was stabilized by either a simple short-range EDC-NHS crosslinking system (HPN-1 scaffold), or a hybrid cross-linking system comprised of a bifunctional long-range cross-linker, e.g. PEG-DBA, and an amide-type short-range cross-linker such as EDC-NHS (HPN-2 scaffold) (See Fig. 3.1(b)).
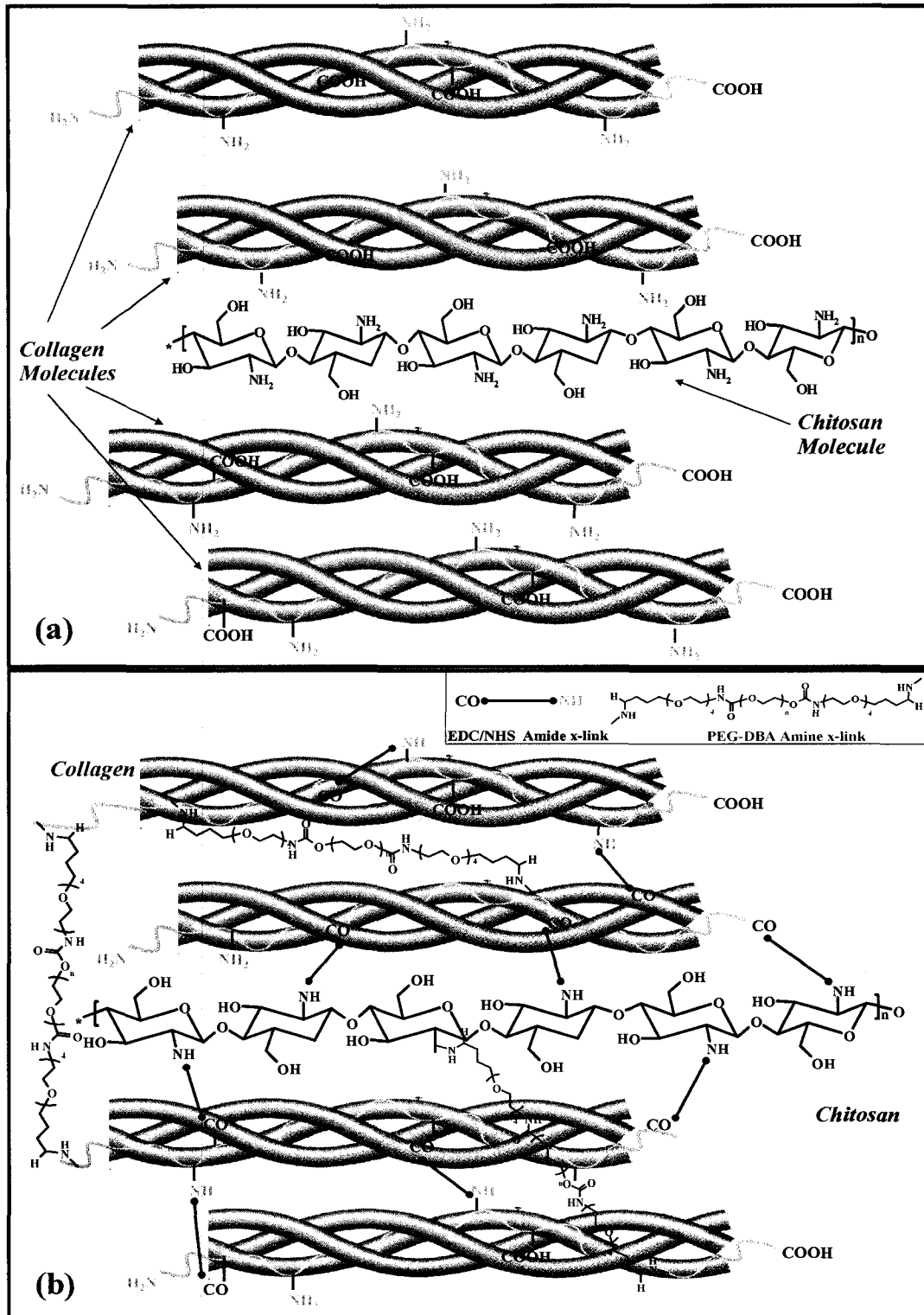
Figure 3.1 Molecular and structural schematics of (a) chitosan-embedded collagen scaffold before cross-linking, (b) HPN scaffold comprised of chitosan-embedded collagen scaffold cross-linked by PEG-DBA and EDC-NHS.

75

As shown in Fig. 3.1 (b), PEG-DBA forms long-range intermolecular/interfibrilar cross-links that may result in significantly enhanced robustness and elasticity by maintaining a larger distance between molecules and fibers. EDC-NHS provides short-range intramolecular/intermolecular cross-links that are necessary to enhance scaffold's strength. Although, covalent bonds are the main interactions that form the polymer networks, other interactions cannot be excluded. Indeed, secondary interactions, such as ionic and hydrogen bonds, participate significantly in the formation of HPN scaffolds [5].

Poly(ethylene glycol) derivatives are biochemically inert and biocompatible polymers that have been widely used in tissue engineering [31-36]. However, the hybrid cross-linking system of PEG-DBA/EDC-NHS has not been reported yet for the reinforcement of collagen/chitosan composites. As with other aldehyde reagents, reaction between a butyraldehyde group and an amino group of a biologically active material such as collagen or chitosan involves reductive amination to provide a secondary amine linkage.

As shown in Fig. 3.2(a), reductive amination comprises the formation of a hydrolysable imine linkage between the PEG-DBA and collagen and/or chitosan (condensation), followed by reduction of the imine to provide a secondary non-hydrolysable amine linkage. The reducing step is accomplished by the addition of a reducing agent, such as sodium cyanoborohydride (NaCNBH$_3$).
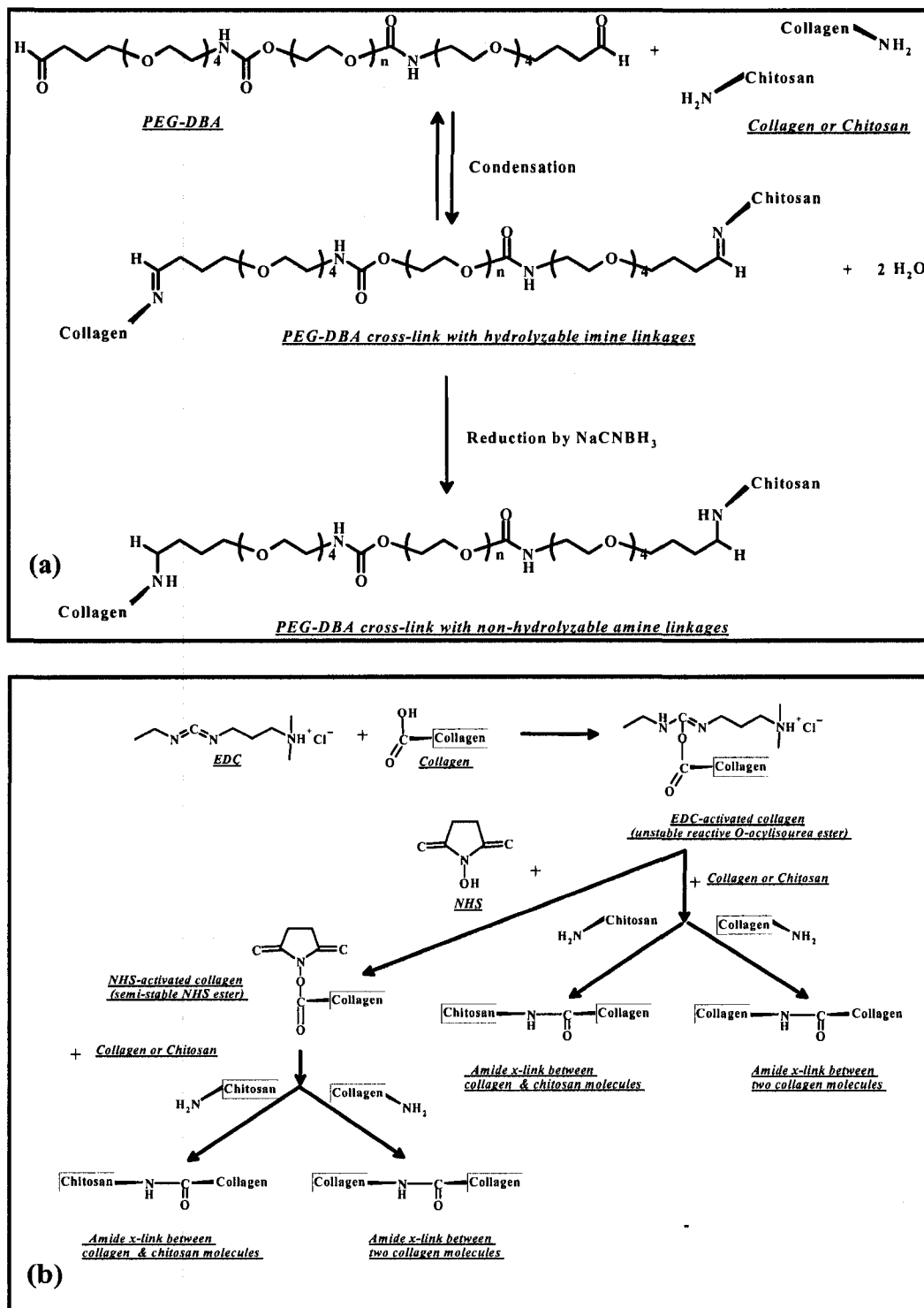
Figure 3.2 Cross-linking reaction mechanisms of collagen and chitosan by (a) PEG-DBA, and (b) EDC-NHS.becoming a part of the actual linkage as opposed to PEG-DBA that become an integral part of the scaffold. collagen with an amine group on either a collagen or chitosan molecule without

As shown in Fig. 3.2(b), EDC-NHS system facilitates the formation of short-range amide bonds by linking a carboxylic group of glutamic or aspartic acid residue on collagen with an amine group on either a collagen or chitosan molecule without becoming a part of the actual linkage as opposed to PEG-DBA that become an integral part of the scaffold.

We hypothesized that long-range amine and short-range amide bonds led to the formation of hydrogels with a network structure. According to *Berger et al.* [5] in order to state that a hybrid network is created it is sufficient to confirm that covalent bonds including "amide" and "amine" cross-links are formed in the scaffold. We will confirm the formation of amine and amide covalent bonds in the HPN scaffolds directly and indirectly by infrared spectroscopy and tensile mechanical test results, respectively.

3.3.2 Fabrication of HPN scaffolds

The base material for HPN scaffolds comprised a mixture of 10% (w/v) atelo-collagen type-I and 3% (w/v) chitosan in sterile distilled deionized water ($_{dd}H_2O$). The two solutions were mixed at predetermined ratios to make a homogeneous blend prior to cross-linking. PEG-dibutyraldehyde (PEG-DBA) (MW 3400 Da from Nektar Inc.), and 1-ethyl-3-(3-dimethylaminopropyl) carbodiimide (EDC) and N-hydroxysuccinimide (NHS) (purchased from Sigma-Aldrich) were added to crosslink the collagen and chitosan blend. Ratios tested are given in Table 3.1. HPN-1 and HPN-2 scaffolds correspond to PN-2 and PN-10 formulations in Chapter 2, respectively. Molar ratios in Table 3.1 were designed and determined by a multivariate experimental design study we recently reported [37] (Please see chapter 2 for the details).

For comparison, two control scaffolds, control-1, and control-2, were also fabricated using 10% (w/v) atelo-collagen type-I and EDC-NHS chemistry using the same cross-linker to amine molar ratios as HPN-1, and HPN-2 scaffolds, respectively.

More specifically, freeze dried porcine collagen powder (Nippon Meat Packers, Inc, Tskuba, Japan) was dissolved in $_{dd}H_2O$ at 4°C to give 10% (w/v) concentration. A 3% (w/v) chitosan solution was also prepared by dissolving chitosan flakes (MW 400,000 Da obtained from Fluka) in 0.2 N hydrochloric acid, also at 4°C. (See Fig. A.1 in Appendix A).

For HPN-1 scaffold, 0.12 ml of 3% chitosan solution and 0.6 ml of a 10% collagen solution were mixed with 0.4 ml 2-(N-morpholino) ethanesulfunic acid (MES) buffer using a Tefzel™ Tee-joint and a syringe pump system we previously described in *Liu et al.* [27] (Also see Figs.A.2 and A.3 in Appendix A). The blend was then mixed with a predetermined amount of EDC-NHS cross-linker agent (See Table 3.1) in 0.35 ml MES buffer and thoroughly mixed at 4°C. Aliquots of the resulting homogeneous solution were immediately dispensed into 500 micron thick, 12 mm diameter moulds with corneal contours and cured first at room temperature for 16 hours, and then at 37°C for another 16 hours, in 100% humidity environments at both temperatures (See Fig. A.4 in Appendix A). De-moulding was achieved by immersion in phosphate buffered saline (PBS) for 2 hours. Samples were then immersed in a 0.1 M Na_2HPO_4 solution for 2 hrs to hydrolyze any remaining 0-acylisourea groups and subsequently washed four times with PBS solution (0.5% (w/v) PBS, containing 1% v/v chloroform) at room temperature to terminate any reactive residues, extract out reaction byproducts, and to sterilize the samples.

Table 3.1 Composition and performance of HPN scaffolds, their non-hybrid control scaffolds, and human cornea.

Scaffold #	Crosslinkers to collagen & chitosan amine molar ratio* [EDC: NHS: PEG:NH$_2$]	Chitosan:collagen molar ratio	Ultimate Stress (kPa)	Ultimate Elongation (%)	Elastic Modulud [Stiffness] (kPa)	Energy to Break [Toughness] (kPa)	Glucose diffusivity cm^2/s	Albumin diffusivity cm^2/s	Water content (%)
Control-1	3.0 : 3.0 : 0.0 : 1.0	0.00 : 1.00	72 ± 9	52 ± 2.8	289 ± 60	13.9 ± 2.0	-	-	93.3 ± 0.6
Control-2	4.5 : 4.5 : 0.0 : 1.0	0.00 : 1.00	112 ± 16	38 ± 2.5	724 ± 89	13.7 ± 2.5	$(2.7 \pm 0.7) \times 10^{-6}$	1.60×10^{-7}	92.5 ± 0.7
HPN-1	3.0 : 3.0 : 0.0 : 1.0	0.05 : 1.00	145 ± 37	39 ± 6.6	838 ± 75	18.8 ± 8.0	-	-	92.1 ± 0.4
HPN-2	4.5 : 4.5 : 0.3 : 1.0	0.01 : 1.00	220 ± 30	45 ± 3.5	1508 ± 59	25.0 ± 5.0	$(2.8 \pm 0.04) \times 10^{-6}$	1.67×10^{-7}	90.0 ± 1.3
Human cornea	-	-	3294 ± 194	60 ± 15	15863 ± 1958	980 ± 200	$[(2.6 \pm 0.3) \times 10^{-6}]^a$	$[1.00 \times 10^{-7}]^b$	78.0 ± 3.0

Note:

* Number of moles of cross-linker (s) divided by number of moles of amine in both collagen and chitosan.

[a] data adopted from the reference [41]

[b] data adopted from the reference [43]

80

The HPN-2 scaffold was prepared as for HPN-1 scaffold using 0.02 ml of 3% chitosan solution and 0.6 ml of a 10% collagen solution and then cross-linked using a hybrid cross-linking system comprised of PEG-DBA and EDC-NHS. The collagen/chitosan mixture was mixed with predetermined amounts of EDC-NHS and PEG-DBA cross-linking agents in 0.35 ml MES buffer to achieve the molar ratios given in Table 3.1. Fabricated HPN-2 hydrogels were then post-treated with sodium cyanoborohydride ($NaCNBH_3$) by immersing in 1% (w/v) $NaCNBH_3$ solution for 2 hrs to reduce the imine bonds to more stable amine linkages. HPN-2 hydrogels were thoroughly rinsed and sterilized as for HPN-1 hydrogels.

3.3.3 Evaluation of mechanical properties

The tensile strength, elongation at break (elasticity), elastic modulus (stiffness), and energy at break (toughness) of tissue-engineered scaffolds were determined using an Instron Series IX Automated Materials Testing System (Model 3344, Norwood, MA, USA) with a load cell of 10N capacity at a crosshead speed of 10 mm/min and an initial grip separation of 6 mm. PBS equilibrated samples were cut into dumb-bell shaped specimens of identical rectangular gage area (width 5 mm, gage length 5 mm, thickness 0.5 mm) with two 3-mm end tabs (See Fig. B.2 in Appendix B). To avoid breakage and slippage of the sample in the jaws, the 6 mm wide tabs on the end of each dumb bell sample were adhesive coated using DERMABOND™ (ETHICON Inc., Somerville, New Jersey, USA), a fast curing, cyanoacrylate-based skin adhesive, and reinforced with tape on both sides. This method of sample mounting completely prevented jaw breaks. Samples were not stress preconditioned prior to testing to failure. Every recorded value is the average of at least three measurements. The same technique was applied for

mechanical testing of human cornea except for the specimen dimension that was 4 mm width, 7 mm gage length, and 1.1 mm thickness. In addition, tensile measurements of human cornea were performed using an Instron Materials Testing System (model 5565) with a load cell of 500N capacity and pneumatic, rubber faced grips (model 2712, jaw pressure 5 bar), at a crosshead speed of 10 mm/min and an initial grip separation of 13 mm.

3.3.4 Suturing to human corneal rim

The human corneal rims and the corneal scaffolds were trephine to appropriate sizes, e.g. 7 mm in diameter. Each corneal scaffold was sutured onto a rim by placing 16 ophthalmic sutures (10-0) while keeping the construct hydrated using Optisol® corneal storage medium. The number of sutures placed, number of knots successfully buried, and the severity of micro-shears were recorded.

3.3.5 Evaluation of optical properties

Light transmission measurement was made at 21°C, both for white light (quartz-halogen lamp source) and for narrow spectral regions (centered at 450, 500, 550, 600, and 650 nm) for corneal materials, human eye bank and rabbit corneas using an optical method developed by Priest et al. [38]. Samples were hydrated in 0.5% (w/v) PBS before and during the measurement.

3.3.6 Glucose and albumin diffusivity measurements

Glucose diffusivity was determined using a modified version of the method described by Liu et al. [39]. Measurements were made at 35°C (the cornea's normal, physiological temperature) using a modified Ussing chamber (Warner Instruments, Hamden, CT) with air-lift mixing. The hydrogel (500 μm in thickness and 12 mm in

diameter) was used as the membrane between the glucose permeation chamber (8 ml of 0.05 g/ml glucose in PBS) and the receptor (PBS) chamber. The receptor chamber was first sampled at 30 min, followed by 15 min sampling intervals with the last two samples collected 20 min apart. For each sample, 5 ml was removed and replaced with the same volume of fresh PBS buffer. These samples were prepared for analysis using a glucose assay kit (Sigma GAGO-20: glucose oxidase/peroxidase reagent and O-dianisidine dihydrochloride reagent) and analyzed using a Shimadzu UV-1601 spectrophotometer at 540 nm.

For albumin diffusivity measurements, a simple temperature-controlled (35°C) side-by side diffusion chamber with magnetic stirring in each chamber (PermeGear, Bethlehem, PA) was employed to avoid foaming problems. Fluorescein isothiocyanate (FITC)-labeled albumin ($\approx$66,000 Da, Sigma) was used as the tracer molecule. Both the receptor and permeation chambers were 3 ml volume, with 50 μM albumin used in the permeation chamber. Sampling was performed as in the glucose measurements. Albumin concentrations in the receptor chamber were determined by measuring the fluorescence value of the samples in a fluorophotometer (Gilford Fluoro IV) and fitting the values to a regression line of standards of known concentrations. Diffusivity values were calculated using these values and the same calculations as described for the glucose diffusivity measurements.

3.3.7 Water content characterization

Water content studies were also performed for various scaffolds using 0.5% (w/v) PBS solution. Equilibrium hydrated mass ($m_{hydrated}$) and dry mass (m_{dry}) were used to

determine water content, defined as: *Water content* $= (\dfrac{m_{hydrated} - m_{dry}}{m_{hydrated}}) \, x \, 100$

3.3.8 Fourier Transform Infrared Spectroscopy (FTIR)

Infrared spectra of corneal scaffolds were obtained using a MIDAC M2000 Series FTIR spectrometer equipped with a diamond compression cell (Greaseby-Specac Diasqueeze) under ambient conditions. All scaffolds were prepared in thin films with a thickness of 80 microns. They were then dried by nitrogen gas for 6 hrs and cut into 5 mm discs. The sample compartment was purged with nitrogen gas for about ½ hr before collecting any spectra. Purging was continued throughout every run. Before acquiring an FTIR spectrum of a sample, a reference or background spectrum was collected. Dry films were placed in the sample holder and placed in the sample compartment which was purged with nitrogen gas for another 30 min. Absorbance IR spectra of dry films were collected by accumulating 54 scans at a resolution of 4 wavenumbers in the spectral range between 4000 and 500 cm^{-1}. All sample spectra were normalized against the dry-cell background of 54 scans collected at the ambient temperature. Each FTIR spectrum reported was selected from a set of at least three samples prepared under identical conditions.

3.3.9 UV photostability of the corneal scaffolds

To determine photostability of HPN corneal materials in comparison with contact lens material (CL), and human cornea (HC), samples were exposed to sunlight-simulated UV irradiation in a solar photoreactor (Luzchem Model LZC-SSR, Ottawa, Canada). The corneal samples were placed face up in sterile PBS solution at pH 7.4 in a beaker on the chamber floor. The solar simulation filters were also placed on a stand about 7 cm above the chamber floor. In addition, a specific filter was used to cut out light wavelengths below 300 nm. Three specimens per formulation were used on three different days. The

received by each corneal specimen was 260 Wm^{-2} for 27 hrs that was the equivalent of the sunlight UV irradiation energy. A spectroradiometer was used to record the spectrum of each specimen before and after irradiation.

3.3.10 Evaluation of human corneal epithelial cells growth on corneal scaffolds

Immortalized human corneal epithelial cells (HCECs) were used to evaluate epithelial coverage. HCECs were seeded on top of 1.5 cm^2 hydrogel pieces and supplemented with a serum-free medium containing epidermal growth factor (keratinocyte serum-free medium-KSFM); Life Technologies, Burlington, Ontario, Canada) until confluence. The medium was then switched to a serum-containing modified supplemented hormonal epithelial medium (SHEM) for 2 days, followed by maintenance at an air–liquid interface. Microscopic images were taken on days 1, 3, 5, and 7 post-seeding and number of cells that had attached and spread were measured using Northern Eclipse software (EMPIX IMAGING Inc., North Tonawanda, NY, USA). Four randomly selected areas of the same dimensions were counted for each sample and the number of cells counted was normalized to the area of gel selected, i.e. counts were expressed as cells per square milimeter of surface area. At two weeks, constructs were fixed in 4% paraformaldehyde in 0.1 M PBS and were processed for routine hematoxylin and eosin (H&E) staining.

3.3.11 Evaluation of surface neurite extension of dorsal root ganglia (DRG) onto tissue-
engineered scaffolds.

DRGs were isolated from 8 day old chick embryos and adhered to the surface of washed scaffolds using an overlay of a lightly crosslinked collagen gel. DRGs were then covered with DRG medium. Neurites were grown for a total of 6 days, with DRG

medium being changed every 2 days. Samples were fixed on day 6 post-adhering using 4% paraformaldehyde followed by staining at 4°C overnight for the presence of neurofilament using mouse anti-NF200 antibody (Sigma Cat# N5389) diluted 1:40 in TCT. Neurofilament was visualized the following day using donkey anti-mouse-Cy2 (Amersham Pharmacia Cat# PA42002, 1:200 in TCT). Whole-mounts were imaged using an Axiovert microscope.

3.3.12 Evaluation of bacterial growth in HPN scaffolds

To determine the susceptibility of corneal materials to bacterial replication, the ability of three bacterial species including *staphylococcus aureus (SA), streptococcus pneumoniae (SP), and pseudomonas aeruginosa (PA)* to proliferate on the scaffolds was tested. *SA, SP, and PA* are known to be the major causes of bacterial keratitis and ocular infections. Each scaffold was injected with 100 µl of each clinical bacterial strain (approximately 107 CFU that is the mean colony counts in colony-forming unit (CFU)). After the injection, the scaffolds were incubated at room temperature for 24 hours. They were then homogenized in saline and quantitative bacterial counts determined. Human donor corneas from the Eye Bank and sterile saline served as controls for comparison to the bioengineered corneas.

3.3.13 Rat subcutaneous implantation

Dorsal, para-vertebral incisions (four per animal) were made in the skin of rats anaesthetized by buprenor/morphine injections and halothane gas. One sample from each hydrogel formulation (n=3) was inserted into one skin incision. After the incision was closed using staples, the area of the implant was marked with a pen. At 30, 60, and 120 days post-operative, each surgical site was dissected out with sufficient surrounding

tissue to allow histological examination of contact sites, and placed immediately into Mirsky's fixative to fix overnight at 4°C. Samples were then equilibrated through a series of increasing concentrations of sucrose in PBS (10%, 20%, 30% w/v) and finally into 30% sucrose/PBS:OCT. They were then flash frozen in 30% sucrose/PBS:OCT (1:1) using liquid nitrogen-cooled pentane and stored at -80°C prior to cryosectioning. Ten –12 μm cryosectioned samples were stained with Hematoxylin & Eosin for histopathological evaluation. Specifically, samples were evaluated for extent of sample degradation, local tissues responses such as leukocyte invasion, neovascularization and fibrosis.

3.3.14 Animal Implantation and Clinical Evaluation

3.3.14.1   Implantation

In accordance to the ARVO Statement for the Use of Animals in Ophthalmic and Vision Research and with ethics approval from the University of Ottawa (Protocol EI-5), HPN-1 and HPN-2 corneal scaffolds (500 μm thick and 6 mm diameter) were implanted into the one cornea of each eight Yucatan porcine subjects (n=4 per group) utilizing deep lamellar keratoplasty (DLKP) with overlying sutures (Zirm retention bridge suturing) [40]. Prior to surgery and at all follow up examinations, animals were anaesthetized with intramuscular (IM) Midazalam (0.05 ml/kg), Glycopyrrolate (0.010 mg/kg), and Ketamine (0.11 ml/kg, Ketalar®, Parke-Davis, Barcelona, Spain). The non-operated, contralateral eye of each animal served as a control, along with four additional animals that received allografts. Animals were not given steroids, only antibiotics and analgesics over the first week post-operative. Sutures were removed at three weeks post-operative.

3.3.14.2   Clinical evaluation

In pigs, follow-up examinations were performed on a daily basis for the first week following surgery, and then weekly. Slit-lamp examinations were performed to ensure that corneas were optically clear, *In vivo* confocal microscopic (IVCM) examinations (ConfoScan3, Nidek, Japan) was utilized to assess cell and nerve in-growth, and determine total corneal thickness in live animals. IVCM was used to obtain full-thickness corneal scans of control and operated eyes from twelve pigs at four examination periods: preoperative, 2, 6, and 12 months postoperative. IVCM images from the central cornea were acquired at 10 μm depth intervals (image size: 440 × 330 μm w × h) and several scans were made through each cornea.

3.3.15 Statistical analysis

One-way ANOVA was performed for all responses to determine whether a difference between each data set and its corresponding control was statistically significant. The values of probability (p-value) were calculated. A significance level of 95% was chosen, thus a combination with a p-value less than 0.05 was considered to be significant.

3.4   Results and Discussion

3.4.1   Mechanical properties

HPN-1 and HPN-2 hybrid scaffolds demonstrated enhanced mechanical and structural properties compared to non-hybrid control-1, and control-2 scaffolds, respectively. They survived handling, suturing, implantation, and post-installation wear and tear. Mechanical properties of hybrid and non-hybrid scaffolds along with those of

human cornea are summarized in Table 3.1. As shown in the table, ultimate stress (US), ultimate elongation (UE), elastic modulus (EM), and energy to break (EB) of HPN-2 scaffold are significantly higher than those of control-2 by about 100%, 20%, 110%, and 80%, respectively. The US, UE, EM, and EB values are also representatives of strength, elasticity, stiffness, and toughness of the scaffolds, respectively. It is interesting to note that despite the increase in the US value for HPN-2, the UE value (45 ± 3.5 %) was also significantly higher than that of control-2 (38 ± 2.5 %)($p<0.05$). The higher UE values for HPN-2 should be mainly attributed to the contribution of PEG-DBA and chitosan in the formation of long-range cross-links (See Fig. 3.1(b), and Fig. 3.2(a)).

It is also interesting to compare the US and UE values for HPN-1 scaffold with that for non-hybrid control-1 scaffold. As expected, despite the higher US value for HPN-1 (145 ± 37 kPa) compared to that of control-1 (72 ± 9), the UE value of the former (39 ± 6.6) is lower than that of the latter (52 ± 2.8 %) ($p<0.05$). The presence of chitosan that incorporates more amine functional groups into the scaffold to form higher density of short-range cross-links and the absence of a long-range cross-linker such as PEG-DBA are likely to be responsible for this pattern. As we discussed earlier, the enhancement of tensile strength, is generally associated with the decrease of elasticity (compare the US and UE values for HPN-1 and control-2 with those of control-1 in Table 3.1). Indeed, this behavior is a characteristic of an increase in short range cross-links. However, simultaneous enhancement of all mechanical properties is achievable by developing hybrid scaffolds such as HPN-2, in which hybrid networks with both short and long-range cross-linking agents are present. Despite the huge difference between mechanical properties of HPN-2 and those of human cornea (Table 3.1) we believe that we are

moving toward the development of bio-scaffolds that will closely mimic mechanical characteristics of native cornea.

3.4.2 PKP suture test

To examine whether the HPN scaffolds withstand suturing for PKP transplantation, they were trephined and sutured onto human corneal rims by placing 16 ophthalmic sutures (size10-0). As depicted in Fig. 3.3, HPN scaffolds were 100% suturable as no tearing or micro-shearing occurred at any suture points and all suture knots were successfully buried.
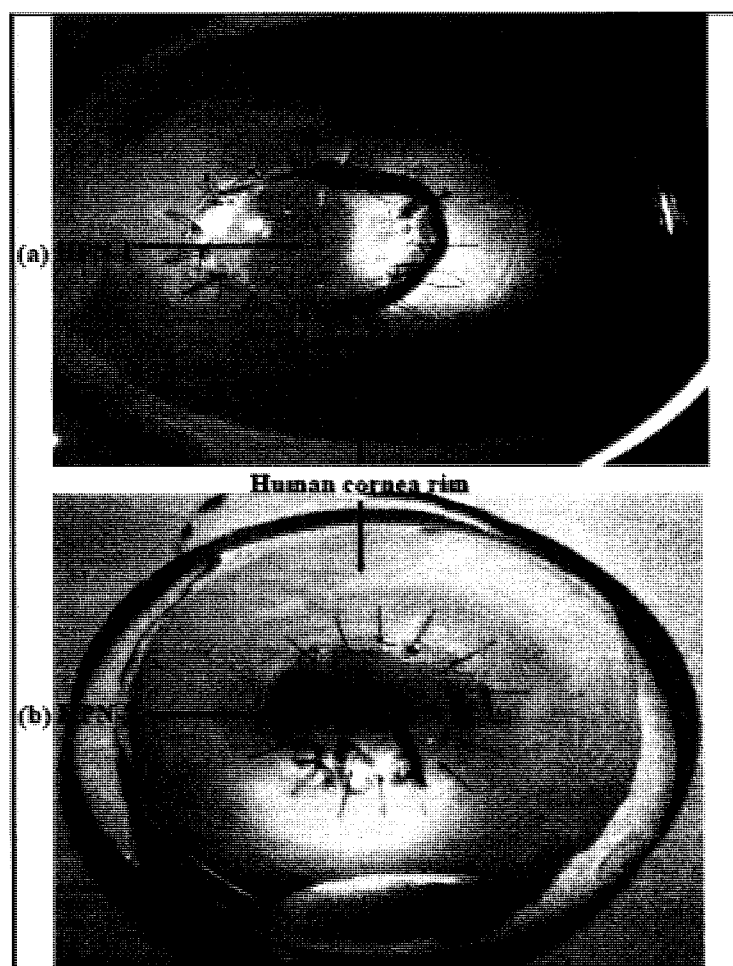
Figure 3.3   PKP suture test of (a) HPN-1 scaffold, and (b) HPN-2 scaffold to human cornea rims by placing 16 ophthalmic sutures (size10-0).

Control non-hybrid scaffolds were also examined and demonstrated poor to moderate suturability and micro-shearing rate between 20 to 60 % depending on their composition.

3.4.3 *Optical properties*

As shown in Fig. 3.4(a), HPN-1 and HPN-2 hybrid scaffolds were optically transparent at all wavelengths of visible light. Although their light transmission values were slightly lower than those for control-1 and control-2, they were still higher than 90% and superior to those of human and rabbit corneas at visible light wavelengths. Figure 3.4 (b) represents % light scatter for the same scaffolds.

HPN scaffolds provided a desired optical light scatter below 7% at all wavelengths of visible light. Although light scatter values for HPN-1 and HPN-2 were slightly higher than those of control-1 and control-2, respectively, they were still lower than those of human and rabbit corneas at all visible light wavelengths. The slightly lower light transmission (or slightly higher light scatter) of HPN-2 scaffold compared to other tissue-engineered scaffolds might be attributed to its morphological changes due to the presence of macromolecules such as chitosan and PEG-DBA and its cross-linking density, as well as shifts in its cloud point during hydrogel formation process.
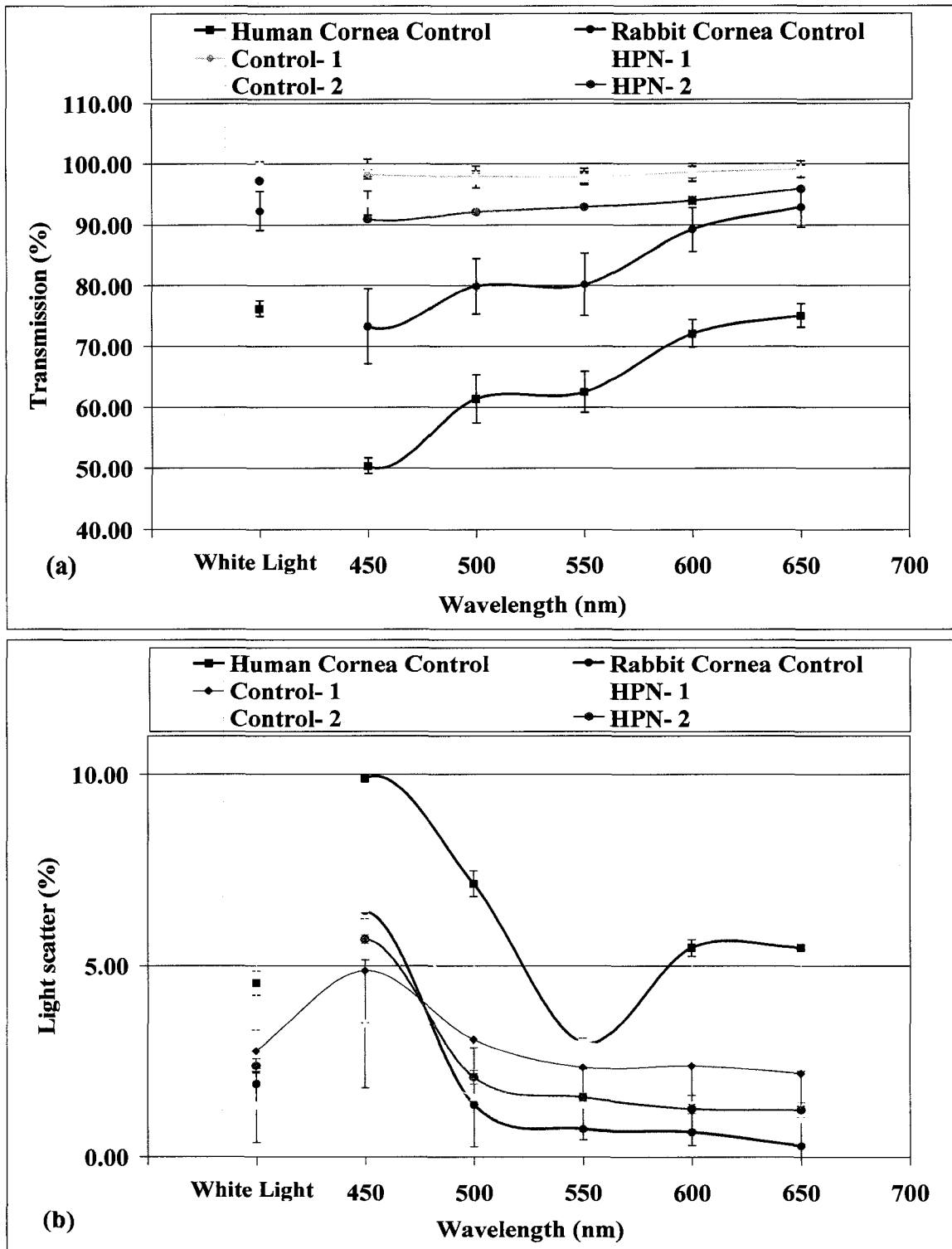
Figure 3.4 Optical properties of HPN scaffolds vs. their corresponding non-hybrid controls, and human, and rabbit corneas: (a) % light transmission, and (b) % light scatters.

3.4.4 Glucose and albumin diffusivity

Permeability to glucose and other molecules such as albumin has been reported to play important roles in the success of ophthalmic materials [41]. Because cornea is an avascular tissue, optimally designed corneal materials must permit effective diffusion of low molecular weight molecules, such as glucose (Mw = 180.2 Da), and components with higher molecular weight, such as albumin (Mw ≈ 66,000 Da) in order to properly nurture corneal cells to spread, grow and stratify. In addition, proteins such as albumin are known to have an impact on the osmotic pressure and swelling of the cornea [42].

Glucose and albumin diffusivity of HPN-2, and control-2 corneal scaffolds and those of human cornea are summarized in Table 3.1. Glucose and albumin diffusivity for HPN-2 scaffold were found to be $(2.8 \pm 0.04) \times 10^{-6}$ cm/s^2 and 1.67×10^{-7} cm/s^2, respectively, that were as good as those of native human cornea and non-hybrid control-2 scaffold (p>0.05). Glucose and albumin diffusivity for human cornea were reported to be $(2.6 \pm 0.33) \times 10^{-6}$ [41], and 1.0×10^{-7} cm^2/s [43], respectively. However, there are arguments that albumin is non-uniformly distributed in human cornea that may be associated with non-uniform albumin diffusivity through the cornea [44].

3.4.5 Water content

The water content data are shown in Table 3.1. Water content of HPN-2 (90.0 ± 1.3) was significantly lower than that of control-2 (92.5 ± 0.7) (p≤0.05). Almost the same trend was observed for HPN-1 and control-1 but the difference was not significant (p=0.12> 0.05). These results are in conformation with the higher mechanical strength of hybrid scaffolds compared to those of non-hybrid ones and may confirm the formation of entangled, cross-linked networks with a relatively dense morphology in hybrid scaffolds,

especially HPN-2, that causes a decrease in water content. We also expected a decrease in glucose and albumin diffusivity of HPN-2 scaffold. However, it was interesting to note that glucose and albumin diffusivity for HPN-2 scaffold remained unchanged (p>0.05) or slightly superior to non-hybrid control-2 scaffold despite the increase in its mechanical strength and density. This might be linked to the presence of chitosan that is known to exhibit favorable biological permeability [45] as well as enhanced elasticity of the scaffold that might compromise for the reduced density of the hybrid scaffold. More elastic scaffolds may allow pores to enlarge more easily and let higher permeation than non-elastic scaffolds.

3.4.6 FTIR characterization

Figure 3.5 shows the mid-infrared spectra (3800-800 cmP^{-1P}) of non-crosslinked collagen film as control-1, EDC-NHS crosslinked collagen (non-hybrid scaffold) as control-2, and two hybrid corneal scaffolds including HPN-1 and HPN-2. The main IR bands associated with collagen were detected. These bands were mostly associated with various types of amide bonds. There are nine such bands called amide A, B, and I to VII, in order of decreasing wavenumber but amide I and II are the most frequently used ones [46]. These bands are shown in Fig. 3.5 and are at $\approx$3320 (amide A) and $\approx$3070 (amide B), $\approx$1656 (amide I), $\approx$1550 (amide II), $\approx$1238 (amide III), and $\approx$1075 cm^{-1}that are mainly attributed to N-H stretching, N-H stretching, C=O stretching, N–H bending, C–N and N–H stretching, and NH^{3+} rocking, respectively.
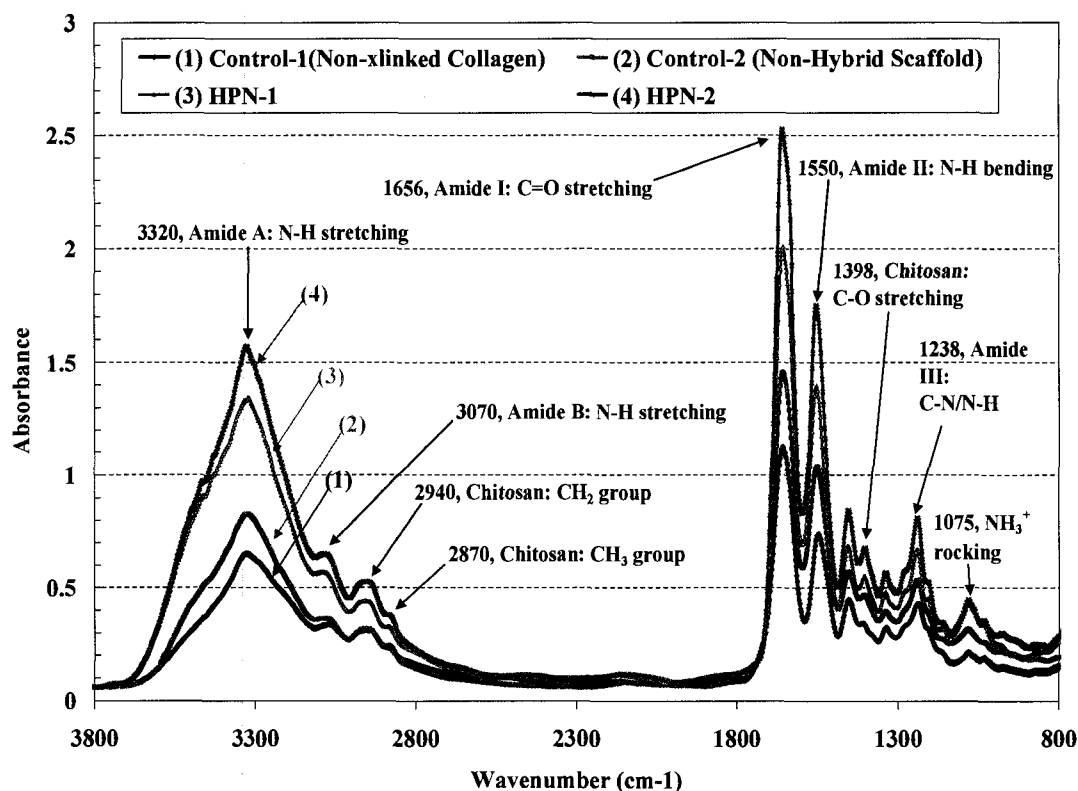
Figure 3.5 The mid-infrared spectra of (1) Control-1 that is a non-crosslinked collagen film, (2) Control-2 that is a EDC-NHS crosslinked collagen non-hybrid corneal scaffold, (3) HPN-1 hybrid scaffold, and (4) HPN-2 hybrid scaffold.

The spectral changes for various materials were also noticed. Spectrum (1) to (4) in Fig. 3.5 show that by moving from non-crosslinked collagen scaffold (control-1) toward the highly crosslinked HPN-2 hybrid scaffold, the spectrum shift upward toward higher absorption intensities. These increases in intensities are more pronounced at collagen amide characteristic peaks, i.e. at ≈ 3320 (amide A), and ≈ 1656 (amide I).

These shifts in absorption intensities are better demonstrated in Fig. 3.6, which illustrates the fingerprint region of the spectra shown in Fig. 3.5. The peak intensities and spectral shifts for HPN-2 at 1238, 1550, and 1656 cm-1 were higher compared to those for HPN-1 and controls. These bands are attributed to amide and amine covalent bonds

among collagen and chitosan that confirm the higher density of "amide" and "amine"

cross-links in HPN-2 than HPN-1 and controls.
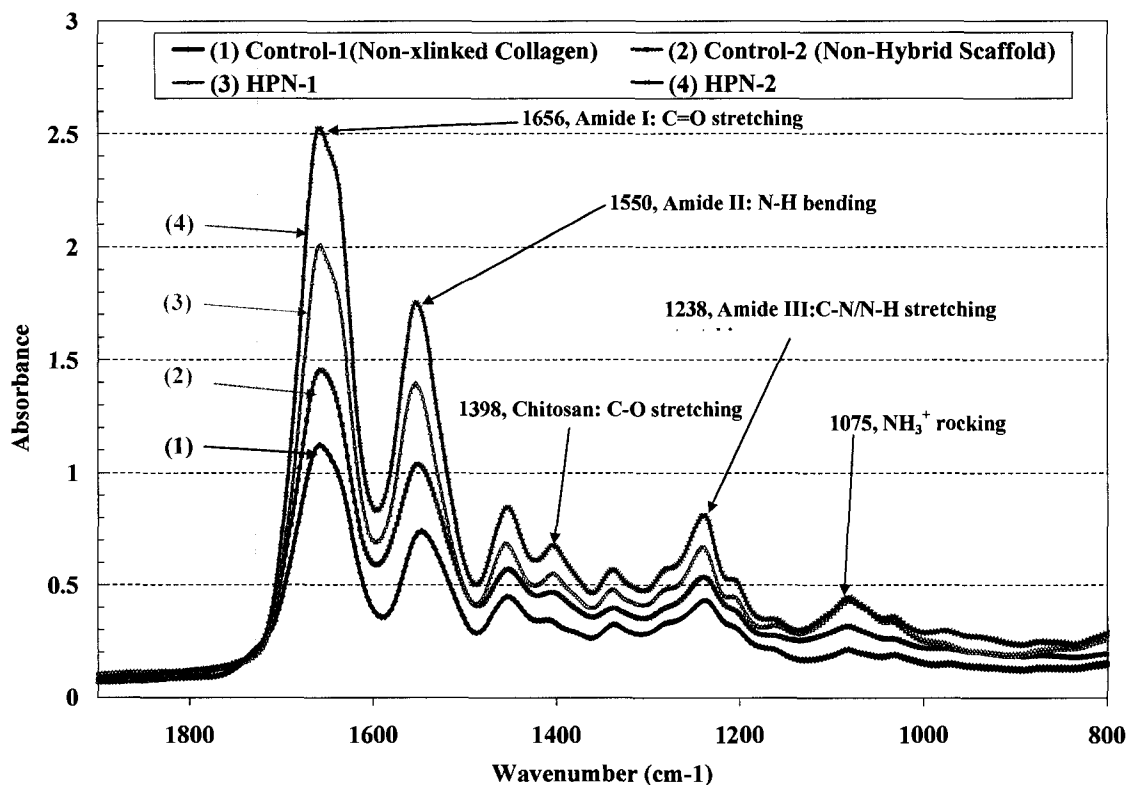
Figure 3.6   Fingerprint region of FTIR spectra of (1) Control-1 that is a non-crosslinked collagen film, (2) Control-2 that is a EDC-NHS crosslinked collagen non-hybrid corneal scaffold, (3) HPN-1 hybrid scaffold, and (4) HPN-2 hybrid scaffold.

This is in conformation with mechanical and water uptake results previously reported. We demonstrated that HPN-2 scaffold was superior to HPN-1 and controls with respect to mechanical strength and elasticity. Therefore, we may argue that there is a direct relationship between FTIR absorption intensity, and degree of crosslinking for the materials examined in this study. These findings are consistent with those of *Chang and Tanaka* [47] who found a conformation of amide bands by the degree of crosslinking of collagen/hydroxyapatite nano-composites.

In addition, some of the characteristic absorption bands of chitosan were identified for HPN-1 and HPN-2 scaffolds. FTIR spectra of HPN-1 and HPN-2 in Fig. 3.5 and Fig. 3.6 depict chitosan characteristic absorption bands with higher intensities than those of controls at 2940 cm^{-1}, 2870 cm^{-1}, and 1398 cm^{-1} that are attributed to CH_2 group, CH_3 group, and C-O stretching of primary alcoholic group (CH2-OH) respectively [48].

3.4.7   UV photodegradibility

The UV absorption spectra for various materials before irradiation (t = 0 hr) and after irradiation (t = 27 hr) are shown in Fig. 3.7. HPN-1 corneal scaffold, contact lens material (CL), and human cornea (HC) demonstrated shifts in their UV absorption spectrum toward higher degree of absorption representative of photodegradation upon UV irradiation for 27 hrs. The differences in the spectra correspond to changes in the UV absorbance of the samples. However, the shift in the HPN-2 spectra before and after irradiation was not noticeable and very small changes could be observed. This may be an indication that HPN-2 is more photostable compared to HPN-1 most likely attributed to its higher degree of crosslinking than HPN-1. It was also noted that the spectra for contact lens was somehow different than others that might be attributed to its synthetic nature.
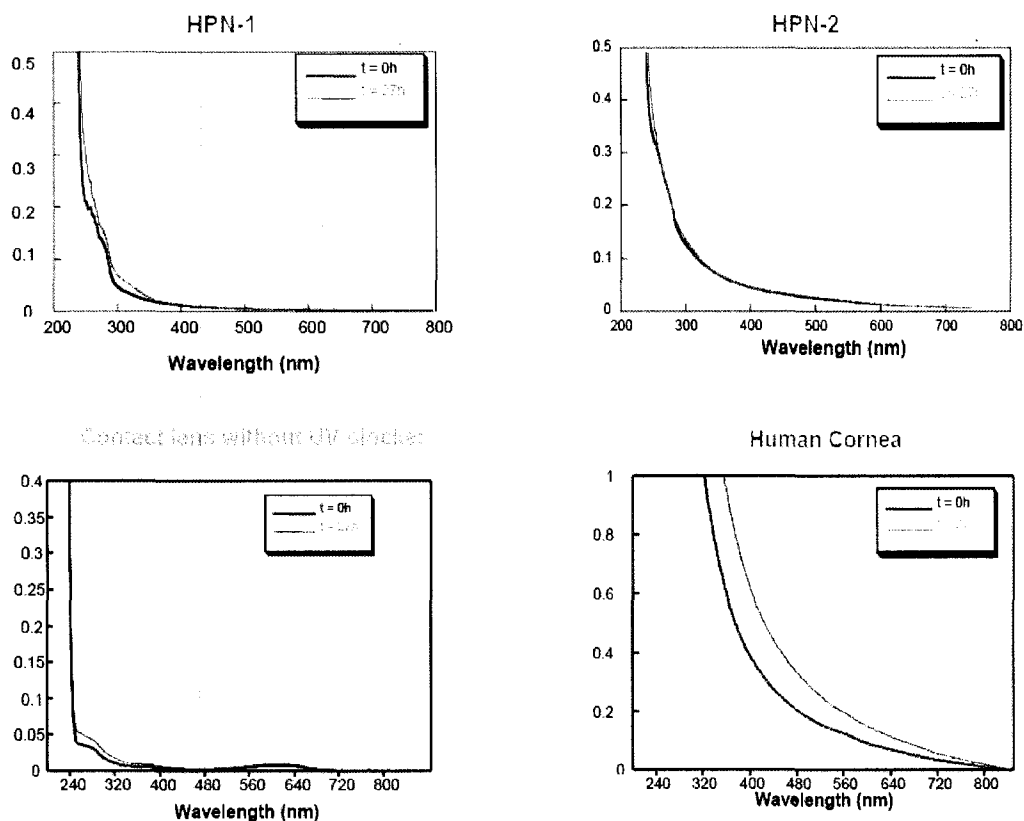
Figure 3.7 UV absorption spectrum for HPN-1 corneal scaffold, HPN-2 corneal scaffold, contact lens material, and human cornea. Each spectrum shows the UV absorption before (t = 0h) and after exposure (t = 27 h).

3.4.8 In vitro biological characterization: HCEC and DRG

The scaffolds were also tested for *in vitro* biocompatibility using immortalized human corneal epithelial cells (HCECs) and dorsal root ganglia (DRG) from chick embryos. It is apparent from Fig. 3.8(a) that all scaffolds supported the attachment and growth of corneal epithelial cells and confluent cell cultures were obtained on day 5 post-seeding. As shown in Fig. 3.8(b), DRG nerve overgrowth was observed for most of the scaffolds. Despite the capability of HPN-2 and control scaffolds for supporting neurite

extension, DRG neurites did not surprisingly extend onto HPN-1 that had significantly higher chitosan content than other scaffolds.

(a)   (b)
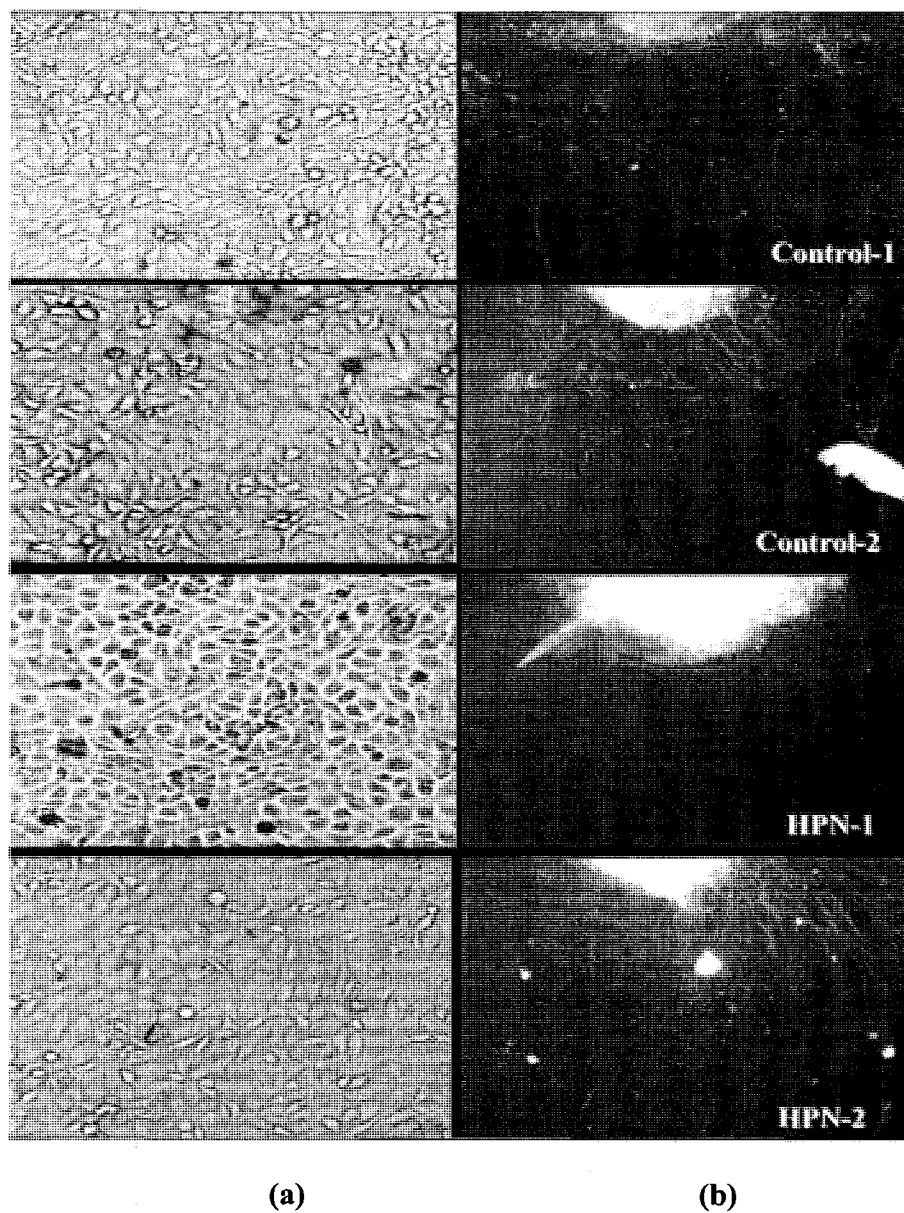
Figure 3.8   Growth of (a) human corneal epithelial cells on day 5 post-seeding, and (b) DRG neurites on HPN scaffolds and their corresponding control scaffolds.

This neurite inhibitory effect may be linked to the polycationic (positively charged) nature of chitosan. A strong relationship between the positive or negative charge of the hydrogel and three-dimensional neurite extension has been reported in the

literature [49]. *Dillon et al.* indicated that primary neural extension process is influenced by the polarity of ambient charge in a dose-responsive manner. They found that incorporation of chitosan into agarose hydrogels had an enhancing effect on neurite extension while incorporation of a polyanionic (negatively charged) component such as chondroitin sulfate had an inhibitory effect. However, this finding does not completely support that previous study. A possible explanation for this might be given by the dose-responsive manner of DRG neurite extension. Low chitosan content might have enhanced the neuritis extension in HPN-2 scaffold, while the high chitosan content in HPN-1 might have inhibited the neurite growth.

3.4.9 Bacterial susceptibility

To determine the susceptibility of corneal materials to bacterial replication, the ability of three bacterial species including *staphylococcus aureus (SA), streptococcus pneumoniae (SP), and pseudomonas aeruginosa (PA)* to proliferate on the scaffolds was tested. The results indicated comparable bacterial counts in HPN materials to that of the eye bank human corneas and saline ($p>0.05$). The mean colony counts in colony-forming unit (CFU) for *SA* were 1.1×10^5 ($\pm 1.6 \times 10^5$) CFU/ml for HPN-2 scaffold, 2.4×10^5 ($\pm 2.1 \times 10^5$) CFU/ml for the human cornea, and 2.6×10^5 ($\pm 2.3 \times 10^5$) CFU/ml for saline. With *SP* there was no growth in HPN-2 scaffold, human cornea or saline. The mean colony counts for *PA* were 6.2×10^3 ($\pm 3.6 \times 10^3$) CFU/ml for HPN-2 scaffold, 6.8×10^2 ($\pm 7.2 \times 10^2$) CFU/ml for the human cornea, and 9.1×10^5 ($\pm 8.3 \times 10^5$) CFU/ml for saline.

There were no statistically significant differences in the colony counts of *SA* and *PA* in different cornea constructs when compared to human donor corneas ($p=0.6$ for *SA* and $p=0.4$ for *PA*). These results suggest that *SA* and *PA* replication within the tissue-

engineered corneas occurred at the same rate as that in human cornea. For *SP*, there was no growth in either engineered corneas or human corneas, presumably because this organism is fastidious and has more stringent growth requirements.

3.4.10 In Vivo biological characterization: subcutaneous biodegradation in rats

Tissue-engineered materials were evaluated for biodegradation and immunocompatibility by subcutaneous implantation in rats for 30, 60, and 120 days. The HPN-2 implants demonstrated biocompatibiliy/stability similar to human cornea (HC). Both HPN-2 and HC were completely retrieved on day 60 while Control-2 and HPN-1 implants were partially retrieved as shown in Fig. 3.9.
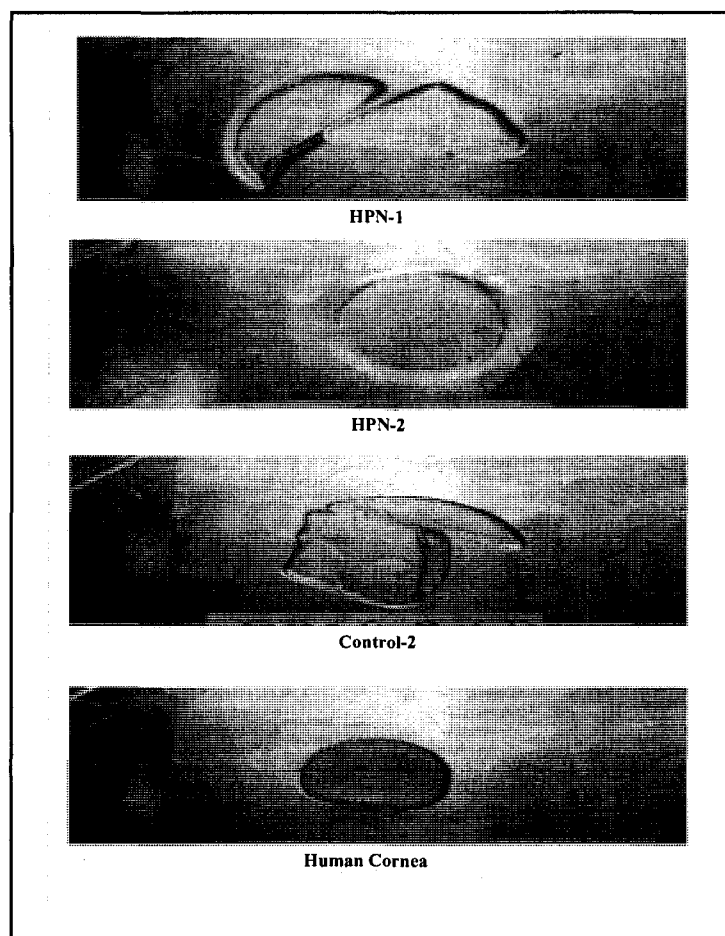
Figure 3.9 Images of HPN-1, HPN-2, and Control-2 scaffolds, and human cornea button retrieved from rats 60 days after subcutaneous implantation.

No fibrosis was observed and no fibrotic capsule was formed around the HPN-2 and HC implants. As demonstrated in Fig. 3.10, some minor infiltration of immune cells was observed in one of three HPN-2 implants but the samples were still intact after 120 days. However, Control-2 and HPN-1 implants showed some degree of fibrosis, inflammatory and immune cells response, and biodegradation.
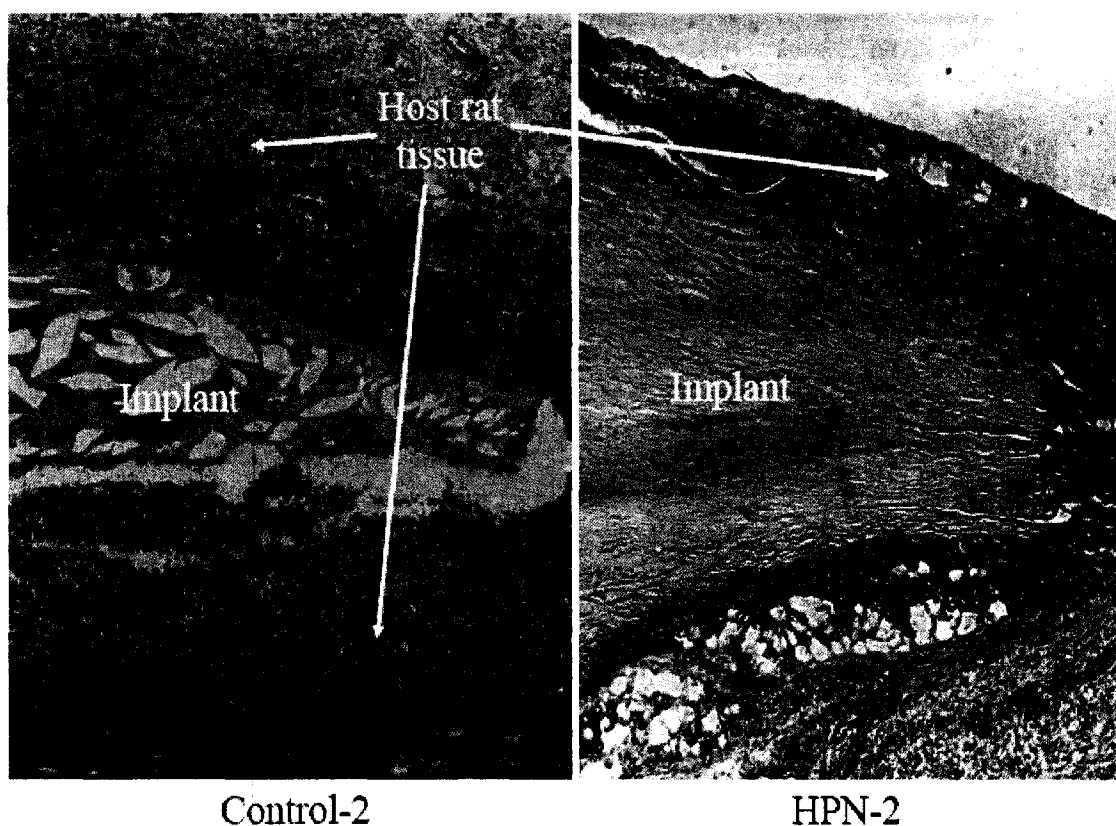
Control-2   HPN-2

Figure 3.10   120-day subcutaneous biodegradation in rats: cross-sectional view of HPN-2 and Control-2 implants surrounded by the host rat tissue after H&E staining.

3.4.11 In Vivo biological characterization: implantation in pigs

3.4.11.1   Two-month post-operative study

Sutures were removed at 4 weeks after surgery. All control eyes remained transparent while all implanted eyes including allografts, and HPN implants exhibited

varying degrees of haze characteristic of stromal wound healing. Implanted eyes exhibited normal epithelial re-growth including re-grown basal epithelial cell layers. About 60% of implanted eyes (7 out of 12) exhibited activated keratocytes in the deeper stromal region posterior to the haze. All endothelial cell layers appeared normal in all control and operated eyes. In comparison to the previous LKP study of simple EDC-NHS-crosslinked implants [27], more basal cell layers were visible, the degree of haze was in general lower, and only one instance of vascular growth was noted. Additionally, sparsely distributed activated keratocytes in the stromal region in 60% of implants indicate a distinct difference in morphology from the dense, clusters of activated keratocytes observed in the previous LKP study. While a morphology possibly indicative of immune rejection was observed frequently in the previous study [27], it was noted less frequently in the present study.

3.4.11.2   Six-month post-operative study

Normal epithelial cells (superficial, wing, and basal) regenerated within the first 2 months over HPN-1 and HPN-2 implants similar to that of control un-operated corneas and allograft control. Despite the mild haze observed initially for most of the implanted eyes in two months, it was significantly diminished for HPN-2. Allografts and HPN-1 showed some degree of haze. However, none of the implants showed any sign of inflammation or rejection over this period. In both HPN-1 and HPN-2 sub-basal nerves regenerated in the 2-6 month time frame. Endothelial cell layers were in place although their densities declined with surgery and even further as time went on for all implanted eyes. Pigs with HPN-1 corneal implants were sacrificed on month 8 post-operative due to high degree of vascularization and haze (See Fig. 3.11).

| Unoperated Cornea | Allograft Control | HPN-2 Implant | HPN-1 Implant* |
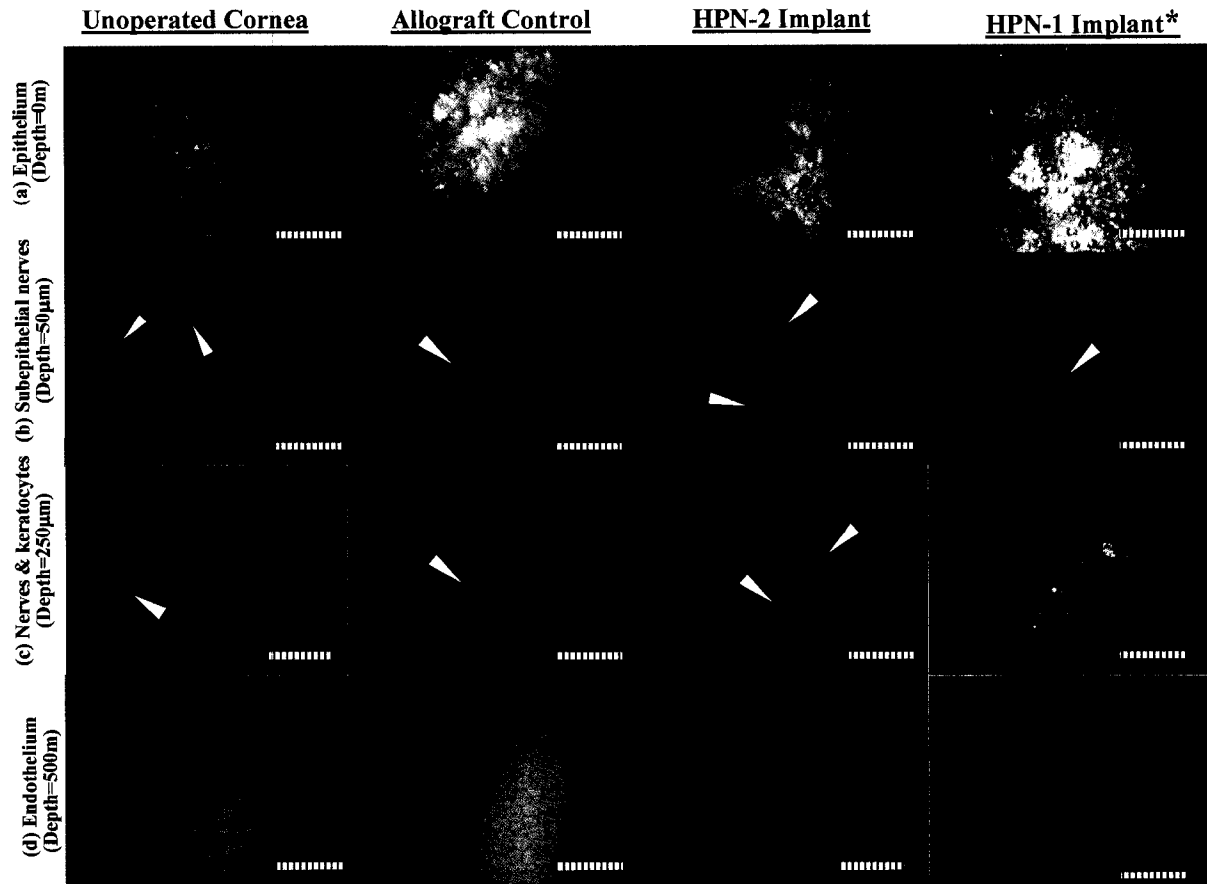
Figure 3.11 In vivo confocal microscopy (IVCM) images from typical 12-month unoperated pig cornea control, allograft control, HPN-2 implant, and 6-month HPN-1 implant at four corneal scan depths:(a) D=0 μm-superficial epithelium, (b) D=50 μm-subepithelial branching nerves with anteroir fibroblast mesh networks, (c) D=250 μm-branching nerve and keratocytes in deeper stroma, and (d) D=500 μm-endothelium. Bar = 100 μm.
* Pigs were scarified on month 8 post-operation due to high haze and extensive blood vessels in HPN-1 implanted corneas.
** Arrows show nerve branches.

3.4.11.3   Twelve-month post-operative study

Figure 3.11 shows IVCM images from typical 12-month unoperated pig cornea, allograft control, HPN-2 implant, and 6-month HPN-1 implant at four corneal scan depths. As shown in Fig. 3.11(a), normal epithelium regenerated early in the study remained intact over implants, and allografts, similar to that of unoperated cornea over

the study periods though some degrees of haze were observable for allografts and HPN-1 implanted corneas. Subepithelial nerves were also observed for implants and allograft with fibroblast mesh networks similar to that of unoperated cornea (See Fig. 3.11(b)). Figure 3.11(c) shows normal branching nerves and keratocytes for unoperated cornea, allograft control, and HPN-2, in deeper stroma at about 250 μm from the anterior surface of the corneas while HPN-1 implants showed abnormal vascularization. As depicted in Fig. 3.11(d), endothelium layers were in place for all operated corneas although their densities slightly declined with surgery and further as time went on compared to unoperated corneas.

3.5   Conclusions

We developed cross-linked composite networks in which chitosan molecules were embedded in and covalently bonded to the collagen molecules by either EDC-NHS or a hybrid PEG-DBA/EDC-NHS even if the crosslinking of two structural units of the same type (e.g. collagen-collagen) and/or belonging to the same polymeric chain cannot be excluded. This hybrid approach resulted in a synergistic effect on physical and biological properties of the materials. For example, it became achievable to simultaneously enhance mechanical strength, and elasticity while retaining biological characteristics and optical clarity of the scaffolds. Such synergy effects might be operating in the unprecedented interactions of HPN components so that their combined effects were greater than the sum of their individual effects.

Although HPN scaffolds are still collagen-based, they incorporate biomimetic molecules, e.g. chitosan, that emulate natural extracellular matrix molecules (ECM) found within the human cornea while conferring significantly increased tensile strength

and elasticity. These hybrid scaffolds were tested for physical (e.g., mechanical, optical, suturability, diffusivity, swelling, UV biodegradation, and FTIR) and biological properties both *in vitro* (e.g., HCEC, and DRG), and *in vivo* (rat subcutaneous and pig cornea implantations). Results suggest that scaffolds are implantable, optimally strong, elastic, biocompatible, bioresorbable, and superior to human eye bank corneas in optical clarity and susceptibility to bacterial infection. Although these HPN scaffolds are specifically designed for corneal applications, they may be tailor-made for development of other organ and tissue transplants such as crystalline lens, liver, and heart. The most favorable HPN hydrogel (HPN-2) optimally meet the requirements for an implantable corneal scaffold. More specifically, the following conclusions could be drawn from this work over the range of investigation:

1. Hybrid corneal scaffolds (HPN-1 and HPN-2) demonstrated significantly higher mechanical strength compared to their corresponding non-hybrid controls.

2. HPN-2 scaffold showed significantly higher mechanical strength and elasticity compared to HPN-1 and non-hybrid controls. This synchronized increase in strength and elasticity is likely associated with the enhanced cross-linking density due to short-range intermolecular and long-range interfibrilar cross-links.

3. Hybrid scaffolds were 100% suturable as opposed to their non-hybrid control scaffolds with an average suturability rate of about 50%.

4. Hybrid scaffolds demonstrated high percentage of light transmission (> 90%) and low light scatter (< 6%). Although their light transmission values were slightly lower than those of non-hybrid controls, they were still superior to human and rabbit corneas.

5. Despite the increase in density and mechanical strength of HPN-2 scaffold compared to control-2 scaffold, glucose and albumin diffusivity of HPN-2 were as good as those of control-2 and human cornea. This was likely associated with the presence of chitosan and enhanced elasticity of HPN-2 scaffold.

6. FTIR spectra for HPN-2 showed the highest absorption intensity especially at bands associated with various types of amide and amine bonds followed by HPN-1, control-2, and non-crosslinked collagen scaffolds. These results suggested a direct relationship between FTIR absorption intensity, and degree of crosslinking of the materials.

7. HPN-2 was found to be more UV photostable than HPN-1 that was likely attributed to its higher degree of crosslinking and more robust structure.

8. All tissue-engineered scaffolds supported the attachment and growth of corneal epithelial cells and no significant differences were found between hybrid and non-hybrid materials.

9. DRG nerve overgrowth was observed for HPN-2 and control scaffolds as opposed to HPN-1 scaffold that surprisingly did not support nerves in vitro.

10. HPN-2 implant indicated significantly lower biodegradation rates and lower degree of immune cells infiltration than HPN-1 and non-hybrid scaffolds when implanted in rats subcutaneously. No fibrosis was observed and no fibrotic capsule was formed around HPN-2 comparable to human cornea implant.

11. Two to 12 month post-implantation studies in pigs' corneas suggested that all implanted corneas, including HPN-1, HPN-2, and allografts, exhibited varying degrees of haze characteristic of stromal wound healing early in the study.

However, HPN-2 and most of the allografts gained back their transparency after 6 months. Normal regeneration of epithelium, subepithelial nerves, and keratocytes were observed for HPN-2 implants and allografts comparable to those of unoperated corneas.

12.   Although normal regeneration of epithelium was observed for HPN-1 implanted corneas, they exhibited high degrees of haze and vascularization compared to other implants and pigs were sacrificed after 8 months.

Acknowledgements

3.6   References

1.   Ratner BD, Hoffman AS, Schoen FJ, Lemons JE. Biomaterials science: an introduction to materials in medicine. San Diego: Academic Press, 1996.

2.   Hollister SJ. Porous scaffold design for tissue engineering, Nat Mater 2005; 4: 518–524.

3.   Nimni ME, Cheung D, Strates B, Kodama M, Sheikh K. Chemically modified collagen: a natural biomaterial for tissue replacement. J Biomed Mater Res 1987; 21: 741-771.

4.   Friess W. Collagen-biomaterial for drug delivery. Eur J Pharm Biopharm 1998; 45: 113–136.

5.   Berger J, Reist M, Mayer JM, Felt O, Peppas NA, Gurny R. Structure and interactions in covalently and ionically crosslinked chitosan hydrogels for biomedical applications. Eur J Pharm Biopharm 2004; 57: 19-34.

6. Sionkowska A, Wisniewski M, Skopinska J, Kennedy CJ, Wess TJ. Molecular interactions in collagen and chitosan blends. Biomaterials 2004; 25: 795–801.

7. Wang XH, Li DP, Wang WJ, Feng QL, Cui FZ, Xu YX, Song XH, Van Der Werf M. Crosslinked collagen/chitosan scaffold for artificial livers. Biomaterials 2003; 24: 3213–3220.

8. Gingras M, Paradis I, Berthod F. Nerve regeneration in a collagen–chitosan tissue-engineered skin transplanted on nude mice. Biomaterials 2003; 24: 1653–1661.

9. Gao CY, Wang DY, Shen JC. Fabrication of collagen/chitosan porous scaffolds with controlling microstructure for dermal equivalent. Polym Adv Technol 2003; 14: 373-379.

10. Thacharodi D, Rao KP. Collagen-chitosan composite membranes for controlled release of propranolol hydrochloride. Int J Pharm 1995; 120: 115–118.

11. Shanmugasundaram N, Ravichandran P, Reddy PN, Ramamurty N, Pal S, Rao KP. Collagen /chitosan polymeric scaffolds for the in vitro culture of human epidermoid carcinoma cells. Biomaterials 2001; 22: 1943-1951.

12. Chen J, Li Q, Xu J, Huang Y, Ding Y, Deng H, Zhao S, Chen R. Study on biocompatibility of complexes of collagen–chitosan–sodium hyaluronate and cornea. Artif Organs 2005; 29(2): 104-113.

13. Damink LHO, Dijkstra PJ, Van Luyn MJ, Van Wachem PB, Nieuwenhuis P, Feijen J. Cross-linking of dermal sheep collagen using a water-soluble carbodiimide. Biomaerials 1996; 17: 765–773.

14. Huang-Lee LLH, Cheung DT, Nimni ME. Biochemical changes and cytotoxicity associated with the degradation of polymeric glutaraldehyde derived crosslinks. J Biomed Mater Res 1990; 24: 1185-1201.

15. Damink LHO, Dijkstra PJ, Van Luyn MJ, Van Wachem PB, Nieuwenhuis P, Feijen J. Glutaraldehyde as a crosslinking agent for collagen-based biomaterials. J Mater Sci Mater Med 1994; 6: 460-472.

16. Doillon CJ, Cote MF, Pietrucha K, Laroche G, Gaudreault RC. Porosity and biological properties of polyethylene glycol-conjugated collagen materials. J Biomat Sci Polym Ed 1994; 6(8): 715–728.

17. Lee HJ, Lee JS, Chansakul T, Yu C, Elisseeff JH, Yu SM. Collagen mimetic peptide-conjugated photopolymerizable PEG hydrogel. Biomaterials 2006; 27: 5268–5276.

18. Chvapil M, Speer D, Mora W, Eskelson C. Effect of tanning agent on tissue reaction to tissue implanted collagen sponge. J Surg Res 1983; 35: 402-409.

19. Van Wachem PB, Plantinga JA, Wissink MJ, Beernink R, Poot AA, Engbers GH, Beugeling T, van Aken WG, Feijen J, van Luyn MJ. In vivo biocompatibility of carbodiimide-crosslinked collagen scaffolds: effects of crosslink density, heparin immobilization, and bFGF loading. J Biomed Mater Res 2001; 55: 368–378.

20. Zeeman R, Dijkstra PJ, Van Wachem PB, Van Luyn MJ, Hendriks M, Cahalan PT, Feijen J. Successive epoxy and carbodiimide cross-linking of dermal sheep collagen. Biomaterials 1999; 20: 921–931.

21. Minami Y, Sugihara H, Oono S. Reconstruction of cornea in three-dimensional collagen gel scaffold. Invest Ophthalmol Vis Sci 1993; 34: 2316-24.

22. Zieske JD, Mason VS, Wasson ME, Meunier SF, Nolte CJ, Fukai N, Olsen BR, Parenteau NL. Basement membrane assembly and differentiation of cultured corneal cells: importance of culture environment and endothelial cell interaction. Exp Cell Res 1994; 214: 621-633.

23. Germain L, Auger FA, Grandbois E, Guignard R, Giasson M, Boisjoly H, Guérin SL. Reconstructed human cornea produced in vitro by tissue engineering. Pathobiol 1999; 67: 140-147.

24. Griffith M, Osborne R, Munger R, Xiong X, Doillon CJ, Laycock NLC, Hakim M, Song Y, Watsky MA. Functional human corneal equivalents constructed from cell lines. Science 1999; 286: 2169-2172.

25. Li F, Carlsson DJ, Lohmann C, Suuronen E, Vascotto S, Kobuch K, Sheardown H, Munger R, Nakamura M, Griffith M. Cellular and nerve regeneration within a biosynthetic extracellular scaffold for corneal transplantation. Proc Nat Acad Sci USA 2003; 100: 15346-15351.

26. Li F, Griffith M, Li Z, Tanodekaew S, Sheardown H, Hakim M, Carlsson DJ. Recruitment of multiple cell lines by collagen-synthetic copolymer scaffolds in corneal regeneration. Biomaterials 2005; 26:3093-3104.

27. Liu Y, Gan L, Carlsson DJ, Fagerholm P, Lagali N, Watsky MA, Munger R, Hodge WJ, Priest D, Griffith M. A simple cross-linked collagen tissue substitute for corneal implantation. IOVS 2006; 47: 1869-1875.

28. Griffith M, Hakim M, Shimmura S, Watsky MA, Li F, Carlsson D, Doillon CJ, Nakamura M, Suuronen E, Shinozaki N, Nakata K, Sheardown H. Artificial human corneas: scaffolds for transplantation and host regeneration. Cornea 2002; 21: S54-S61.

29. Eye Bank Association of America, Eye Banking Statistical Report 1999; Washington, EBAA.

30. Whitcher JP, Srinivasan M, Upadhyay MP. Corneal blindness: a global perspective. Bull World Health Organ 2001; 79: 214-221.

31. Ramos VM, Rodriguez NM, Henning I, Diaz MF, Monachesi MP, Rodriguez MS, Abarrategi A, Correas-Magan V, Lopez-Lacomba JL, Agullo E. Poly(ethylene glycol)-crosslinked N-methylene phosphonic chitosan. Preparation and characterization. Carbohydr Polym 2006 ; 64 : 328–336.

32. Xiea, D, Smyth CA, Eckstein C, Bilbao G, Mays J, Eckhoff DE, Contreras JL. Cytoprotection of PEG-modified adult porcine pancreatic islets for improved xenotransplantation. Biomaterials 2005; 26: 403–412.

33. Rathna GVN. Hydrogels of modified ethylenediaminetetraacetic dianhydride gelatin conjugated with poly(ethylene glycol) dialdehyde as a drug-release scaffold. J Appl Polym Sci 2004; 91: 1059–1067.

34. Kirker KR, Prestwich GD. Physical properties of glycosaminoglycan hydrogels. J Polym Sci B Polym Phys 2004; 42: 4344–4356.

35. Tan J, SaltzmanWM. Influence of synthetic polymers on neutrophil migration in three-dimensional collagen gels. J Biomed Mater Res 1999; 46: 465–474.

36. Halstenberg S, Panitch A, Rizzi S, Hall H, Hubbell JA. Biologically engineered protein-graft-poly(ethylene glycol) hydrogels: a cell adhesive and plasmin-degradable biosynthetic material for tissue repair. Biomacromol 2002; 3: 710-723.

37. Rafat M, Griffith M, Li F, Matsuura T. Multivariate experimental design for rational development of bioengineered hybrid polymer networks for corneal tissue engineering. Biomaterials, to be submitted in January 2008.

38. Priest D, Munger R. A new instrument for monitoring the optical properties of corneas. Invest Ophthalmol Vis Sci 1998; 39: 352.

39. Liu L, Sheardown H. Glucose permeable poly (dimethyl siloxane), poly(N-isopropyl acrylamide) interpenetration networks as ophthalmic biomaterials. Biomaterials 2005; 26: 233–244.

40. Forrester JV, Kuffova L. Corneal Transplantation. London Imperial College Press 2004; 18–21.

41. McCarey BE, Schmidt FH. Modeling glucose distribution in the cornea. Curr Eye Res 1990; 11: 1025–1039.

42.   Harris JE. Introduction: Factors influencing corneal hydration. Invest Ophthalmol 1962; 1(2): 151-157.

43.   Maurice DM, Watson PG. The distribution and movement of serum albumin in the cornea. Exp Eye Res 1965; 4: 355-363.

44.   Gong H, Johnson M, YE W, Kamm RD, Freddo TF. The non-uniform distribution of albumin in human and bovine cornea. Exp Eye Res 1997; 65: 747-756.

45.   Chen J, Li Q, Xu J, HuangY, DingY, Deng H, Zhao S, Chen R.Study on biocompatibility of complexes of collagen--chitosan--sodium hyaluronate and cornea. Artif Organs 2005; 29(2): 104–113.

46.   Stuart B. Infrared spectroscopy: fundamentals and applications. West Sussex, England: John Wiley & Sons Ltd, 2004.

47.   Chang MC, Tanaka J. FTIR study for hydroxyapatite/collagen nanocompositescross-linked by glutaraldehyde. Biomaterials 2002; 23: 4811-4818.

48.   Shanmugasundaram N, Ravichandran P, Reddy, PN, Ramamurty, N, Pal, S, Rao, KP. Collagen /chitosan polymeric scaffolds for the in vitro culture of human epidermoid carcinoma cells. Biomaterials 2001; 22: 1943-1951.

49.   Dillon GP, Yu X, Bellamkonda RV. The polarity and magnitude of ambient charge influences three-dimensional neurite extension from DRGs. J Biomed Mater Res 2000; 51: 510–519.

Chapter 4

Plasma Surface Modification and Characterization of Collagen-based Artificial Cornea for Enhanced Epithelialization*

Mehrdad Rafat[1,2]**, May Griffith**[2,3]**, Malik Hakim**[1,2]
Lea Muzakare[2]**, Frank Li**[2]**, K.C. Khulbe**[1]**, and Takeshi Matsuura**[1]

[1] Department of Chemical Engineering, University of Ottawa, Ottawa, Ontario, K1N 6N5, Canada

[2] University of Ottawa Eye Institute, Ottawa, Ontario, K1H 8L6, Canada

[3] Department of Cellular and Molecular Medicine, University of Ottawa, Ottawa, Ontario, K1H 8M5, Canada

4.1 Abstract

Argon plasma treatment enhanced the attachment of epithelial cells to a collagen-based artificial cornea crosslinked using glutaraldehyde (GA) and glutaraldehyde-polyethylene oxide dialdehyde (GA-PEODA) systems. The epithelialization of untreated and treated surfaces was evaluated by the seeding and growth of human corneal epithelial cells. Characterization of polymer surface properties such as surface hydrophilicity and roughness was also made by contact angle measurement (CAM) and atomic force microscopy (AFM), respectively. Contact angle analysis revealed that the surface hydrophilicity significantly increased after the treatment. In addition, AFM characterization showed an increase in surface roughness through argon plasma treatment. Based on the biological and surface analysis, argon plasma treatment displays promising potential for biocompatibility enhancement of collagen-based artificial corneas. It was also found that the cell attachment to artificial cornea surfaces was influenced by the combined effects of surface chemistry (i.e., surface energy), polymer surface morphology (i.e., surface roughness), and polar interactions between functional groups at the polymer surface and cell membrane proteins.

Key words: AFM (atomic force microscopy), biocompatibility, crosslinking, modification, plasma

4.2   Introduction

The cornea is an avascular transparent tissue as window to the eye. It forms part of the outer tunic of the eyeball that protects the inner contents of the eye, and functions as the main refractive component. When irreversibly diseased or damaged, corneas lose their transparency, leading to vision loss and/or blindness. Corneal blindness may be treatable by donor cadaver corneas [1]. However, at the present time, supply of healthy donated tissue is short and an estimated 10 million patients worldwide are in need of corneas [2]. As a consequence, there have been considerable efforts put into the development of artificial replacements as keratoprostheses (KPros) [3].

One major complication in the development of KPros is the lack of adequate biocompatibility. It is generally agreed that the growth of corneal epithelial cells over the external surface of KPros is desirable for smooth integration of the devices into the host tissue [4]. The absence of a continuous sheet of epithelium exposes the eye to bacterial invasion, inhibits the formation of a tear film, permits epithelial down-growth, and may results in a rough, dry surface. Therefore, an important criterion for a successful KPro is that the anterior surface rapidly becomes covered with a continuous sheet of epithelium [5].

The past decade has witnessed a tremendous surge in interest regarding various techniques for surface modification of biomaterials. Typically, surface modification strategies such as grafting, immobilization, coating, plasma deposition, and plasma surface treatments are applied to impart desirable chemistry and morphology to facilitate interfacial interactions between biomaterials and biological species [6]. The critical principle behind these technologies is that they make it possible to change surface

properties of a biomaterial without altering the bulk properties [7]. Plasma treatment is a promising tool for the surface modification of polymeric biomaterials, in particular to improve their biocompatibility [8]. A surface layer of a few nanometers is modified while the bulk properties of the material remain unchanged [9]. There are various approaches to obtain tailored surface properties using low-pressure plasma techniques [10].

Several studies have been reported on the enhancement of corneal epithelial cell attachment and growth on synthetic biomaterials. For example, an ammonia plasma treatment was applied to artificial corneas fabricated from poly (2-hydroxyethyl methacrylate) (pHEMA) and intraocular lenses fabricated from poly (methyl methacrylate) (PMMA) to promote the migration of corneal endothelial cells during wound healing [11]. The attachment of the cells onto control untreated PMMA and pHEMA surfaces was found to be negligible, whereas, there was an enhanced attachment of endothelial cells to the ammonia plasma treated surfaces. In another study, various plasma modification techniques were used to modify a synthetic cornea containing poly (vinyl alcohol) (PVA) hydrogel. Results from both the *in vitro* study and *in vivo* implantation in a rabbit model indicated that an enhanced epithelial layer was obtained on the plasma modified PVA surface compared with the untreated surfaces [5]. Despite the great deal of research performed previously on plasma modification techniques, the effects of surface properties of collagen-based polymers, such as surface morphology and surface energetic, on cell attachment have not been addressed adequately.

Various in vitro experiments have shown that the cell behavior is influenced by the physicochemical properties of synthetic polymer surfaces. However, the relationship between surface properties and in vitro cell response is not well understood [12]. Surface

116

energy of the substratum was shown to influence the adhesion of various cells [13-16]. Materials with high surface energy were generally reported to promote cell adhesion, as opposed to low-energy surfaces which deterred cell adhesion. The influence of surface chemical composition may also be related to such a macroscopic property or to the presence of specific chemical groups [17-20].

In this paper, the relationship between surface properties of cross-linked collagen and adhesion of epithelial cells has been studies. Argon plasma was used to modify the surface of collagen-based artificial cornea. Artificial corneas were biologically characterized in vitro by epithelial cell assay. Surfaces of artificial corneas were also characterized by contact angle measurement and atomic force microscopy (AFM). Results from the *in vitro* study indicated that epithelial cells attachment was enhanced on the argon plasma modified surfaces. Surface roughness and hydrophilicity were also increased by plasma treatment.

4.3   Materials and Methods

4.3.1   Fabrication of Artificial Cornea Hydrogels

Artificial cornea hydrogels were prepared from purified, acid soluble rat-tail collagen films (Telo collagen type I from BD) cross-linked with glutaraldehyde (GA) and poly ethylene oxide dialdehyde (PEODA). Three stages involved in the fabrication process of artificial cornea hydrogels are summarized below:

4.3.1.1 Production of Collagen Films

An evaporation technique was developed to produce solid collagen films prior to crosslinking. Purified rat-tail Type I (telo-) collagen (0.45 w/v% in 0.05N acetic acid from Becton-Dickinson Canada) was used for this study. Collagen solution was poured

into a 35 mm diameter sterile culture dish. The culture dish was placed in a cold chamber at 4°C temperature and nitrogen gas was purged parallel to the surface of the solution in the evaporation dish using a gas flow distributor. Additional collagen solution was added to the dish and then dried until sufficient collagen film thickness was obtained (i.e., 300 μm). The final collagen film that was transparent and flat was cut into 7 mm diameter disks, weighed, and prepared for the crosslinking reaction.

4.3.1.2 Fabrication of Artificial Cornea Hydrogels Using GA Crosslinker

Selected collagen films were placed in flat Teflon reaction moulds. A certain amount of GA solution (12 μl, 8.5 v/v %) was added to the top and bottom surfaces of each film at a GA to collagen molar ratio of 1.3 (1.3 aldehyde group in GA to 1 amine in collagen). The flat Teflon reaction mould was then closed and held in place using two aluminium plates and two clips. The reaction moulds were placed in an isolated dust-free chamber at room temperature for 72 hours. The top portion of the mould was then removed and the samples were dried at room temperature for 24 hours and rehydrated in sterile distilled-deionised water ($_{dd}$H20).

4.3.1.3 Further Crosslinking of GA-Crosslinked Hydrogels With Poly (Ethylene Oxide

   Dialdehyde) (PEODA)

PEODA crosslinking was performed to enhance elastic properties of GA-crosslinked hydrogels. Some of the samples that were initially crosslinked with GA were post-crosslinked with PEODA at a molar ratio of 0.07 (0.07 aldehyde groups in PEODA to 1 amine group in collagen). PEODA was used at 0.07-fold molar aldehyde to collagen amine based on our previous unpublished work. We found that the optimal PEODA-to-collagen molar ratio (aldehyde to amine groups) was about 0.07 that enhanced

mechanical properties while biological activity of the protein was well retained. 45 mg of PEODA (poly ethylene oxide dialdehyde, ALD-3400 Shearwater Polymers USA) was dissolved in 300 μl of $_{dd}H_2O$ to make a 15% (w/v) solution. Each GA-crosslinked sample was dried and subjected to 12 μl of PEODA crosslinking. The procedure of PEODA-crosslinking was the same as GA-crosslinking.

4.3.2 Modification of Artificial Cornea Hydrogels

Artificial cornea hydrogels were subsequently dried using nitrogen gas in an isolated clean chamber (refrigerated at 4°C) before being exposed to argon plasma. Samples were then placed in the middle of a radio frequency (RF) plasma system (SP 100 Anatech Ltd, Springfield, VA, USA). This is a small laboratory-scaled plasma system that generally comprises five main components: the reactor chamber in which the samples are treated, a vacuum system, a gas-introduction and gas-control system, a high-frequency generator, and a microprocessor-based system controller as shown in Fig. 4.1.
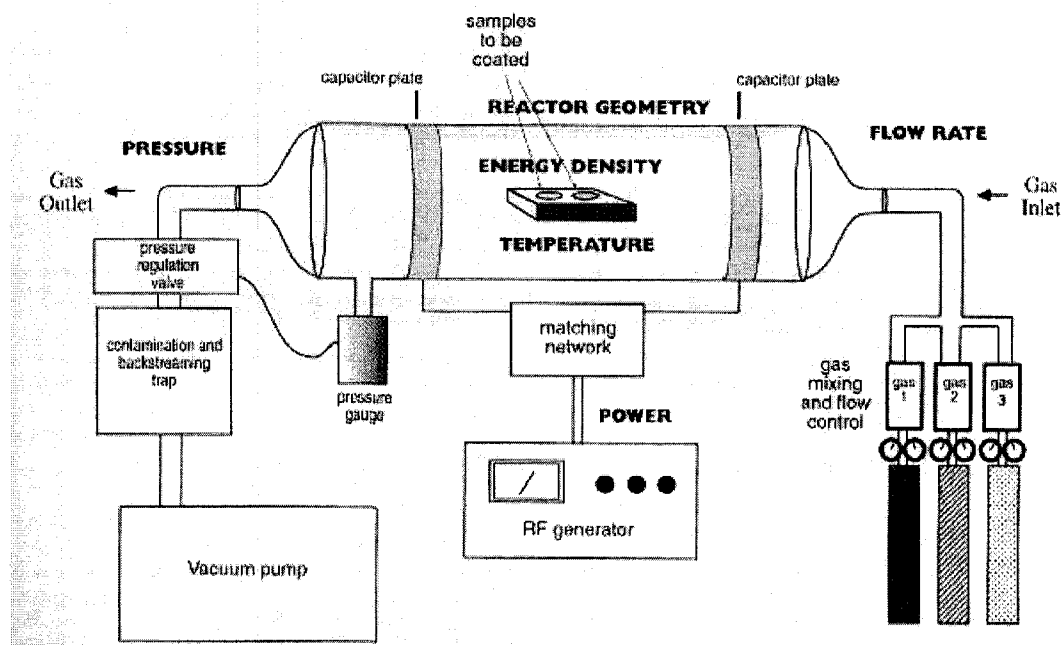
Figure 4.1   A diagram of a typical RF plasma reactor [9].

Air in the plasma reactor chamber was removed through three evacuation-purge cycles with argon gas to around 2000 mtorr. After three evacuation/purge cycles, argon gas (Ultra High Purity from PRAXAIR) was again introduced to the system at a constant flow rate of 250 CC/min. The plasma reactor pressure was controlled and kept at 80 mtorr by adjusting the gas flow rate. Argon plasma was excited in the plasma reactor at 100 Watts for 30 minutes. After the plasma was turned off, the reactor was returned to atmospheric pressure while purging with argon and samples were further quenched in argon for ten minutes. The treated samples were dehydrated in a PBS solution with 1 v/v% chloroform for sterilization. Prior to evaluating the cellular response, samples were extraneously rinsed in sterile PBS/chloroform solution.

4.3.3 In Vitro Biocompatibility Assessment

The *in vitro* biocompatibility test required two stages. The first stage involved the construction of a fixed volume of collagen lightly crosslinked by GA that was also used as an in vitro control for epithelial cells growth. Aliquots of 1.5 ml of this viscous collagen were placed into a 12 well culture dish with inserts and incubated at 37 °C for less than one hour until it was partially gelled to give a stromal equivalent.

In the second stage, each sterile sample disk was laid on top of a lightly gelled stromal equivalent and pressed into the matrix to give good contact between the two components (See Fig. 4.2). Immortalized human epithelial cells were seeded on top of the exposed portions of the stromal equivalent and the samples at a concentration of 1000 cells per insert. Approximately 4 ml of KSFM^{++} growth medium was added to the inside and outside of the insert. The system was then incubated at 37 °C and the medium was replaced every 48 hours. Epithelial cell density and morphology were monitored using a

digital camera attached to a light microscope (10 to 40X magnification, Olympus IMT-2 Optical Company Ltd., Japan with Nikon Coolpix 990 Nikon, Japan) on days one, two, and three post seeding.
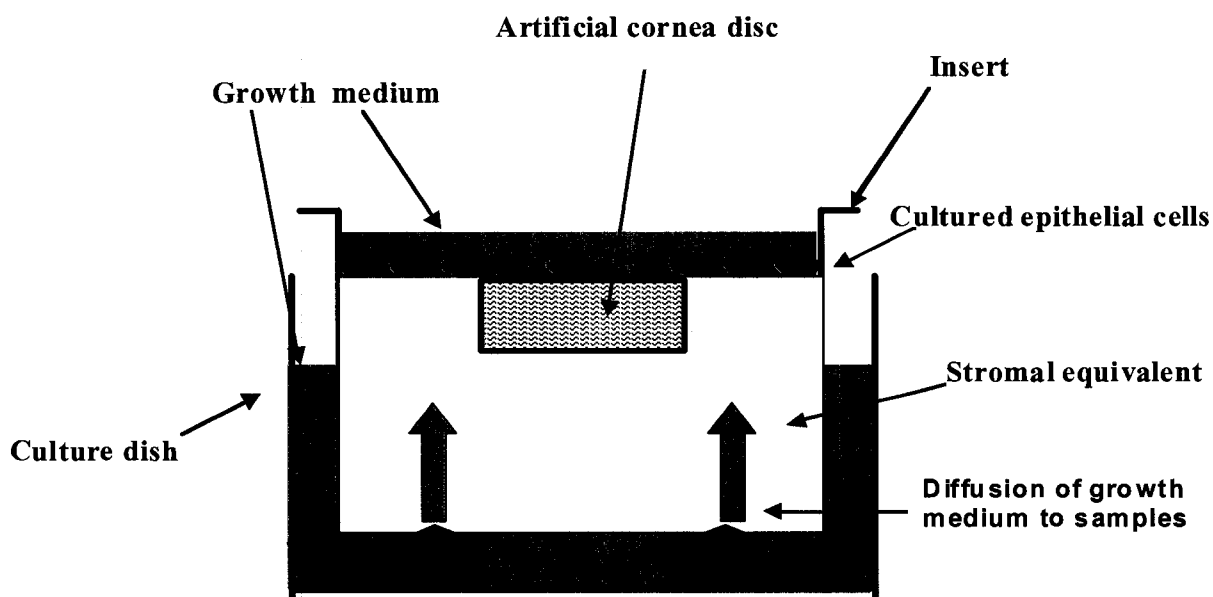
Figure 4.2   Schematic of an insert in a culture dish in which artificial cornea samples were placed and *in vitro* biocompatibility test was performed.

4.3.4   Contact Angle Measurements

To measure the contact angle, artificial cornea samples were soaked in sterile distilled water for 1-2 h prior to measurement. Each artificial cornea sample was placed on a glass plate and then on the sample holder of a Horizontal Beam Comparator (Scherr Tumico Model 20-4200 Series, St. James, Minnisota). Excess water on the sample surface was removed by a lightweight lint free cloth (Kimwipe). A five microliter (5 µl) drop of distilled, deionised water was deposited onto the artificial cornea surface by a micro-syringe and the equilibrium contact angle (θ_e) was measured.

121

4.3.5 Atomic Force Microscopy Characterisation

AFM studies were conducted by tapping mode using a MultiMode™ scanning probe microscope (MM-SPM) (Nanoscope III equipped with 1553D scanner, Digital Instruments, CA). Artificial cornea samples were soaked in distilled water prior to AFM studies. Excess water on the surface was removed by a lightweight lint free cloth (Kimwipe). Each sample was then placed on a metal disc and the disc was magnetically attached to the top of the scanner tube. Images produced from scans were analyzed using the microscope's software. The mean surface roughness (R_a) is the mean value of the surface relative to the centre plane, the plane for which the volumes enclosed by the image above and below this plane are equal, and is calculated as

$$R_a = \frac{1}{L_x L_y} \int_0^{L_y} \int_0^{L_x} |f(x,y)| dx dy \qquad (1)$$

Where f (x, y) is the surface relative to the center plane and L_x and L_y are the surface dimensions in x and y directions, respectively [21].

4.4   Results and Discussion

Enhanced attachment of epithelial cells to artificial cornea surfaces was observed after argon plasma treatment as compared to the low degree of cell attachment onto untreated surfaces (Fig. 4.3). The number of epithelial cells attached to the polymer surfaces on day one and day three was quantified in Fig. 4.4. As shown in Fig. 4.3 and Fig. 4.4, attachment of the cells onto untreated surfaces was found to be significantly lower than the plasma treated surfaces on days 1 and 3 post seeding ($p < 0.05$). A confluent epithelium was observed on stromal equivalents (controls) on day 3. In addition, comparing the plasma treated surfaces, those cross-linked using GA-PEODA system showed better cell attachment than those cross-linked using GA system.
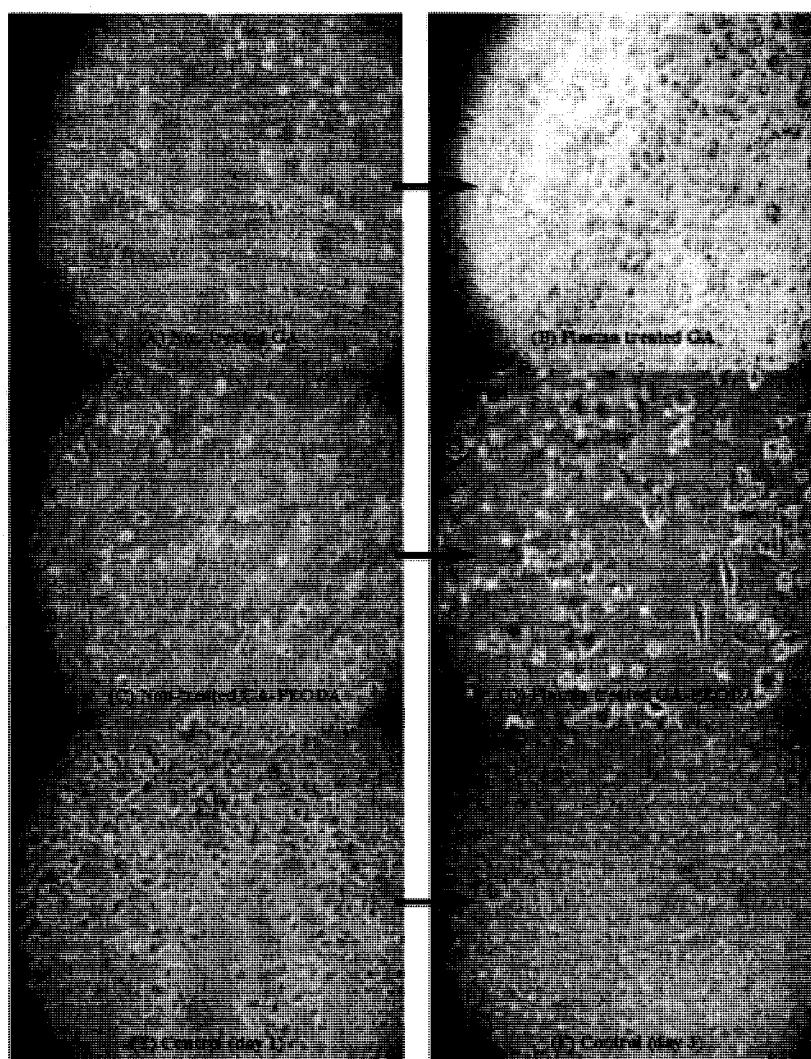
Figure 4.3   Microscopic images of epithelial cells cultured on various cross-linked matrices: **(A)** GA¥ [day3]; **(B)** Argon-plasma-treated GA [day3]; **(C)** GA-PEODA¥¥ [day3]; **(D)** Argon-plasma-treated GA-PEODA [day3]; **(E)** Stromal Equivalent (control) [day 1]; and **(F)** Stromal Equivalent (control) [day 3].

¥ GA: Artificial corneas fabricated by glutaraldehyde crosslinking of collagen matrices.

¥¥ GA-PEODA: Artificial corneas fabricated by glutaraldehyde crosslinking of collagen matrices followed by crosslinking with poly (ethylene oxide dialdehyde).
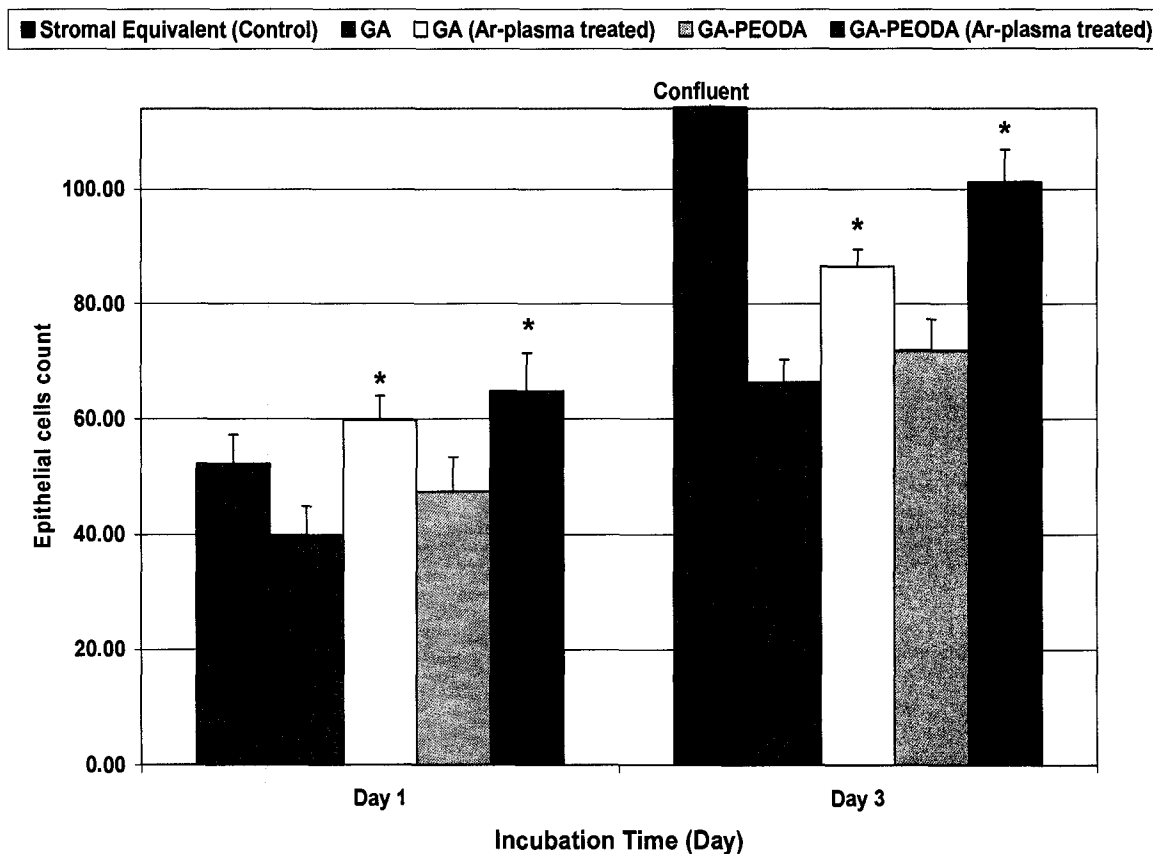
Figure 4.4 Effect of argon plasma treatment on epithelial cells attachment on
GA and GA-PEODA cross-linked matrices.

¥ Five replicate samples were used in determining the mean value and standard deviation
for each data set.

¥¥ The statistical difference between data sets was analyzed using one-way ANOVA.

* $p= 0.0025$ and $p=0.0022$ for the differences between GA & Plasma-treated-GA on
day 1 and day 3, respectively.

** $p= 0.0264$ and $p=0.0032$ for the differences between GA-PEODA & Plasma-treated-
GA-PEODA on day 1 and day 3, respectively.

The plasma-treated surfaces had significant increase in wettability compared to

the untreated ones, with the equilibrium contact angle decreasing from 70 ° to 32 ° on

average by argon plasma treatment as shown in Fig. 4.5 ($p=2.2 \times 10^{-14} \ll 5 \times 10^{-2}$ for GA

and $p=1.2 \times 10^{-5} \ll 5 \times 10^{-2}$ for GA-PEODA). The contact angle measurement of the

plasma-treated surfaces was repeated over a period of 30 days. As shown in Fig. 4.5, the

contact angle was decreased slightly over time for plasma-treated surfaces but variations

were not significant ($p=0.25>0.05$). This is important because it has been reported that

treatment with ionized gases, in most cases, was not of lasting nature and the effect of

treatment normally disappeared within days or even hours [22]. Also, it can be seen that

collagen matrices cross-linked with GA-PEODA system had a lower contact angle

compared to those cross-linked using GA system (Fig. 4.5). This was likely due to

hydrophilic nature of PEODA that also enhanced cell attachment.
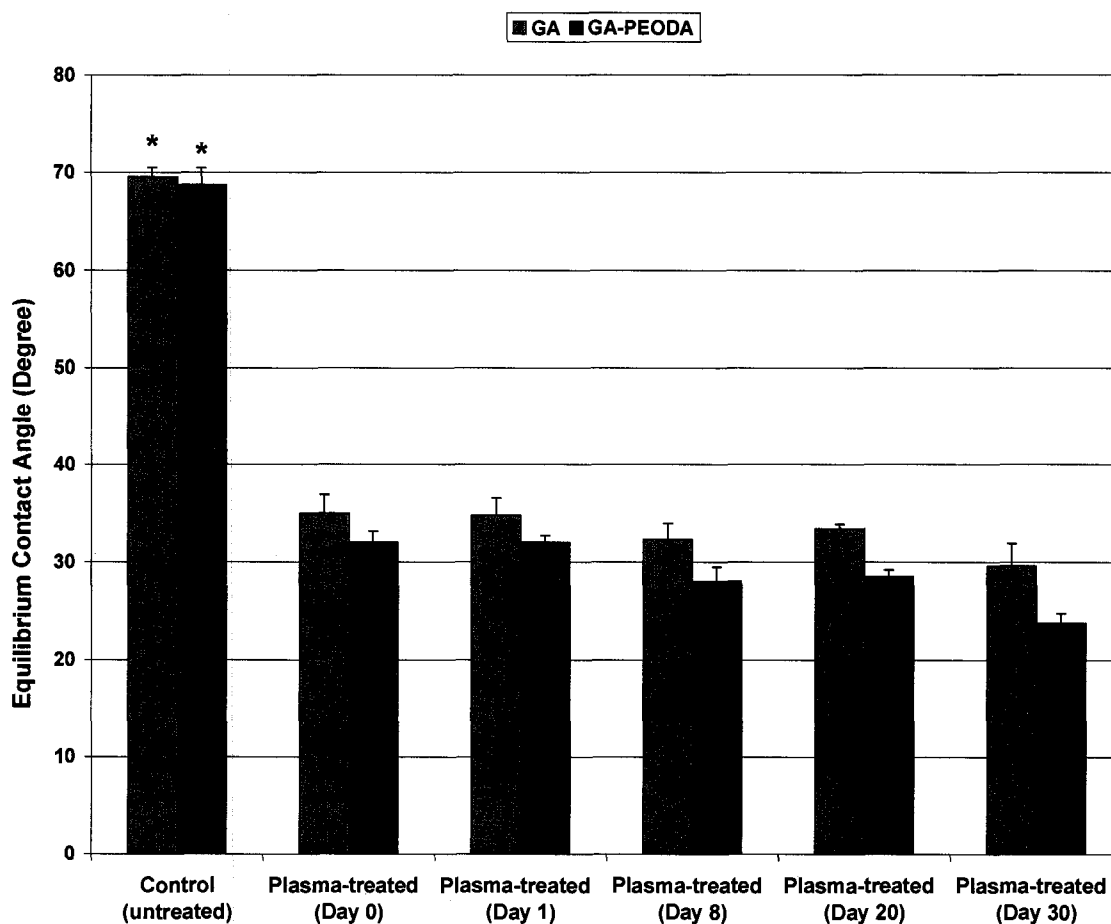
Figure 4.5   Effect of plasma treatment on surface hydrophilicity of the artificial cornea matrices fabricated by GA and GA-PEODA crosslinking of collagen films.

¥   Five replicate samples were used in determining the mean value and standard deviation for each data set. The statistical difference between untreated and plasma treated data sets was analyzed using one-way ANOVA.

¥¥ The information shown in the parenthesis below X axis represents the number of days elapsed after plasma treatment.

* $p=2.2 \times 10^{-14}$ for GA and $p=1.2 \times 10^{-5}$ for GA-PEODA.

125

Surface morphology of plasma-treated and untreated polymers was studied by AFM. Figure 4.6 and Fig.4.7 represent AFM topographical images of the surface of the polymers cross-linked using GA, and GA-PEODA systems, respectively.

G14 (Glut-40%), Ra=28.7 nm, (Sep 04 2003)   G-14.PLO, Ra=32.3 nm

Untreated   Argon Plasma-treated
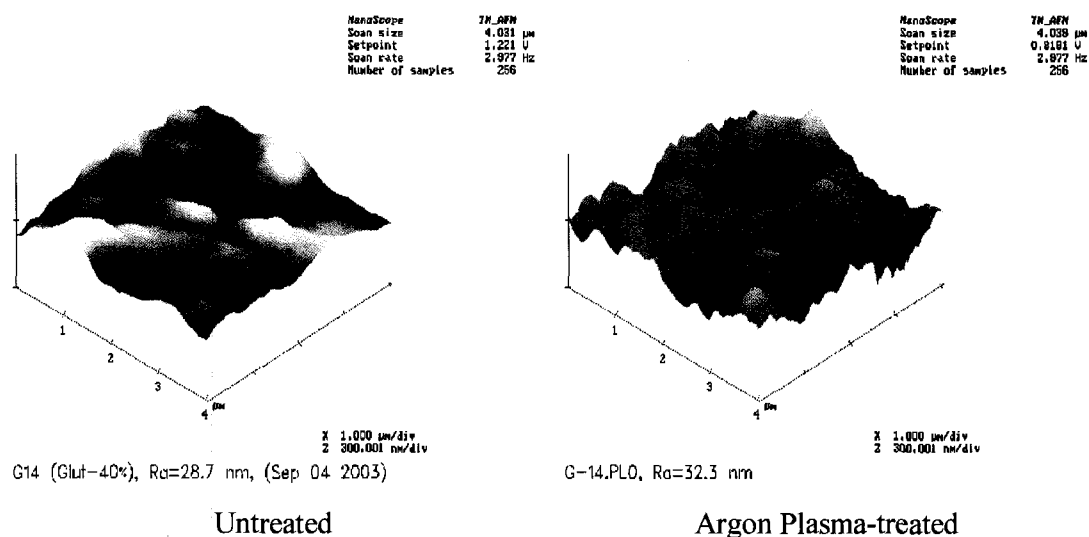
Figure 4.6   AFM images representing the effect of argon plasma treatment on surface morphology of matrices x-linked by GA.

For both cases, the surface roughness was increased after argon plasma treatment. Upon plasma treatment, the AFM mean surface roughness significantly increased from 30 ± 2.5 to 35 ± 1.7 nanometers (nm), and from 24.0 ± 1.9 to 40.0 ± 2.5 nm for collagen matrices cross-linked by GA and by GA-PEODA, respectively (Fig. 4.8). This increase may be due to the etching that took place at the artificial cornea surfaces during plasma treatment. Also, untreated samples cross-linked by GA-PEODA system demonstrated a

126

smoother surface compared to those cross-linked by GA while it was the opposite for the

plasma treated samples. Incorporation of PEODA into the collagen matrices may have

filled up the gaps between collagen chains resulting in a smoother surface.

GPM-19-50%, Ro=20.9 nm   GPM-19.PL4, Ro=39.8 nm

Untreated   Argon Plasma-treated
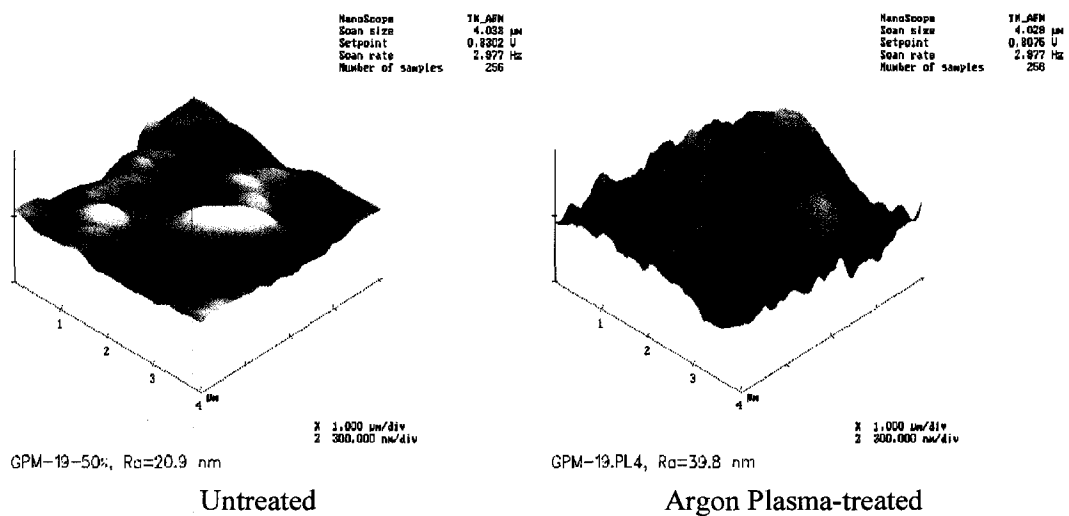
Figure 4.7   AFM images representing the effect of argon plasma treatment on surface morphology of matrices consecutively x-linked by GA-PEODA.

As depicted in Fig. 4.8, the increase in surface roughness was more significant for

GA-PEODA cross-linked materials (p=0.002) compared to GA cross-linked materials

(p=0.049). We have hypothesized that high-energy plasma treatment, may have caused

the scission of PEODA chains as well as removal of low-molecular-weight materials

from the surface of the corneas resulting in a higher increase in the roughness.
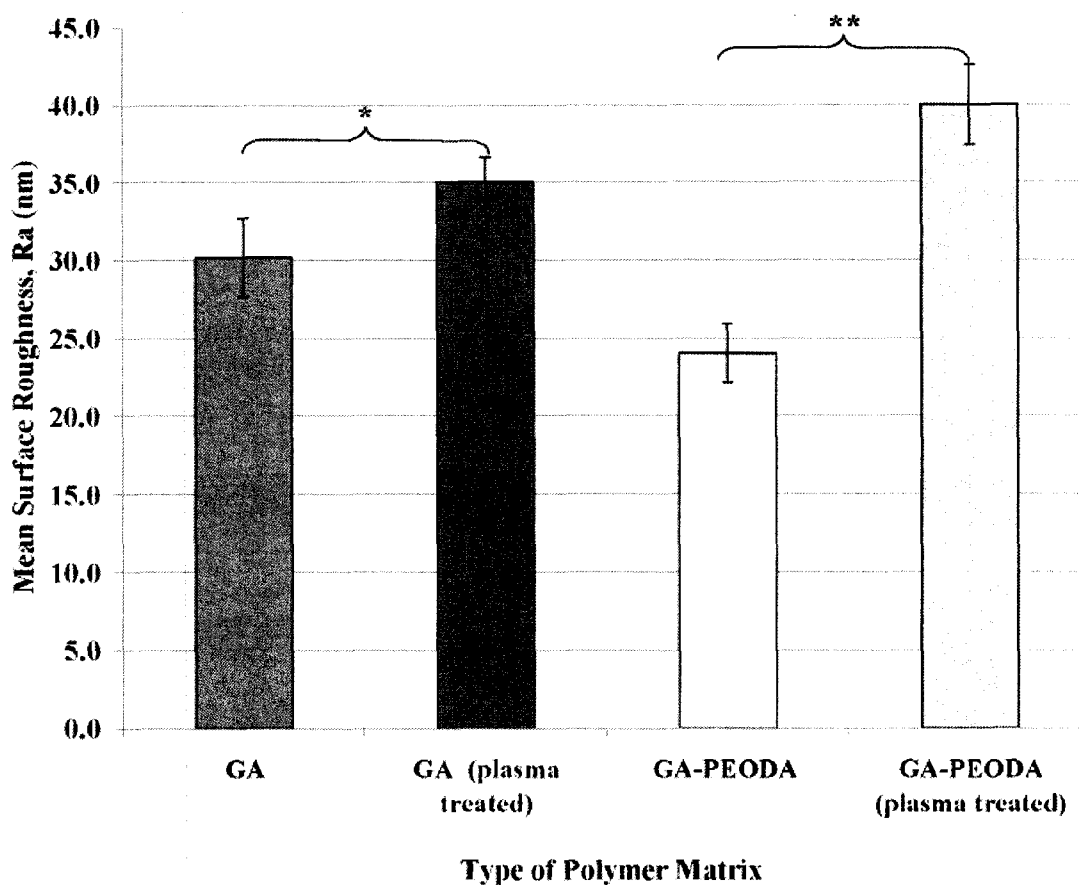
Figure 4.8   Effect of plasma treatment on surface roughness of GA and GA-PEODA cross-linked matrices.

¥   The statistical difference between data sets was analyzed using one-way ANOVA.
¥¥   Three replicate samples were used in determining the mean value and standard
      deviation for each data set.
*   p=0.049 <0.05
**   p=0.002 <0.05

The mechanism of cell adhesion to biomaterial surfaces has been extensively studied and documented [23, 24]. There are two theories on how cells interact with biomaterials surfaces. The surfaces are either capable of (1) selectively adsorbing intact, functional proteins in the biological environments (i.e., cell culture medium) that in turn can interact with receptors from a targeted cell type or (2) directly interacting with cell surface receptors through the functional polar groups or ligand motifs [6]. Our results are

consistent with the second theory although further surface studies should be conducted to confirm our findings. It is reported that the increase in surface energy (reduced contact angle) after argon plasma treatment is caused by formation of hydroxyl (OH), carbonyl (CO), and carboxyl (COOH) functional groups that exhibit negative charges [5]. Also, cells are normally believed to exhibit polarity. This polarity is important because normal cell function can only be expressed if the cell has the correct orientation [25]. Therefore, it was hypothesized in this study that enhanced cell attachment was the result of polar interactions (i.e., hydrogen bonding) between hydrophilic functional groups at the polymer surface and cell membrane proteins. The functional groups at the polymer surface were either created by plasma or already existing particularly when the polymer matrices contain PEODA component.

More specifically, the cells may be held to the polymer surface through hydrogen bonding between the oxygen of the CO or OH functional groups at the polymer surface and the hydrogen of NH_2 or COOH groups in the polypeptide chains of cell membrane proteins. Hydrogen bonding is found very often in proteins, especially those having α-helical and/or β-pleated structures. In these structures every peptide bond is essentially involved in at least one hydrogen bond [26]. In addition to surface chemistry and polar interactions, surface morphology has been a factor in cell attachment mechanism. For example, the increase in surface roughness increased the effective surface area resulting in more sites available for the interaction between the cells and the polymer surfaces.

The results presented above suggest that the epithelial cell attachment to artificial cornea surfaces was influenced by the combined effects of plasma-induced surface chemistry (i.e., surface energy), polar interactions between functional groups at the

129

polymer surface and cell membrane proteins, and polymer surface morphology (i.e., surface roughness).

4.5 Conclusions

In conclusion, plasma surface modification of collagen-based artificial cornea was found to be a promising technique to:

- Enhance epithelial cells attachment to collagen-base surfaces.

- Enhance surface hydrophilicity

- Enhance surface roughness

More specifically, the following conclusions are drawn from this work:

1. Enhanced attachment of epithelial cells to collagen-based artificial cornea surfaces was

    observed after argon plasma treatment as compared to the untreated surfaces.

2. Among plasma treated surfaces, those cross-linked by consecutive application of GA and PEODA cross-linkers showed better cell attachment compared to those cross-linked with GA only.

3. Equilibrium contact angle significantly decreased from 70 ° to 32 ° on average after argon plasma treatment.

4. The contact angle of the plasma-treated samples did not change over a period of 30 days.

5. Upon plasma treatment, the mean surface roughness increased from 24.0±1.9 to 40.0±2.5 for collagen matrices cross-linked by GA-PEODA, and from 30±2.5 to 35±1.7 nm for collagen matrices cross-linked by GA.

6. Increased epithelial cells attachment to plasma-treated surfaces is most likely due

to the increase in number of hydrophilic functional groups, and increased

roughness, endowing the surface with increased effective surface area made

available for specific interactions with corneal cells.

Acknowledgement

4.6   References

1. Chirila, T.V.; Hicks, C.R.; Dalton, P.D.; Vijayasekaran, S.; Luo, X.; Hong, Y.; Clayton, A. B.; Ziegelaar, B.W.; Fitton, J.H.; Platten, S.; Crawford, G.J.; Constable, I.J. Prog. Polym. Sci. 1998, 23, 447.

2. Eye Bank Association of America; 1999 Eye Banking Statistical Report. Washington EBAA; 1999.

3. Carlsson, D.J.; Li, F.; Shimmura, S.; Griffith, M. Curr. Opin. Ophthalmol. 2003, 14,192.

4. Leibowitz, H.M.; Trinkaus-Randall, V.; Tsuk, A.; Franzblau, C. Prog. Retinal Eye Res. 1994, 13, 605.

5. Latkany, R.; Tsuk, A.; Sheu, M.S.; Loh, I.H.; Trinkaus-Randall, V. J. Biomed. Mater. Res. 1997, 36, 29.

6. Koenig, A.L.; Grainger, D.W. In Methods of Tissue Engineering, Atala A.; Lanza R.P.; Eds.; Academic Press: San Diego, 2002, Chap. 66.

7. Ratner, B.D.; Chilkoti, A.; Lopez, G.P. In Plasma Deposition; Treatment and Etching of Polymers, d'Agostino R.; Ed.; Academic Press: San Diego, 1990, 463.

8. Schroder, K.; Meyer-Plath, A.; Keller, D.; Ohl, A. Plasmas Polym. 2002, 2, 103.

9. Ratner, B.D.; Hoffman, A.S. In Biomaterials Science: An Introduction to Materials in Medicine; Ratner, B.D.; Hoffman, A.S.; Schoen, F.J.; Lemons, J.E.; Eds.; Academic Press: San Diego, 1996, 111.

10. Nitschke, M. (2002). Surface Modification by Low Pressure Plasma Techniques. On-line; Deutsche Ophthalmologische Gesellschaft (DOG) Symposium; 17 Nov., 2002; Available: http://www.dog.org/termin/biomaterials.html#intro

11. Sipehia, R.; Garfinkle, A.; Jackson, W.B.; Chang, T.M.S. Biomat.: Artif. Cells & Artif. Org. 1990, 18, 643.

12. Dewez, J. L.; Doren, A.; Schneider, Y.J.; Rouxhet, P.G. Biomaterials 1999, 20, 547.

13. Schakenraad, J.M.; Busscher, H.J.; Wildevuur, C.R.; Arends, J. In Biological and Biomechanical Performance of Biomaterials, Christel P.; Meunier A.; Lee A.J., Eds. Elsevier:Amsterdam, 1986, 263.

14. Vogler, E.A. Colloids Surf. 1989, 42, 233.

15. Busscher, H.J.; Stokroos, I.; Golverdingen, J.G.; Schakenraad, J.M. Cells Mater. 1991,1, 234.

16. Altankov, G.; Groth, T. ,J Biomater Sci Polym Edn 1997, 8, 299.

17. Saltzman, W.M.; Parsons-Wingerter, P.; Leong, K.W.; Shin Lin, J. Biomed. Mater. Res. 1991, 25, 741.

18. Kowalczynska, H.A.; Kaminski, J. J. Cell Sci. 1991, 99, 587.

19. Lee, H.J.; Jung, H.W.; Lee, H.B. Biomater. 1994, 15, 705.

20. Curtis, A.S.G.; Forrester, J.V.; Clark, P. J. Cell Sci. 1986, 86, 924.

21. Singh, S.; Khulbe, K.C.; Matsuura, T.; Ramamurthy, P. J. Membr. Sci. 1998, 142, 111.

22. Decker, W.; Pirzada, S.; Michael, M.; Yializiz, A. Long lasting surface activation of polymer webs; 43rd Annual technical conference proceedings; Society of vacuum coaters 2000; 7188: 505-856.

23. Hubbell, J.A.; J. Biotechnol. 1995, 13, 565.

24. Hammer, D.A.; Tirrell, M. Annu. Rev. Mater. Sci. 1996, 26, 651.

25. Silver, F.H.; Christansen, D.L. Biomaterials Science and Biocompatibility; Springer: New York, 1999.

26. Hein, M.; Best, L.R.; Pattison, S.; Arena, S. Introduction to General, Organic, and Biochemistry; Brooks Cole Publishing Company: Toronto, 1993.

Chapter 5

Surface Modification of Collagen-based Artificial Cornea for Reduced Endothelialization*

Mehrdad Rafat[1,2], Takeshi Matsuura[1], Fengfu Li[2], May Griffith[2,3],

[1] Department of Chemical Engineering, University of Ottawa,
Ottawa, Ontario, K1N 6N5, Canada

[2]University of Ottawa Eye Institute, Ottawa, Ontario, K1H 8L6, Canada

[3]Department of Cellular and Molecular Medicine, University of Ottawa,
Ottawa, Ontario, K1H 8M5, Canada

5.1 Abstract

Our objective was to develop collagen-based hydrogels as tissue substitutes for corneal transplantation. The design of the full-thickness corneal grafts includes prevention of cell migration onto the posterior surface of the implants, using a plasma-assisted surface modification technique. Briefly, the hydrogel materials were subjected to ammonia plasma functionalization followed by grafting of alginate macromolecules to the target surface. The treated materials surfaces showed observable decreases in endothelial cell attachment. The decrease in cell attachment and adhesion was dependant upon the concentration of alginate and plasma radio frequency (RF) power. High concentrations of alginate 5% (w/v) and high RF power of 100 W produced surfaces with minimal cell attachment. The plasma-alginate treatment did not adversely affect the optical or swelling properties of the constructs. Contact angle measurement (CAM) analysis revealed that the posterior surface hydrophilicity significantly increased after the treatment. The grafting of alginate to the implants surfaces was confirmed by Fourier Transform Infrared Spectroscopy (FTIR). Both of the untreated and treated corneal materials were found to be superior to human cornea in optical and swelling properties.

Key words: artificial cornea, collagen, endothelialization, contact angle, infrared spectroscopy,

5.2   Introduction

The human cornea is the transparent window to the eye and is the main refractive organ that is responsible for over 75% of the transmission of light to the back of the eye for vision. As such, its functionality is highly dependent upon its optical clarity (high light transmission with low backscatter). Anatomically, it consists of an outermost, stratified epithelial and an innermost single endothelial layer, sandwiching a largely collagenous extracellular matrix (ECM) containing stromal cells. The human cornea is a highly innervated, but avascular structure, the latter feature rendering it immune privileged. Corneal clarity is highly dependent upon the ability of the organ to osmoregulate and control the hydration of the stroma. This very important physiological function is undertaken by the single layer of endothelial cells. The primary function of the endothelial layer is to pump excess water out of the stroma. Without this pumping function, the stroma would swell with water, becoming hazy and eventually opaque [1].

We have previously developed collagen-based corneal substitutes to address the shortage of high quality donor tissues for transplantation to prevent corneal blindness or to restore vision to patients with damaged corneas. We have shown that collagen, crosslinked with either carbodiimide [2] or synthetic copolymer poly(N-isopropylacrylamide-co-acrylic acid-co-acryloxysuccinimide) [3], when implanted into the corneas of pigs promoted regeneration of corneal cells and nerves. However, these surgeries were performed by lamellar and deep lamellar keratoplasty, i.e. the posterior lamellae of the stroma, Descemet's membrane which underlies the stroma and the endothelium, were left intact. While successful as lamellar implants, these current constructs are not suitable for full-thickness grafts (penetrating keratoplasty), as the

endothelial layer, its special pumping functions and its lack of capacity to regenerate have not been addressed. In the present form, therefore, our previous corneal substitutes will be of no value to patients with endothelial failure or for indications requiring full-thickness grafts, i.e., majority of grafts performed in North America.

The endothelial cells of humans and primates have minimal or no capacity to replicate and therefore endothelial wound healing is largely dependant on the enlargement and movement of the surrounding cells to cover a wound site. This is in contrast to rabbits whose endothelial cells are capable of extensive mitosis, and cats that are capable of limited endothelial mitosis. Human endothelial wound repair is thus achieved by the endothelial cells sliding over the stromal or Descemet's membrane surface. The endothelium is responsible for the deposition of a new Descemet's layer throughout the wound area. Under certain circumstances, a tissue layer forms posterior to the newly formed Descemet's membrane, which also contains fibroblast-like cells, collagen fibrils, basement membrane proteins and junctional complexes that are also termed retrocorneal fibrous membrane (RCFM) [4].

Hydrogels suitable for use as corneal substitutes are designed to swell up to a specific point that provides the optimal optical, mechanical strength and hydration for nutrient transport. This characteristic discourages excessive diffusion of the aqueous humour into the artificial cornea matrix even in the absence of the endothelial layer. Therefore, an artificial cornea would potentially not require an endothelium as long as sufficient diffusion of the factors in the aqueous humor could occur through the implant to provide nutrition to resident cells [5].

There are therefore two diametrically opposed options for designing corneal substitutes to replace the full thickness of the human cornea. The first is to ensure that the posterior surface of an implant is conducive to rapid and stable colonization by pre-seeded corneal endothelial cells. The second option is to modify the posterior surface of implants to prevent endothelial cell adhesion, as the artificial corneas potentially would not require an endothelium as discussed above. The rationale for the latter approach is that any remaining cells on the host corneal rim may migrate onto the implants and thereby further depleting the rims and causing even more swelling of the host tissues around the implant. Although the first option is viable, the cultivation of endothelial cells at various clinics where transplants are performed, especially in developing countries where the need for transplantation is most acute, is not very feasible. The second option, on the other hand, addresses the prevention of retroprosthetic membranes or RCFM that is one of the contributing factors to the post-surgical corneal opacification and failure [6, 7]. Hence, the present study focuses on a strategy based on the second option to inhibit cell adhesion using a novel surface modification technique.

Plasma-assisted surface modification techniques have been previously used for enhancing biocompatibility and cell-material interaction of various biomaterials [8]. These techniques are mostly aimed at enhancing cells attachment onto biomaterials as opposed to the inhibition of attachment, as reported in this work. More specifically, plasma-assisted generation of surface functional groups serves as the initial step of a number of different coupling reaction sequences that aim at covering surfaces with biofunctional macromolecules, which are intended to control the interaction with living matters [9]. Often, extracellular matrix proteins like collagen, fibronectin or laminin are

used to improve cells attachment while hydrophilic polysaccharides, such as dextran, hyaluronan, and other macromolecules such as Poly(hydroxyethyl methacrylate) (PHEMA) and Poly(ethylene oxide)(PEO) have been used to generate cell-adhesion-resistant surfaces [10-13]. PHEMA hydrogel coating is one of the most common techniques used in routine cell culturing to prevent adhesion of cells to tissue culture polystyrene plastic ware [14, 15]. It is believed that water content and mechanical properties of PHEMA hydrogel do not allow anchorage of adhering cells to the substrate [16, 17]. Sheu et al. [18] has also investigated the effect of PEO immobilization onto hydrophobic biomaterials to generate protein-resistant surfaces.

Polysaccharides-coated surfaces are also known for their cell-resistant properties. Osterberg et al. [12] has reported that polysaccharide (dextran) modified surfaces yielded better resistance to protein adsorption in comparison with PEO-modified ones. The high hydrophilicity of these natural macromolecules that promotes minimal protein adsorption, as well as steric effect and lack of the receptors for cell binding are generally known accountable for their anti-cell adhesion properties [14, 19].

Alginate is a naturally abundant anionic hydrophilic polysaccharide that is extracted from seaweed. Although, it is widely used in biomedical applications such as dental impression materials, wound dressing, and cell encapsulation, it cannot specifically interact with mammalian cells and has a limited range of mechanical properties [19]. Alginate hydrogels are considered biocompatible, but have only been documented to be useful as cell immobilization matrices after modification with cell adhesion peptides, such as RGD [20]. In this study, we describe the development of a two-stage plasma-assisted surface modification technique to covalently graft alginate

macromolecules to the posterior surface of collagen-based artificial cornea hydrogels to prevent endothelial cell attachment and proliferation.

5.3   Materials

Freeze dried porcine type I atelo-collagen was obtained from Nippon Meat Packers, Inc, (Japan) and was dissolved readily in sterile distilled deionized water ($_{dd}$ H_2O) and stirred at 4°C to give 10% (w/w) concentration. 1-ethyl-3-(3-dimethylaminopropyl) carbodiimide (EDC) and N-hydroxysuccinimide (NHS) were purchased from Sigma-Aldrich. The 3% chitosan solution was prepared by dissolving chitosan powder (Mw = 400 kDa, Fluka) in 0.2 N hydrochloric acid (HCl) and stirring at 4°C. Sodium alginate (Mw = 20 kDa) from *Macrocystis pyrifera* (Kelp) was obtained from Sigma-Aldrich.

5.4   Methods

5.4.1   Factorial experimental design (FED) and statistical analysis

A full factorial design was performed to investigate the impact of three factors including substrate hydrogel material, plasma RF power, and alginate solution concentration on the effectiveness of the surface modification. The number of levels for substrate hydrogel material was two and it was three for other factors. The number of possible treatments was determined to be 2 x 3 x 3 =18. The total factors to be varied and their levels are listed in Table 5.1.

Table 5.1 A three factors full factorial design table showing factors, number of levels and their settings.

Factor	Description	No. of levels	Level settings
X_1	Substrate material	2	A, B
X_2	Plasma RF Power (W)	3	0, 40, 100
X_3	Alginate Concentration, % (g/100ml)	3	0, 1, 5

Note: Control unmodified surfaces are denoted by RF power and alginate concentration of zero.

Five parameters (or responses in statistical terms) including percent light transmission, water content, contact angle, FTIR peak intensity, and endothelial cell count (ECC) of adhered cells to the hydrogel surface were determined. However, only three of the key responses including CAM, FTIR, and ECC were used for FED. The results were subjected to analysis of variance (ANOVA) test using Minitab statistical software to identify the vital few factors or key variables that influence the responses the most, and to evaluate the interactions among responses.

Because three factors were investigated, a total of seven combinations were possible: three main factor effects, three two-factor interaction effects, and one three-factor interaction effect. The values of Test Statistics [F-value], and probability [P-value] were calculated for each of the combinations. P-values from multivariate and one-way ANOVA are represented by capital "P" and small "p", respectively. A significance level of 95% was chosen, thus a combination with a P-value less than 0.05 was considered to be significant. One-way ANOVA was also performed for all responses to determine whether the difference between each data set and its corresponding control was statistically significant.

5.4.2   Preparation of substrate corneal materials

Hydrogels designed as corneal implants are comprised of either collagen alone or collagen/chitosan composites, crosslinked using 1-ethyl-3-(3-dimethylaminopropyl) carbodiimide (EDC) and N-hydroxysuccinimide (NHS). Two types of hydrogels were developed: collagen/EDC-NHS (type A) and collagen/chitosan/ EDC-NHS (type B).

5.4.2.1 Preparation of material A (collagen + EDC-NHS): 0.6 ml of an aqueous 10% (w/v) collagen, 0.4 ml of 2-(N-Morpholino) ethanesulfunic acid (MES) buffer, and 0.35 ml EDC/NHS crosslinker in MES were mixed together in a syringe system at a predetermined molar equivalent ratio of EDC:NHS:Collagen-NH$_2$ (Collagen-NH$_2$ denotes the ε-amine groups on collagen molecules) at 3:2:1 to make a homogeneous solution at pH 5. Aliquots of the homogenous solution was then dispensed into polypropylene contact lens molds (CooperVision, Pleasanton, CA), and were allowed to cure first at room temperature for 24 hours, and then at 37°C for 24 hours, in 100% humidity environments at both temperatures. De-molding of the corneal samples was achieved by immersion in phosphate buffered saline (PBS) for 2 hours. The samples were then immersed in a 0.1 M Na$_2$HPO$_4$ solution for 2 hrs to hydrolyze any remaining O-acylisourea groups [21] and subsequently rinsed four times with PBS solution (0.5% (w/v) PBS, containing 1% v/v chloroform) at room temperature to terminate any reactive residues, extract out reaction byproducts, and to sterilize the samples. The corneal samples were then stored in PBS solution (0.5 %(w/v) PBS, containing 1% v/v chloroform) at 4 °C.

5.4.2.2 Preparation of material B (collagen + chitosan + EDC-NHS): 0.6 ml of 10% collagen solution, 0.12 ml of 3% (w/w) chitosan solution, 0.4 ml of MES solution, and

141

0.35 ml of EDC/NHS crosslinker in MES were mixed together in a syringe system at a predetermined molar equivalent ratio of EDC:NHS:(Collagen/Chitosan)-NH$_2$ ((Collagen/chitosan)-NH$_2$ denotes the ε-amine groups on collagen and the amine groups on chitosan) at 3:2:1 to make a homogeneous solution at pH 5. The molded samples of material B were prepared as for material A.

5.4.3 Surface modification:

The posterior surfaces of corneal implants were modified to prevent cell attachment in a two-step process (Fig. 5.1):

5.4.3.1 Surface functionalization by ammonia (NH$_3$) plasma treatment: Surface functionalization was achieved by the introduction of amino groups onto the posterior surfaces of hydrogels by NH$_3$ plasma treatment. Hydrogels were partially dried by air for half hour in an isolated cold chamber at 4°C while concaved up in the fabrication molds. Only the posterior surface was dried to ensure that the anterior surface would not be affected by the treatment as well as preventing the distortion of hydrogels upon drying. The corneal samples, which were still concaved up in the molds, were placed in a radio frequency (RF) plasma reactor (SP100, Anatech Ltd, Springfield, VA, USA) at 7.5 cm downstream from the NH$_3$ gas inlet. The air in the reactor was removed by three evacuations (<30 mtorr) and purged with NH$_3$ gas to around 2000 mtorr. After three repeated evacuations, NH$_3$ gas was introduced to the system at a constant flow rate. The reactor pressure was controlled at 200 mtorr by adjusting the gas flow rate.

The samples were then plasma treated for 15 min at two RF powers of 40 and 100 W as indicated in Table 5.1. The treated samples were then quenched in NH$_3$ and

removed from the plasma reactor and prepared for alginate grafting. The samples that were not treated considered as controls and denoted by a RF power of zero.
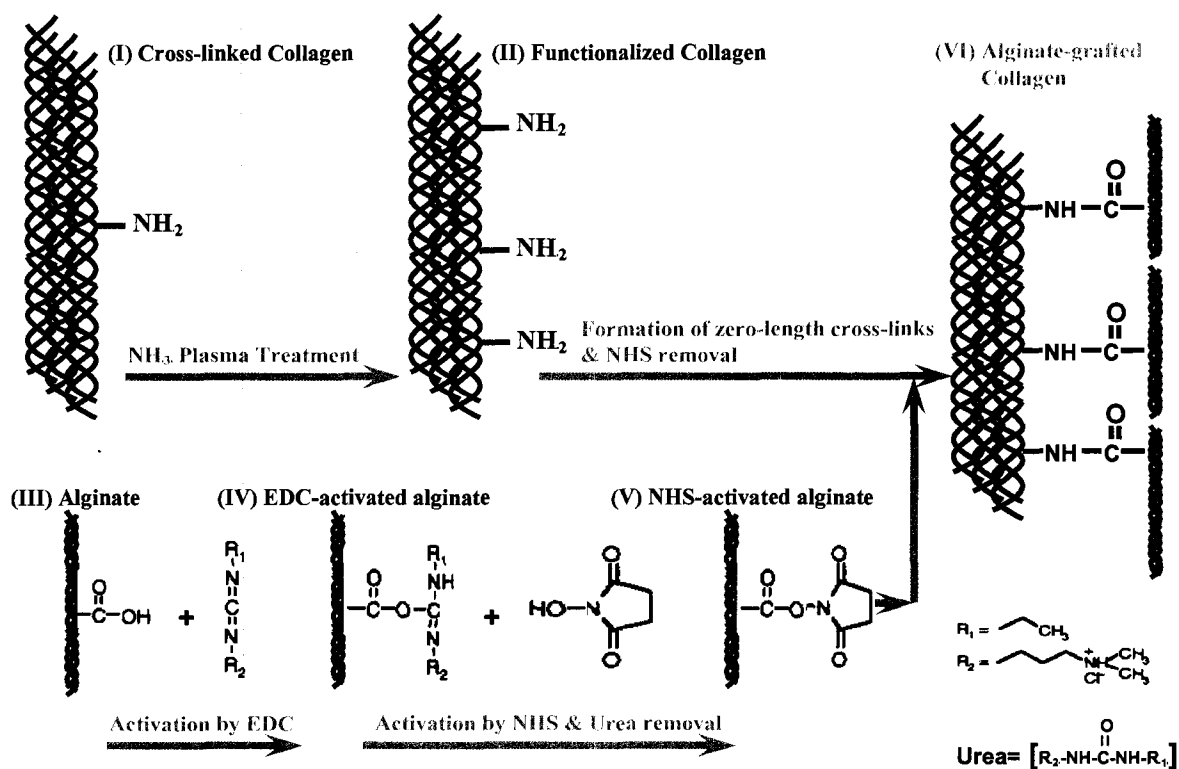
Figure 5.1   Mechanism of alginate surface grafting to a typical cross-linked collagen matrix.

5.4.3.2 Alginate grafting: Alginate was covalently coupled to the surface amino groups of collagen (native and plasma-induced groups) to produce cell-adhesion-resistant surfaces. The mechanism of alginate surface grafting to a typical cross-linked collagen matrix is shown in Fig. 5.1. One ml of 1% (w/v) alginate solution was mixed with 4.0 mg EDC, 2.3 mg NHS, and 0.4 ml MES solution (Alg-COOH:EDC:NHS molar equivalent = 1:4:4; Alg-COOH denotes carboxylic acid groups on alginate molecules). The solution was then placed onto the posterior surface of hydrogels while still concaved up in the fabrication mold. The same procedure was repeated for 5% (w/v) alginate solution with 19.6 mg

EDC, 11.6 mg NHS, and 0.4 ml MES (Alg-COOH:EDC:NHS molar equivalent = 1:4:4). The reaction was carried out at room temperature overnight. The viscous alginate solution (5%) was used to minimize diffusion of the solution into the implant bulk that could affect the anterior surface. It also provided enough alginate molecules for surface grafting compared to the 1% solution.

5.4.4 Water content measurements

The water content study was performed for corneal materials and human eye bank corneas. The corneal samples were dried in a cold chamber purged by filtered dry air at 4 °C. The pre-weighed dry samples were then immersed in PBS (0.5% w/v) buffer solution at pH 7.4 at room temperature. The immersion time was 24 hrs. The swelled samples were withdrawn from the solution and their wet weights were determined after first blotting with a filter paper to remove the surface water and immediately weighing the samples. Equilibrium hydrated mass ($m_{hydrated}$) and dry mass (m_{dry}) were used to determine water content, defined as:

$$water\ content = \left(\frac{m_{hydrated} - m_{dry}}{m_{hydrated}}\right) x\ 100$$

5.4.5 Measurement of optical properties

Light transmission measurement was made at 21°C, both for white light (quartz-halogen lamp source) and for narrow spectral regions (centered at 450, 500, 550, 600, and 650 nm) for corneal materials, and human eye bank corneas using an optical method developed by Priest et al. [22]. Samples were hydrated in 0.5% (w/v) PBS before and during the measurement.

5.4.6 Contact angle measurements

The surface hydrophilicity of treated and untreated hydrogels was studied by contact angle measurement. To measure the contact angle, artificial cornea hydrogels were soaked in sterile $_{dd}H_2O$ for 2 hr prior to measurement. Each artificial cornea sample was placed on a glass plate and then on the sample holder of a Horizontal Beam Comparator (Model 20-4200 Series, Scherr Tumico, St. James, Minnesota). Excess water on the sample surface was removed by a lightweight lint free cloth (Kimwipe). A 10 μl drop of $_{dd}H_2O$ was deposited onto the artificial cornea surface by a micro-syringe and the equilibrium contact angle (θ_e) was measured. Each measurement was performed in less than 10 seconds so that the bulk dehydration did not have any significant impact on the final contact angle values. Also, the same procedure was repeated for all measurements.

5.4.7 Fourier Transform Infrared Spectroscopy (FTIR)

Infrared spectra of the modified and unmodified hydrogels were obtained using a M4000 Series FTIR spectrometer (MIDAC Corporation, Costa Mesa, California) equipped with a diamond compression cell (Greaseby-Specac Diasqueeze) under ambient conditions. All hydrogel materials were prepared in thin films with a thickness of 80 microns. They were then dried by nitrogen gas for 6 hrs and cut into 5 mm discs. The sample compartment was purged with nitrogen gas for about ½ hr before collecting any spectra. Purging was continued throughout every run. Before acquiring an FTIR spectrum of a sample, a reference or background spectrum was collected. Dry films were placed in the sample holder and placed in the sample compartment which was purged with nitrogen gas for another 30 min. Absorbance IR spectra of dry films were collected by

accumulating 54 scans at a resolution of 4 wavenumbers in the spectral range between 4000 and 500 cm^{-1}. All sample spectra were normalized against the dry-cell background of 54 scans collected at the ambient temperature. Each FTIR spectrum reported was selected from a set of at least three samples prepared under identical conditions. In order to determine the relative absorbance peak intensity values and to normalize the data against the reference absorbance, the reference absorbance at 4000 cm^{-1} was subtracted from the absorbance value at each wavenumber (i.e. 1036 cm^{-1}).

5.4.8 Biological characterization: endothelial cell culture

The corneal samples were used within two weeks of fabrication. Prior to use, they were rinsed repeatedly in 0.5 % phosphate buffered saline (1XPBS; Invitrogen, Carlsbad, CA, USA) and placed into individual wells in a 24-well plate. The hydrogels' modified posterior or unmodified control surfaces were seeded with human corneal endothelial cells to evaluate the effect of the surface modification on endothelial cells attachment and growth. Briefly, human endothelial cells with extended lifespans [23] were seeded on the surface of each sample at a cell concentration of 5000 cells/well.

The cultures were supplanted with M199 tissue culture medium (Invitrogen) containing 10% foetal bovine serum (FBS), insulin-transferrin-selenium (ITS+ supplement, Invitrogen) and Glutamax (Invitrogen) and maintained in a humidified incubator at 37°C and at 5% CO_2. The tissue culture medium was changed every 48 hrs as of the beginning of the incubation period. Microscopic images were taken on days 1, 3, 5, and 7 post-seeding and number of cells that had attached and spread were measured using Northern Eclipse software (EMPIX IMAGING Inc., North Tonawanda, NY, USA). Four randomly selected areas of the same dimensions were counted for each sample and

the number of cells counted was normalized to the area of gel selected, i.e. counts were

expressed as cells per square milimeter of surface area.

5.5 Results

5.5.1 Water content

The water content of untreated, and alginate-grafted corneal materials, and that of

human cornea are plotted on the average of three trials in Fig.5.2.
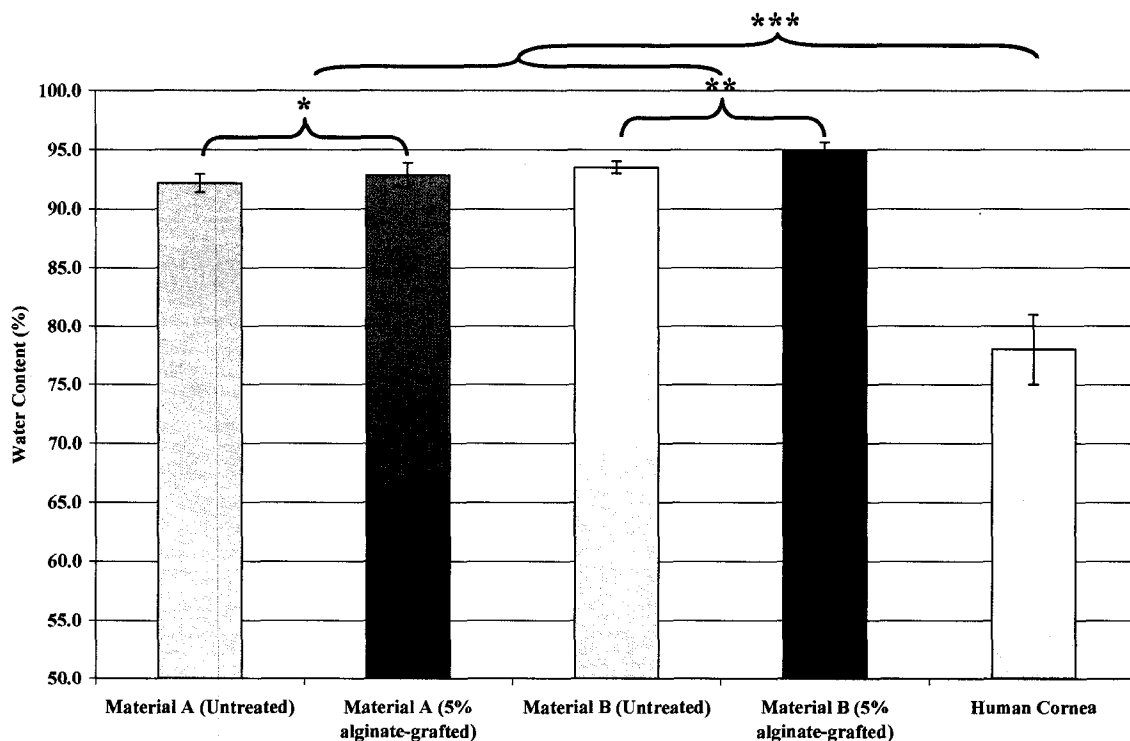
Figure 5.2 Water content data for various surface treated and untreated corneal materials compared to that of the human cornea (HC). The variation of group means is represented by standard deviation (n=3).

* denotes insignificant difference between untreated and treated material A using ANOVA (p=0.422 ≥ 0.050).

** denotes insignificant difference between untreated and treated material B using ANOVA (p=0.065 ≥ 0.050).

*** denotes significant difference between corneal materials average and HC using ANOVA (p=0.001 ≤ 0.050).

All corneal materials exhibited high degree of swelling behavior specific to high

water content hydrogels. Surface modification did not have any significant impact on

water content of material A (p=0.422 ≥ 0.050) and material B (p=0.065 ≥ 0.050). All

corneal materials demonstrated a significantly higher degree of water content compared

to native human cornea (p=0.001 ≤ 0.050). Material B (5% alginate-grafted) had the

highest water content that might be attributed to the presence of hydrophilic molecules in

the hydrogel's bulk, e.g. chitosan, and on the hydrogel's surface, e.g. alginate.

5.5.2 Optical properties

As shown in Fig. 5.3, all corneal constructs, treated or untreated, were optically

transparent and superior to human cornea at all wavelengths of visible light (p ≤ 0.050,

i.e. p=0.011 for white light).
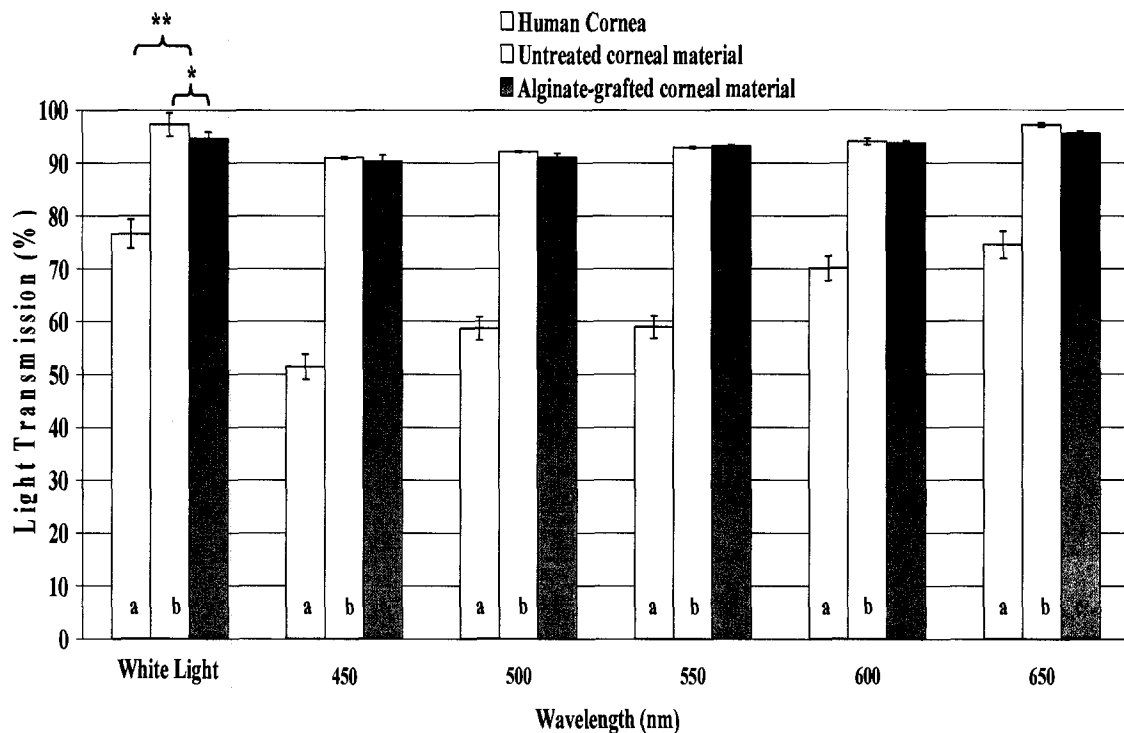
Figure 5.3 Optical light transmission of (a) human cornea, (b) untreated
corneal materials, (c) alginate-grafted corneal materials.

*   denotes insignificant difference between untreated and treated materials using ANOVA
     (p=0.161 ≥ 0.050 for white light data).
**   denotes significant difference between corneal materials average and HC using ANOVA
     (p=0.011 ≤ 0.050 for white light data).

148

Light transmission values for alginate-grafted materials were not significantly different than that of untreated materials ($p \geq 0.050$, i.e. $p=0.161$ for white light).

5.5.3 Contact angle

Figure 5.4 presents the results of equilibrium contact angle as a function of substrate material, RF power (W), and alginate concentration.
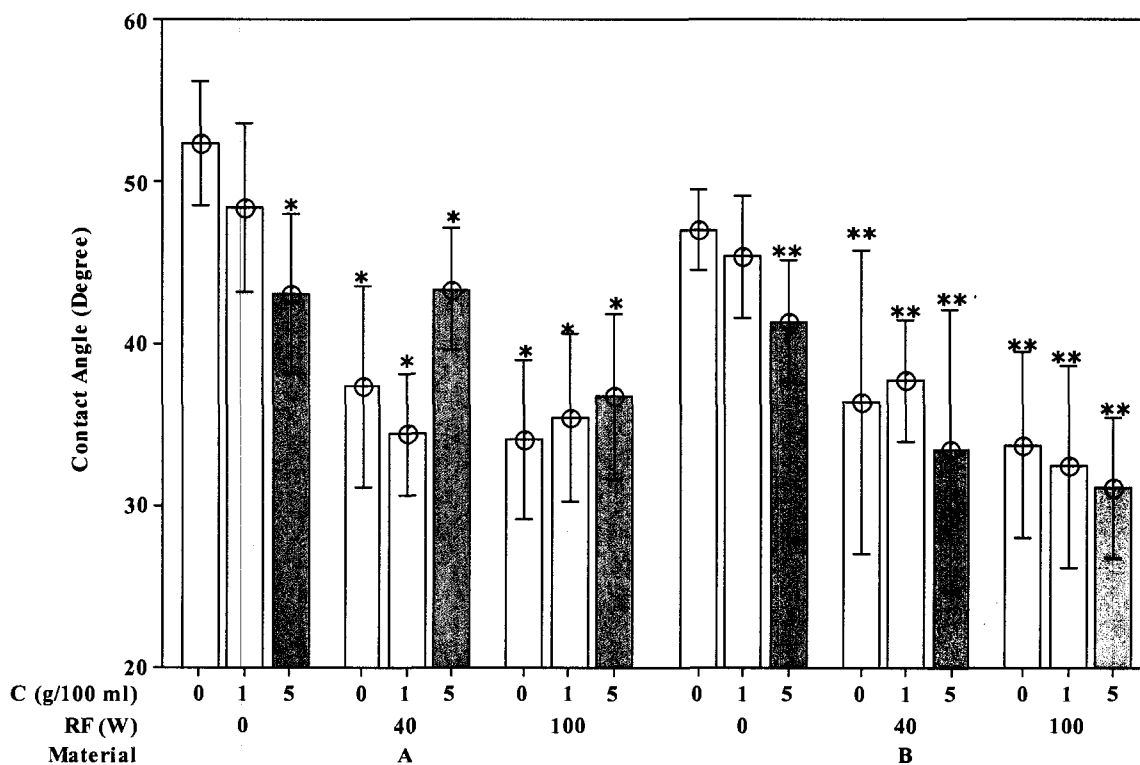
Figure 5.4 Interval plots of equilibrium contact angle values for treated and untreated corneal materials as a function of substrate material, RF power (W), and alginate concentration, C (g/100 ml). Control unmodified surfaces are denoted by RF power and alginate concentration of zero for material groups A (i.e., A-0-0) and B (i.e., B-0-0). The variation of group means is represented by 95% confidence interval.

* denotes significant difference from unmodified material A using ANOVA ($p \leq 0.05$).
** denotes significant difference from unmodified material B using ANOVA ($p \leq 0.05$).

Contact angle was found to be inversely related to RF power for most of the cases. For example, for substrate material A, by increasing the RF power from 0 to 100

W the contact angle significantly decreased from 52±1.5 to 34±2 (p=0.0002) resulted in more hydrophilic surfaces. Similar trend was observed for substrate material B for which by increasing the RF power from 0 to 100 W the contact angle decreased from 47±2 to 34±2.5 (p=0.0008).

Also, the data suggests that the contact angle for non-plasma treated samples was the lowest for those treated with 5% alginate in comparison with those treated with 1% alginate and non-alginate treated ones. Not such clear trend was observed for samples that were both plasma and alginate-treated. This observation could be explained by the fact that both plasma and alginate treatments have significant decreasing impacts on contact angle and these impacts are more noticeable when only one treatment is applied.

As detailed in Table 5.2, large value of r^2 (92.2 %) for CAM implies that the model is capable of providing good predictions. We can also see that all factors had significant effects on contact angle (P<0.05) while alginate concentration had the least significant effect (P=0.028, and F= 4) in comparison with other two factors. Contact angle was generally lower for material B compared to material A, most likely attributed to hydrophilic nature of chitosan incorporated into the hydrogel structure.

The values in the "F" column suggest that plasma power has the highest influence on the contact angle followed by substrate material, and alginate concentration $(F_{X2}>F_{X1}>F_{X3})$. This phenomenon could be explained by the fact that by increasing the RF power more hydrophilic amine groups were formed on the surface resulting in a significant increase in surface hydrophilicity. Using the values in the "P" column of Table 5.2 we can determine that all of the effects are significant with the exception of the two-way interaction effect "X_1*X_2", that is, its P-value is larger than 0.05 (P=0.863).

Table 5.2 ANOVA data (F and P values) for three responses including contact angle measurement (CAM), FTIR intensity, and endothelial cell count (cell/mm2).

Source	CAM		FTIR		Cell Count	
	F	P	F	P	F	P
X_1	25	0.000	286.2	0.000	19.5	0.000
X_2	160	0.000	193.6	0.000	214.6	0.000
X_3	4	0.028	266.0	0.000	1114.6	0.000
X_1*X_2	0.15	0.863	20.2	0.000	14.8	0.000
X_1*X_3	6	0.005	15.1	0.000	7.1	0.002
X_2*X_3	8	0.000	35.1	0.000	125.7	0.000
$X_1*X_2*X_3$	6	0.001	2.3	0.082	1.3	0.296
r^2	92.2 %		97.5 %		98.9 %	

Notes: F: Test Statistics = (Variance between samples/Variance within samples)
P: The probability that the means of dependent variable do not statistically differ from each other.
r^2: Coefficient of determination. Model is a perfect fit if $r^2=100\%$

This means that substrate material, and RF power have independently influenced the contact angle values and the changes in the setting of one does not affect the influence of the other on contact angle. There is also a significant difference between the contact angle for material A and B ($P<0.05$) especially at 5% alginate concentration while the difference is less significant at 1%, and 0% concentrations. It seems possible that these results are due to the higher density of alginate grafted to substrate material B that has more reaction sites (amine groups) for alginate grafting resulting in lower contact angle.

Low P-value of zero and higher F-value of 8 for X_2*X_3 term reveal the interaction between RF plasma power and alginate concentration and their effects on contact angle. At RF power of 100W, the effect of plasma dominates over the effect of alginate concentration so that contact angle remains unchanged at different alginate concentrations. At RF=40 W, the results at 5% alginate concentration is rather contradictory, which may be due to experimental error (n=3) as contact angle should have decreased instead of increasing. In the absence of plasma treatment (RF=0 W), it is obvious that alginate concentration is dominating. The higher the alginate concentration the lower was the contact angle.

5.5.4   FTIR Analysis

Figure 5.5 shows the mid-infrared spectra (4000-500 cm^{-1}) of corneal material B that was untreated, NH_3-plasma treated, plasma-assisted 1% alginate-grafted, and plasma-assisted 5% alginate-grafted. Spectrum of sodium alginate film is also demonstrated as one of the controls.
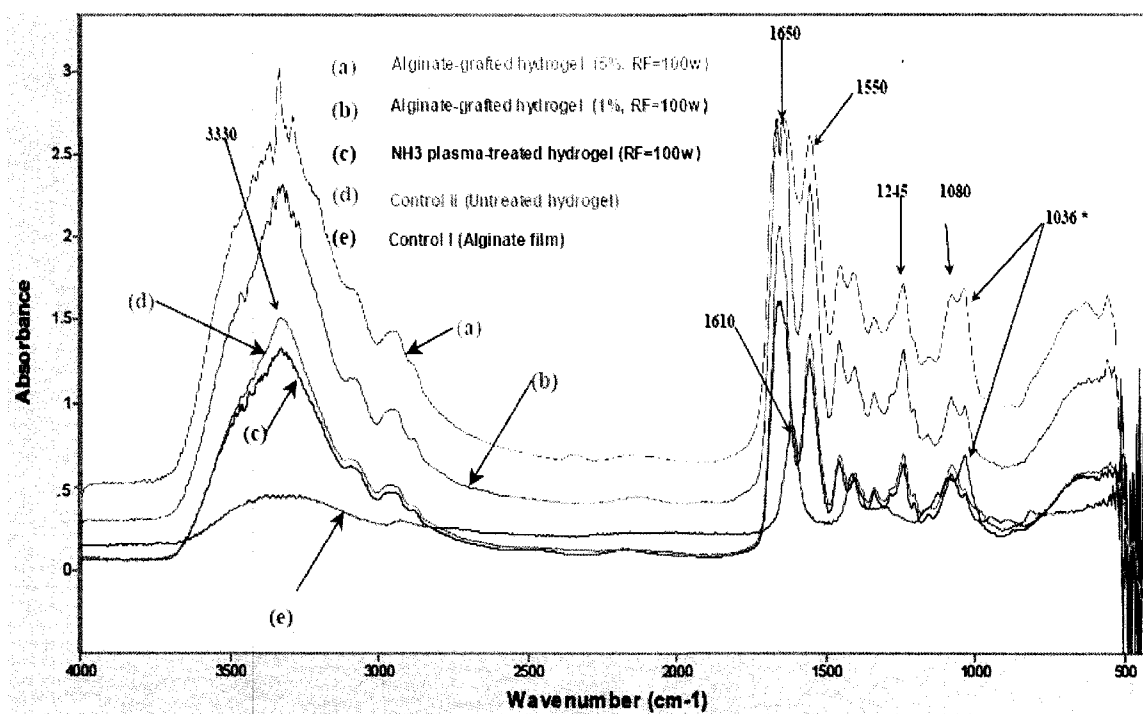
Figure 5.5   FTIR spectra of cross-linked collagen/chitosan films that were (a) 5% alginate-grafted, (b) 1% alginate-grafted, (c) NH₃-plasma treated, (d) untreated, and (e) the spectrum for pure alginate film.

Each mid-infrared spectrum can be approximately divided into four regions and the nature of a group frequency may be determined by the region in which it is located [24]. For example, the vibrations in the 4000-2500 cm^{-1} region are generally due to O-H, C-H, and N-H stretching. The 2500-2000 cm^{-1} region is called triple-bond region as most of the C≡C and C≡N triple bonds stretching fall in that region. The principal bands in the 2000-1500 cm^{-1} region are due to C=O, and C=C stretching. The fourth region is from 1500-650 cm^{-1} that is also called fingerprint region and is of more importance in this study. The absorption bands in this region are mostly due to intra-molecular phenomena and are highly specific for each material while the absorption bands in other regions are typically due to functional groups.

153

As depicted in Fig.5.5, the main IR bands associated with collagen were detected (see spectra (a) to (d)). These bands are mostly associated with various types of amide bonds. There are nine such bands called amide A, B, and I to VII, in order of decreasing wavenumber but amide I and II are the most frequently used ones. These bands were at ~3330 (amide A), ~1650 (amide I), ~1550 (amide II), ~1245 (amide III), and ~1080 cm^{-1} that were mainly attributed to N-H stretching, N–H stretching, C=O stretching, N–H bending, C–N and N–H stretching, and O-H bending, respectively [25]. The main IR bands associated with sodium alginate (spectrum (e)) were also detected for alginate-grafted materials (spectra (a) and (b)). These bands were at ~3450, ~1610, ~1080, and ~1036 cm^{-1} that were attributed to O-H stretching, C–O–O$^-$ (carboxylate ion) stretching, C–O–C stretching, and O-H bending, respectively. The entire bands specific to alginate had overlaps with collagen bands except for the one at ~1036 cm^{-1}. Therefore, this band was selected for further investigation to identify the presence of alginate onto the surface of corneal materials.

Figure 5.6 illustrates the fingerprint region of the spectra shown in Fig.5.5. To determine if the spectral differences at 1036 cm^{-1} were associated with alginate, spectrum of 5% alginate-grafted (a), and 1% alginate-grafted (b), were compared to the ones for untreated (c), NH$_3$-plasma treated (d), and pure alginate (e). It was obvious that the peak intensities at 1036 cm^{-1} for alginate-grafted materials were much higher than those for untreated (c) and plasma treated (d) materials and very similar to the peak for pure alginate. It was also observed that the peak intensity for the material grafted with 5% alginate was more pronounced compared to the one grafted with 1% alginate confirming the effect of concentration on the peak intensity.
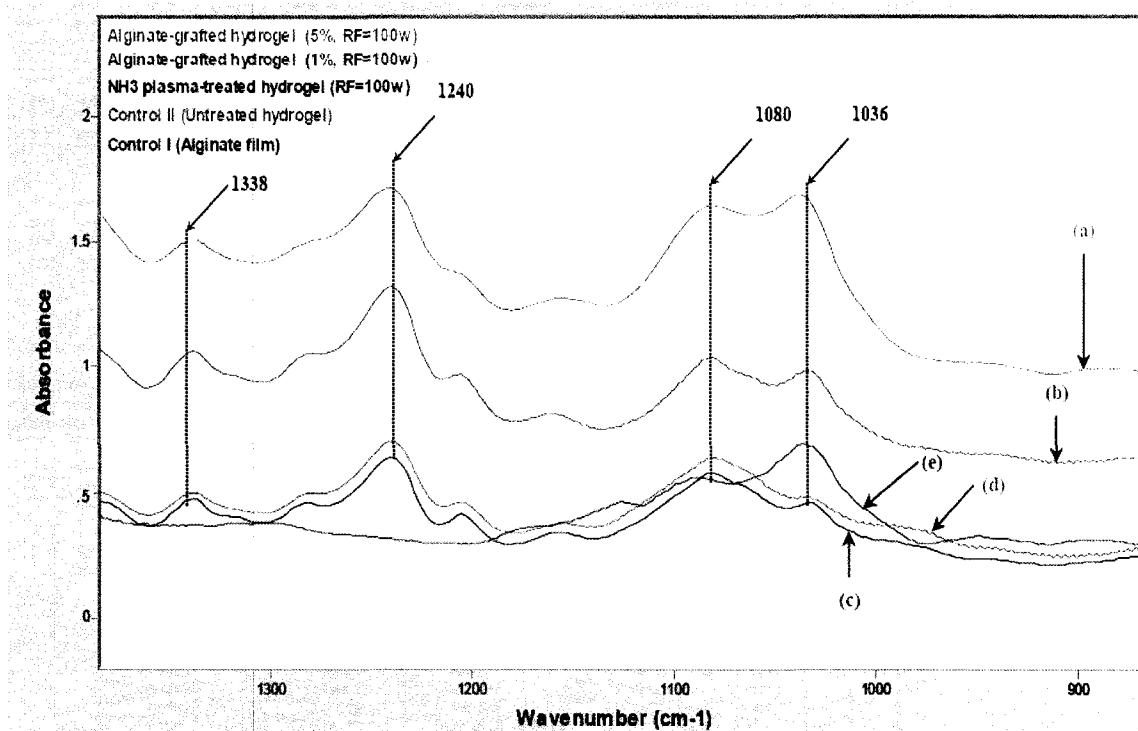
Figure 5.6 Fingerprint region of FTIR spectra of cross-linked collagen/chitosan films
That were (a) 5% alginate-grafted, (b) 1% alginate- grafted, (c) 100 W
NH_3-plasma treated, (d) untreated, and (e) the spectrum for pure alginate
film.

To quantify and statistically analyze FTIR results, the peak absorbance values at

1036 cm^{-1} were plotted for all treated and untreated materials in Fig.5.7. The surfaces

treated with alginate at a concentration of 5% appeared to have the highest intensity

especially for material B. These results confirm that alginate grafting density is directly

proportional to RF power, and alginate concentration in the range of treatment. The FTIR

results were also subjected to ANOVA. Details of ANOVA (P-value and F-values) for

FTIR absorption intensity at 1036 cm^{-1} are summarized in Table 5.2.

Large value of r^2 (97.5 %) for FTIR implies that the model is capable of providing

good predictions. Using the values in the "P" and "F" columns of Table 5.2, we can

determine that all of the effects are significant with the exception of three-way effect

"$X_1*X_2*X_3$" , that is, its P-value larger than 0.05 (P=0.082) and its F-value is close to 1

(F=2.3). Therefore, the main effects for substrate material, RF power, and alginate

concentration, and all two-way interaction effects are significant; that is, their P-values

are less than 0.05.
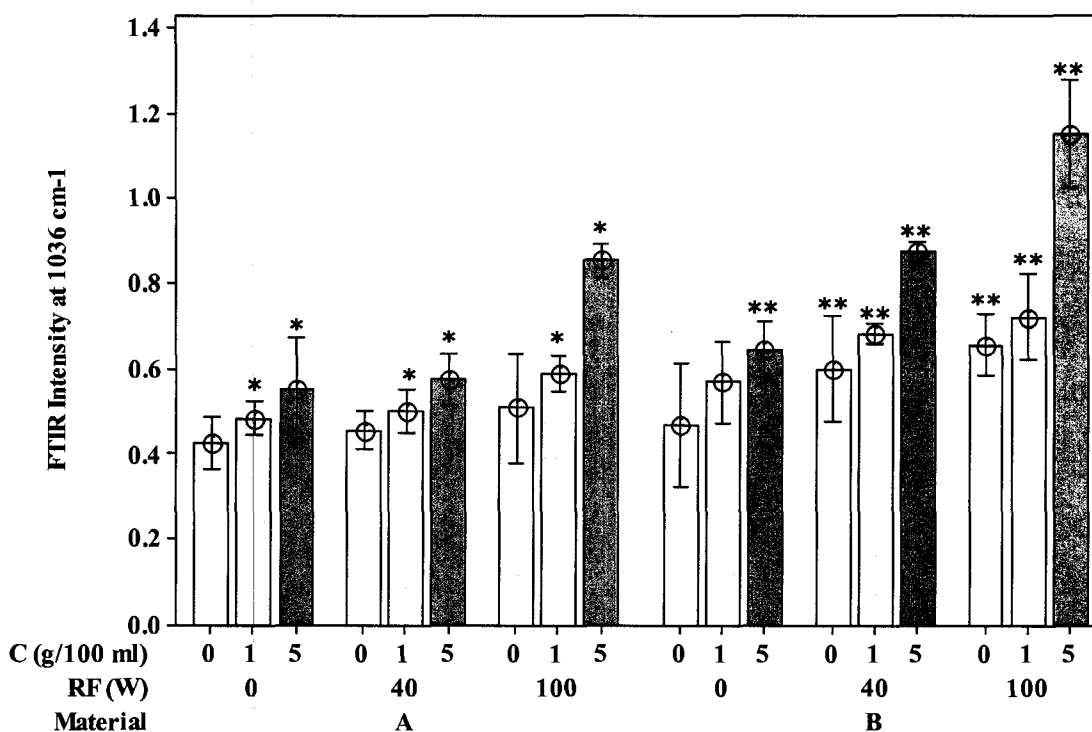
Figure 5.7   Interval plot of FTIR peak absorbance values at 1036 cm^{-1} for all treated
and untreated materials vs. substrate material, RF power, and alginate
concentration. Control unmodified surfaces are denoted by RF power and
alginate concentration of zero for material groups A (i.e., A-0-0) and B
(i.e., B-0-0). The variation of group means is represented by 95%
confidence interval.

*   denotes significant difference from unmodified material A using ANOVA ($p \leq 0.05$).
** denotes significant difference from unmodified material B using ANOVA ($p \leq 0.05$).

5.5.5   Human corneal endothelial cells attachment

The results obtained from endothelial cell growth study showed that alginate

surface grafting generally decreased endothelial cell adhesion to the posterior surfaces of

the hydrogels. Figure 5.8 shows microscopic images of the endothelial cells on the

posterior surfaces of treated and untreated collagen/chitosan hydrogels (material B) on

day 5 post-seeding.
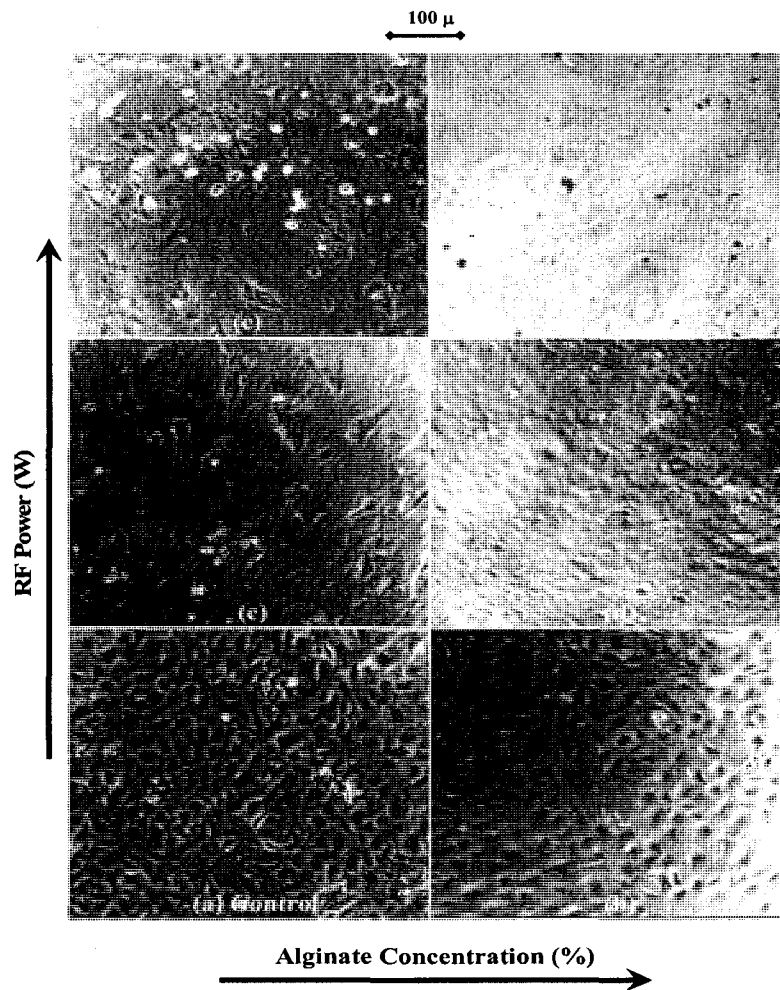
Figure 5.8 Microscopic images of the endothelial cells on the posterior surfaces of treated and untreated corneal materials (material B) on day 5 post seeding: (a) Untreated control [RF=0 W, Alg.=0%], (b) Non-plasma alginate-grafted [RF=0 W, Alg.= 5 %], (c) Plasma-assisted alginate-grafted [RF=40 W, Alg.=1%], (d) Plasma-assisted alginate-grafted [RF=40 W, Alg.= 5%], (e) Plasma-assisted alginate-grafted [RF=100 W, Alg.=1 %], (f) Plasma-assisted alginate-grafted [RF=100 W, Alg.=5 %].

The cell deterrence was observed for plasma-assisted alginate-grafted surfaces (Fig.5.8c to Fig.5.8f) while cells were attached and spread onto the untreated control

surfaces (Fig.5.8a), and non-plasma alginate-grafted surfaces (Fig.5.8b). We also found that among plasma-assisted alginate-grafted surfaces, the decrease in the endothelial cells adhesion was more pronounced at an RF power of 100 W and alginate concentration of 5% (Fig.5.8f). This phenomenon is likely associated with the higher grafting density of alginate onto the surfaces of the materials.

Figure 5.9 is an interval plot that depicts the variation of group means by plotting confidence intervals and shows the number of endothelial cells attached to the posterior surfaces of corneal materials on day five post-seeding as a function of substrate material, plasma RF power, and alginate solution concentration. Comparing the data at various alginate concentrations, inhibition of cell adhesion increased by increasing alginate concentration. However, the impact of alginate concentration was less pronounced in the absence of plasma treatment. Looking at the data for zero % alginate in Fig.5.9, we notice that the values for NH_3 plasma-treated surfaces do not significantly differ from those of control surfaces ($p \geq 0.05$). This means that NH_3 plasma treatment alone did not deter cells in the absence of alginate.

The cell count data was statistically analyzed by ANOVA and summarized in Table 5.2. Large value of r^2 (98.9 %) for cell count in Table 5.2 implies that the model is capable of providing good predictions. Using the low values in the "P" column for cell count in that table, we can claim that all of the effects including the main effects for substrate material, RF power, and alginate concentration, and all two-way interaction effects are significant ($P < 0.05$) with the exception of three-way effect "$X_1*X_2*X_3$" ($P = 0.296 > 0.05$). The values in the "F" column suggest that alginate concentration has the

highest influence on the deterrence of epithelial cells followed by plasma power, and

substrate material ($F_{X3} > F_{X2} > F_{X1}$).
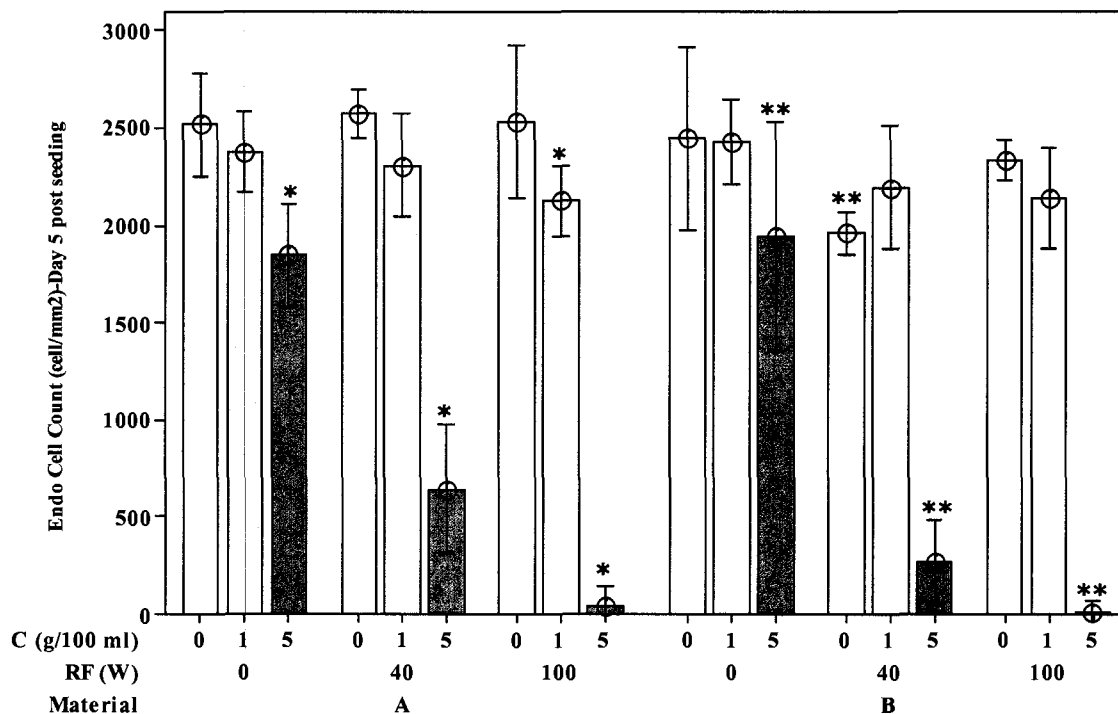
Figure 5.9   Interval plot of endothelial cell count on corneal materials as a function of
substrate material, RF plasma power (W), and alginate concentration
(g/100ml). Control unmodified surfaces are denoted by RF power and
alginate concentration of zero for material groups A (i.e., A-0-0) and B
(i.e., B-0-0). The variation of group means is represented by 95%
confidence interval.

*   denotes significant difference from unmodified material A using ANOVA ($p \leq 0.05$).
** denotes significant difference from unmodified material B using ANOVA ($p \leq 0.05$).

We also studied the interaction effects among factors to determine the impact that

changing the settings of one factor had on another. For example, the impact of substrate

material on cells inhibition at various RF power (X_1*X_2 Binteraction) has been shown in

Fig.5.9 and Table 5.2. The interaction between substrate material and RF power was

found to be significant ($P_{X1*X2} \ll 0.05$ and $F_{X1*X2} = 14.8 > 1$).

As detailed in Table 5.2, the interaction between substrate material and alginate concentration is not as significant as the interaction between substrate material and RF power ($P_{X1*X3} > P_{X1*X2}$) that is also confirmed by "F-values" ($F_{X1*X3} < F_{X1*X2}$). The interaction between RF power and alginate concentration ($X_{2B}*X_3$) is the most significant one because of the highest "F-value" ($F_{X2*X3} > F_{X1*X2} > F_{X1*X3}$). This explains the synergic effect of RF power and alginate concentration on endothelial cell inhibition meaning that their combined effects were greater than the sum of their individual effects. In summary, despite general inhibition of endothelial cell growth observed for all of the alginate-grafted surfaces, the surfaces treated using plasma-assisted alginate grafting at a plasma power of 100 W and alginate concentration of 5% appeared to significantly inhibit endothelial cell growth by 99% for both materials A and B. Plasma power of 40 W and alginate concentration of 5% appeared to deter endothelial cell growth by about 75% for material A and 89% for material B.

5.6   Discussion

This work is the first report on the use of alginate grafting for the inhibition of corneal endothelial cell attachment onto the surfaces of implantable corneal substitutes. The unique biological and physical properties of alginate make it an excellent candidate for surface modification of artificial cornea to deter endothelial cell attachment. Alginate is a non-cytotoxic natural polymer and its lack of cell-binding receptors is accountable for its anti-cell adhesion properties, while some synthetic polymers such as PHEMA and its co-polymers, which have been widely used for creating cell-deterring surfaces, have shown mild to moderate cytotoxicity [26].

We have also demonstrated that alginate surface grafting did not have any adverse effect on water content and optical transparency of the implants. For corneal application, this may be another advantage of alginate over PEO or PHEMA, which may produce opaque films or gels under certain conditions [27, 28]. In addition, it confirms that alginate is likely grafted to the surface only and the cell-resistant molecules did not change the bulk properties of the corneal materials.

By comparing the contact angle data in Fig.5.4 and cell inhibition results in Fig. 5.9, we demonstrated that the sample with the lowest contact angle showed the highest cell resistance while for the rest of the samples no strong correlation was found between resistance to cell adhesion and surface hydrophilicity. This finding is consistent with that of Morra et al. [14] who suggested the inadequacy of simple relationships between wettability by water and cell adhesion reported in some published studies [29-36]. As illustrated in Fig.5.4, the contact angle decreased with the increase in alginate concentration and RF power for most cases.

The FTIR results in Figs 5.5 to 5.7, suggest that it is easy to control or achieve a high density of alginate at the surface of corneal materials by increasing the alginate concentration in the grafting solution as well as RF power. This phenomenon is likely attributed to the fact that alginate has a linear un-branched structure [36] and can be attached to substrate at multiple points contrary to PEO moieties that are terminally attached to the substrate surface [14]. This property makes alginate surface grafting less complicated than PEO grafting in which a high density of end-point-attached, freely fluctuating PEO chains is hard to achieve by RF methods. It is known that for PEO-

immobilized surfaces, it is mostly the steric effect of freely fluctuating PEO chains that is accountable for its cell inhibiting properties [28].

Another important finding is that the higher the RF power and alginate concentration the higher is the FTIR intensity for the peak at 1036 cm^{-1} that is attributed to O-H bending of alginate (Fig.5.6). This is likely due to higher grafting density of alginate. As summarized in Table 2.2, ANOVA analysis enabled us to determine the influence of each factor on FTIR spectrum. The values in the "F" column suggest that substrate material has the highest influence on FTIR intensity followed by alginate concentration and plasma power ($F_{X1} > F_{X3} > F_{X2}$). However, low variation in F-values for three factors indicate that none of the impacts was dominant as opposed to the results for cells attachment for which alginate concentration and RF power were more influential than substrate material. Also, the order of F-values for FTIR results were different than the ones for epithelial cells attachment ($F_{X3} > F_{X2} > F_{X1}$).

The above discrepancies may be explained by the strength and density of alginate grafted to the surfaces. It is possible that at low settings of RF power and alginate concentration, alginate molecules were loosely linked to the surface at a low grafting density. When these loosely grafted molecules were exposed to the biological environment of cell culture medium (higher temperature, presence of proteins, enzymes, and so on), detachment of alginate molecules from the surface allowed cells to grow back onto the surfaces in a few days post-seeding. As for high settings for RF power and alginate concentration, which resulted in higher and stronger bonding between alginate and substrate, alginate molecules did not detach from the substrate and remained intact. This phenomenon resulted in a very significant difference between number of cells

attached to substrate materials that were alginate-grafted at high settings (i.e. 100 W and 5% concentration) compared to those grafted at lower setting values. As shown in Table 5.2, F-value for alginate concentration for cell count ($F_{X3}=1114.6$) was much higher than the value for FTIR intensity ($F_{X3}=266$). In the case of FTIR results, this high level of significance was not observed. This phenomenon was likely due to the fact that none of the surfaces was exposed to biological environments in which loosely grafted alginate molecules could detach from the surfaces of the materials. Therefore, most of the loosely-attached alginate molecules remained on the surface and detected by FTIR leading to less variation in their FTIR intensity.

In addition to the significant effects of alginate concentration and RF power on the inhibition of the endothelial cells demonstrated in Table 2.2, it is clear that substrate material has a considerable impact on cell adhesion. For instance, substrate material B deters cells to a higher extent compared to material A when both surfaces were plasma treated at 40 W. In material B, the amine groups were provided mostly from chitosan since each mole of chitosan has about 22 times more amine groups than collagen, while there was no chitosan in material A. When the RF power was low at 40 W, the plasma treatment did not create as many additional amine groups as when the RF power was 100 W. Hence material B would have substantially more amine groups than material A, even when the plasma treatment was applied. When the RF power is increased to 100W, a large number of amine groups are generated, the number of which surpasses those of amine groups provided from chitosan. Hence the difference between material A and material B will disappear. This phenomenon may be the reason for the observation of stronger substrate effect at the RF power of 40W.

The current study confirms the cell deterring characteristics of alginate as demonstrated in Fig.5.8, and Fig.5.9. These results are in good agreement with the results for CAM and FTIR. The higher the alginate concentration and RF power resulted in higher degree of alginate grafting, more hydrophilic surface, higher FTIR peak intensity, and consequently achieving synergy toward endothelial cell inhibition. However, there are major challenges that still need to be addressed in the near future, such as the interaction of modified corneal implants with *in vivo* biological environments. In addition, more studies are needed to determine if the alginate surface treatment is stable *in vivo* and the effects of treatment do not disappear in the long term.

5.7   Conclusions

We have shown that plasma-assisted alginate grafting is an effective technique for selective creation of anti-cell adhesion surfaces. The anti-adhesive properties achieved were dependent upon nature of the substrate hydrogel, plasma RF power, and alginate solution concentration. High concentrations of alginate 5% (w/v) and high RF power of 100 W produced surfaces with minimal cell attachment in this study. This technique may be useful in future applications such as the modification of biomaterials used for transplantation where anti-cell adhesive or anti-fouling properties are required. More specifically, the following conclusions could be drawn from this work:

1.   Surface modification did not significantly change water content and optical properties of corneal materials. This is most likely attributed to the fact that surface treatment was limited only to the surface and did not have impact on bulk properties.

2. The higher the RF power the lower was the contact angle for most of the materials. For example, the contact angle decreased from 52 ± 1.5 to 34 ± 2 degree for substrate material A, by increasing the RF power from 0 to 100 W.

3. The presence of alginate molecules on the surface of corneal materials was confirmed by FTIR.

4. The FTIR peak intensities at 1036 cm^{-1} for alginate-grafted materials were much higher than those for untreated and plasma treated materials and very similar to the peak for pure alginate film.

5. The higher the alginate concentration the higher was the FTIR peak intensity at 1036cm^{-1}.

6. Endothelial cells inhibition was the most effective at the highest plasma RF power (e.g., 100 W) and the highest alginate concentration (e.g., 5% w/v).

7. Corneal materials comprised of cross-linked collagen/chitosan, demonstrated better alginate grafting compared to cross-linked collagen without chitosan. As a result, the former material showed higher extent of endothelial cell deterrence.

Acknowledgements

5.8 References

1. Nishida T. Cornea. In: Krachmer JH, Mannis MJ, Holland EJ, editors. Cornea. Philadelphia: Elsevier Mosby, 2005. p. 3- 26.

2. Liu Y, Gan L, Carlsson DJ, Fagerholm P, Lagali N, Watsky MA, Munger R, Hodge WJ, Priest D, Griffith M. A simple cross-linked collagen tissue substitute for corneal implantation. IOVS 2006; 47: 1869-1875.

3. Li F, Carlsson DJ, Lohmann C, Suuronen E, Vascotto S, Kobuch K, Sheardown H, Munger R, Nakamura M, Griffith M. Cellular and nerve regeneration within a biosynthetic ECM for corneal transplantation. Proc. Nat. Acad. Sci. USA 2003; 100: 15346-51.

4. Leung EW, Rife L, Smith RE, Kay EP, Extracellular matrix components in retrocorneal fibrous membrane in comparison to corneal endothelium and Descemet's membrane. Molecular Vision 2000; 6: 15-23.

5. Griffith M, Trinkaus-Randall V, Watsky MA, Liu CY, Sheardown H. Cornea. In: Methods of tissue engineering. New York: Academic Press, 2002. p.927-941.

6. Kremer I, Rapuano CJ, Cohen EJ, Laibson PR, Eagle RC. Retrocorneal fibrous membranes in failed corneal grafts. Am J Ophthalmol. 1993; 115(4):478-483.

7. Steel C, Corneal wound healing: a review. Optometry Today 1999; 28-32.

8. Ratner BD, Castner DG. Surface modification of polymeric biomaterials. New York: Plenum Press, 1997.

9. Schroder K, Meyer-Plath A, Keller D, Oh A. On the applicability of plasma assisted chemical micropatterning to different polymeric biomaterials. Plasmas and Polymers 2002; 7(2):103-125.

10. Morra M, Cassinelli C. Hydrophilic polysaccharides coatings. In: Morra M, editor. Water in biomaterials surface science. New York: John Wiley, 2001.

11. Brink C, Osterberg E, Holmberg K, Tiberg F. Using poly(ethylene imine) to graft poly(ethylene glycol) or polysaccharide to polystyrene. Colloids and Surfaces 1992; 66: 149-156.

12. Osterberg E, Bergstrom K, Holmberg K, Schuman TP, Riggs JA, Burns NL, Van Alstine JM, Harris JM. Protein-rejecting ability of surface-bound dextran in end-on and side-on configurations: comparison to PEG. J Biomed Mater Res 1995; 29: 741-747.

13. Elbert DL, Herbert CB, Hubbell JA. Thin polymer layers formed by polyelectrolyte multilayer techniques on biological surfaces. Langmuir 1999; 15: 5355 5362.

14. Morra M, Cassinelli C. Surface studies on a model cell-resistant system. Langmuir 1999; 15: 4658-4663.

15. Horbett TA, Klumb LA, Cell culturing: surface aspects and considerations. In: Brash JL, Wojciechowski PW, editors. Interfacial Phenomena and Bioproducts. New York: Marcel Dekker, 1996. p. 351-445.

16. Lydon MJ, Minett TW, Tighe BJ. Cellular interactions with synthetic polymer surfaces in culture. Biomaterials 1985; 6: 396-402.

17. Rollason G, Davies JE, Sefton MV. Preliminary report of cell culture on a thermally reversible copolymer. Biomaterials 1993; 14: 153-155.

18. Sheu MS, Hoffman AS, Ratner BD, Feijen J, Harris JM. Immobilization of polyethylene oxide surfactants for non-fouling biomaterial surfaces using an argon glow discharge treatment. J Adhesion Sci Technol 1993; 7 (10): 1065-1076.

19. Bouhadir KH, Mooney DJ. Synthesis of hydrogels: alginate hydrogels. In: Atala A, Polanza R, editors. Methods of tissue engineering. New York: Academic Press, 2002. p.653-662.

20. Chaplin M, Online: Alginate, October 25, 2005, Accessed on April 2, 2006, Available: http://www.lsbu.ac.uk/water/hyalg.html.

21. Damink LHO, Dijkstra PJ, Van Luyn MJ, Van Wachem PB, Nieuwenhuis P, Feijen J. Cross-linking of dermal sheep collagen using a water-soluble carbodiimide. Biomaerials 1996; 17: 765–773.

22. Priest D, Munger R. A new instrument for monitoring the optical properties of corneas. Invest Ophthalmol Vis Sci 1998; 39: 352.

23. Griffith M, Osborne R, Munger R, Xiong X, Doillon CJ, Laycock NLC, Hakim M, Song Y, Watsky MA. Functional human corneal equivalents constructed from cell lines. Science 1999; 286: 2169-2172.

24. Lin-Vien D, Colthup NB, Fateley WG, Grasselli JG. The handbook of infrared and characteristic frequencies of organic molecules. Boston: Academic Press, Inc., 1991.

25. Stuart B, Infrared spectroscopy: fundamentals and applications. West Sussex, England: John Wiley & Sons Ltd, 2004.

26. Prasitsilp M, Siriwittayakorn T, Molloy R, Suebsanit N, Siriwittayakorn P, Veeranondha S. Cytotoxicity study of homopolymers and copolymers of 2-hydroxyethyl methacrylate and some alkyl acrylates for potential use as temporary skin substitutes. J Mater Sci Mater Med 2003; 14: 595-600.

27. Lou X, Dalton PD, Chirila TV. Hydrophilic sponges based on 2-hydroxyethyl methacrylate. Part VII: Modulation of sponge characteristics by changes in reactivity and hydrophilicity of crosslinking agents. J Mater Sci Mater Med 2000; 11: 319-325.

28. Desai NP, Hubbell JA, Biological responses to polyethylene oxide modified polyethylene terephthalate surfaces. J Biomed Mater Res 1991; 25: 829-843.

29. Morra M, Cassinelli C. Simple model for the XPS analysis of polysaccharide-coated surfaces. Surface Interface Anal 1998; 26: 742 - 747.

30. Refojo MF. Ophthalmologic applications. In: Ratner BD, Hoffman AS, Schoen FJ, Lemons JE, editors. Biomaterials science: an introduction to materials in medicine. San Diego: Academic Press, 1996. p.328-335.

31. Hom MM, Bennett ES. Manual of contact lens prescribing and fitting. Newton, MA: Butterworth-Heinemann, 1997.

32. Bourne WM, Cellular changes in transplanted human corneas. Cornea 2001; 20(6): 560–69.

33. Wenkel H, Calabrese S, Seitz B, Küchle M, Naumann GOH. Histopathologic evaluation of retrocorneal membranes in failed corneal grafts. Proceedings of T99P[thP] Annual Meeting of German Ophthalmological Society, Berlin, 2001.

34. Busscher HJ, Stokroos I, Golverdingen JG, Schakenraad JM. Adhesion and spreading of human fibroblast on superhydrophobic FEP-Teflon. Cells Mater 1991; 1: 243-249.

35. Altankov G, Groth T. Fibronectin matrix formation by human fibroblasts on surfaces varying in wettability. J Biomater Sci Polym Edn 1997; 8: 299-310.

36. CyberColloids LTD Online: "Alginate", April 1, 2006, Available: http://www.cybercolloids.net/library/alginate/properties.php?printversion=yes

Chapter 6

General Discussions, Conclusions, and Recommendations

The primary goal of this thesis research was to develop bio-engineered materials with proper bulk and surface characteristics that meet the requirements of a transplantable artificial cornea. This research is an attempt to respond to the urgent need for corneal replacements, and the severe limitations of donor corneas and currently available synthetic artificial corneas. These limitations include the worldwide shortage of donor corneas, the increasing risk of transmissible diseases, the widespread use of corrective surgery that may render donor corneas unsuitable for grafting, and non-biocompatible nature of synthetic artificial corneas.

Despite the tremendous progress made in tissue engineering of the cornea in the last decade, we are still far from full understanding of the entire complexity of this system to predict the result of various factors on tissue formation and growth and try to emulate human corneal tissue. Although some success has been achieved with various tissues such as skin and cartilage, it is much more complicated when dealing with three dimensional corneal tissue. It is very challenging to develop scaffold materials that mimic extra-cellular matrix of the cornea because in addition to sufficient mechanical and biological properties, which are vital to the development of other types of tissues, optical transparency and extensive nerve innervations are necessary characteristics for a successful corneal tissue. To this effect, naturally derived biopolymers such as collagen, which constitutes more than 70% of the dry weight of the native cornea, play a significant role in developing such scaffolds.

To date, mechanical integrity and viscoelasticity of collagenous materials have not been sufficient for full thickness corneal implantation though attempts have been made to enhance these properties by synthetic supports. There are a multitude of factors at play that affect mechanical, biological, and optical properties of corneal materials such as chemical composition (e.g. molar ratios), physical and chemical properties of core materials (e.g. density of collagen solution) as well as those of stabilizers/additives (e.g. density of biomimetic macromolecules and cross-linking agents), and chemical reaction conditions (e.g. pH and temperature). In this research, I have tried to tackle some of the issues in tissue engineering of the cornea by developing multivariate strategies for bulk design and surface modification of corneal scaffolds. The material design and development strategies have been summarized under two main categories: bulk and surface strategies as follows.

6.1 Design and development of hybrid polymer networks (HPN) using multivariate experimental design (MED) methods.

The systematic experimental approaches of factorial design and response surface design provided good insights into the design of complex materials systems such as hybrid polymer networks (HPNs) and also made it possible to optimize the fabrication process of implantable materials that mimic human tissues such as cornea. These hybrid polymer networks are comprised of naturally derived materials such as collagen, and chitosan, as well as synthetic cross-linkers such as PEG-DBA and EDC/NHS.

The multivariate approach helped me to effectively determine the controlling factors, their interactions and their impacts on key physical and biological responses such as elastic modulus [EM], energy to break [ETB], optical light transmission [LT], and cell

growth [ECG]. More specifically, the results demonstrated that factors representative of materials' composition (e.g. chitosan to collagen molar ratio [CTN], EDC to collagen/chitosan molar ratio [EDC], and PEG to collagen/chitosan molar ratio [PEG]) had significant impacts on four responses. In addition, they suggested that there were no simple linear correlations between these factors and the responses were largely governed by interactions among factors. For example, higher levels of CTN, EDC, and PEG favored elastic modulus [EM] at low factor levels, while at high levels of factors a decreasing impact on EM was observed. The impacts of factors on energy to break [ETB] were similar to those of EM. As for light transmission, higher levels of chitosan had a significant decreasing impact on the transparency of the scaffolds. EDC ratio did not have a significant effect on LT on its own while its interaction terms with chitosan and PEG were significantly influential. PEG had a negative impact on light transmission when conjugated with EDC while it had an increasing impact in the absence of EDC. EDC and PEG had negative impacts on ECG while chitosan was not that influential.

Based on the above results, mathematical models were developed to help identify the shortest path toward the conditions for an optimum scaffold. As a result, it became possible to develop an optimum hybrid formulation (PN-10 or HPN-2) that satisfied the initial key requirements for a transplantable artificial cornea using a more accurate technique in a shorter time and at a lower cost compared to OFAT approach. The optimum formulation was further tested for physical properties (e.g. suturability, diffusivity, swelling, UV biodegradation, and FTIR) and biological properties both *in vitro* (e.g., HCEC cell growth, and DRG nerve innervation), and *in vivo* (rat subcutaneous and pig cornea implantations). Results suggested that optimum formulation was

optimally strong, elastic, bio-absorbable, and superior to human eye bank corneas in optical clarity and susceptibility to bacterial infection. It had excellent suturability, UV resistance, and biocompatibility. When implanted into pig corneas for 12 months, the optimum scaffold allowed seamless host-graft integration with successful regeneration of host corneal epithelium, stroma, and nerves. The implant gained back its optical transparency, which was affected by some early haze characteristic of stromal wound healing, by month six post-implantation. The techniques developed in this study may form a platform technology for development of implantable materials for other tissue and organ transplants such as skin, crystalline lens, liver, and heart.

Although the current findings add substantially to the understanding of the hybrid polymer networks for corneal applications, further studies are recommended to microscopically evaluate HPNs structures using scanning electron microscopy (SEM), XPS and atomic force microscopy (AFM). It is also recommended to further study the opacification process of the scaffolds by measuring lower critical solution temperature (LCST) or cloud point for each formulation. Measurement of the denaturing temperature (T_d) by differential scanning calorimetry is also suggested to better understand the degree of crosslinking of the scaffold materials.

It would be interesting to assess the effects of factors beyond the limits of this study using similar systematic approaches to determine the extent of experimental area over which these findings are valid and to explore the responses over a wider experimental range. It is also recommended that further research be undertaken to fabricate the optimum scaffold formulation using human recombinant collagen as base material instead of porcine collagen used in this study. This is to ensure that the base

material is free from prions and impurities that may originate from animal sources. The clinical trial would be the next step to assess the safety and effectiveness of the optimum corneal implant using lamellar or penetrating keratoplasty in subjects with keratoconus or blind eyes.

6.2 Engineering of anterior and posterior surfaces of corneal implants for controlled attachment of epithelial and endothelial cells, respectively.

The complete design of a full-thickness corneal graft includes not only the architecture of the bulk structure but also engineering of surfaces for proper interactions with corneal cells, for example, enhancing epithelial cells onto the anterior surface while deterring endothelial cells onto the posterior surface of an implant. This was achieved by implementing plasma or plasma-assisted surface modification techniques.

As for epithelial cells attachment, most of the corneal materials developed in this work were capable of supporting epithelial cells growth over their anterior surfaces except for the ones cross-linked with glutaraldehyde or glutaraldehyde-PEODA. To promote epithelial cells attachment onto these materials' surfaces, argon plasma modification was used. Results from the *in vitro* study indicated that attachment of epithelial cells was enhanced on the argon plasma modified surfaces. Surface roughness and hydrophilicity of argon plasma treated materials were found to be higher than those of untreated ones. It was found that the cell attachment to corneal surfaces was influenced by the combined effects of surface chemistry (i.e., surface energy), and polymer surface morphology (i.e., surface roughness). Further investigation and experimentation is recommended to determine *in vivo* performance of argon plasma surface-modified implants.

Prevention of endothelial cells migration onto the posterior surface of the implants was performed by subjecting the implant surface to ammonia plasma functionalization followed by grafting of alginate macromolecules to the target surface. A full factorial design was performed to investigate the impact of three factors including substrate material, plasma RF power, and alginate solution concentration on three responses including contact angle measurements (CAM), FTIR peak intensity, and endothelial cell count (ECC) of adhered cells to the hydrogel surfaces. Large values of coefficient of determination (r^2) for three factorial models developed for three responses implied that the models were capable of providing good predictions. It was also found that all three factors had significant impacts on CAM, FTIR, and ECC while they did not significantly affect water content and optical properties of corneal materials. This was likely attributed to the fact that surface treatment was limited only to the surface and did not have significant impact on bulk properties.

FTIR spectrum of modified and unmodified surfaces confirmed the presence of alginate molecules onto the modified surfaces. Factorial design made it possible to determine significant interaction effects among factors. I also found that among plasma-assisted alginate-grafted surfaces, the decrease in the endothelial cells adhesion was more pronounced at an RF power of 100 W and alginate concentration of 5% that was likely associated with the higher grafting density of alginate onto the implant surface. Another important finding was that the corneal materials comprised of cross-linked collagen/chitosan, demonstrated better alginate grafting compared to cross-linked collagen without chitosan. As a result, the former material showed higher extent of endothelial cell deterrence.

In summary, surface-treated materials showed observable decreases in endothelial cell attachment. The decrease in cell attachment and adhesion was dependant upon alginate concentration and RF plasma power. No further optimization process was necessary as the optimum desirable condition for endothelial cell deterrence was achieved at a 5% alginate and RF power of 100 W that was one of the factorial combinations. It is recommended that the interaction of alginate modified corneal implants be determined with *in vivo* biological environments. In addition, more studies are needed to confirm if the alginate surface treatment is stable *in vivo* and the effects of treatment will remain intact in the long term.

Chapter 7

APPENDICES
Appendix A:

7.1 Supplementary Material on Fabrication and Testing of Tissue-engineered Artificial Corneas

The following supplementary material is provided for better understanding of the fabrication, testing, and *in vivo* implantation processes of the tissue-engineered corneal materials developed in this study.
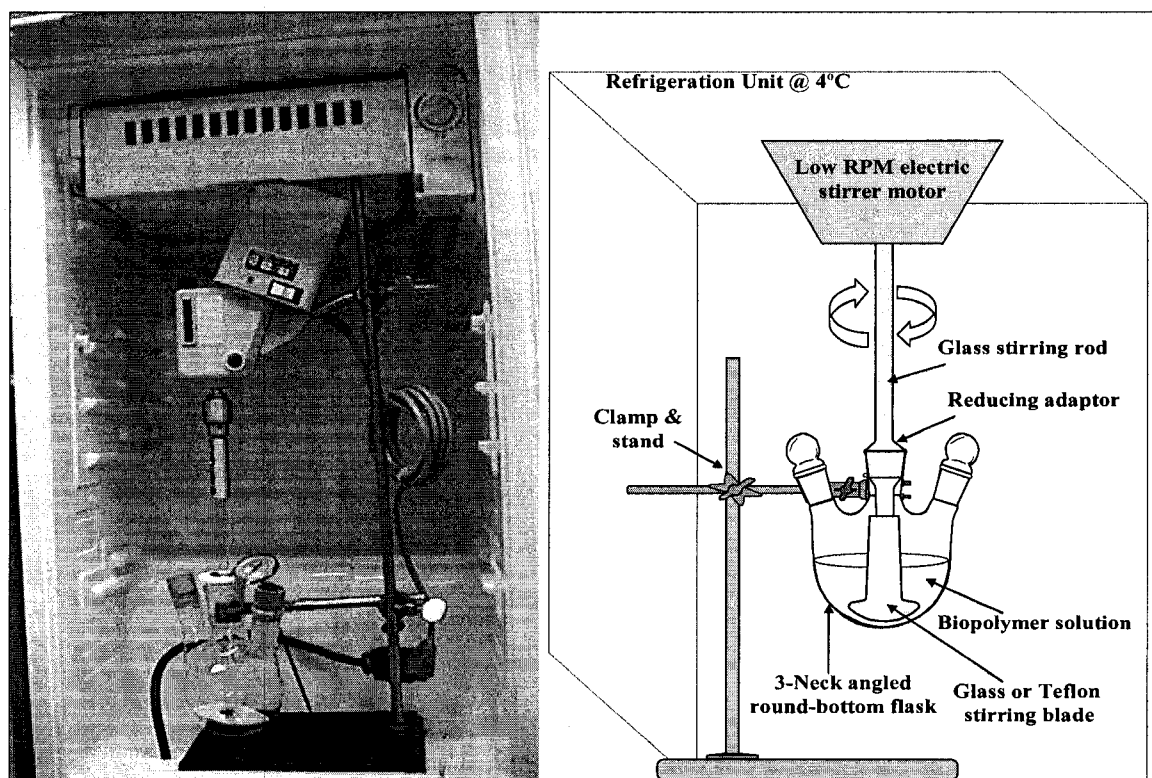
Figure A.1 Biopolymer solution preparation and mixing set up.

176

(1) Biopolymer solution stirring

(2) Transfer solution to 10 ml plastic syringes.

(3) Centrifuging biopolymer solution to get rid of trapped bubbles.

(4) Transfer solution from stock plastic syringe to glass dispensing syringe.
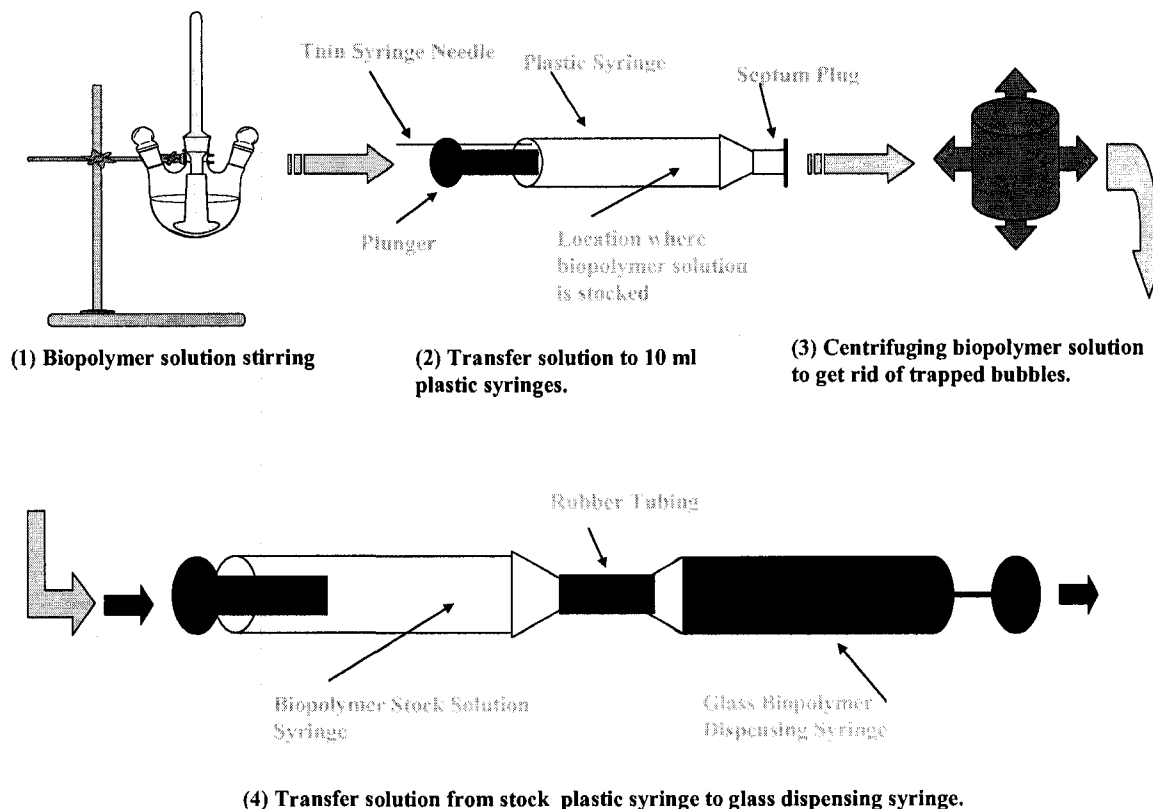
Figure A.2   Schematic of biopolymer solution handling process from initial mixing step to centrifuging, and eventually transferring to dispensing syringes prior to crosslinking reaction.

7.1.1   Fabrication of corneal implants:

A first syringe containing about 0.2 ml of buffer solution is connected to the T-connector (See Fig. A.3) to pump out trapped air in the connector. Biopolymer solution, i.e. collagen, chitosan, or both, placed into the second dispensing syringe, is coupled to the first buffer syringe through the T-connector. To adjust the pH, microliter quantities of NaOH solution can be injected through the septum in the connector followed by complete mixing affected by pumping the combined solutions between the two main syringes. Cross-linking solutions were then added sequentially using a Hamilton syringe via the septum, followed again by complete mixing. The whole process was performed under

iced water to prevent any immature gel formation before molding. The final mixture was then dispensed into the molds shown in Fig. A.4.
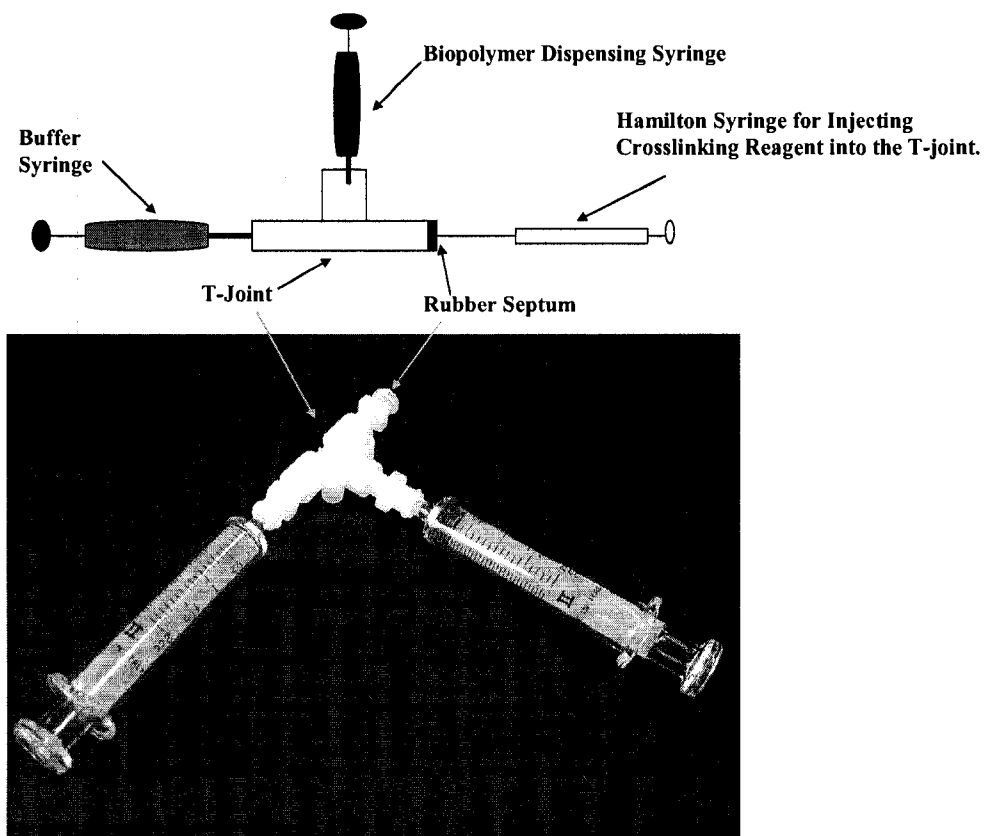
Figure A.3 Schematic of crosslinking reaction mixing system including Tefzel T-Piece assembly, 2ml Leur tip glass dispensing syringes, rubber septum, and 0.5 ml Hamilton syringe for injection of crosslinking solution.
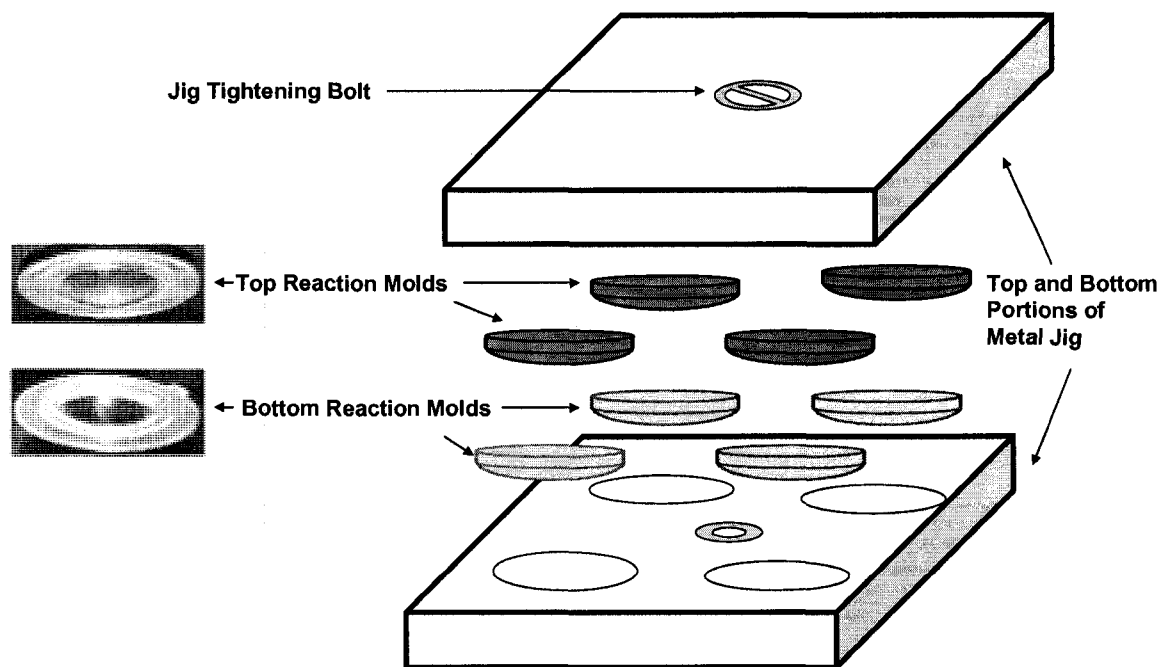
Figure A.4   Schematic of the hydrogels molding system including polypropylene reaction molds, and stainless steel jigs.

179
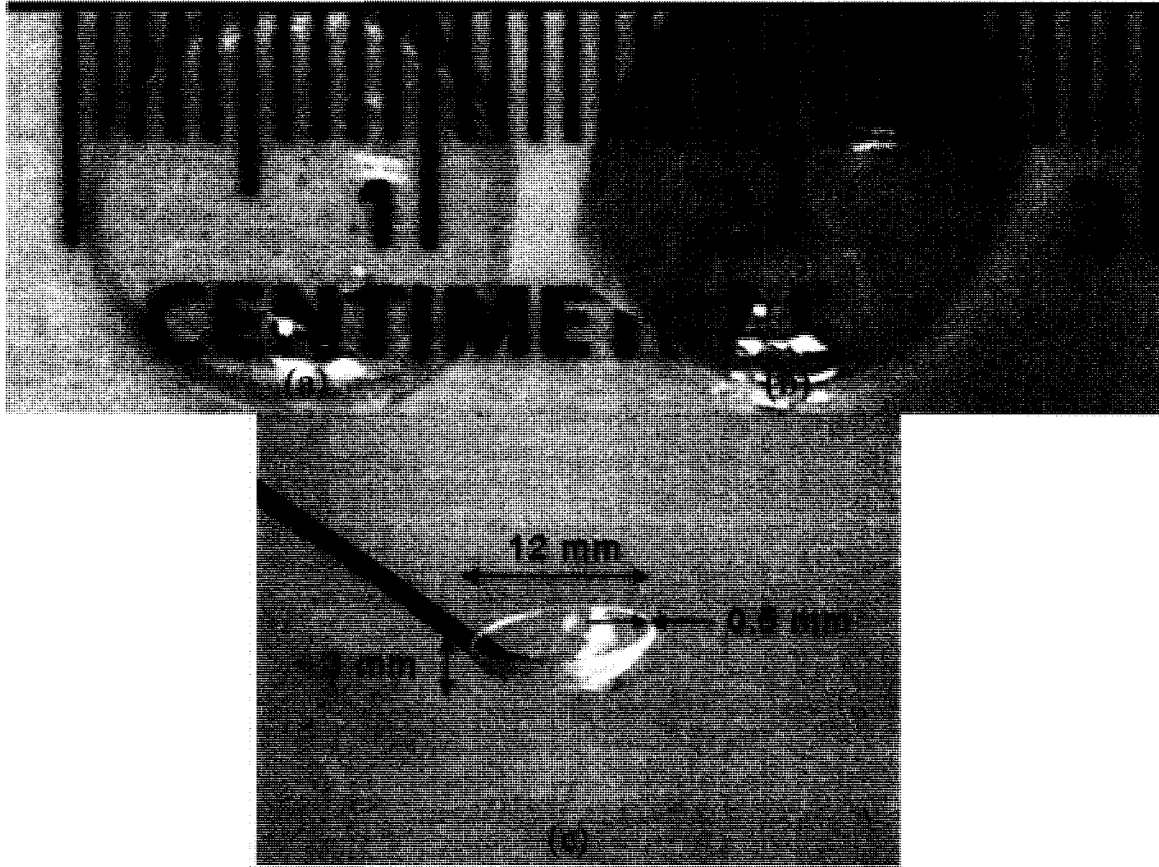
Figure A.5 Corneal implants: (a) tissue engineered corneal implant (HPN-2), (b) Eye bank human donor cornea, and (c) dimensions of a typical tissue engineered corneal implant.

Cloudy cornea

Corneal "button" removed

Graft   Sutures

1   2   3
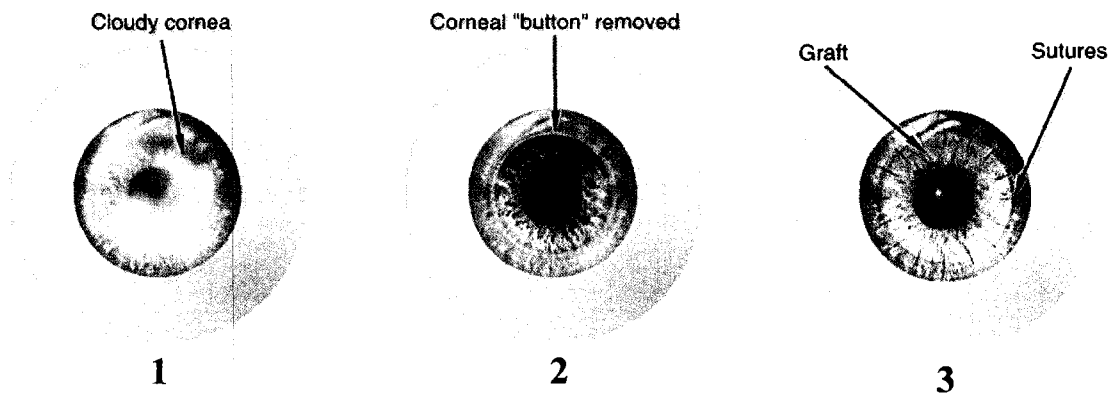
Figure A.6   Corneal replacement surgery (Penetrating or Lamellar Keratoplasty): (4) diseased and cloudy cornea, (2) removal of the central portion of the cloudy cornea, (3) replacement with a donor graft or an artificial cornea.

(A1) (A2) (A3)

(B1) (B2) (B3)
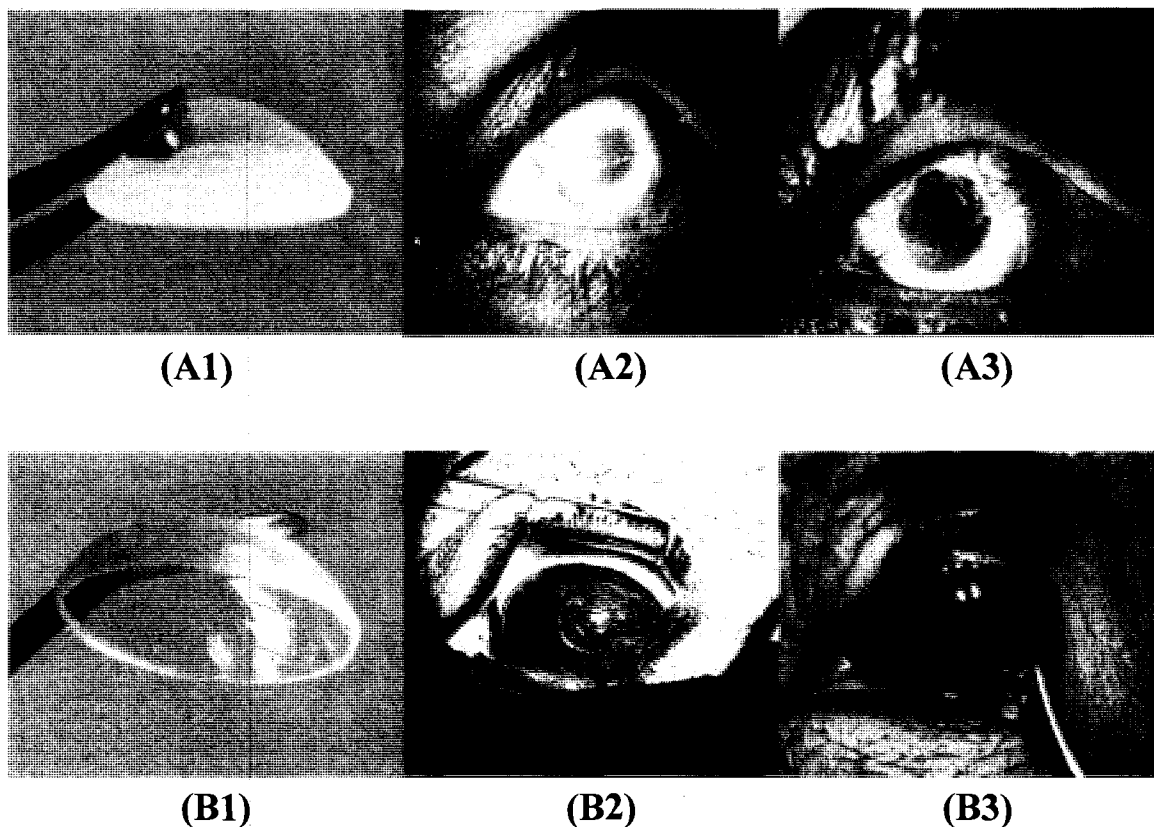
Figure A.7   *In-vivo* assessment of AlphaCor artificial cornea in a human model before implantation (A1), 2-month post operative follow-up (A2)[1], 6-month post operative follow-up (A3)[1], and that of HPN-2 tissue-engineered material in a pig model before implantation (B1), right after implantation (B2), and 2-month post operative follow-up (B3).

The AlphaCor™ device may provide a substitute for donor corneal tissue in desperate cases. However, it involves many post-surgical complications that make it less attractive than our tissue-engineered materials that integrate well into the host corneal rim by allowing re-growth of nerves and corneal cells resulting in regeneration and healing of the host cornea.

---

1. Bleckmann H, and Holak S. Preliminary results after implantation of four AlphaCor artificial corneas. Graefe's Arch Clin Exp Ophthalmol (2006) 244: 502–506

182
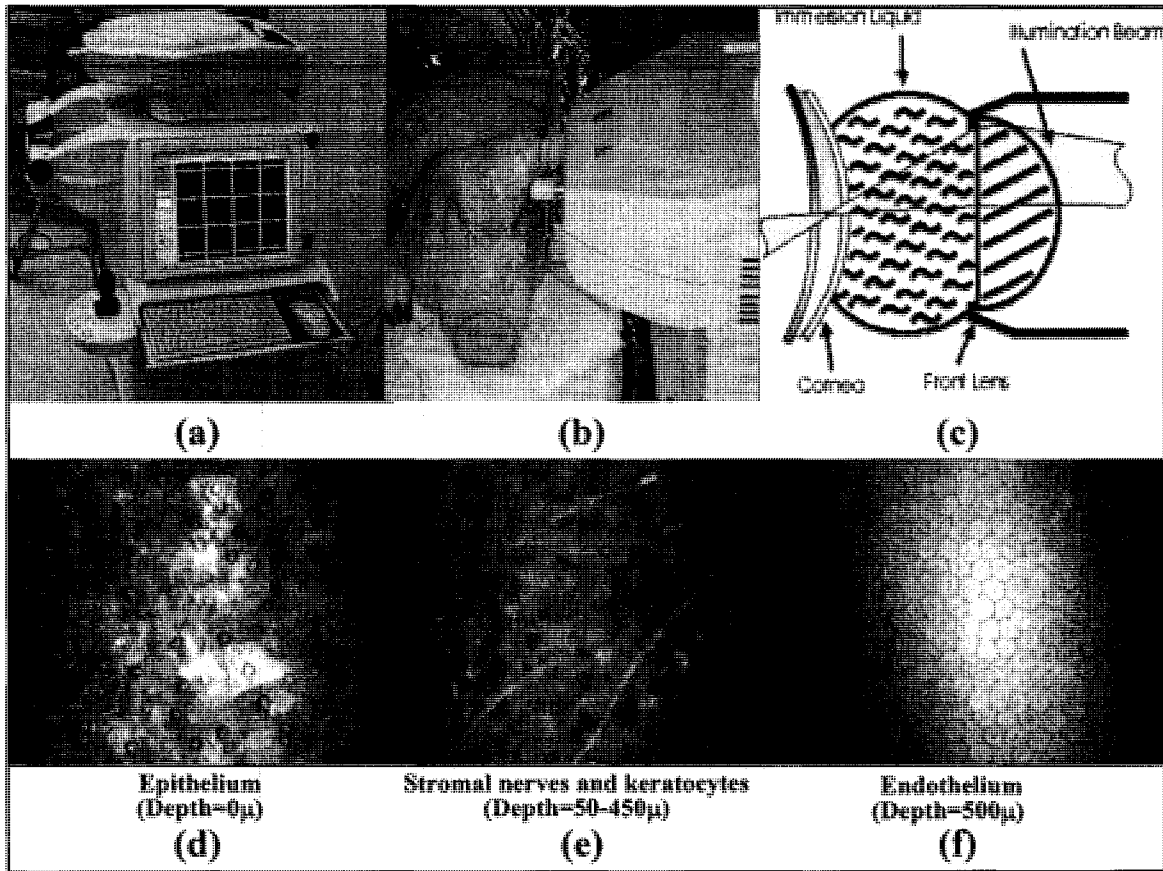
Figure A.8 In-Vivo Confocal Microscopy (IVCM) is a powerful non-invasive Technique for microscopic examination of living tissue: (a) In-vivo confocal microscope, (b) IVCM of pig's cornea, (c) IVCM capable of complete scan through the depth of the cornea and taking high-resolution images of all layers of the cornea. IVCM typical scans of HPN-2 tissue-engineered corneal material demonstrating cells and nerve branches at various depths of the regenerated cornea: (d) epithelial cells (D=0µm), (e) stromal nerves (D=50-450µm), and (f) endothelial cells (D=500µm).

7.1.2 FTIR Analysis of corneal materials

Figure A.9 shows the mid-infrared spectra (3800-800 cm^{-1}) of non-crosslinked collagen film. Each mid-infrared spectrum can be approximately divided into four regions and the nature of a group frequency may be determined by the region in which it is located.
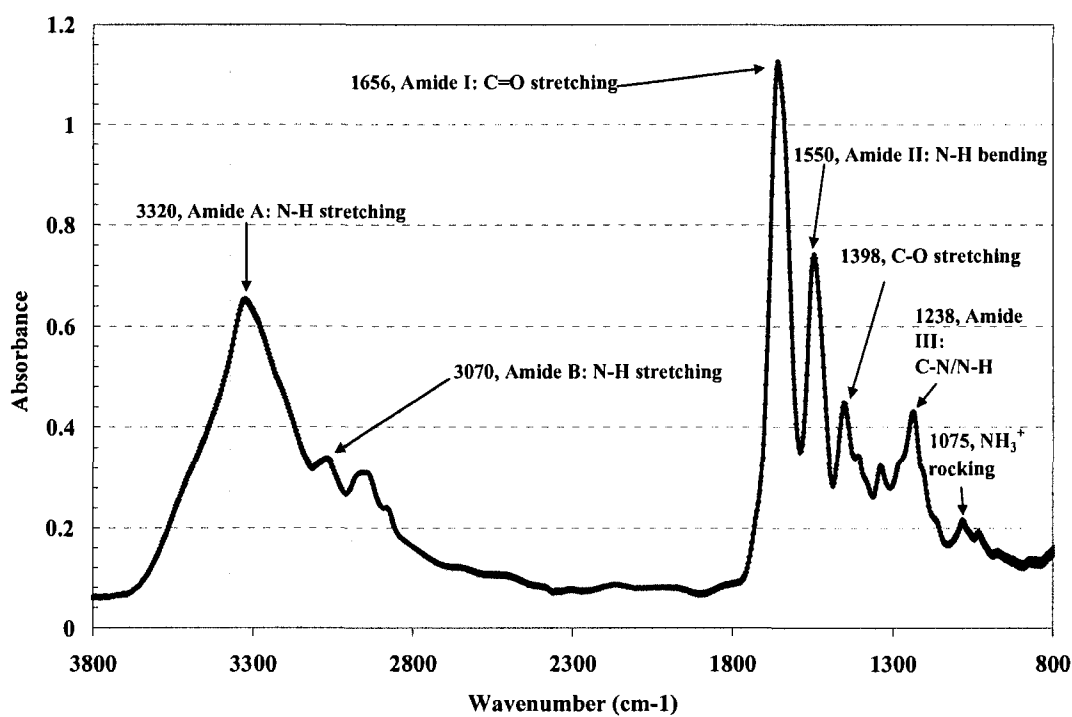
Figure A.9 Typical mid-infrared FTIR spectra of collagen.

For example, the vibrations in the 3800-2500 cm^{-1} region are generally due to O-H, C-H, and N-H stretching. The 2500-2000 region is called triple-bond region as most of the C≡C and C≡N triple bonds stretching fall in that region. The principal bands in the 2000-1500 cm^{-1} Pare due to C=O, and C=C stretching. The fourth region is from 1500-650 that is also called fingerprint region and is of great importance for identification of materials and their components. The absorption bands in this region are mostly due to

intra-molecular phenomena and are highly specific for each material while the absorption

bands in other regions are typically due to functional groups[1].

7.1.3 UV Photostability of the corneal materials.

To determine photostability of corneal materials, contact lens (CL), and human

cornea (HC) when exposed to sunlight-simulated UV irradiation a solar photoreactor and

a spectroradiometer were used. As shown in Fig. D1, the photoreactor utilizes a Xenon

lamp placed at the top of the photoreactor chamber. The solar simulation filters are

placed on a stand about 7 cm above the chamber floor, with samples beneath. The corneal

samples were placed in sterile PBS solution (pH 7.4, GIBCO) face up, during the

irradiation (See Fig. A.10).
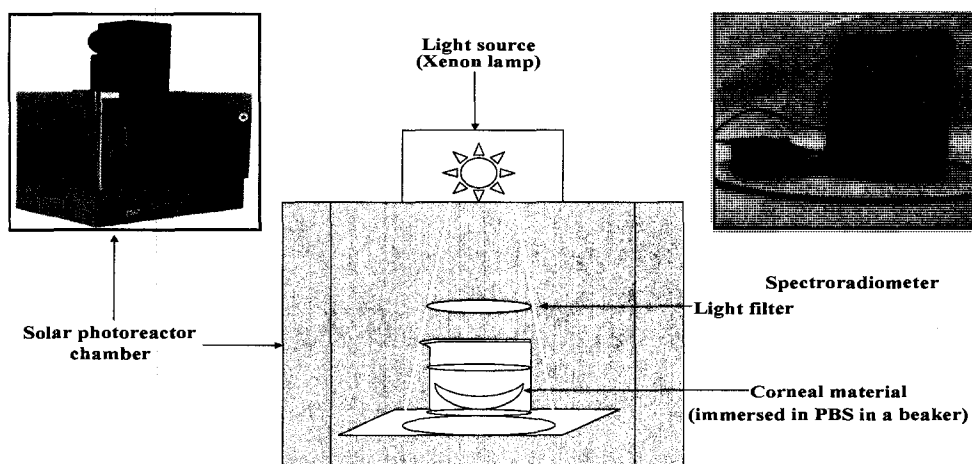
Figure A.10 Experimental set up for photostability testing of corneal materials: a solar
simulator consisting of a photoreactor (i.e., Luzchem Model LZC-SSR)
and a spectroradiometer[2].

----

1. Lin-Vien D, Colthup NB, Fateley WG, Grasselli JG. The handbook of infrared and characteristic
   frequencies of organic molecules. Boston: Academic Press, Inc., 1991.
2. Luzchem Solar Simulator, 2006, Available: http://luzchem.solsim.com/products/solar_sim.php

The photoreactor provides solar simulated radiation based on a powerful ceramic Xenon lamp. Enclosed in a standard photoreactor cabinet, the unit produces, under recommended illumination conditions, a circle of approximately 16 cm in diameter matching spectrally and approximately in intensity the AM1.5 solar spectrum.
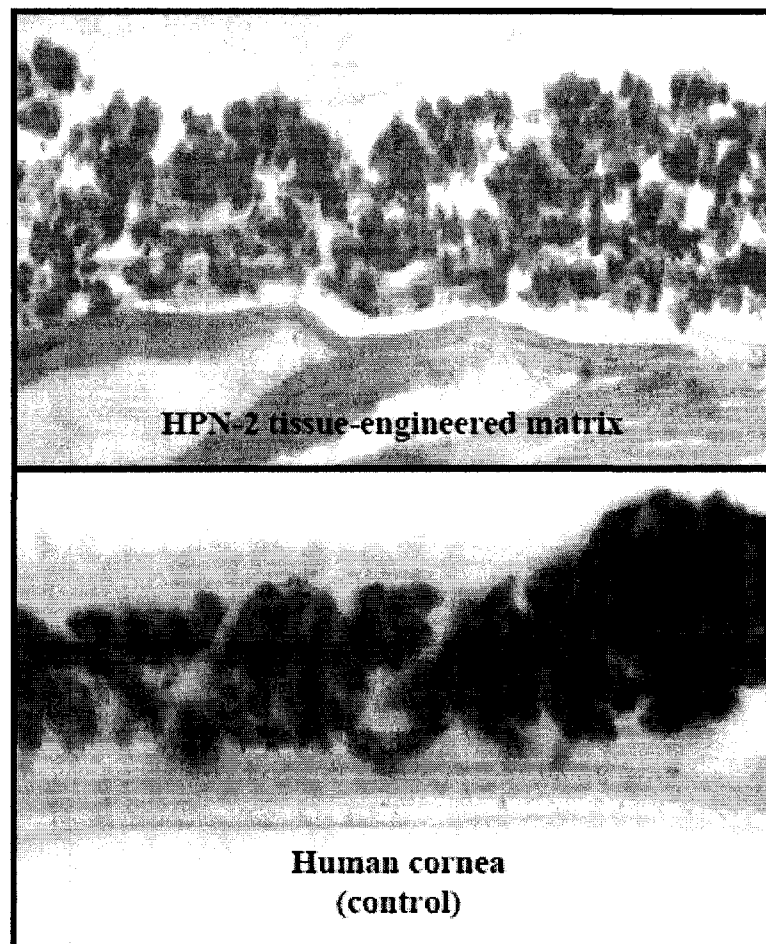
Figure A.11 Cross-sectional view of epithelial cells onto HPN-2 and human cornea after H&E staining on day 14 post-seeding. Almost similar epithelial cells stratification was observed on HPN-2 matrix and human cornea.

Appendix B:

7.2 Mechanical Tensile Testing and Differential Scanning Calorimetry

7.2.1 Development of a standard methodology for mechanical tensile testing of biological tissues and tissue-engineered materials.

Objectives:

To develop a standard tensile testing method that determines both structural properties (i.e. load and deformation) and materials' properties (i.e. stress, strain, and modulus) of biological tissues and tissue-engineered materials.

Need:

The past few decades have seen increasingly rapid advances in the field of mechanical testing of materials. However, most studies in the field have mostly been carried out in the area of synthetic and non-biological materials most likely due to the complexities involved with handling and testing of natural tissues. In addition, far too little attention has been paid to the geometry of the test specimen. Mechanical properties of a material vary with the geometry of the test specimen as well as its composition. It is, therefore, difficult to compare mechanical properties of different materials when the geometry of the material is not taken into consideration. It will also be challenging to predict the load-carrying capacities of structures with complex shapes for which geometry and size are not known.

Definitions:

Structural and material properties:

Structural properties refer to properties that change with the geometry and size of the test specimen (i.e. "load" and "deformation") while material properties refer to those

that are independent of the specimen's geometry and size (i.e. "stress" and "strain") as

shown in Fig. B.1. Important mechanical properties are summarized below:
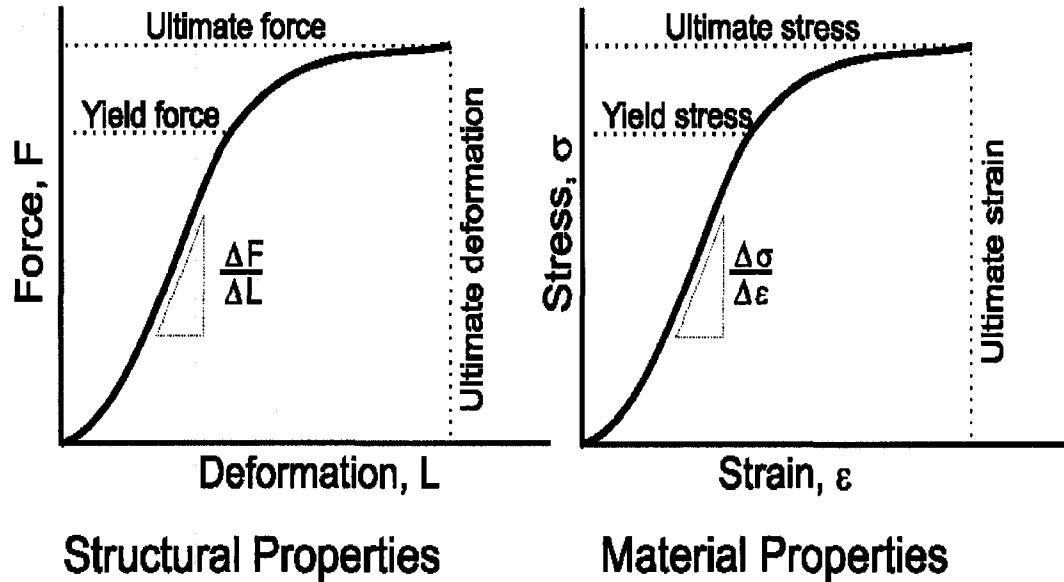
Figure B.1   Comparison between structural and material properties.

a) Load (F): A force to which materials are subjected to for deformation.

b) Deformation (Elongation, ΔL): The change in the length of a material subjected to a load.

c) Stress (σ =F/A): A normalized load or force accounting for differences in a specimen's size, but not the "quality" of the material. "A" is the cross-sectional area of the test specimen.

d) Strain (ε = ΔL/L₀): The amount of deformation that a material experiences normalized with respect to the original length of the specimen.

e) Ultimate Tensile Stress: Maximum stress that if exceeded the material will fail or break.

f) Ultimate Tensile Strain (Ultimate Elongation): Percent elongation that if exceeded the material will fail or break.

g) Elastic or Young's Modulus (E): The slope of the linear region of a stress-strain curve (See Fig.1). It is a measure of the *stiffness* of a material. The greater the modulus the higher is the stiffness.

h) Stiffness: Represents the materials ability to resist deformation. The larger the stiffness, the greater the force required to cause a given deformation.

i) Toughness or Resilience (T): The area under the force-deformation curve of a material taken to failure is a measure of the material's *toughness* (See Fig. B.1). It is also called *"energy to break"* as represents the energy (per unit volume) absorbed by the material until it breaks.

Methodology:

To resolve the problem, load and elongation can be normalized when divided by cross-sectional area and original length of the test specimen, respectively. A standard tensile test method was utilized along with a new method of sample mounting developed by the author to prevent breakage and slippage of the tissue-engineered corneas or natural tissue (Human corneas (HC) and pig corneas (PC) samples in the jaws.

The tensile strength, elongation at break (elasticity), elastic modulus (stiffness), and energy at break (toughness) of human and pig corneas were determined using an Instron Materials Testing System (model 5565) with a load cell of 500N capacity and pneumatic rubber faced grips (model 2712, jaw pressure 5 bar), at a crosshead speed of 10 mm/min and an initial grip separation of 13 mm. HC and PC that were equilibrated in Optisol corneal storage media were cut into dumb-bell shaped specimens of identical gage area (width 4 mm, gage lengths of 7 mm for HC and 10 mm for PC, and thickness

1.1 mm) with rectangular cross sections and two 3 mm end tabs as shown in Fig. B2. Each specimen was cut so that it included the central implant area to ensure that the central gauge length of each tensile sample contained the maximum area of the tissue or implanted gel.

To avoid breakage and slippage of the sample in the jaws, the 6 mm wide tabs on the end of each dumb bell sample were adhesive coated (using DERMABOND™, a fast curing, cyanoacrylate-based skin adhesive) and reinforced with tape on both sides. This method of sample mounting completely prevented jaw breaks. Samples were not stress preconditioned prior to testing to failure. Every recorded value is the average of three to five measurements. The same technique used for HC and PC was applied for mechanical testing of PBS equilibrated tissue-engineered corneal samples except for the specimen dimension that was 5 mm width, 5 mm gage length, and thickness 0.5 mm. In addition, tensile measurement was performed using an Instron Series IX Automated Materials Testing System with a low capacity load cell (10 N) at a crosshead speed of 10 mm/min and an initial grip separation of 6 mm.
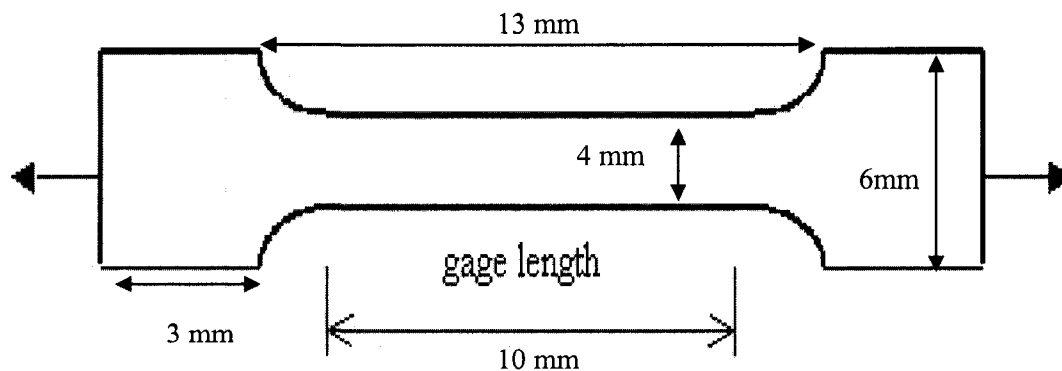
Figure B.2   Dumb-bell shape tensile specimen of pig cornea. The same shape specimen was used for human corneas and tissue-engineered corneas with different dimensions.

7.2.2 Mechanical tensile testing of pig corneas 12 months post surgery

Objectives:

To quantitatively evaluate mechanical properties of corneal lamellar implants compared to control eye corneas in pigs 10-12 months post surgery. Relative values of ultimate tensile strength, elongation, Young's modulus, and energy to break are determined.

Materials and Methods:

After 10 to 12 months post-surgery, corneas with tissue-engineered implants (two formulations) were harvested from pigs and cut into dumbbell shapes and tested for their mechanical properties according to the technique described above. The two tissue-engineered formulations consisted of non-hybrid formulation (NH-1), which was consisted of 10% collagen cross-linked with EDC/NHS, and hybrid formulation (HPN-2). Controls that consisted of unoperated contralateral corneas were also tested. The mechanical properties for each sample were calculated from the raw stress-strain data, using the Instron's Bluehill software, and the initial cross-sectional area. Elastic (tangent) moduli were calculated from the linear part of the stress/strain curves. Three replicates were used to determine the average and standard deviation of the data for all controls and NH-1 formulation while only one replicate was available for HPN-2 formulation.

Results and Discussions:

Tensile data showed that the corneas harvested from implanted eyes (both NH-1 and HPN-2 formulations) were similar to normal pig corneas in key mechanical properties. Typical stress vs. strain curves for corneas harvested from a non-operated eye and a HPN-2 implanted eye are demonstrated in Fig. B3 and Fig. B4, respectively.
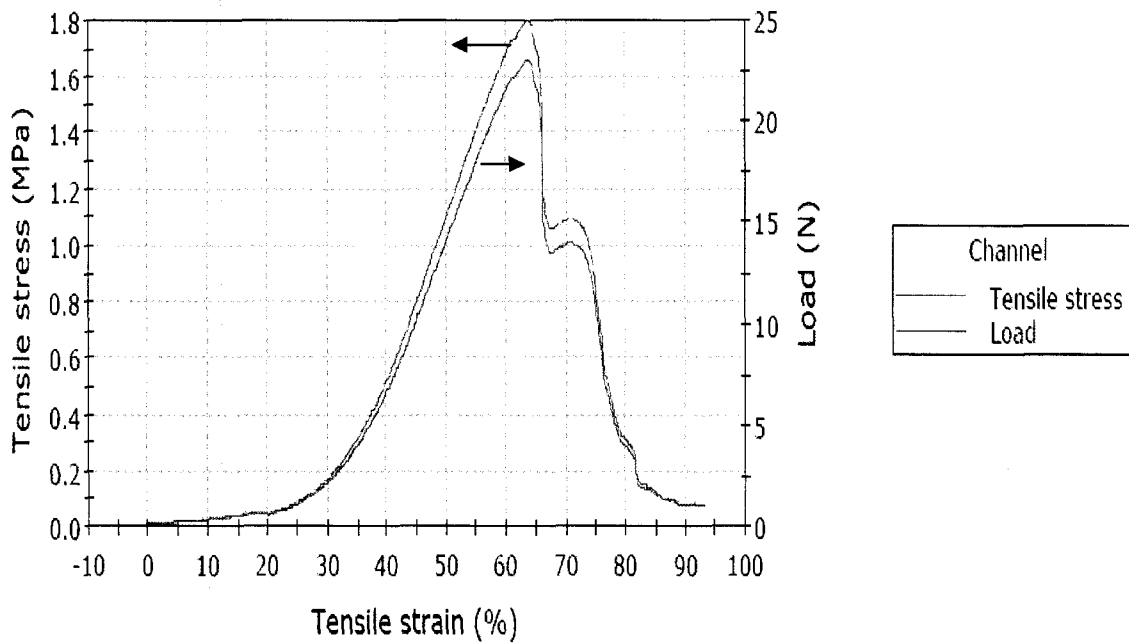
Figure B.3   Stress/Strain (Load/Deformation) curve for a typical pig cornea harvested from non-operated control eye.
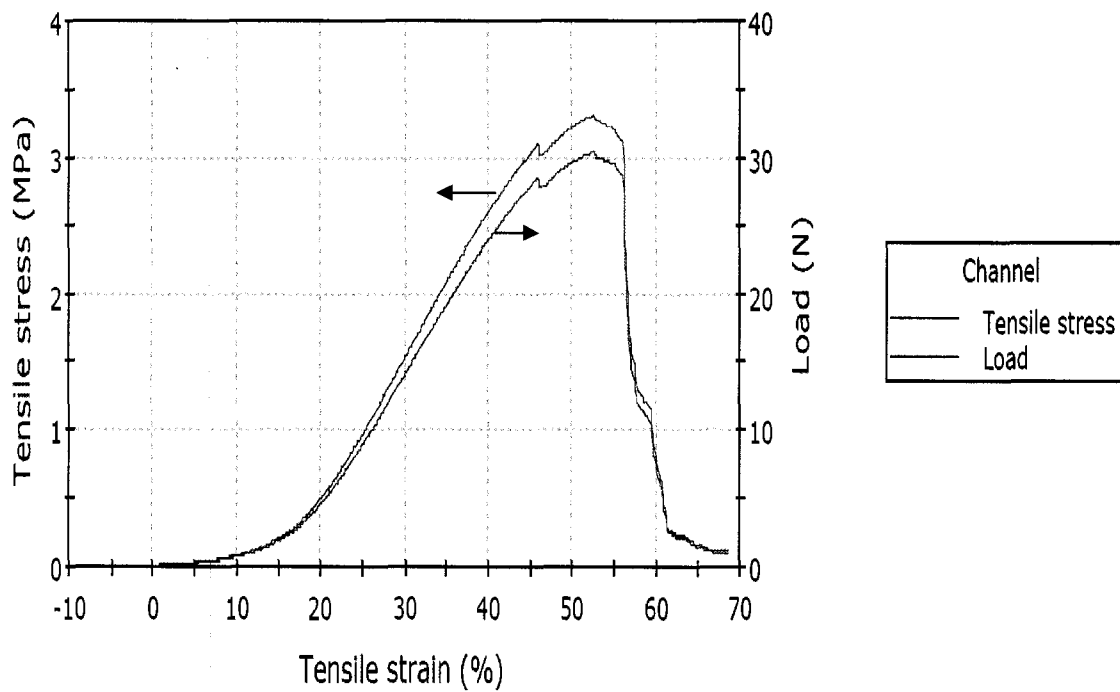
Figure B.4   Stress/Strain (Load/Deformation) curve for a typical pig cornea harvested from a HPN-2 implanted eye.

Some animal to animal variation is to be expected and was found between the tensile properties of control cornea samples harvested from pigs at 12 month post operation. Consequently, we believe that it is more statistically meaningful to compare the ratio of each specific tensile property of the cornea sample harvested from an implanted eye to that from the corresponding contra lateral control eye. These ratios are shown in Table B.1 and Fig. B.5.

Some animal to animal variation is to be expected and was found between the tensile properties of control cornea samples harvested from pigs at 12 month post operation. Consequently, we believe that it is more statistically meaningful to compare the ratio of each specific tensile property of the cornea sample harvested from an implanted eye to that from the corresponding contra lateral control eye. These ratios are shown in Table B.1 and Fig. B.5.

Table B.1 The ratio of mechanical properties of pig corneas harvested from implanted eyes to the ones from control eyes derived from the tensile test.

ID	UTSR [Strength], (MPa / MPa)	UTER [Elasticity], (% / %)	EMR [Stiffness], (MPa / MPa)	ETBR [Toughness], (MPa / MPa)
NH-1	1.00±0.19	1.4±0.10	0.76±0.04	1.14±0.26
HPN-2	0.96	0.93	0.88	1.00

Note: **UTSR:** Ultimate tensile stress ratio
UTER: Ultimate tensile elongation ratio
EMR : Elastic modulus ratio
ETBR: Energy to break ratio

The maximum tensile stress ratio is very close to unity for both NH-1 and HPN-2 implants, that is the relative strength of each implant and its corresponding control was very similar. The average value of the elongation ratio was significantly greater than

unity, whereas the elastic modulus ratio was below unity, for NH-1 implant indicating

that the implants were less stiff and could be stretched more before failure as compared to

the controls. The elongation, modulus, and energy to break ratios for HPN-2 implant

were close to unity that may suggest better integration and regeneration of HPN-2

implants into the host cornea than NH-1.

In general, mechanical testing showed that corneas from implanted eyes were as

robust as the untreated contralateral corneas representing stable regeneration and

integration of tissue-engineered implants in the host pig corneas.
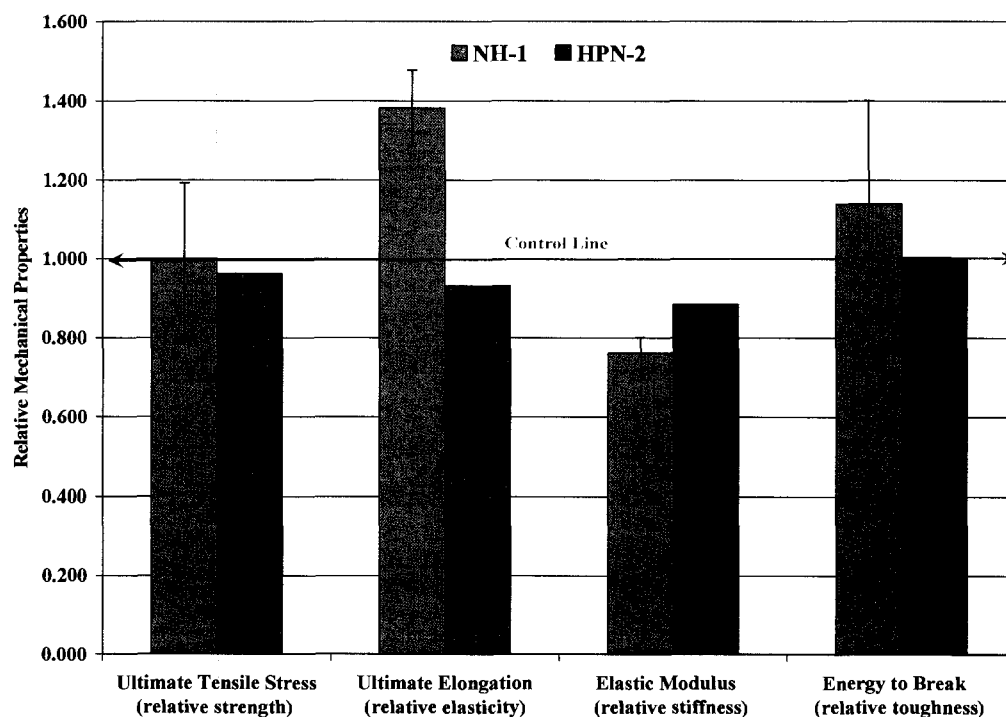
Figure B.5   The ratio of each specific tensile property of the pig cornea samples
harvested from NH-1 and HPN-2 implanted eyes to that from the
corresponding contralateral control eye.
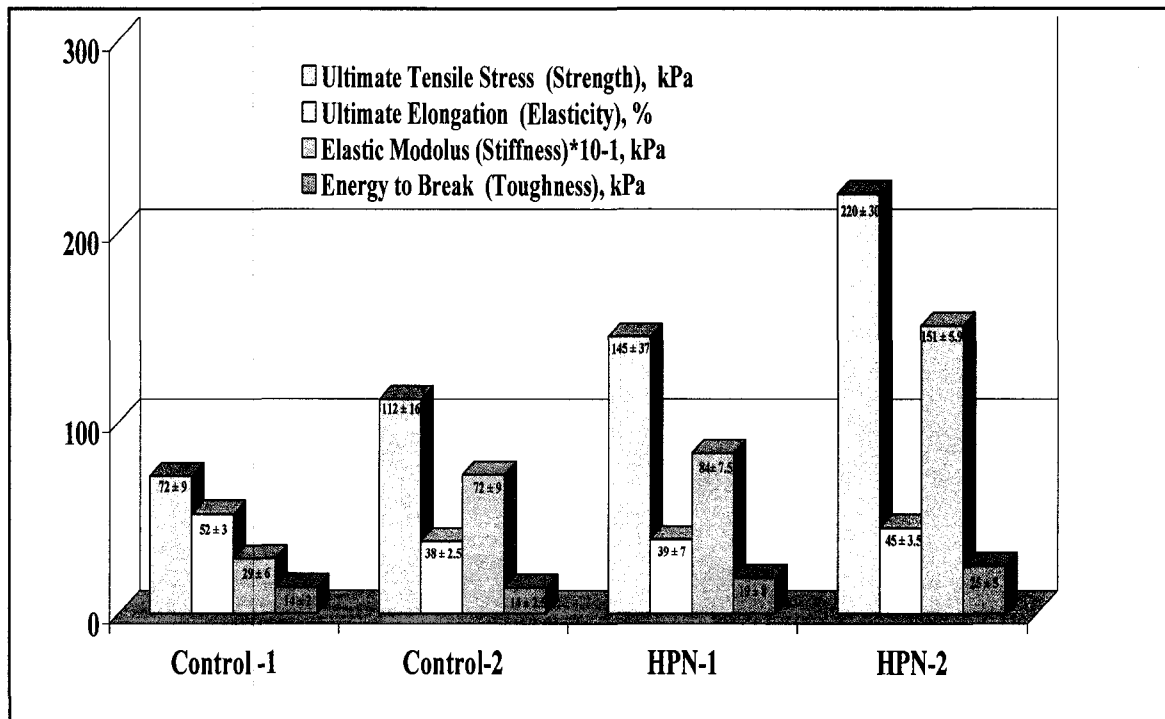
Figure B.6 Mechanical properties of HPN scaffolds vs. non-hybrid control scaffolds.

7.2.3 Differential Scanning Calorimetry (DSC)

Differential scanning calorimetry or DSC is a thermoanalytical technique in which the difference in the amount of heat required to increase the temperature of a sample and reference are measured as a function of temperature. Both the sample and reference are maintained at very nearly the same temperature throughout the experiment. Generally, the temperature program for a DSC analysis is designed such that the sample holder temperature increases linearly as a function of time [1]. The reference sample should have a well-defined heat capacity over the range of temperatures to be scanned. Figure B.7 shows a typical differential scanning calorimeter.
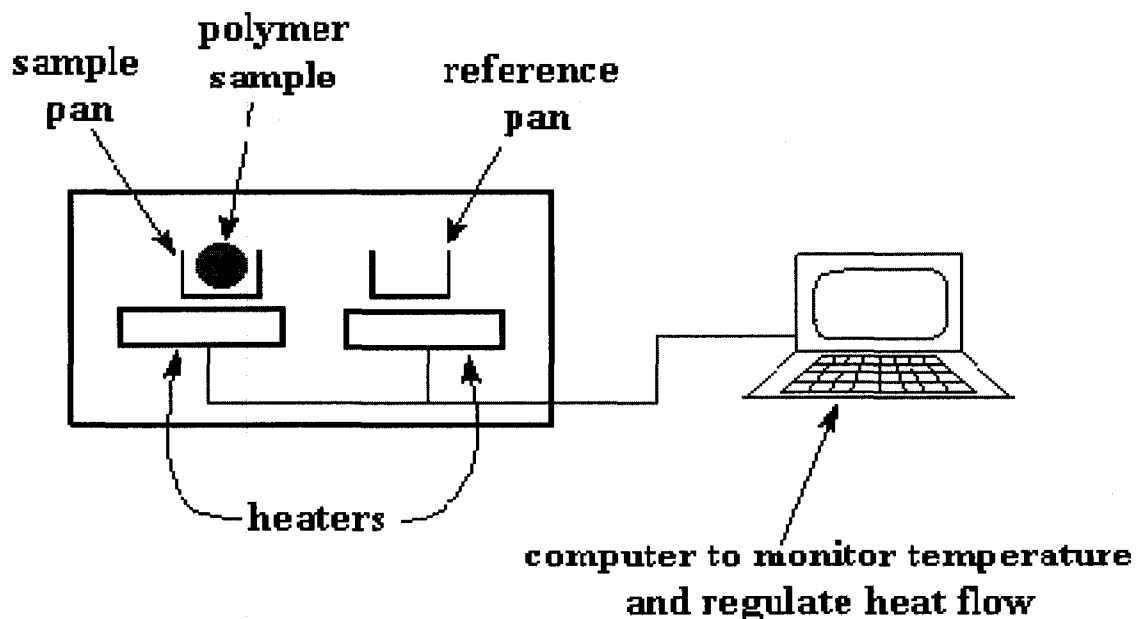
Figure B.7 A typical differential scanning calorimeter.

The basic principle underlying this technique is that, when the sample undergoes a physical transformation such as phase transitions, more (or less) heat will need to flow to it than the reference to maintain both at the same temperature. Whether more or less heat must flow to the sample depends on whether the process is exothermic or endothermic. For example, as a solid sample melts to a liquid it will require more heat flowing to the sample to increase its temperature at the same rate as the reference. This is due to the absorption of heat by the sample as it undergoes the endothermic phase transition from solid to liquid. Likewise, as the sample undergoes exothermic processes (such as crystallization) less heat is required to raise the sample temperature. By observing the difference in heat flow between the sample and reference, differential scanning calorimeters are able to measure the amount of heat absorbed or released during such transitions. DSC may also be used to observe more subtle phase changes, such as glass

transitions of polymers or denaturing temperature (T_d) of biopolymers [2,3]. Various collagen-based samples (10% v/v Nippon Ham collagen) including uncrosslinked collagen, EDC-NHS-crosslinked collagen (Control-1), and EDC-NHS-crosslinked collagen/chitosan (HPN-1) scaffolds were tested for DSC at a constant thermal rate of 2 °C/min from 20 to 80 °C.

Figure B.8 shows DSC calorimetric curves for Control-1, and HPN-1 corneal scaffolds. HPN-1 demonstrated a higher denaturing temperature (T_d= 67 °C) than that of Control-1 (T_d= 60 °C), and uncrosslinked collagen (T_d= 36 °C). The area of the peak (or dip) for HPN-1 seems to be larger than that of the control-1. We can measure the latent heat of melting by measuring the area of this peak. This confirms that HPN-1 has formed a more stable structure with a higher degree of crosslinking than Control-1 and uncrosslinked collagen scaffolds.
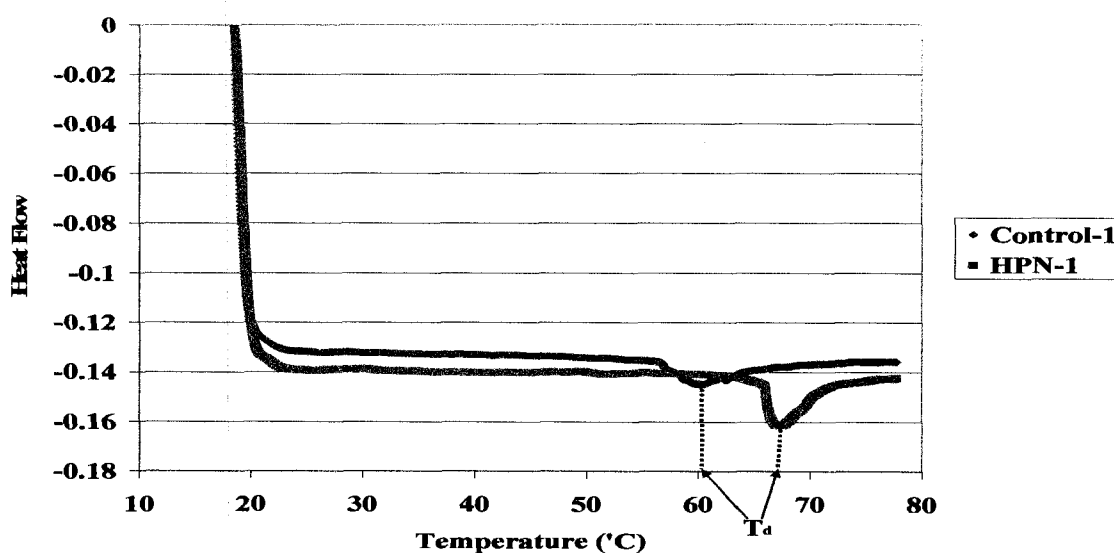
Figure B.8   DSC calorimetric curves for Control-1, and HPN-1 corneal scaffolds.

1. Dean J A. The Analytical Chemistry Handbook. New York, McGraw Hill, Inc.: 1995, 15.1–15.5.
2. Pungor E. A Practical Guide to Instrumental Analysis. Florida, Boca Raton: 1995, 181–191.
3. Skoog DA., Holler FJ, Nieman T. Principles of Instrumental Analysis. New York, Fifth Edition: 1998, 905–908

Appendix C:

7.3 Supplementary Statistical Data and Analysis for Paper I (Chapter 2).

This section details supplementary information on FED, RSD, and ANOVA statistical analysis performed for the study in Chapter 2. It includes FED and RSD Minitab[TM] statistical output data, and their corresponding residual plots for four responses, i.e. Elastic Modulus (kPa), Energy to Break (kPa), Light Transmission (%),and Epithelial Cells Count (Cell /mm^2).

7.3.1 FED Minitab[TM] Output Data:

Full Factorial Design
```
Factors:    3   Base Design:        3, 8
Runs:      27   Replicates:            3
Blocks:     3   Center pts (total):    3
Block Generators:  replicates
All terms are free from aliasing.
Design Table
Run  Block  A  B  C
  1    1    -  -  -
  2    1    +  -  -
  3    1    -  +  -
  4    1    +  +  -
  5    1    -  -  +
  6    1    +  -  +
  7    1    -  +  +
  8    1    +  +  +
  9    1    0  0  0
 10    2    -  -  -
 11    2    +  -  -
 12    2    -  +  -
 13    2    +  +  -
 14    2    -  -  +
 15    2    +  -  +
 16    2    -  +  +
 17    2    +  +  +
 18    2    0  0  0
 19    3    -  -  -
 20    3    +  -  -
 21    3    -  +  -
 22    3    +  +  -
 23    3    -  -  +
 24    3    +  -  +
 25    3    -  +  +
 26    3    +  +  +
 27    3    0  0  0
```

7.3.1.1 Minitab™ Output Data: Factorial Fit: Elastic Modulus vs. Block, X1 (CTN), X2 (EDC), X3 (PEG)

```
Estimated Effects and Coefficients for Elastic Modulus (kPa) (coded units)

Term                          Effect    Coef  SE Coef      T       P
Constant                               553.5    13.69   40.42   0.000
Block 1                                -46.6    18.25   -2.55   0.021
Block 2                                 35.1    18.25    1.92   0.073
X1 (CTN)                       109.1    54.5    13.69    3.98   0.001
X2 (EDC)                       368.9   184.5    13.69   13.47   0.000
X3 (PEG)                      -465.8  -232.9    13.69  -17.01   0.000
X1 (CTN)*X2 (EDC)             -170.6   -85.3    13.69   -6.23   0.000
X1 (CTN)*X3 (PEG)             -15.2     -7.6    13.69   -0.56   0.585
X2 (EDC)*X3 (PEG)            -76.8     -38.4    13.69   -2.80   0.013
X1 (CTN)*X2 (EDC)*X3 (PEG)   254.1    127.0    13.69    9.28   0.000
Ct Pt                                 1140.2    41.07   27.76   0.000


S = 67.0726   R-Sq = 98.87%   R-Sq(adj) = 98.16%

Analysis of Variance for Elastic Modulus (kPa) (coded units)

Source              DF    Seq SS     Adj SS    Adj MS       F       P
Blocks               2     31804      31804     15902    3.53   0.054
Main Effects         3   2189530    2189530    729843  162.23   0.000
2-Way Interactions   3    211331     211331     70444   15.66   0.000
3-Way Interactions   1    387350     387350    387350   86.10   0.000
  Curvature          1   3466867    3466867   3466867  770.63   0.000
Residual Error      16     71980      71980      4499
Total               26   6358861
```
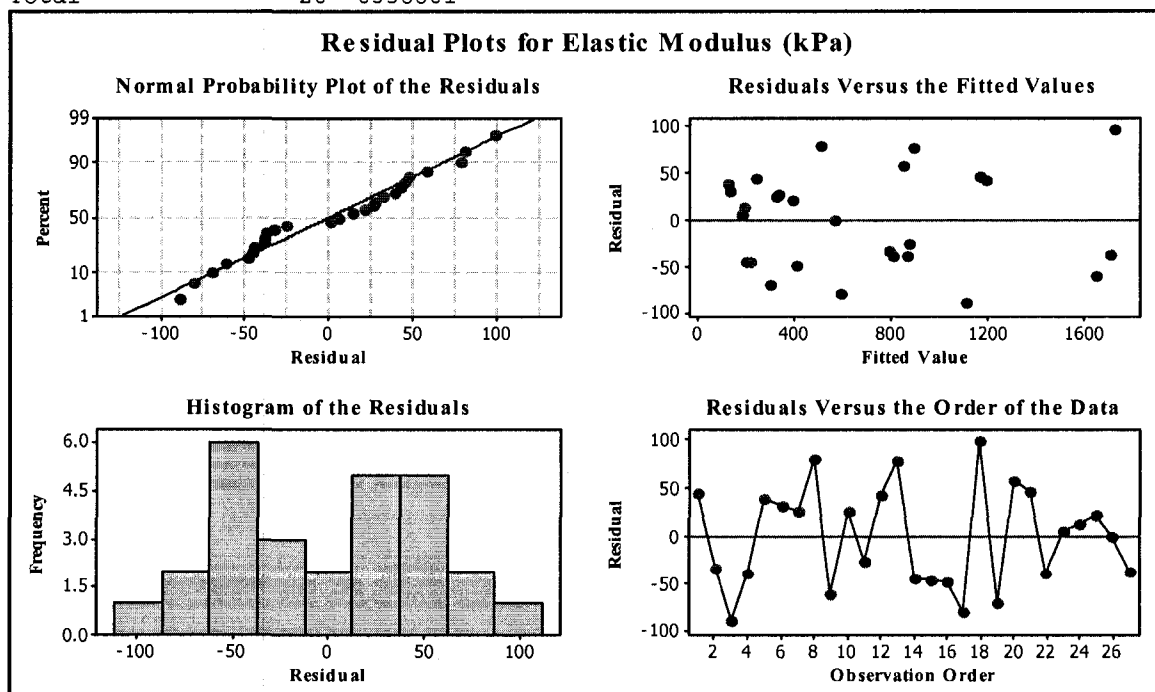

Figure C.1.1   FED residual plots for elastic modulus data.

199

7.3.1.2 Minitab™ Output Data: Factorial Fit: Energy to Break versus Block, X1 (CTN), X2 (EDC), X3 (PEG).

```
Estimated Effects and Coefficients for Energy to Break (kPa) (coded units)

Term                         Effect    Coef  SE Coef       T      P
Constant                             12.925   0.3102   41.66  0.000
Block 1                              -1.319   0.4136   -3.19  0.006
Block 2                               0.159   0.4136    0.39  0.705
X1 (CTN)                      3.400   1.700   0.3102    5.48  0.000
X2 (EDC)                     -4.767  -2.383   0.3102   -7.68  0.000
X3 (PEG)                     -7.517  -3.758   0.3102  -12.11  0.000
X1 (CTN)*X2 (EDC)             0.350   0.175   0.3102    0.56  0.581
X1 (CTN)*X3 (PEG)           -2.400  -1.200   0.3102   -3.87  0.001
X2 (EDC)*X3 (PEG)           -5.400  -2.700   0.3102   -8.70  0.000
X1 (CTN)*X2 (EDC)*X3 (PEG)  -0.517  -0.258   0.3102   -0.83  0.417
Ct Pt                                17.742   0.9307   19.06  0.000


S = 1.51981   R-Sq = 97.77%   R-Sq(adj) = 96.38%


Analysis of Variance for Energy to Break (kPa) (coded units)

Source              DF   Seq SS   Adj SS   Adj MS        F      P
Blocks               2    27.97   27.970   13.985     6.05  0.011
Main Effects         3   544.69  544.688  181.563    78.60  0.000
2-Way Interactions   3   210.26  210.255   70.085    30.34  0.000
3-Way Interactions   1     1.60    1.602    1.602     0.69  0.417
  Curvature          1   839.38  839.378  839.378   363.40  0.000
Residual Error      16    36.96   36.957    2.310
Total               26  1660.85
```
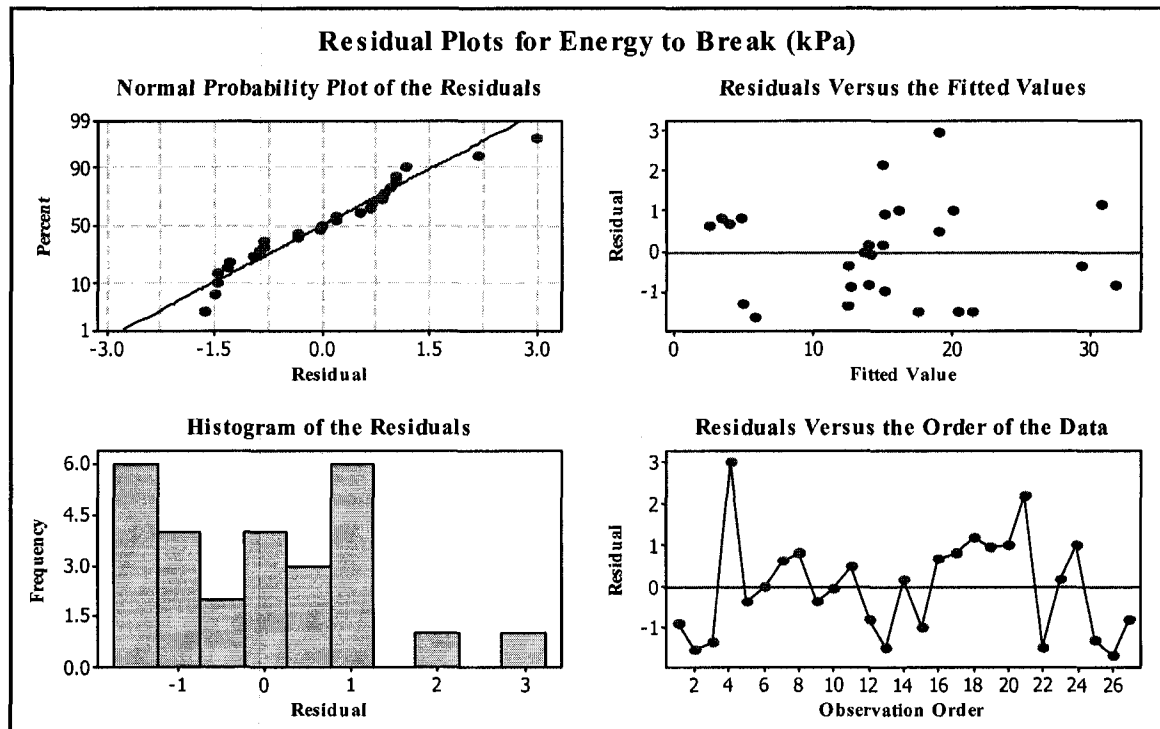

Figure C.1.2 FED residual plots for energy to break data.

7.3.1.3 Minitab™ Output Data: Factorial Fit: White Light Transmission vs. Block, X₁ (CTN), X₂ (EDC), X₃ (PEG).

```
Estimated Effects and Coefficients for White Light Transmission (%) (coded
    units)

Term                       Effect   Coef  SE Coef        T      P
Constant                            86.22   0.3014   286.02  0.000
Block 1                             -0.11   0.4019    -0.27  0.793
Block 2                              0.80   0.4019     2.00  0.063
X1 (CTN)                    -5.12   -2.56   0.3014    -8.49  0.000
X2 (EDC)                   -26.37  -13.18   0.3014   -43.73  0.000
X3 (PEG)                   -25.67  -12.83   0.3014   -42.57  0.000
X1 (CTN)*X2 (EDC)           -5.08   -2.54   0.3014    -8.43  0.000
X1 (CTN)*X3 (PEG)           -4.38   -2.19   0.3014    -7.27  0.000
X2 (EDC)*X3 (PEG)          -26.07  -13.03   0.3014   -43.24  0.000
X1 (CTN)*X2 (EDC)*X3 (PEG)  -4.42   -2.21   0.3014    -7.33  0.000
Ct Pt                              -12.88   0.9043   -14.25  0.000


S = 1.47675   R-Sq = 99.74%   R-Sq(adj) = 99.57%


Analysis of Variance for White Light Transmission (%) (coded units)

Source              DF    Seq SS    Adj SS    Adj MS        F      P
Blocks               2      10.3     10.28      5.14     2.36  0.127
Main Effects         3    8281.0   8280.96   2760.32  1265.74  0.000
2-Way Interactions   3    4347.2   4347.15   1449.05   664.46  0.000
3-Way Interactions   1     117.0    117.04    117.04    53.67  0.000
  Curvature          1     442.6    442.61    442.61   202.96  0.000
Residual Error      16      34.9     34.89      2.18
Total               26   13232.9
```


Residual Plots for White Light Transmission (%)
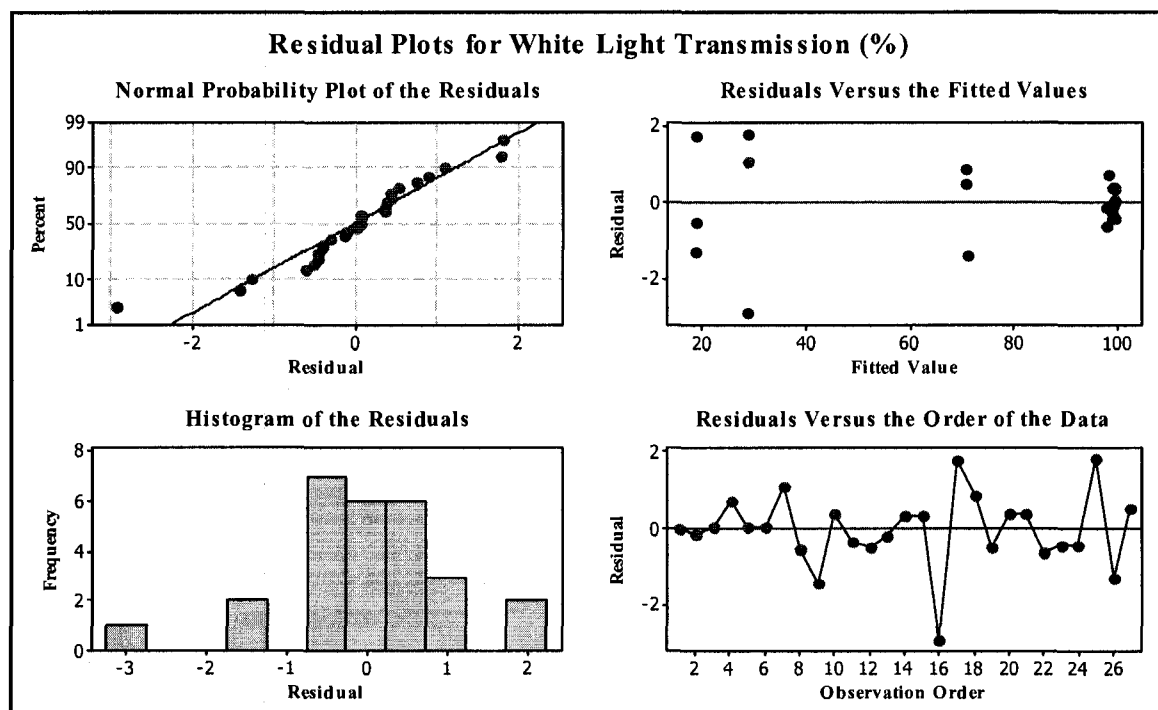
Figure C.1.3   FED residual plots for white light transmission data.

7.3.1.4 Minitab™ Output Data: Factorial Fit: Epithelial Cells Count vs. Block, X₁ (CTN), X₂ (EDC), X₃ (PEG).

```
Estimated Effects and Coefficients for Epithelial Cell Count-cell/mm2 (coded
     units)

Term                              Effect    Coef  SE Coef      T      P
Constant                                   2801.7    81.73  34.28  0.000
Block 1                                    -148.3   108.98  -1.36  0.193
Block 2                                     151.9   108.98   1.39  0.183
X1 (CTN)                          -477.0   -238.5    81.73  -2.92  0.010
X2 (EDC)                          -897.2   -448.6    81.73  -5.49  0.000
X3 (PEG)                          -159.8    -79.9    81.73  -0.98  0.343
X1 (CTN)*X2 (EDC)                 -436.2   -218.1    81.73  -2.67  0.017
X1 (CTN)*X3 (PEG)                  499.8    249.9    81.73   3.06  0.008
X2 (EDC)*X3 (PEG)                  682.3    341.2    81.73   4.17  0.001
X1 (CTN)*X2 (EDC)*X3 (PEG)         384.7    192.3    81.73   2.35  0.032
Ct Pt                                       670.3   245.20   2.73  0.015

S = 400.414   R-Sq = 84.77%   R-Sq(adj) = 75.24%

Analysis of Variance for Epithelial Cell Count-cell/mm2 (coded units)

Source              DF     Seq SS    Adj SS    Adj MS      F      P
Blocks               2     405474    405474    202737   1.26  0.309
Main Effects         3    6347902   6347902   2115967  13.20  0.000
2-Way Interactions   3    5433921   5433921   1811307  11.30  0.000
3-Way Interactions   1     887811    887811    887811   5.54  0.032
  Curvature          1    1198258   1198258   1198258   7.47  0.015
Residual Error      16    2565305   2565305    160332
Total               26   16838671
```


Figure C.1.4   FED residual plots for epithelial cell count data.

7.3.2 RSD Minitab™ Output Data:

7.3.2.1 Response Surface Regression: Elastic Modulus vs. X₁ (CTN), X₂ (EDC), X₃ (PEG)

```
The analysis was done using uncoded units.
Estimated Regression Coefficients for Elastic Modulus (kPa)

Term                       Coef  SE Coef        T      P
Constant                   -1781     313   -5.694  0.000
X1 (CTN)                   56000    9092    6.160  0.000
X2 (EDC)                    1020      98   10.399  0.000
X3 (PEG)                    1236     619    1.996  0.054
X1 (CTN)*X1 (CTN)        -913323  123845   -7.375  0.000
X2 (EDC)*X2 (EDC)            -91       9  -10.518  0.000
X3 (PEG)*X3 (PEG)          -2207     423   -5.220  0.000
X1 (CTN)*X2 (EDC)          -2274    1281   -1.775  0.085
X1 (CTN)*X3 (PEG)          -1017    6406   -0.159  0.875
X2 (EDC)*X3 (PEG)            -85     107   -0.799  0.430


S = 235.4   R-Sq = 82.6%   R-Sq(adj) = 78.2%

Analysis of Variance for Elastic Modulus (kPa)

Source          DF     Seq SS     Adj SS    Adj MS      F      P
Regression       9    9238021    9238021   1026447  18.53  0.000
  Linear         3    2679828    6513874   2171291  39.19  0.000
  Square         3    6346862    6346862   2115621  38.18  0.000
  Interaction    3     211331     211331     70444   1.27  0.299
Residual Error  35    1939262    1939262     55407
  Lack-of-Fit    5    1814831    1814831    362966  87.51  0.000
  Pure Error    30     124431     124431      4148
Total           44   11177283
```
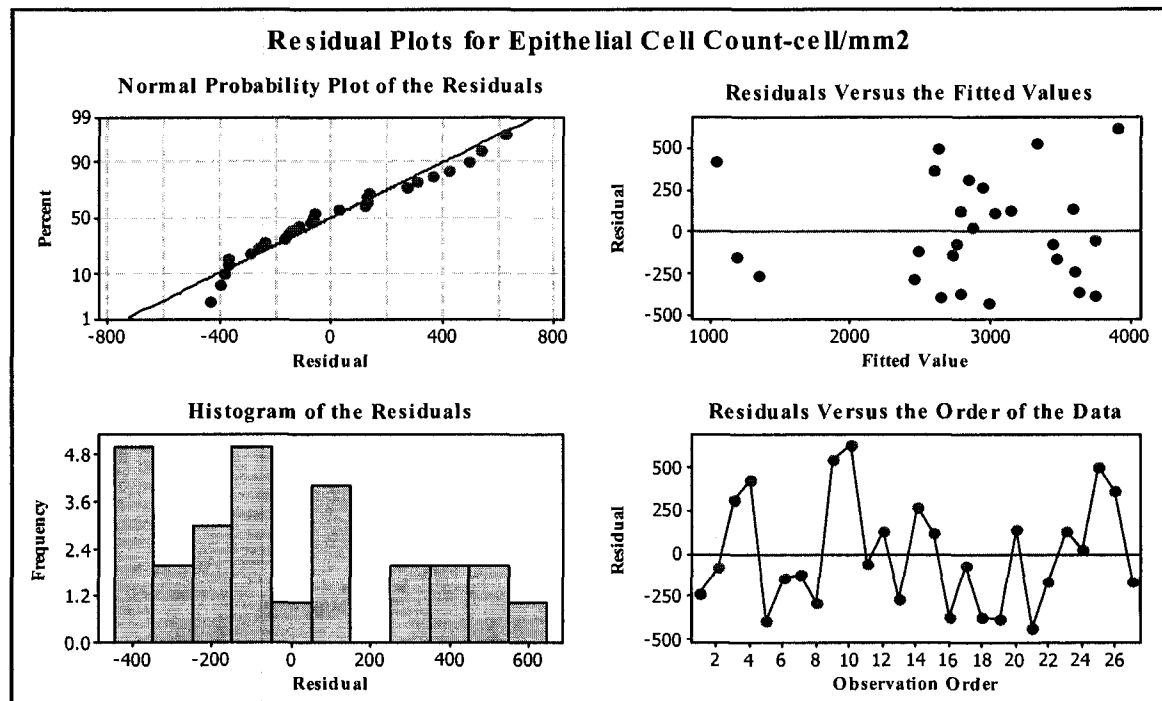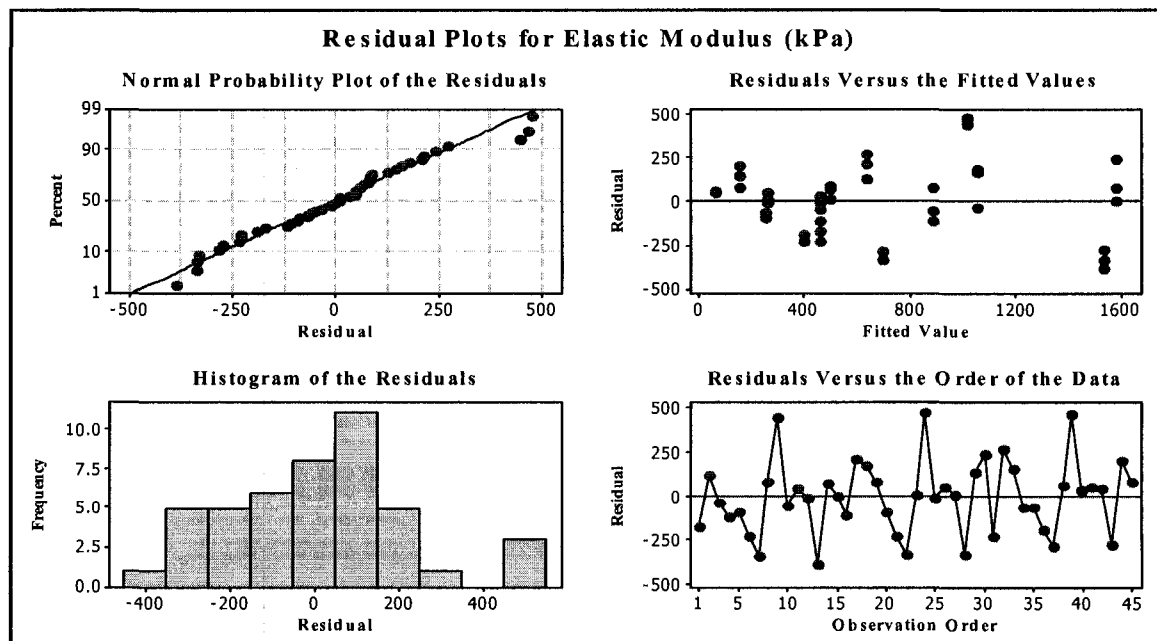

Figure C.2.1 RSD residual plots for elastic modulus data.

7.3.2.2 Response Surface Regression: Energy to Break vs. X_1 (CTN), X_2 (EDC), X_3 (PEG)

The analysis was done using uncoded units.
Estimated Regression Coefficients for Energy to Break (kPa)

Term			Coef	SE Coef	T	P
Constant			-3.2	4.92	-0.661	0.513
X1 (CTN)			801.2	143.00	5.603	0.000
X2 (EDC)			7.1	1.54	4.622	0.000
X3 (PEG)			42.2	9.74	4.331	0.000
X1 (CTN)*X1	(CTN)		-14962.7	1947.97	-7.681	0.000
X2 (EDC)*X2	(EDC)		-0.7	0.14	-4.923	0.000
X3 (PEG)*X3	(PEG)		-33.2	6.65	-4.988	0.000
X1 (CTN)*X2	(EDC)		4.7	20.15	0.232	0.818
X1 (CTN)*X3	(PEG)		-160.0	100.77	-1.588	0.121
X2 (EDC)*X3	(PEG)		-6.0	1.68	-3.573	0.001

S = 3.702   R-Sq = 79.9%   R-Sq(adj) = 74.7%

Analysis of Variance for Energy to Break (kPa)

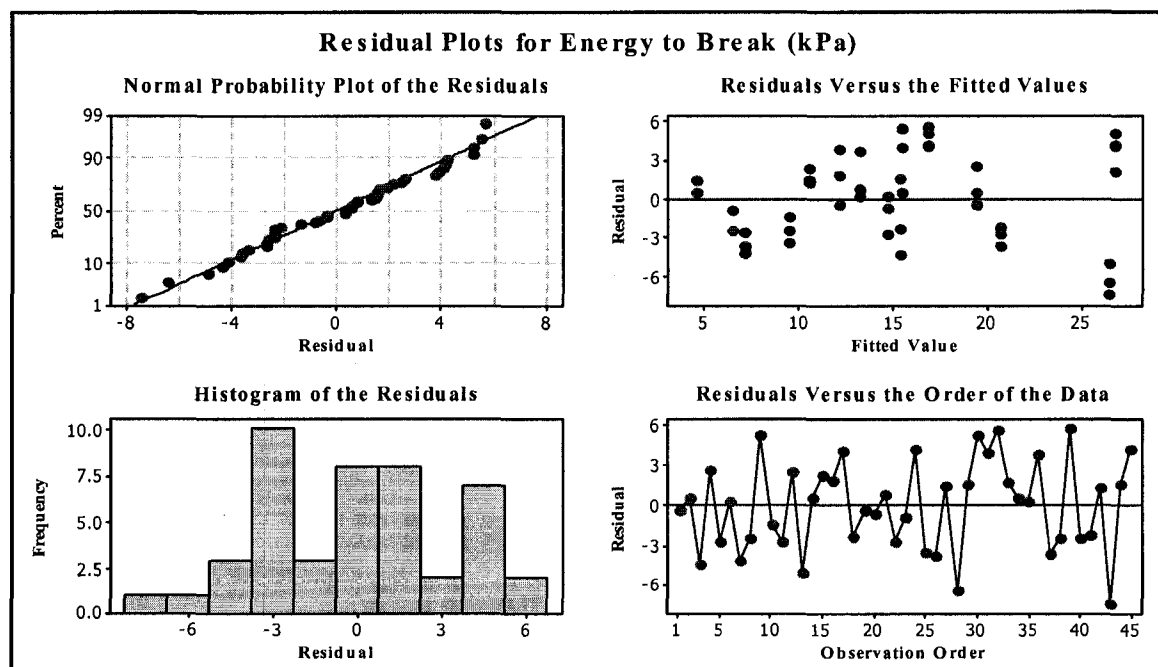| Source	DF	Seq SS	Adj SS	Adj MS	F	P
Regression	9	1902.74	1902.74	211.415	15.42	0.000
Linear	3	826.25	586.50	195.502	14.26	0.000
Square	3	866.23	866.23	288.744	21.06	0.000
Interaction	3	210.26	210.26	70.085	5.11	0.005
Residual Error	35	479.79	479.79	13.708		
Lack-of-Fit	5	405.87	405.87	81.173	32.94	0.000
Pure Error	30	73.92	73.92	2.464		
Total	44	2382.52				

Figure C.2.2 RSD residual plots for energy to break data.

7.3.2.3 Response Surface Regression: White Light Transmission vs. X_1 (CTN), X_2 (EDC), X_3 (PEG)

The analysis was done using uncoded units.
Estimated Regression Coefficients for White Light Transmission (%)

Term			Coef	SE Coef	T	P
Constant			88.0	6.59	13.340	0.000
X1 (CTN)			-510.1	191.68	-2.661	0.012
X2 (EDC)			2.2	2.07	1.051	0.300
X3 (PEG)			94.6	13.05	7.252	0.000
X1 (CTN)*X1	(CTN)		15285.1	2611.08	5.854	0.000
X2 (EDC)*X2	(EDC)		0.2	0.18	0.899	0.375
X3 (PEG)*X3	(PEG)		-3.1	8.91	-0.351	0.727
X1 (CTN)*X2	(EDC)		-67.8	27.01	-2.509	0.017
X1 (CTN)*X3	(PEG)		-292.2	135.07	-2.163	0.037
X2 (EDC)*X3	(PEG)		-29.0	2.25	-12.866	0.000

S = 4.963   R-Sq = 96.1%   R-Sq(adj) = 95.1%

Analysis of Variance for White Light Transmission (%)

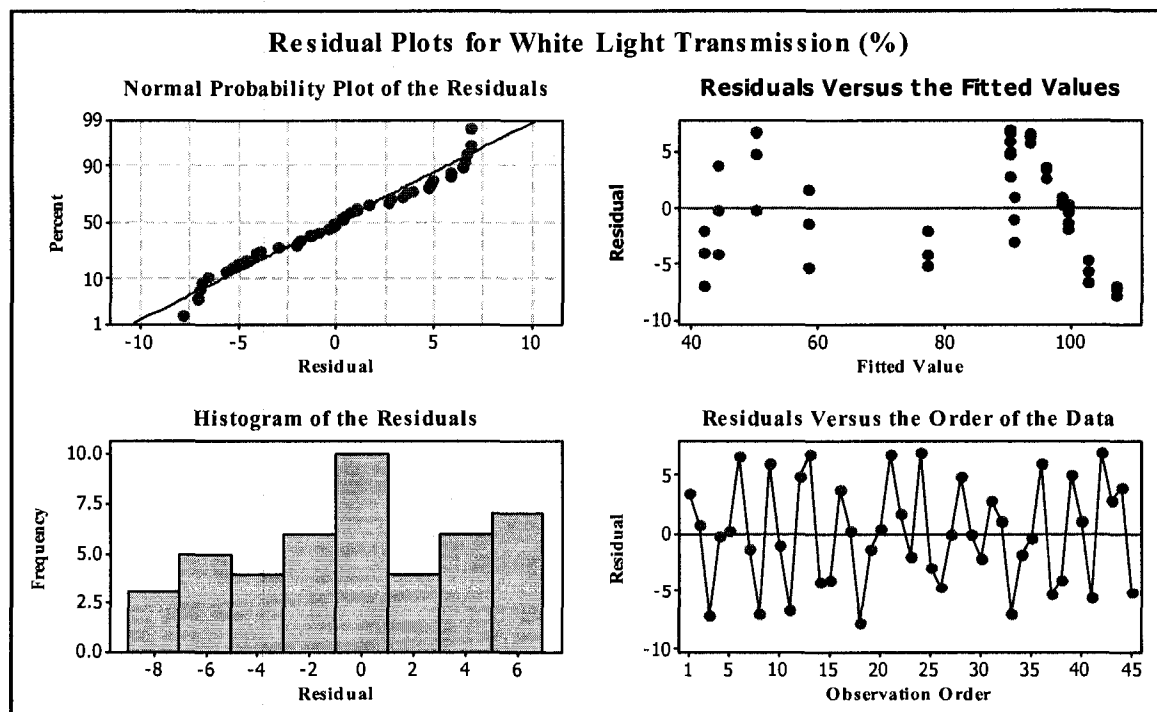| Source	DF	Seq SS	Adj SS	Adj MS	F	P
Regression	9	21287.9	21287.9	2365.32	96.04	0.000
Linear	3	15791.9	1716.9	572.31	23.24	0.000
Square	3	1148.8	1148.8	382.95	15.55	0.000
Interaction	3	4347.2	4347.2	1449.05	58.83	0.000
Residual Error	35	862.0	862.0	24.63		
Lack-of-Fit	5	738.9	738.9	147.77	35.99	0.000
Pure Error	30	123.2	123.2	4.11		
Total	44	22149.9				

Figure C.2.3 RSD residual plots for white light transmission data.

205

7.3.2.4 Response Surface Regression: Epithelial Cell Count vs. X1 (CTN), X2 (EDC), X3 (PEG)

The analysis was done using uncoded units.
Estimated Regression Coefficients for Epithelial Cell Count-cell/mm2

Term			Coef	SE Coef	T	P
Constant			4147	484	8.564	0.000
X1 (CTN)			13517	14078	0.960	0.344
X2 (EDC)			79	152	0.521	0.606
X3 (PEG)			-2743	958	-2.862	0.007
X1 (CTN)*X1	(CTN)		-138343	191769	-0.721	0.475
X2 (EDC)*X2	(EDC)		-51	13	-3.784	0.001
X3 (PEG)*X3	(PEG)		-2571	655	-3.929	0.000
X1 (CTN)*X2	(EDC)		-5816	1984	-2.931	0.006
X1 (CTN)*X3	(PEG)		33322	9920	3.359	0.002
X2 (EDC)*X3	(PEG)		758	165	4.585	0.000

S = 364.5   R-Sq = 86.1%   R-Sq(adj) = 82.5%

Analysis of Variance for Epithelial Cell Count-cell/mm2

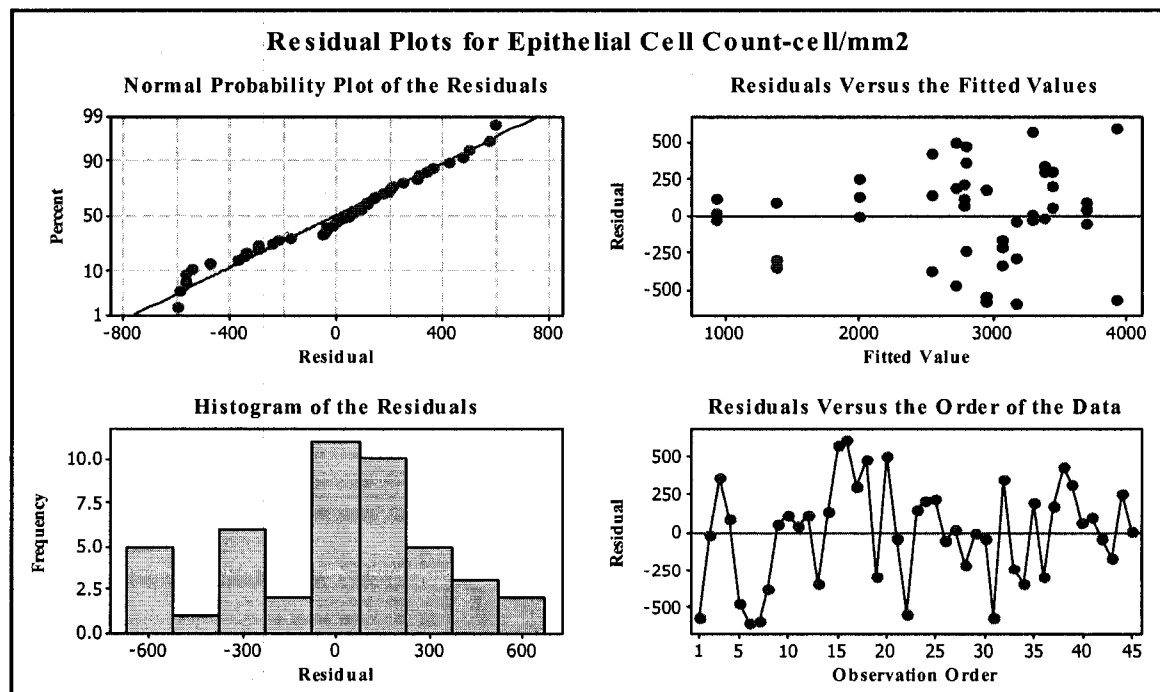| Source	DF	Seq SS	Adj SS	Adj MS	F	P
Regression	9	28725380	28725380	3191709	24.02	0.000
Linear	3	19999388	1680387	560129	4.22	0.012
Square	3	3292071	3292071	1097357	8.26	0.000
Interaction	3	5433921	5433921	1811307	13.63	0.000
Residual Error	35	4649857	4649857	132853		
Lack-of-Fit	5	1565978	1565978	313196	3.05	0.024
Pure Error	30	3083879	3083879	102796		
Total	44	33375237				

Figure C.2.4 RSD residual plots for epithelial cell count data.
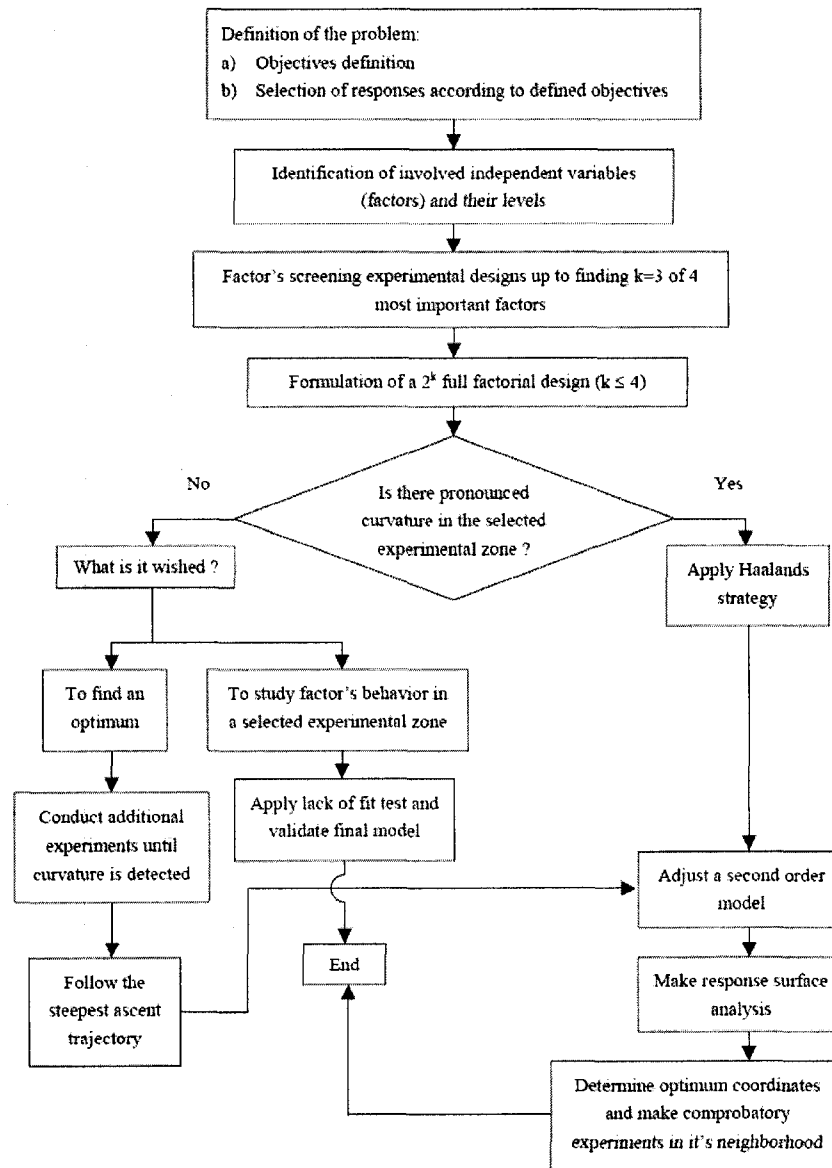
Figure C.3   Scheme showing the strategy of an empirical optimization process (SEROP)[1].

1.   Brossard Perez LE, Cortez LAB, Mesa J, Bezzon G, Olivares Gómez E. The strategy of empirical research and optimization process. Pesquisa Operacional 2001; 21(1): 89-105.

Appendix D:

7.4 Supplementary Statistical Data and Analysis for Paper IV (Chapter 5).

This section details supplementary information on FED and ANOVA analysis performed for Chapter 4. It includes complete ANOVA tables, residual plots, main effect plots, and interaction plots for three responses, i.e. contact angle measurements, FTIR, and endothelial cells numbers.

7.4.1 Contact Angle Measurement

Table D.1 Analysis of variance for contact angle measurements, using adjusted sum of squares for tests.

Source	DF	Seq SS	Adj SS	Adj MS	F	P
X_1	1	118	118	118	25	0.000
X_2	2	1487	1487	744	160	0.000
X_3	2	37	37	18	4	0.028
X_1*X_2	2	1.4	1.4	0.7	0.15	0.863
X_1*X_3	2	57	57	29	6	0.005
X_2*X_3	4	152	152	38	8	0.000
$X_1*X_2*X_3$	4	113	113	28	6	0.001
Error	36	167	167	4.6		
Total	53	2134				

*X1: Substrate Material
*X2: RF Power (W)
*X3: Alginate Concentration (g/100ml)
*DF: Degree of Freedom = n-1
*SS: Sum of Squares
*Seq. SS: sequential sums of squares
*Adj. SS: adjusted sums of squares (if the model is orthogonal and does not contain covariates then Adj. SS = Seq. SS).
*MS: Mean of Squares
*F: Test Statistics = (Variance between samples/Variance within samples) = $(MSB_{siteB}/MSB_{errorB})$
*P: The probability that the means of dependent variable do not statistically differ from each other.

208
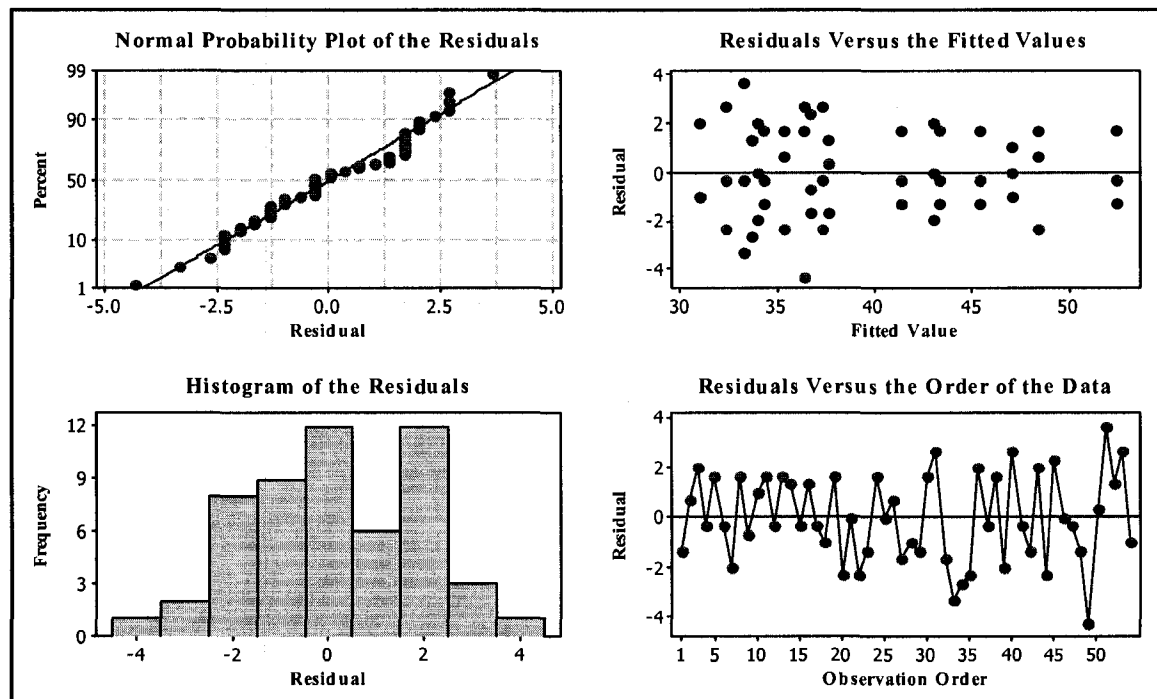
**Figure D.1**   Residual plots for contact angle measurement data.

The residual plots are used to check the models and normality of the data. The residuals are the actual yields minus the predicted yields. The fitted values are the results predicted by our model. A quick look at these plots in Fig. D.1 reveals that the residuals are normally distributed and that the data contain no outlier. Therefore, the plots are satisfactory, and show no cause for concern. To visualize the effects of factors, main effect plots and interaction plots are generated and shown in Fig. D.2 and Fig. D.3, respectively. These plots are based on the means of the response data and indicate the differences between the low setting and the high setting as well as between the categories on the graph. In other word, to calculate main effects, Minitab subtracts the mean response at the low or first level of the factor from the mean response at the high or second level of the factor. Three main effects plots are displayed in Fig. D.2: one for substrate material (a), one for RF power (b), and one for alginate concentration (c).
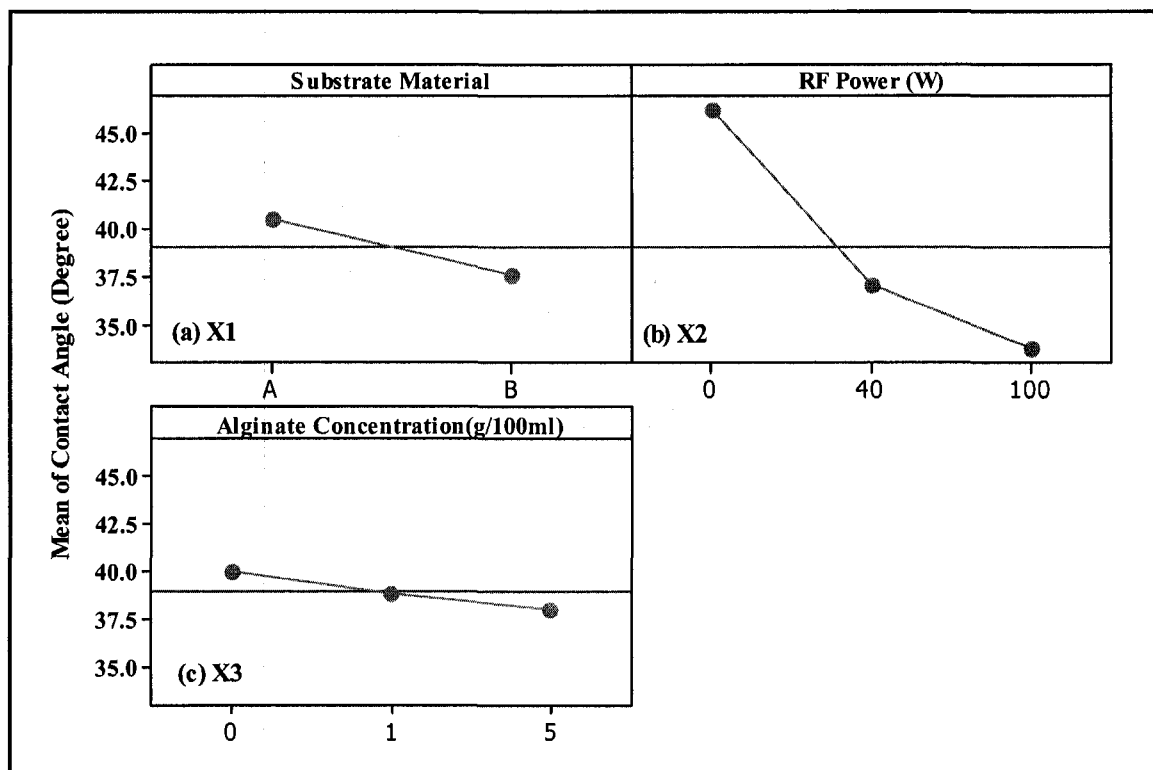
Figure D.2   Main effect plots for contact angle as a function of (a) substrate material, (b) RF power, and (c) alginate concentration.

Figure D.2 shows the main effects of all three factors on contact angle. We mentioned before that the values in the "F" column of Table D.1 suggested that plasma power had the highest influence on the contact angle followed by substrate material, and alginate concentration ($FB_{X2B}>FB_{X1B}>FB_{X3B}$). These effects are confirmed by the slope (S) of the lines in Fig. D.2 ($SB_{X2B}>SB_{X1B}>SB_{X3}$). A sharp decrease in contact angle was observed by increasing RF power (See steep line in Fig. D.2 (b)). This could be explained by the fact that by increasing the RF power more hydrophilic amine groups were formed on the surface contributing significantly into the increase in surface hydrophilicity. It can be seen from the main effect plot for alginate concentration in Fig. D.2 (c) that contact angle decreased with the increase of alginate concentration. This may be due to the higher grafting density of alginate at higher concentration.

Although RF power appears to affect the contact angle more than other factors, and it has already been verified in Table D.1, it is still very important to look at the interaction plots to see how big these effects are. An interaction can magnify or cancel out a main effect. An interaction plot shows the impact that changing the settings of one factor has on another factor. Usually, the significant interaction between two factors shows up as lines, which connect their settings, with sharply differing slopes. Figure D.3 summarizes the interaction effects.
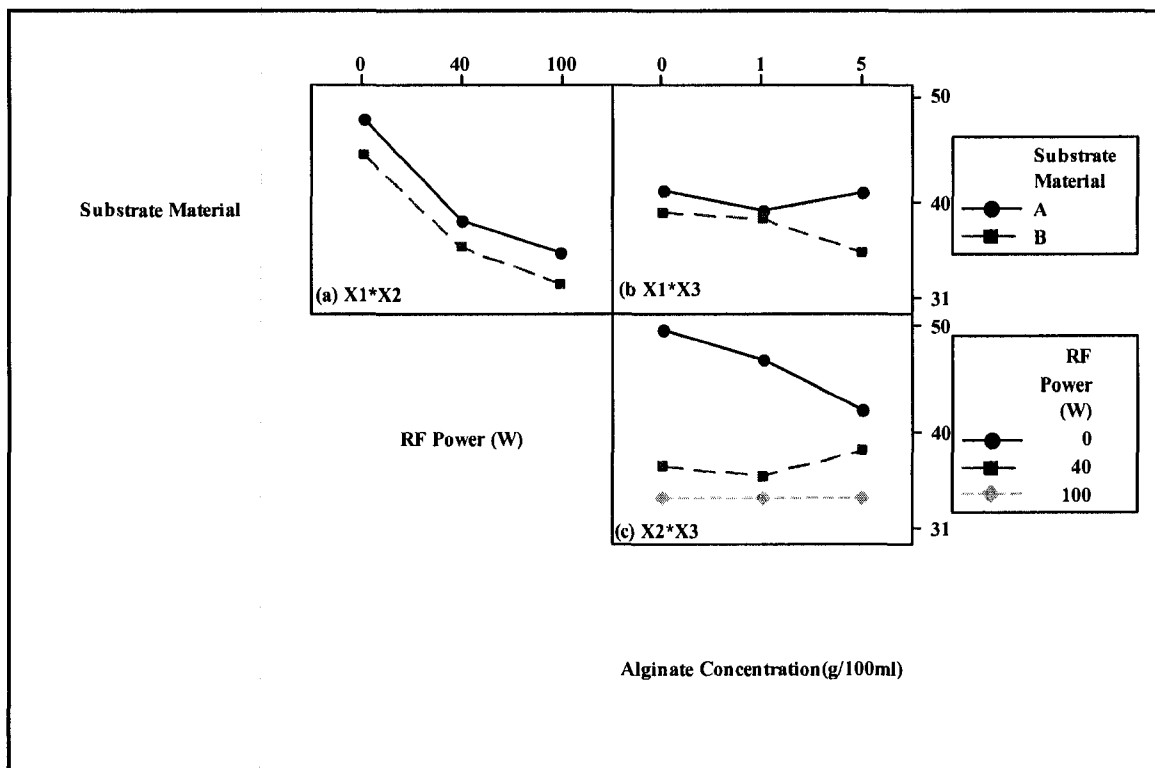
Figure D.3   Interaction plots for contact angle as a function of (a) substrate material and RF power or X_1*X_2 interaction, (b) substrate material and alginate concentration or X_1*X_3 interaction, and (c) RF power and alginate concentration or X_2*X_3 interaction.

For example, by looking at the slope of the lines in Fig. D.3, we can determine that all of the effects are significant with the exception of two-way interaction effect $XB_{1B}*XB_2$. This behavior has been clearly demonstrated by parallel lines in $XB_{1B}*XB_2$ interaction plot (Fig. D.3 (a)). This means that substrate material, and RF power have

211

independently influenced the contact angle values and the changes in the setting of one does not affect the influence of the other on contact angle.

As Fig. D.3 (b) shows, there is a significant difference (P = 0.005) between the contact angle for material A and B at 5% alginate concentration while the difference is not that significant at 1%, and 0% concentrations. It seems possible that these results are due to the higher alginate grafting performance to substrate material B that has more reaction sites (amine groups) for alginate molecules to bond to its surface resulting in lower contact angle.

Figure D.3(c) reveals the interaction between RF plasma power and alginate concentration and their effects on contact angle. At RF power of 100w, the effect of plasma is extremely dominating the effect of alginate concentration so that contact angle remains unchanged at different alginate concentrations. At RF=40 w, the results at 5% alginate concentration is rather contradictory and may be due to experimental error as contact angle should have decreased instead of increasing. In the absence of plasma treatment (RF=0 w), it is obvious that alginate concentration is dominating. The higher the alginate concentration the lower was the contact angle.

7.4.2 FTIR Analysis

Details of ANOVA for FTIR absorption intensity at 1036 cm^{-1} are summarized in Table D.2 and plotted in Figs D.4 to D.6.

Table D.2   Analysis of variance for FTIR peak absorbance values at 1036 cm^{-1} using adjusted sum of squares for tests.

Source	DF	Seq SS	Adj SS	Adj MS	F	P
X_1	1	0.3367	0.3367	0.3367	286.2	0.000
X_2	2	0.4557	0.4557	0.2278	193.6	0.000
X_3	2	0.6260	0.6260	0.3130	266.0	0.000
X_1*X_2	2	0.0476	0.0476	0.0238	20.2	0.000
X_1*X_3	2	0.0356	0.0356	0.0177	15.1	0.000
X_2*X_3	4	0.1653	0.1653	0.0413	35.1	0.000
$X_1*X_2*X_3$	4	0.0106	0.0106	0.0027	2.3	0.082
Error	36	0.0423	0.0423	0.0012		
Total	53	1.7200				
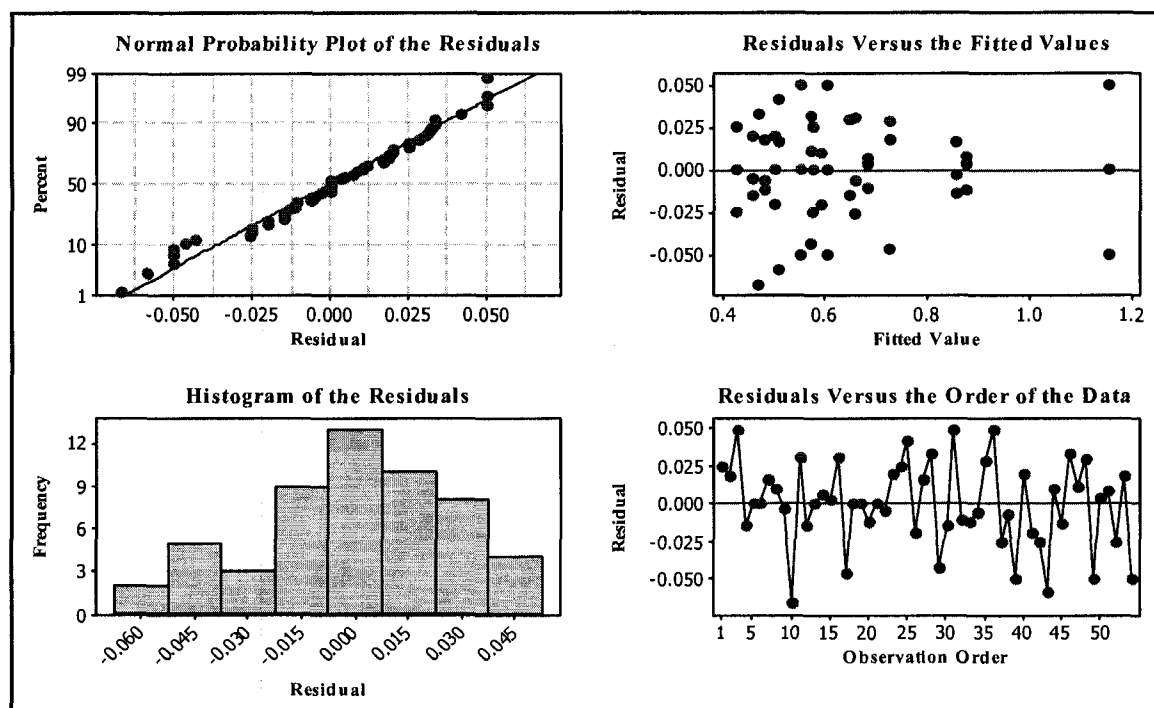
Figure D.4   Residual Plots for FTIR Intensity data at 1036 cm^{-1}

A quick look at residual plots in Fig. D.4 reveals that the residuals are normally distributed and that the data contain no outlier. Therefore, the plots are satisfactory, and show no cause for concern.

The steep lines in Fig. D.5 (a), (b), and (c) suggest that all three factors were influential on FTIR Peak intensity. However, the low variation in slope of the lines in Fig. D.5 indicates that none of the factors was more influential on FTIR intensity than the others. Also, the higher the RF power and alginate concentration the higher was the FTIR intensity at 1036 cm^{-1} a direct result of higher grafting density.
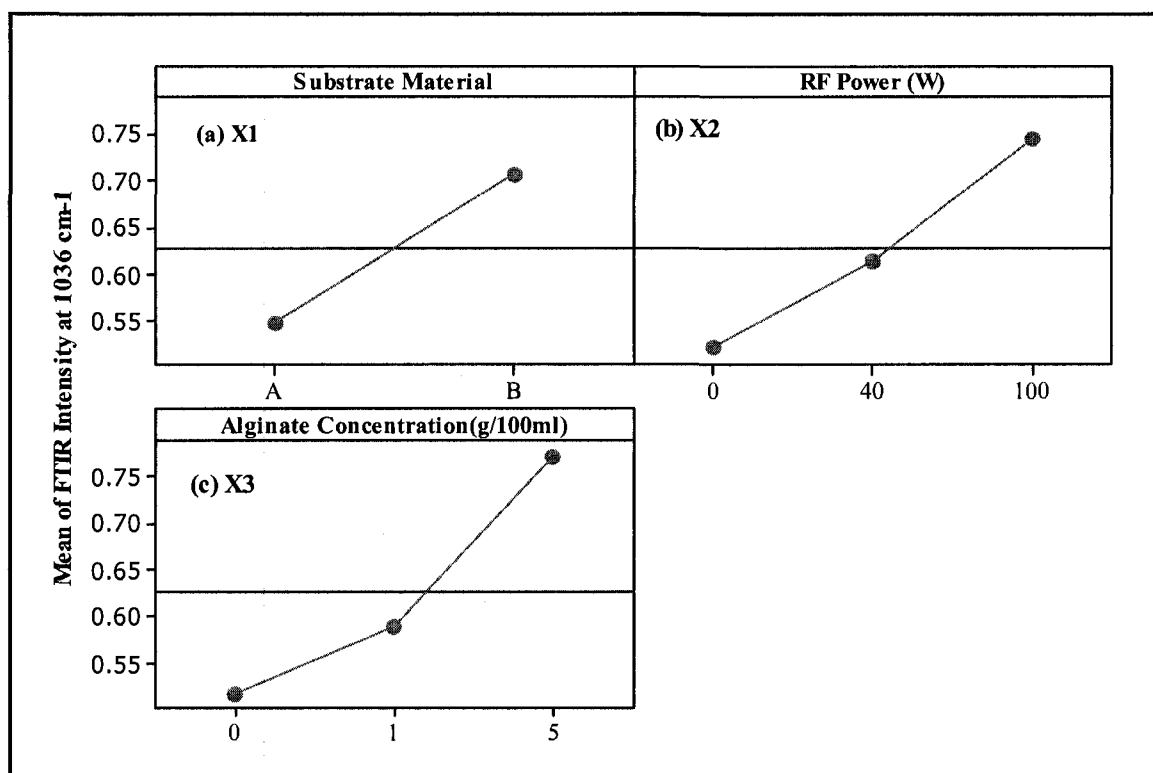
Figure D.5 Main effect plots for FTIR absorption intensity at 1036 cm^{-1} vs. (a) substrate material, (b) RF power, and (c) alginate concentration.

As shown in Fig. D.6, all factors are uniformly involved in two-way interactions and changes in the settings of one factor have a significant impact on the other factor. For example, looking at the interaction plot for alginate concentration and RF power (Fig.

214

D.6(c)), we can observe that at all alginate concentrations; the higher the RF power the higher is the alginate peak intensity.
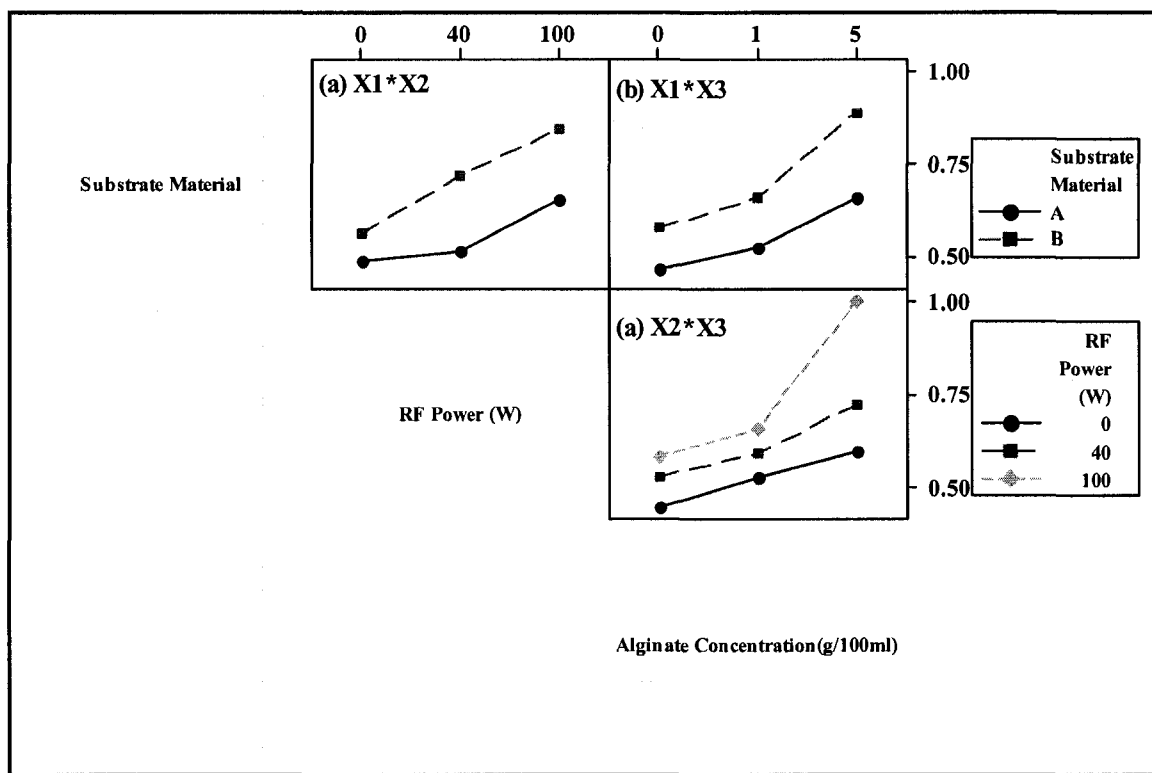

Figure D.6   Two-way interaction plots for FTIR absorption intensity at 1036 cm $^{-1}$ as a function of (a) substrate material and RF power or X_1*X_2 interaction, (b) substrate material and alginate concentration or X_1*X_3 interaction, and (c) RF power and alginate concentration or X_2*X_3 interaction.

7.4.3   Endothelial Cell Count Analysis

Details of ANOVA for endothelial cell count data are summarized in Table D.3 and plotted in Figs D.7 to D.9.

Table D.3   Analysis of variance for endothelial cell count (cell/mm2)-day5, using adjusted sum of squares for tests.

Source	DF	Seq SS	Adj SS	Adj MS	F	P
X_1	1	143.4	143.4	143.4	**19.51**	**0.000**
X_2	2	3153.0	3153.0	1576.5	**214.44**	**0.000**
X_3	2	16367.4	16367.4	8183.7	**1113.15**	**0.000**
X_1*X_2	2	217.8	217.8	108.9	**14.81**	**0.000**
X_1*X_3	2	104.5	104.5	52.2	**7.11**	**0.003**
X_2*X_3	4	3692.9	3692.9	923.2	**125.58**	**0.000**
$X_1*X_2*X_3$	4	37.6	37.6	9.4	**1.28**	**0.296**
Error	**36**	264.7	264.7	7.4		
Total	**53**	23981.3				
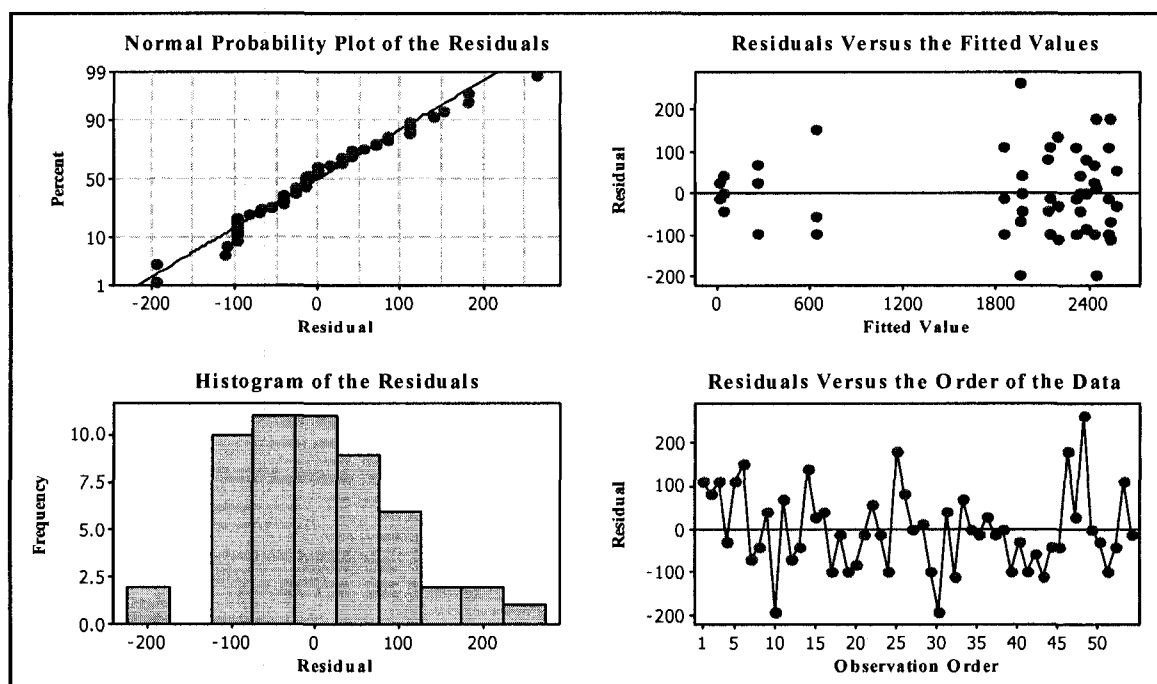
**Figure D.7**   Residual plots for endothelial cell count data (cell/mm2) on Day 5 post-seeding.

A quick look at residual plots in Fig. D.7 reveals that the residuals are normally distributed and that the data contain no outlier. Therefore, the plots are satisfactory, and show no cause for concern. It can be seen from the main effect plots in Fig. D.8 that the

alginate concentration has a bigger main effect than RF power, and substrate material. That is, the lines connecting the mean responses at various settings for alginate concentration (Fig. D.8 (c)) is steeper than the line connecting the mean responses at different settings of RF power (Fig. D.8 (b)), and category A and B of substrate material (Fig. D.8 (a)). It is also clear that substrate material B deters cells to a higher extent compared to material A likely due to the presence of chitosan in material B.
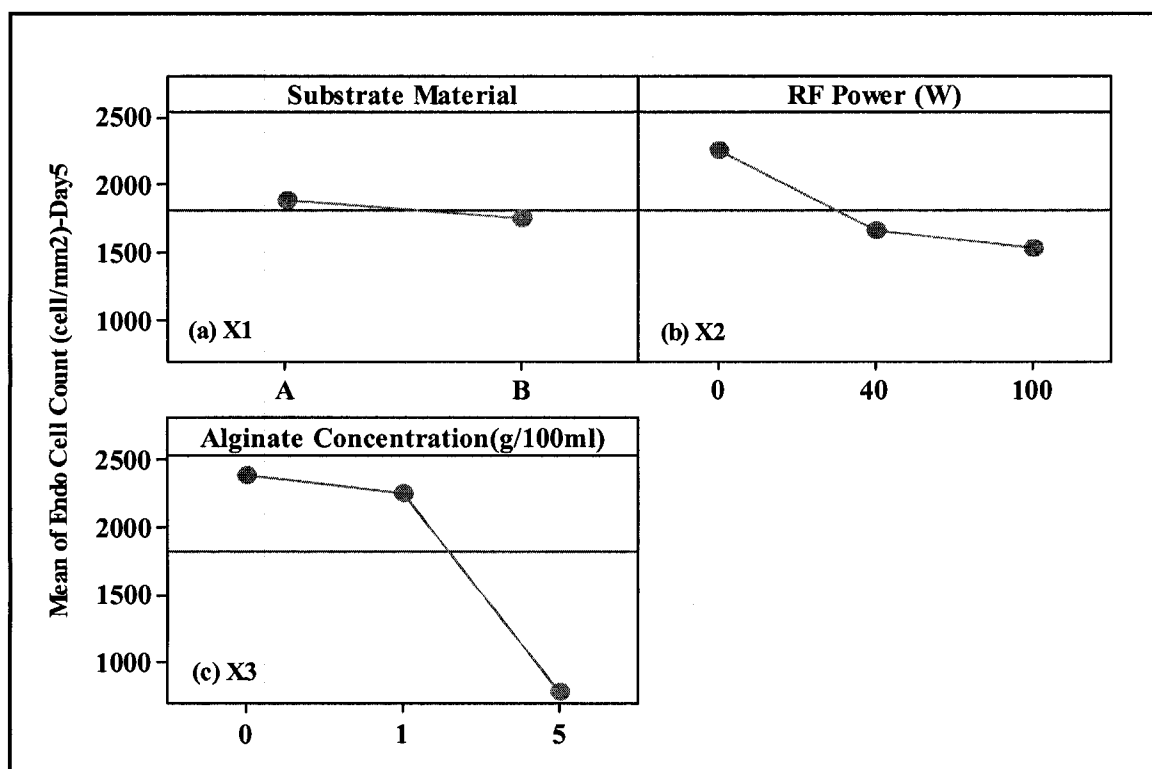
Figure D.8   Main effects plot (data means) for number of endothelial cells (cells/mm^2) attached to the treated and untreated surfaces on day 5 post-seeding vs. (a) substrate material, (b) RF power, and (c) alginate concentration.

Although alginate concentration appears to affect the cells attachment more than other factors, and it has already been verified in Table D.3, it is still very important to look at the interaction plots to see how big these effects are. An interaction can magnify or cancel out a main effect. Figure D.9 summarizes the interaction effects.
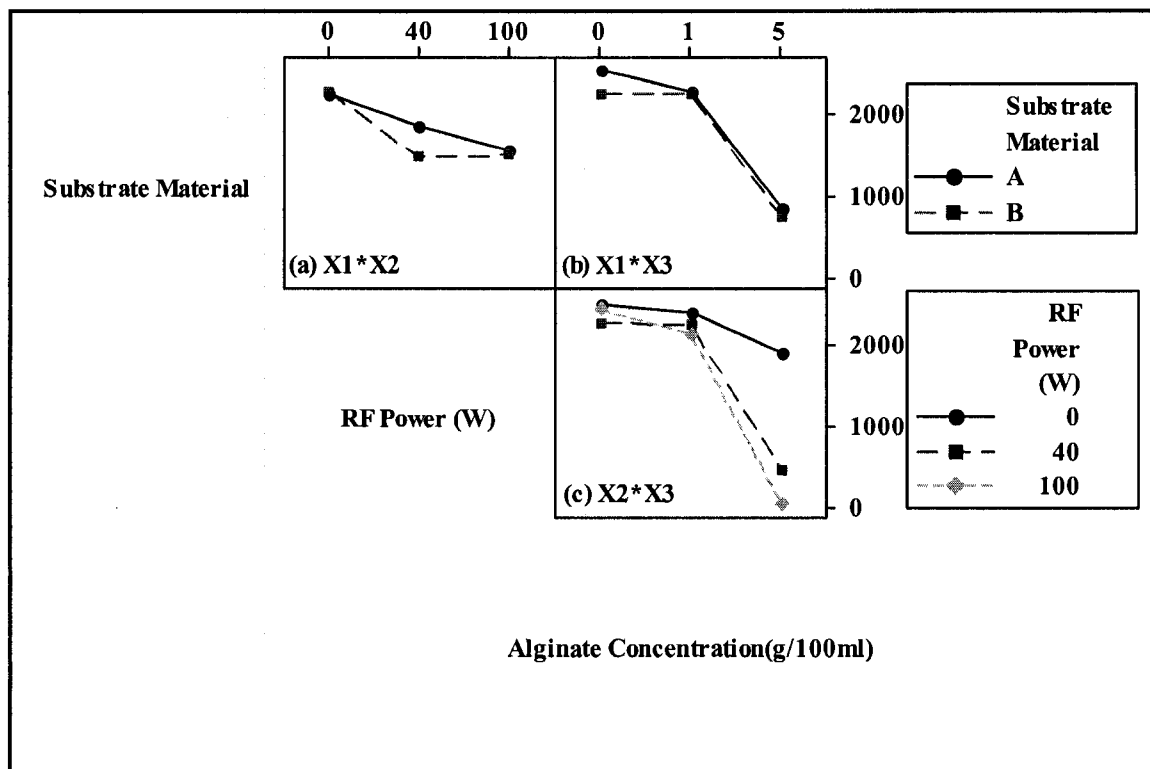
Figure D.9   Two way interaction plots (data means) for number of endothelial cells (cells/mm^2) attached to the treated and untreated surfaces on day 5 post-seeding as a function of (a) substrate material and RF power or X_1*X_2 interaction, (b) substrate material and alginate concentration or X_1*X_3 interaction, and (c) RF power and alginate concentration or X_2*X_3 interaction.

The interaction plot in Fig. D.9 (a) shows the impact of changing the type of substrate material on cells attachment at various RF power (X_1*X_2 interaction). It indicates that the interaction is only significant at RF power of 40w and the effect of material is more pronounced on cells inhibition while no significant effect can be observed at RF power 0 and 100 w. This could be due to the fact that at low RF power the number of amine groups introduced by plasma is not sufficient enough and the amine groups from chitosan becomes more dominant as compared to RF power of 100w that more amine groups are created via plasma and the effect of material becomes less important.

218

As shown in Fig. D.9 (b), the lines have almost similar slopes and the interaction between substrate material and alginate concentration (X_1*X_3 interaction) is not as significant as the interaction between substrate material and RF power (X_1*X_2 interaction). This is in close agreement with "F-values" in Table D.3 ($F_{X1X2} > F_{X1X3}$).

The interaction between RF power and alginate concentration (X_2*X_3 interaction) is depicted in Fig. D.9(c). This interaction is the most significant one because of the sharp slope of the lines especially at RF powers of 40 and 100w. This is again in good agreement with "F-values" in Table D.3 ($F_{X2X3} > F_{X1X2} > F_{X1X3}$). The cells inhibition for alginate concentration of 5% is greater than cells inhibition for alginate concentration of 1% and 0% at RF powers of 0, 40, and 100w. You can also see that the difference in cells inhibition for alginate concentration of 5% is more significant at RF power of 100w compared to 40w and 0w.